Constraints on the Evolution of Magmas from Diffusion-driven Chemical and Fe-Mg Isotopic Zoning in Natural Olivines analyzed by Femtosecond-LA-ICP-MS

Von der Naturwissenschaftlichen Fakultät der
Gottfried Wilhelm Leibniz Universität Hannover

zur Erlangung des Grades
Doktor der Naturwissenschaften (Dr. rer. nat.)

genehmigte Dissertation
von

Master of Science Martin Alexander Oeser-Rabe

geboren am 02.08.1984 in Siegburg

2015

Referent: Prof. Dr. Stefan Weyer

Korreferenten: PD Dr. Ingo Horn

Prof. Dr. Sumit Chakraborty

Tag der Promotion: 13.02.2015

Zusammenfassung

Die Untersuchung der Fraktionierung stabiler Isotope von Metallen hat sich in den letzten Jahren zu einem effektiven Instrument entwickelt, um Massenbewegungen bei hohen Temperaturen zu rekonstruieren. In der vorliegenden Doktorarbeit wurden Fe- und Mg-Isotopenverhältnisse mit höher Präzision *in situ* an natürlichen Olivinen gemessen mittels Femtosekunden-Laserablation-MC-ICP-MS, um (diffusionsbedingte) Fe- und Mg-Isotopenfraktionierung während der magmatischen Differentiation zu analysieren. Die Methode wurde durch die Analyse von silikatischen Referenzgläsern entwickelt und getestet. Die Ergebnisse dieser methodischen Untersuchung zeigen, (i) dass sich die Genauigkeit und die Reproduzierbarkeit der Fe-Isotopenanalysen verbessern, wenn Ni zur externen Massendiskriminierungskontrolle eingesetzt wird und (ii) dass δ^{56}Fe- und δ^{26}Mg-Werte in Silikaten mit hoher Präzision bestimmt werden können, d.h. die analytische Unsicherheit ist <0,13‰ (2 SD). Da die *in situ*-Analysen und die Analysen mittels lösungsbasierter MC-ICP-MS identische δ^{56}Fe- und δ^{26}Mg-Werte lieferten, können die ermittelten Fe- und Mg-Isotopendaten als Referenzwerte für die silikatischen Gläser betrachtet werden. Dies ermöglicht es, letztere als externe Standards bei Fe- und Mg-Isotopenanalysen von Silikat-Mineralen und -Gläsern zu verwenden.

Die Untersuchung natürlicher Olivine in Intraplattenvulkaniten und in Basalten von mittelozeanischen Rücken ergab, dass eine chemische Zonierung dieser Minerale (hinsichtlich des Fe-Mg-Verhältnisses) häufig mit einer Zonierung der Fe- und Mg-Isotope assoziiert ist. Die beobachteten Variationen in δ^{56}Fe und δ^{26}Mg (bis zu 1,6‰ bzw. 0,8‰) weisen im Allgemeinen auf diffusionsbedingte Fe- und Mg-Isotopenfraktionierung hin. Beim Großteil der analysierten Olivine zeigen die Fe-Mg-Isotopenprofile eine negative Korrelation. Dies ist ein starkes Argument dafür, dass sowohl die chemische als auch die isotopische Zonierung durch Austauschdiffusion von Fe und Mg erzeugt wurden, z.B. während der Differentiation des Magmas. Theoretische Modellierungen, welche im Rahmen dieser Arbeit entwickelt und auf die gemessenen Profile angewendet wurden, zeigen, dass die Kombination von chemischer *und* isotopischer Zonierung eine Rekonstruktion unterschiedlicher Prozesse während der magmatischen Differentiation ermöglicht. Die beobachteten diffusionsbedingten chemischen und isotopischen Zonierungen wurden schließlich genutzt, um die Dauer der diffusiven Äquilibrierung eines Olivins mittels Diffusionsmodellierung abzuschätzen. Diese Modellierungen liefern nützliche Erkenntnisse über die zeitlichen Dimensionen magmatischer Prozesse, wie z.B. die Zeitspanne zwischen einem Magmenmischungsereignis und einer Eruption.

Ein chemisches Ungleichgewicht zwischen Olivin und Schmelze wirkt sich nicht nur auf das Fe-Mg-Verhältnis, sondern auch auf die Konzentrationen der Spurenelemente im Olivin aus. Im Rahmen dieser Doktorarbeit wurden auch *in situ*-Analysen von Spurenelement-Konzentrationen in Olivinen durchgeführt, um Diffusionsgeschwindigkeiten dieser Elemente relativ zu Fe-Mg abzuschätzen und um ein besseres Verständnis der Diffusionsmechanismen in Olivin zu erhalten. Die Ergebnisse dieser Untersuchung zeigen, dass viele Kationen mit ähnlicher Geschwindigkeit durch das Olivin-Kristallgitter diffundieren. Die Unterschiede zwischen den Diffusionsraten der schnellsten (Li, Fe-Mg) und der langsamsten (Ti, Ca) Elemente betragen meist weniger als eine Größenordnung und können am ehesten mit der Fähigkeit der Elemente, unterschiedliche Diffusionspfade im Olivin zu nutzen, erklärt werden.

Schlagwörter: Eisen, Magnesium, stabile Isotope, Laserablation, geologisches Referenzmaterial, magmatische Differentiation, Olivin, Diffusion, Spurenelemente, Diffusionsmodellierung

Abstract

In recent years, the investigation of stable metal isotope fractionation has been proven to be a powerful means to characterize mass flux at high temperatures. In this study, high-precision *in situ* analyses of Fe- and Mg isotope ratios were performed on natural olivines by femtosecond-LA-MC-ICP-MS in order to investigate the fractionation of Fe- and Mg isotopes during magma evolution. The technique was developed and tested by analyzing a series of silicate reference glasses both *in situ* and by conventional solution nebulization MC-ICP-MS. The results of this methodical investigation show (i) that accuracy and reproducibility of the Fe isotope analyses are improved if Ni is used as an external mass discrimination monitor, and (ii) that *in situ* determinations of δ^{56}Fe and δ^{26}Mg values in silicates can be acquired with high precision, i.e. the analytical uncertainty is <0.13‰ (2 SD). Furthermore, the consistent results of bulk (solution nebulization MC-ICP-MS) and *in situ* (fs-LA-MC-ICP-MS) Fe- and Mg isotope analyses provide robust reference values for these glasses which can now be used for external standardization of *in situ* determinations of Fe- and Mg isotope ratios in silicate minerals and glasses.

The investigation of natural olivines in intra-plate volcanic rocks and in mid-ocean ridge basalts shows that Fe-Mg chemical zoning of these minerals is commonly coupled with Fe-Mg isotopic zoning. The observed intra-mineral variations in δ^{56}Fe and δ^{26}Mg (up to 1.6‰ and 0.8‰, respectively) point to, in general, diffusion-driven isotope fractionation. For the majority of the investigated olivines, the Fe-Mg isotopic profiles are inversely correlated which strongly indicates that the chemical as well as the isotopic zoning were generated by Fe-Mg inter-diffusion, e.g. diffusion of Fe into and Mg out of the olivines during magma differentiation. As shown by theoretical modeling (also performed in this study), combining the information of chemical *and* isotopic zoning in olivine allows to distinguish between various processes that may occur during magma evolution, namely diffusive Fe-Mg exchange between olivine and melt, rapid crystal growth, and Fe-Mg inter-diffusion simultaneous to crystal dissolution or growth. The observed diffusion-generated Fe-Mg chemical and isotopic zonations in natural olivines were used to estimate time spans of diffusive re-equilibration by diffusion modeling, which provides valuable information about the time scales of magmatic processes, e.g. the duration between a magma mixing event and eruption.

A chemical disequilibrium between olivine and melt, as frequently observed for the sample suite of this study, also affects the concentration of trace elements in olivine. In order to estimate diffusion rates of these elements relative to that of Fe-Mg and to obtain a better understanding of diffusion mechanisms in natural olivine, *in situ* analyses of minor and trace element contents in olivines by fs-LA-sector field-ICP-MS were also performed in the framework of this study. The results of this investigation indicate that many cations diffuse through olivine at similar rates. Although differences in the diffusion rates of the fastest (Li, Fe-Mg) and the slowest (Ti, Ca) elements certainly exist, this variation does not exceed one order of magnitude. Differences in diffusion rates are probably best explained by the ability of these elements to use different diffusion pathways in olivine, which in turn depends on charge and radius of their cations.

Keywords: iron, magnesium, stable isotopes, laser ablation, geological reference materials, magma differentiation, olivine, chemical diffusion, trace elements, diffusion modeling

TABLE OF CONTENTS

Zusammenfassung 3

Abstract 5

Introduction 9

Chapter I: High-precision Fe and Mg isotope ratios of silicate reference glasses determined *in situ* by femtosecond LA-MC-ICP-MS and by solution nebulization MC-ICP-MS 15

I.Abstract 15

I.1 Introduction 16

I.2 Reference materials and samples 17

I.3 Methods 17

I.3.1 *In situ* Fe isotope analyses by fs-LA-MC-ICP-MS 17

I.3.2 *In situ* Mg isotope analyses by fs-LA-MC-ICP-MS 22

I.3.3 Uncertainties of the laser ablation data 24

I.3.4 Sample preparation for solution nebulization MC-ICP-MS analyses 25

I.3.5 Solution nebulization MC-ICP-MS 27

I.4 Results and Discussion 28

I.4.1 Solution nebulization MC-ICP-MS data 28

I.4.2 Laser ablation data 30

I.4.3 Application to chemically zoned olivines 34

I.5 Conclusions 36

I.Tables 37

Chapter II: Processes and time scales of magmatic evolution as revealed by Fe-Mg chemical and isotopic zoning in natural olivines 41

II.Abstract 41

II.1 Introduction 42

II.2 Samples 43

II.3 Methods 45

II.3.1 Electron Microprobe Analyses 45

II.3.2 *In situ* Fe- and Mg isotope analyses 45
II.3.3 Modeling of chemical and isotopic zoning in olivines 47
II.4 Results 52
II.4.1 Fe-Mg chemical and isotopic zoning in natural "intra-plate" olivines 52
II.5 Discussion 55
II.5.1 Isotope effects in olivine during magma evolution 55
II.5.2 Origin of the chemical and isotopic zoning in "intra-plate" olivines 66
II.5.3 Diffusion modeling 70
II.6 Conclusions 77
II.Tables 78

Chapter III: Fe-Mg chemical and isotopic zoning in olivines from mid-ocean ridge basalts 83
III.Abstract 83
III.1 Introduction 83
III.2 Samples 84
III.3 Methods 86
III.3.1 Electron microprobe and *in situ* Fe- and Mg isotope analyses 86
III.3.2 Diffusion modeling and determination of time scales 87
III.4 Results and Discussion 88
III.4.1 Fe-Mg chemical and isotopic zoning in MORB olivines 88
III.4.2 Estimation of time scales by diffusion modeling 93
III.5 Conclusions 98
III.Tables 99

Chapter IV: Diffusion rates of minor and trace elements in natural olivines 103
IV.Abstract 103
IV.1 Introduction 103
IV.2 Samples 105
IV.3 Methods 105
IV.3.1 Electron microprobe and *in situ* trace element analyses 105
IV.3.2 Estimation of comparative diffusion coefficients in olivines 106
IV.4 Results and Discussion 108

IV.4.1 Trace element profiles across natural olivines 108
IV.4.2 Diffusion rates of trace elements relative to Fe-Mg 112
IV.5 Conclusions 116
IV.Tables 117

References 120

Appendix I 133
Appendix II 141
Appendix III 151
Appendix IV 157

Acknowledgements 167
Curriculum Vitae 168
List of Publications 171

Introduction

Fe- and Mg isotope fractionation during magma differentiation and the objectives of this study

Stable metal isotope fractionation represents a powerful tracer for a variety of geological processes in low- and high-temperature environments. For example, the investigation of Fe- and Mo isotope signatures in black shales and Fe-Mn crusts allows to elucidate the Earth's atmosphere-ocean redox evolution for the last ~3 billion years (e.g., Arnold et al., 2004a; Rouxel et al., 2005; Anbar and Rouxel, 2007). Also for high-temperature environments, large variations of Mg- and Fe isotopes (of up to 1‰) have been observed, in particular for rocks and minerals from the Earth's mantle (e.g., Williams et al., 2005; Pearson et al., 2006; Weyer and Ionov, 2007; Yang et al., 2009; Zhao et al., 2010; Pogge von Strandmann et al., 2011). In many cases, these isotope variations record metasomatic processes, i.e. disequilibrium processes that are typically associated with kinetic isotope effects. At high temperatures, these effects result in much larger isotope fractionations than equilibrium processes as the magnitude of equilibrium isotope fractionation is proportional to $1/T^2$. Nevertheless, several studies have observed a systematic difference between the Fe isotopic compositions of basalts and mantle rocks (e.g., Weyer et al., 2005; Schoenberg and Von Blanckenburg, 2006; Weyer et al., 2007; Weyer and Ionov, 2007; Teng et al., 2013; Craddock et al., 2013), pointing to a small, but detectable equilibrium fractionation of Fe isotopes (on the order of 0.1‰ in $^{56}Fe/^{54}Fe$) during partial melting of the mantle and/or fractional crystallization of mantle-derived melts. The silicate mineral olivine ($[Fe,Mg]_2SiO_4$) and the redox-sensitivity of iron appear to play a decisive role in generating this fractionation of Fe isotopes. Experimental studies as well as theoretical modeling indicate that Fe^{3+}-bearing phases are relatively enriched in heavy Fe isotopes (e.g., Polyakov and Mineev, 2000; Shahar et al., 2008; Dauphas et al., 2014). During partial melting of the mantle, Fe^{3+} behaves as an incompatible element and, therefore, preferentially enters into the melt (Weyer, 2008; Dauphas et al., 2009). Hence, a mantle-derived melt should show a heavier Fe isotopic composition than the residual mantle (mainly olivine, which incorporates only trace amounts of Fe^{3+}). This hypothesis was corroborated by a study by Teng et al. (2008), which showed that during fractional crystallization of olivine from a basaltic melt, the melt appears to be continuously enriched in heavy Fe isotopes, resulting in high $\delta^{56}Fe$ values for differentiated basalts and low $\delta^{56}Fe$ values for olivine phenocrysts in these rocks.

In contrast to Fe, a correlation between the Mg isotopic compositions of basalts and the degree of magma differentiation has not been observed yet, indicating that an equilibrium fractionation of Mg isotopes during crystal-melt fractionation at magmatic temperatures is negligibly small (<0.07‰ in $^{26}Mg/^{24}Mg$; Teng et al., 2007). However, recent investigations of olivine pheno- and xenocrysts in basaltic rocks have revealed highly variable Fe- and Mg isotopic compositions which are unlikely generated in equilibrium with the host magma (Dauphas et al., 2010; Teng et al., 2011; Weyer and Seitz, 2012). In particular, Fe isotopic compositions of bulk olivines are up to 1‰ (in $^{56}Fe/^{54}Fe$) lower than expected from equilibrium with the host magma, while Mg isotopic compositions are up to 0.35‰ too high (in $^{26}Mg/^{24}Mg$). Such large isotope variations strongly point to kinetic isotope effects, e.g. by diffusive processes during magma evolution, and the negatively correlated Fe- and Mg isotopic compositions found in olivines are very likely generated by the diffusion of Fe into and Mg out of olivine driven by a chemical gradient between crystal and melt (e.g., Teng et al., 2011; Weyer and Seitz, 2012). As light isotopes always diffuse slightly faster than their heavier counterparts (e.g., Richter et al., 2009a), the olivine should be relatively enriched in light Fe and heavy Mg isotopes. These conclusions were strongly supported by the findings of Sio et al. (2013) who observed inversely correlated Fe- and Mg isotopic zoning in a mm-sized, chemically zoned olivine phenocryst from Hawaiian basaltic lava. Sio et al. (2013) applied – *inter alia* – a microdrilling technique coupled with solution-based multi collector-ICP-MS analyses and, thus, demonstrated the potential of *in situ* Fe- and Mg isotope analyses to trace diffusion-driven processes during magma evolution. However, improvements regarding analytical uncertainty and spatial resolution are necessary to reliably resolve Fe-Mg isotopic zoning in smaller olivines. Furthermore, it is still unclear, whether Fe-Mg isotopic zoning is common in chemically zoned olivines and which processes exactly may be recorded by such zoning. Finally, a chemical disequilibrium between olivine and melt should not only affect the Fe-Mg ratio of the olivine, but also the concentration of trace elements in this crystal. However, diffusion rates of trace elements in olivine are often a subject of debate (see Chakraborty 2010 for a review). To address these open questions, the major subjects of the present dissertation are:

- The development of a method for high-precision *in situ* analyses of Fe- and Mg isotopic compositions of silicates by femtosecond- LA-MC-ICP-MS (**Chapter I**) in order to establish (i) appropriate standard material for *in situ* Fe- and Mg isotope analyses and (ii) an analytical routine for investigating potential Fe-Mg isotopic zoning in olivine (and other silicate minerals).

- The investigation of olivine pheno- and xenocrysts in intra-plate volcanic rocks (**Chapter II**) as well as in mid-ocean ridge basalts (**Chapter III**) in order to address the following questions:

  (a) Do chemically zoned olivine crystals commonly show zoning in δ^{56}Fe and δ^{26}Mg?

  (b) Can the isotopic zoning (combined with the chemical zoning) be used to gain information on magma evolution in different geological settings?

  (c) Can simplified diffusion modeling reproduce the chemical and isotopic zoning in magmatic olivine and thus provide information about the time scales of magma evolution?
- The investigation of trace element zoning in olivines from the same sample suite (**Chapter IV**) in order to estimate diffusion rates of minor and trace elements relative to that of Fe-Mg and to obtain a better understanding of diffusion mechanisms in natural olivine.

Olivine

As most investigations of this study have been performed on olivine crystals, the following section will give some basic information about its mineral chemistry. Olivine is the most abundant mineral of the Earth's upper mantle, and it occurs as a phenocryst phase as well as a groundmass constituent in a broad variety of volcanic rocks. It is also a common constituent in gabbroic rocks (Deer et al., 1992). There is a complete solid solution between the two end-members forsterite (Mg_2SiO_4) and fayalite (Fe_2SiO_4). Olivine crystallizes with orthorhombic symmetry, its structure consists of independent SiO_4 tetrahedra linked by divalent cations (mainly Fe^{2+} and Mg^{2+}) in sixfold coordination (Fig. 1; Deer et al., 1992). These octahedral sites (M1 and M2) can also be occupied by monovalent or trivalent cations (e.g., Li^{1+}, Cr^{3+}, Sc^{3+}) if charge balance is maintained by, for example, the incorporation of vacancies (e.g., Spandler and O'Neill, 2010). In general, large cations, such as Ca^{2+}, preferably enter the larger M2 site, although exceptions exist, e.g. Co^{2+} is larger than Mg^{2+}, but the former is preferentially incorporated into the smaller M1 site (see Brown 1982 for details). The M1 octahedra form a continuous chain along the crystallographic c-axis (direction z in Fig. 1), which may be an explanation for the fast diffusion of cations along [001] compared to [100] or [010] (e.g., Chakraborty, 2010; Spandler and O'Neill, 2010).

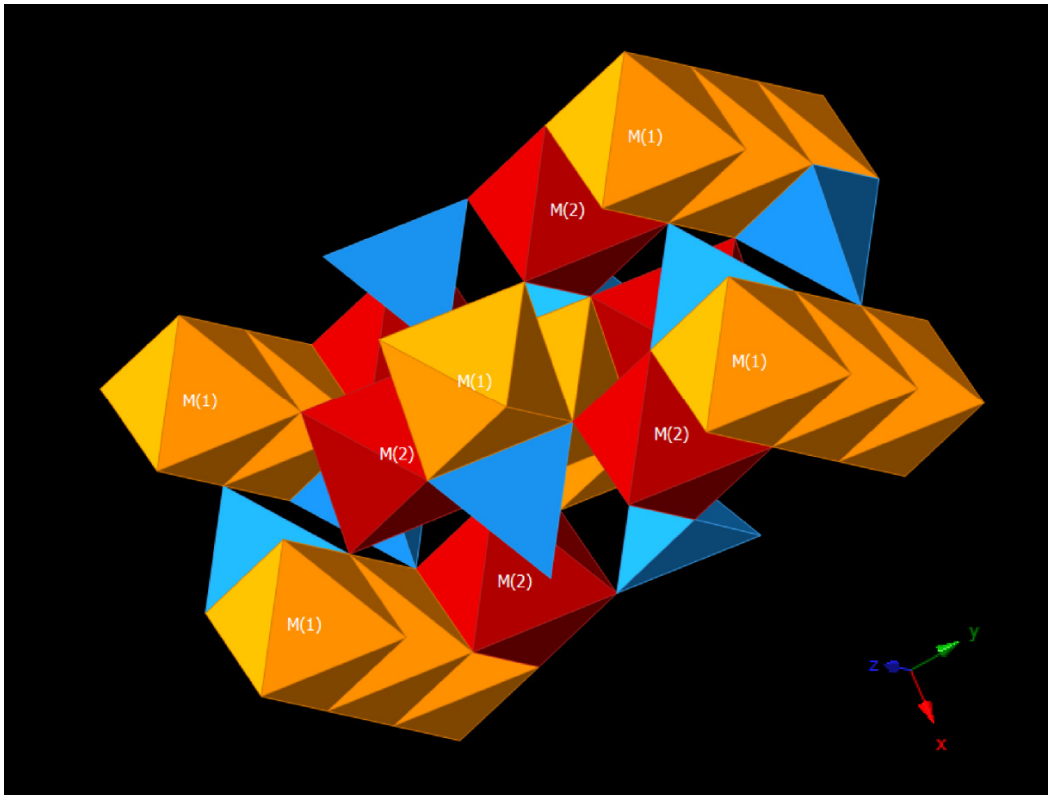

Figure 1: 3-dimensional crystal structure of olivine generated using the software CrystalMaker® . SiO_4 tetrahedra are shown in blue.

At 1 bar, pure forsterite has a liquidus temperature of ~1890°C, the melting point of pure fayalite is ~1205°C (Deer et al., 1992). As Mg-rich olivines crystallize earlier (i.e. at higher temperature) than Fe-rich olivines, a basaltic melt will become progressively enriched in Fe and other less compatible elements during cooling. The relative enrichment of Fe in a basaltic melt combined with rapid cooling can lead to an increasing chemical disequilibrium between olivines and melt, which will expedite diffusive Fe-Mg exchange between olivine and melt. If the system "freezes" (e.g., the magma erupts) before diffusive re-equilibration of the olivines has been completed, the result will be a volcanic rock with chemically zoned olivines. Several studies have obtained time information about magma evolution by diffusion modeling of such intra-mineral chemical zoning (e.g., Costa and Dungan, 2005; Kahl et al., 2011). However, diffusion-generated chemical zoning cannot always easily be distinguished from zoning that results mainly from prolonged crystal growth in an evolving melt (e.g., Dauphas et al., 2010). As outlined above, *in situ* analyses of Fe- and Mg isotope ratios in olivine provide a powerful tool to trace diffusion-driven processes during magma differentiation.

Chapter I: High-precision Fe and Mg isotope ratios of silicate reference glasses determined *in situ* by femtosecond LA-MC-ICP-MS and by solution nebulization MC-ICP-MS*

* A modified version of Chapter I has been published as: Oeser M., Weyer S., Horn I., Schuth S. (2014) High-Precision Fe and Mg Isotope Ratios of Silicate Reference Glasses Determined *In Situ* by Femtosecond LA-MC-ICP-MS and by Solution Nebulisation MC-ICP-MS. *Geostandards and Geoanalytical Research* **38**, 311-328.

I.Abstract

In this study, a technique for high precision-*in situ* Fe and Mg isotope analyses by femtosecond-laser ablation-multi collector-ICP-MS (fs-LA-MC-ICP-MS) was developed. This technique was employed to determine reference values for a series of common reference glasses that may be used for external standardization of *in situ* Fe and Mg isotope analyses of silicates. The analyzed glasses are part of the MPI-DING and USGS reference glass series and they consist of basaltic (BIR-1G, BCR-2G, BHVO-2G, KL2-G, ML3B-G) and komatiitic (GOR128-G and GOR132-G) compositions. Their Fe and Mg isotope compositions were determined by *in situ* fs-LA-MC-ICP-MS and by conventional solution nebulization multi-collector ICP-MS analyses. We determined δ^{56}Fe values for these glasses ranging between -0.04‰ and 0.10‰ (relative to IRMM-014) and δ^{26}Mg values ranging between -0.40‰ and -0.15‰ (relative to DSM-3). Our fs-LA-MC-ICP-MS results for both, Fe and Mg isotope compositions agree with solution nebulization analyses within analytical uncertainties. Furthermore, the results of three USGS reference glasses (BIR-1G, BHVO-2G, and BCR-2G) agree with previous results for powdered and dissolved aliquots of the same reference materials. Reproducibilities of the *in situ* analyses of δ^{56}Fe and δ^{26}Mg values are usually better than 0.12‰ and 0.13‰ (2 standard deviations = 2 SD), respectively. We further demonstrate that our technique is a suitable tool to resolve isotopic zoning in chemically zoned olivine crystals. It may be used for a variety of different applications on isotopically zoned minerals, e.g. in magmatic or metamorphic rocks or meteorites, to unravel their formation or cooling rates.

I.1 Introduction

High precision *in situ* stable isotope analyses of metals provide a powerful tool to resolve isotopic zoning and small-scale isotopic heterogeneities of geological materials (Horn et al., 2006; Jeffcoate et al., 2007; Steinhoefel et al., 2009b; Sio et al., 2013), allowing the elucidation of kinetic reactions and the genetic relationship between minerals and rocks. The availability of micro-analytical reference materials with well-characterized major and trace element and, in particular, isotope compositions is a prerequisite for such analyses. Various silicate reference glasses of natural composition are provided by the United States Geological Survey (USGS) as well as by the Max-Planck-Institut (MPI) in Mainz, Germany, (now denoted as "MPI-DING" glasses [Jochum et al., 2000]). The major and trace element contents of these glasses have been determined by different analytical methods, such as electron probe microanalysis, laser ablation ICP-MS, isotope dilution ICP-MS (Gao et al., 2002; Jochum et al., 2000, 2005b, 2006); however, *in situ* isotope data for these reference glasses are rare, e.g., only B, Li, Si, Sr and Pb isotope data are available for the MPI-DING glasses (Jochum et al., 2006, 2011). Yet, neither Fe nor Mg isotope compositions have been determined *in situ* for the USGS or MPI-DING reference materials. For the USGS glasses, Fe and Mg isotope data only exist for powdered and dissolved aliquots of the same materials used to make the glasses (e.g., Craddock and Dauphas, 2011; Pogge von Strandmann et al., 2011). Theoretically, the Fe- and Mg isotopic compositions of the powders should be identical to those of their respective glasses; however, this has not yet been proven. Furthermore, the Fe-Mg isotopic homogeneity of these reference materials needs to be assessed.

Femtosecond laser ablation (fs-LA) MC-ICP-MS is capable of high precision *in situ* Fe isotope analyses without apparent laser-induced isotopic fractionation (Horn and von Blanckenburg, 2007; Steinhoefel et al., 2009a). Accordingly, this technique is advantageous compared to conventional nanosecond LA-MC-ICP-MS techniques, as the latter frequently suffer from composition-dependent matrix effects during laser ablation, as e.g. reported for *in situ* Mg isotope analyses by Norman et al. (2006) and Janney et al. (2011). Xie et al. (2011) have demonstrated that *in situ* Mg isotope analyses of olivines by excimer LA-MC-ICP-MS can be precise (<0.1‰, 2 SD, for δ^{26}Mg) if a chemically and isotopically homogeneous olivine is used as a standard for the laser ablation isotope analyses, i.e. the matrices of standard and sample are matched. Similarly, Sio et al. (2013) used a San Carlos

olivine for their *in situ* Fe isotope analyses of a large chemically zoned Hawaiian olivine phenocryst and achieved precisions of ~0.2‰ (1 SD). Here we show that fs-LA-MC-ICP-MS is capable of (within analytical uncertainties) matrix-independent high precision Mg and Fe isotope analyses. We report Fe and Mg isotopic compositions of six MPI-DING and three USGS reference glasses (BIR-1G, BCR-2G, and BHVO-2G) that have been determined both *in situ* by fs-LA-MC-ICP-MS, as well as conventionally by (more precise) solution nebulization MC-ICP-MS. Finally, an application to chemically zoned olivine phenocrysts highlights the potential of *in situ* Fe-Mg isotope analyses to unravel diffusion-driven processes during magma differentiation (Sio et al., 2013).

I.2 Reference materials and samples

The investigated samples include the MPI-DING reference glasses KL2-G, ML3B-G, GOR128-G, GOR132-G, T1-G (Jochum et al., 2000) as well as the USGS reference glasses BIR-1G, BCR-2G and BHVO-2G, all of which have been analyzed both *in situ and* by solution nebulization MC-ICP-MS. Additionally, solution nebulization Fe and Mg isotope data were acquired for the MPI-DING reference glass StHs6/80-G. *In situ* analyses of Mg isotopes were conducted relative to the USGS reference glass BHVO-2G, the MPI-DING reference glass GOR132-G, or a synthetic MgO crystal from SPI Supplies, Inc., USA. *In situ* analyses of Fe isotopes were carried out relative to the USGS reference glass BCR-2G or the pure Fe-metal IRMM-014. Furthermore, we investigated chemically zoned olivine phenocrysts in basaltic rocks from the Massif Central, France. These fresh olivine basalts erupted during the late Miocene to early Pliocene (Lorand et al., 2003, Nehlig et al., 2003) and were taken in a former quarry (N45°54.858‘; E02°55.674‘) near the village of Sauterre.

I.3 Methods

I.3.1 *In situ* Fe isotope analyses by fs-LA-MC-ICP-MS

In situ Fe and Mg isotope analyses were performed using high mass resolution MC-ICP-MS with a ThermoFinnigan Neptune connected to a Spectra-Physics Solstice femtosecond laser ablation system at the Leibniz Universität Hannover, Germany. The laser ablation system is based on a 100 femtosecond Ti-sapphire regenerative amplifier (Solstice, Spectra-Physics) working at a fundamental wavelength of 775 nm, which is consecutively frequency-quadrupled, thus resulting in an output laser beam with a wavelength of 194 nm. The final

output energy is ~3.2 mJ/pulse at a fundamental wavelength of 775 nm. Pumping with 500 Hz results in a pulse energy of 70 µJ at a wavelength of 194 nm. The ablation cell and the stage/visualization system (a modified New Wave LUV 266) used in this study are the same as the ones described in Horn et al. (2006) and Horn and von Blanckenburg (2007). An overview of the instrumental parameters of the fs-LA system and the Neptune MC-ICP-MS for the *in situ* analyses of Fe- and Mg isotopes is given in Table I.1a in section I.Tables.

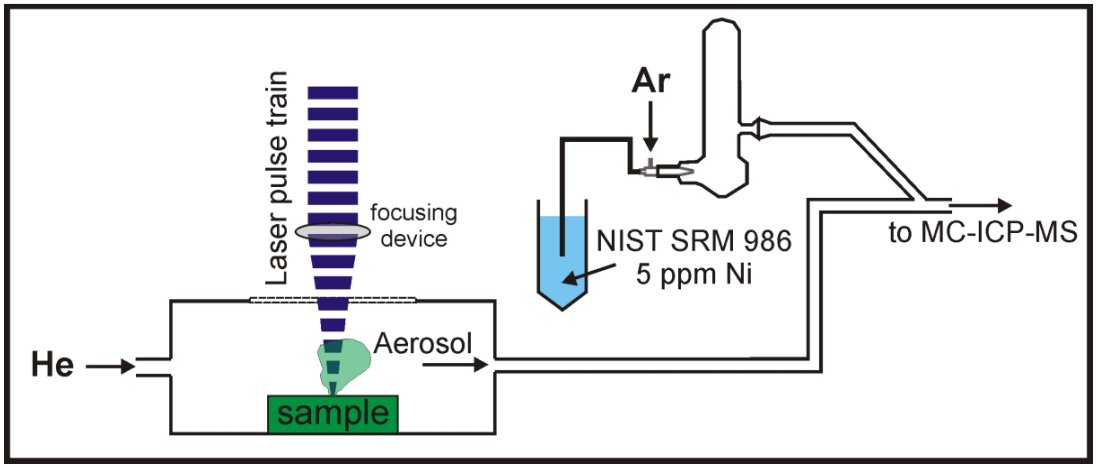

Figure I.1: Schematic sketch of the on-line addition of a Ni standard solution to the plasma during laser ablation of the sample (for *in situ* Fe isotope analyses), modified after Horn et al. (2006). For *in situ* Mg isotope analyses Milli-Q water (instead of the Ni standard solution) is introduced to the plasma.

In situ Fe isotope measurements were performed at high mass resolution (m/Δm ≈ 9000, 5-95% peak side width definition) in order to resolve molecular interferences of argon nitrides and argon oxides on Fe isotopes (and also potentially sample-induced interferences of CaO and CaN; see Weyer and Schwieters 2003). Employment of an X-type skimmer cone for the *in situ* Fe isotope analyses resulted in five times higher intensities of interfering argon oxides and argon nitrides compared to solution analyses, e.g. $(^{40}Ar^{16}O)^+$ yielded ~5 V during *in situ* analyses and ~1 V during solution analyses. The high mass resolving power provides sufficiently wide flat plateaus to determine interference-free Fe isotope signals for stable and precise Fe isotope measurements. Assuming an abundance sensitivity of 50 ppm for the Neptune MC-ICP-MS (cf. Weyer and Schwieters 2003), the contribution of the $(^{40}Ar^{16}O)^+$ tail on the middle of the $^{56}Fe^+$ plateau is <20 ppm if the $^{56}Fe^+/(^{40}Ar^{16}O)^+$ ratio is >2.5 which

was typically the case during our *in situ* Fe isotope analyses. Furthermore, any significant contribution from interfering argon oxides and argon nitrides would have resulted in a deviation of the measured δ^{56}Fe and δ^{57}Fe values from the mass-dependent fractionation line, which was not observed (Fig. A-I.1 in Appendix I).

The detector array of the Faraday cups was positioned for simultaneous detection of ^{53}Cr, ^{54}Fe, ^{56}Fe, ^{57}Fe, ^{58}Ni and ^{60}Ni (Table I.1b). ^{53}Cr is monitored to correct for the isobaric interference of ^{54}Cr on ^{54}Fe. Instrumental mass bias was monitored by simultaneous analyses of Ni isotopes (Poitrasson and Freydier 2005) of a Ni standard solution (NIST SRM 986, 5 µg ml^{-1}) combined with a sample-standard bracketing protocol. The advantage of using Ni rather than Cu isotopes for instrumental mass bias correction (e.g., Sharma et al., 2001; Arnold et al., 2004b) is that both Fe and Ni isotopes can be collected simultaneously in static mode which is ideal for transient laser ablation signals. The Ni solution was added via a quartz glass spray chamber (double pass Scott design) – which is equipped with an ESI PFA-ST nebulizer connected to a 100 µl min^{-1} capillary – and introduced into the plasma along with the ablation aerosol (Fig. I.1). We achieved better precisions using ^{60}Ni/^{58}Ni instead of ^{61}Ni/^{60}Ni (see Poitrasson and Freydier 2005) for mass bias correction, likely as ^{61}Ni/^{60}Ni has a mass difference of only one and ^{61}Ni has a relatively low abundance. For ^{60}Ni/^{58}Ni we used the certified ratio of the NIST SRM 986 of 0.385199 (Gramlich et al., 1989) and the exponential law to correct for instrumental mass bias after correction for the isobaric interference of ^{58}Fe on ^{58}Ni. The above described technique of mass bias correction has essentially three sources of uncertainties: 1) The interference of ^{58}Fe on ^{58}Ni: This interference was monitored with ^{56}Fe. The uncertainty of the interference correction was minimized by applying a mass bias term to the natural ^{56}Fe/^{58}Fe (325.4842; Taylor et al., 1992) that was taken from the measured ^{57}Fe-^{56}Fe ratio (assuming a natural ratio of 0.023095; Taylor et al., 1992) and applying the exponential law. Figure A-I.2 (in Appendix I) gives a graphical description and further details of this mass bias corrected interference correction. The uncertainty introduced by this mass bias corrected interference correction on the measured ^{56}Fe/^{54}Fe and ^{57}Fe/^{54}Fe is negligible (<0.005‰) as the high Ni concentration of our standard solution (5 µg ml^{-1}) resulted in high Ni signals of ~28 V on mass 58 (≡ ~11 V on mass 60, using a 10^{11} Ω resistor) and accordingly in very high ^{58}Ni/^{58}Fe (typically of 500-800). 2) Some of the Ni signal originates from laser ablation of the samples, as the analyzed glasses and olivines also contain Ni (ca. 10-3000 µg g^{-1}) which may have a variable Ni isotope composition. However, as the Ni signal from laser ablation of the samples was always <1% of the total Ni signal, the resulting uncertainty was also negligible (<0.02‰)

within the overall uncertainty of our measurements, assuming Ni isotope variations in the investigated samples do not exceed the variations so far observed in terrestrial rocks (≈ 2‰; Gueguen et al., 2013). 3) Mass bias variations of Fe, from laser ablation, and of Ni, from aspiration, may be decoupled. However, this appears to not be the case as the interference-corrected $^{60}Ni/^{58}Ni$ and $^{56}Fe/^{54}Fe$ ratios are well correlated (Fig. I.2), indicating that the instrumental mass discrimination follows the same law for both elements. The positive effect on reproducibility and accuracy of the *in situ* analyses by using the $^{60}Ni/^{58}Ni$ as an external mass bias monitor is illustrated exemplarily in Figure I.3.

There are two limitations of using a Ni standard for instrumental mass bias correction: 1) ^{58}Fe cannot be determined. However, a mass-independent behavior of ^{58}Fe has not yet been observed for terrestrial or extraterrestrial samples (e.g., Dauphas et al., 2008, 2004; Wang et al., 2011), except for some unique meteorite inclusions (Völkening and Papanastassiou, 1989). 2) A straightforward use is only feasible for samples with low Ni concentrations (i.e. <2% of the Fe concentration) because potential variations in the Ni isotope composition of the samples may affect the accuracy of the Fe isotope analyses.

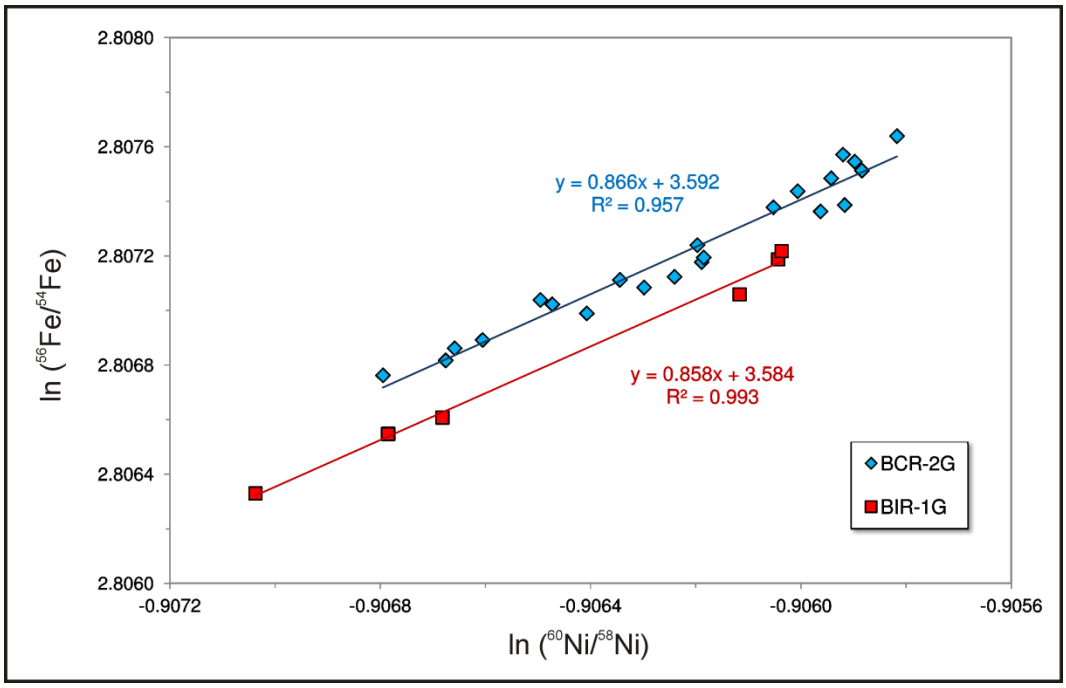

Figure I.2: Plot of the natural logarithms of the interference-corrected $^{60}Ni/^{58}Ni$- and $^{56}Fe/^{54}Fe$ ratios, which show a good correlation indicating that the instrumental mass discriminations of Fe and Ni are coupled. However, the slope of ~0.86 shows that the mass discrimination of Fe is slightly lower than that of Ni.

Using a laser repetition rate of 25 Hz and a spot diameter of 50 µm for the ablation of the reference material BCR-2G (9.7% m/m Fe) resulted routinely in signal intensities of 16 V on mass 56. The Fe signal intensities were matched by an increase in the laser repetition rate to a maximum of 70 Hz for standards and samples with Fe concentrations as low as 5% m/m. As already shown in a previous study (Steinhoefel et al., 2009a), variable repetition rates during fs-LA-MC-ICP-MS have no effect on the measured isotope ratios. All samples and reference materials were analyzed in raster-mode, except for the chemically zoned (with respect to Mg#) olivine crystals, where ablation was performed along lines parallel to the crystal rim (i.e. parallel to the chemical and isotopic zoning; see Fig. I.7). An individual analysis consisted of one block of 180 cycles with a cycle integration time of 1.05 seconds. Each analysis started with the acquisition of a ~35 second gas blank, followed by an ablation interval of ~130 seconds. With this acquisition protocol the internal precision of a single analysis (~125 cycles) is typically better than ±0.035‰ (2 standard errors = 2 SE) for $^{56}Fe/^{54}Fe$. The external reproducibility of $\delta^{56}Fe$ values determined for a certain sample relative to a laser ablation standard (LAS) is better than ±0.12‰ (2 SD), based on repeated analyses of standards and samples over a period of 12 months. The calculation of the overall uncertainty (2 σ_{LA}) for the reported $\delta^{56}Fe$ values relative to IRMM-014 is described below in section I.3.3. All samples were measured at least four times (Table I.2). For analyses relative to the pure Fe-metal IRMM-014, $\delta^{56}Fe$ values were determined as follows:

$$\delta^{56}\mathrm{Fe} = \left[\frac{\left(\frac{^{56}\mathrm{Fe}}{^{54}\mathrm{Fe}}\right)_{\mathrm{sample}}}{\left(\frac{^{56}\mathrm{Fe}}{^{54}\mathrm{Fe}}\right)_{\mathrm{IRMM014}}} - 1\right] * 1000$$

(Eqn. I.1)

For samples that were analyzed relative to BCR-2G, $\delta^{56}Fe$ were re-calculated relative to IRMM-014 as follows:

$$\delta^{56}\mathrm{Fe}_{\mathrm{sample/IRMM\text{-}014}} = \delta^{56}\mathrm{Fe}_{\mathrm{sample/BCR\text{-}2G}} + \delta^{56}\mathrm{Fe}_{\mathrm{BCR\text{-}2G/IRMM\text{-}014}} \qquad \text{(Eqn. I.2)}$$

where $\delta^{56}Fe_{sample/BCR\text{-}2G}$ is the measured (*in situ*) δ value of the sample relative to BCR-2G, and $\delta^{56}Fe_{BCR\text{-}2G/IRMM\text{-}014}$ is the δ value of BCR-2G relative to IRMM-014 determined by solution nebulization MC-ICP-MS (see section I.3.5).

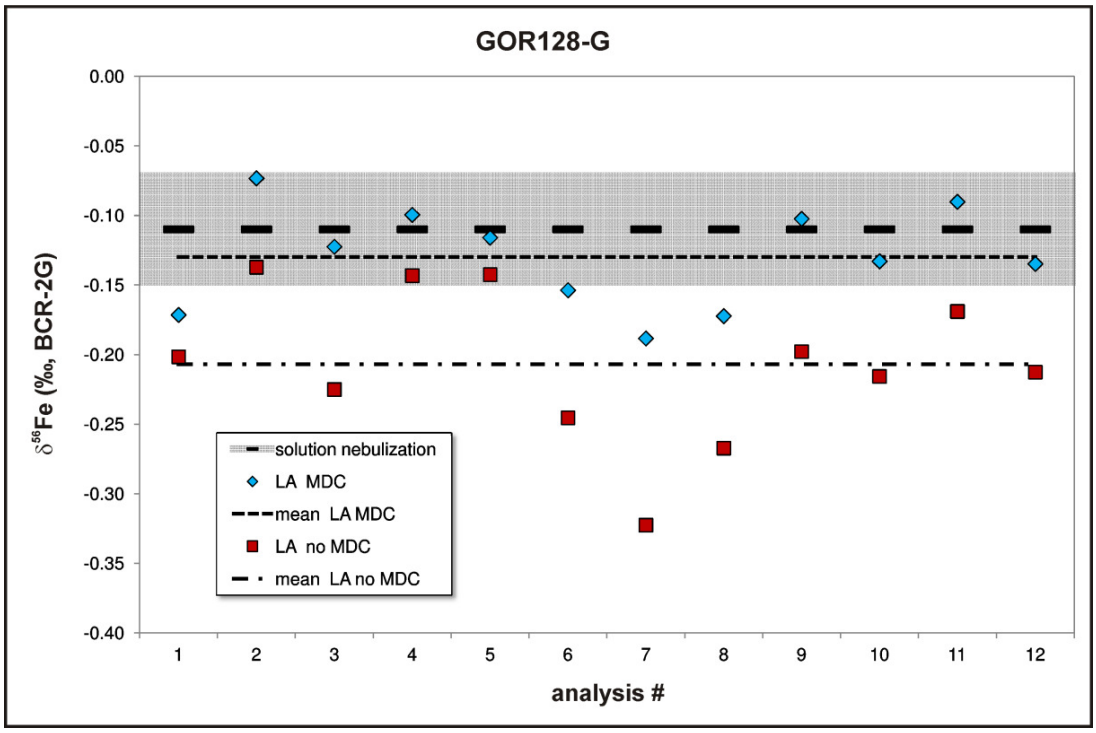

Figure I.3: Fe isotope data for the komatiitic MPI-DING reference glass GOR128-G acquired using fs-laser ablation- and solution nebulization MC-ICP-MS. The grey bar represents the typical analytical uncertainty (0.04‰, 2 standard deviations) of the solution nebulization analyses. "LA MDC" and "LA no MDC" show the δ^{56}Fe values obtained for 12 fs-laser ablation analyses with and without an external mass discrimination correction, respectively. The average of the δ^{56}Fe values acquired with a mass discrimination correction is close to the value determined by solution nebulization MC-ICP-MS. Furthermore, applying the mass discrimination correction leads to a better reproducibility of the laser ablation measurements (0.07‰ vs. 0.11‰, 2 SD).

I.3.2 *In situ* Mg isotope analyses by fs-LA-MC-ICP-MS

In situ Mg isotope measurements were performed with standard-sample-standard bracketing and in high mass resolution mode (m/Δm ≈ 9000) to resolve sample-dependent isobaric interferences on Mg isotopes such as $^{52}Cr^{2+}$ on $^{26}Mg^{+}$, $^{50}Ti^{2+}$ and $^{50}Cr^{2+}$ on $^{25}Mg^{+}$, or $^{48}Ca^{2+}$ and $^{48}Ti^{2+}$on $^{24}Mg^{+}$. A mass resolution (m/Δm) between 1800 and 2800 is needed to resolve these interferences. These interferences occur at the low mass side of the Mg isotope peaks. Possible molecular interferences on Mg isotopes include $(^{12}C^{12}C)^{+}$ on $^{24}Mg^{+}$, $(^{12}C^{13}C)^{+}$ on $^{25}Mg^{+}$, and $(^{12}C^{14}N)^{+}$ on $^{26}Mg^{+}$. These interferences occur at high mass side of the Mg isotope. The Mg isotopes can thus not be resolved simultaneously from the above-described interferences with the collector setting of the Neptune. However, (1) the occurrence of these

interferences was always monitored, but found to be negligible (e.g. signal intensities of $^{12}C^{14}N^{+}$ were always <0.4 mV). (2) As these interferences are generated by the plasma gas, they are effectively subtracted with the background and additionally by the signal-matched sample-standard bracketing. Interferences from $^{9}Be^{16}O$ and $^{10}B^{16}O$ are also negligible because of the low Be and B contents of the analyzed samples. Finally, any significant contribution from such interferences would have resulted in a deviation of the measured $\delta^{25}Mg$ and $\delta^{26}Mg$ values from the mass-dependent fractionation line, which was not observed (see Fig. I.5 and Fig. A-I.3).

Analyses were performed at wet plasma conditions by continuously introducing Milli-Q water (18.2 MΩ grade) to the plasma using a quartz glass spray chamber (double pass Scott design) and an ESI PFA-ST nebulizer (uptake rate of 100 µl min^{-1}) simultaneously to laser ablation of the sample. This enhanced the stability of the plasma conditions and improved the precision of the LA-MC-ICP-MS analyses (e.g., O'Connor et al., 2006; Janney et al., 2011). Furthermore, as pointed out by Pogge von Strandmann et al. (2011), the wet plasma conditions appear to additionally suppress the formation of interfering molecules such as $(^{12}C^{14}N)^{+}$ on $^{26}Mg^{+}$.

A laser repetition rate of 6 Hz and a spot diameter of 50 µm for the MgO standard (60% m/m Mg) resulted in signal intensities of 9 V on mass 24. However, silicates have much lower Mg concentrations compared to the MgO standard. Consequently, laser repetition rates were increased to a maximum of 100 Hz to match the Mg signal intensities between standards and samples. All samples and reference materials were analyzed in raster-mode, with the exception of the chemically zoned domains of the olivine crystals. For the latter, ablation of sample material was performed along lines parallel to the crystal rim (parallel to the chemical/isotopic zoning; see Fig. I.7). As with Fe isotope analyses, an individual analysis consisted of one block of 180 cycles with a cycle integration time of 1.05 seconds, and we also measured the instrumental background (~35 cycles) on Mg masses prior to each analysis of the sample (~125 cycles). With this technique the internal precision of a single analysis (~125 cycles) for $^{26}Mg/^{24}Mg$ is identical to that achieved for the Fe isotope analyses (better than ±0.035‰; 2 SE). The external reproducibility based on repeated analyses of standards and samples over a period of 12 months, is typically better than ±0.13‰ (2 SD) for $\delta^{26}Mg$. All samples were measured at least three times (Table I.3). The $\delta^{26}Mg$ values of the samples relative to our laser ablation standards (LAS, i.e. MgO, BHVO-2G, GOR132-G) are converted to delta values relative to DSM-3, which is the most widely used reference for Mg

isotopes, but only available as a Mg solution (Galy et al., 2003), by using the following equation:

$$\delta^{26}Mg_{sample/DSM\text{-}3} = \delta^{26}Mg_{sample/LAS} + \delta^{26}Mg_{LAS/DSM\text{-}3} \qquad \text{(Eqn. I.3)}$$

where

$$\delta^{26}Mg_{sample/LAS} = \left[\frac{\left(\frac{^{26}Mg}{^{24}Mg}\right)_{sample}}{\left(\frac{^{26}Mg}{^{24}Mg}\right)_{LAS}} - 1\right] * 1000$$

(Eqn. I.4)

which is the measured value of the sample relative to the laser ablation standard and $\delta^{26}Mg_{LAS/DSM\text{-}3}$ is the δ value of the laser ablation standard relative to DSM-3 determined by solution nebulization MC-ICP-MS (see section I.3.5). The calculation of the overall uncertainty (2 σ_{LA}) for the reported $\delta^{26}Mg$ values relative to DSM-3 is described in the following section.

I.3.3 Uncertainties of the laser ablation data

The overall uncertainty (2 σ_{LA}) for the *in situ* $\delta^{56}Fe$ values relative to IRMM-014 can be calculated from the individual errors, as follows:

$$2\,\sigma_{LA} = 2 \cdot \sqrt{(\sigma_{sol})^2 + (SD_{rl})^2 + (\sigma_{Ni})^2 + (\sigma_{ic})^2}$$

(Eqn. I.5)

where σ_{sol} is the overall uncertainty for the solution $\delta^{56}Fe$ value of the LAS used (see section I.3.5), SD_{rl} represents the standard deviation of all $\delta^{56}Fe$ values determined *in situ* for a certain sample, σ_{Ni} is the error introduced by the addition of Ni from the sample during laser ablation (<0.02‰), and σ_{ic} represents the error added by the interference correction for ^{58}Fe on ^{58}Ni (<0.005‰; see section I.3.1 for details).

A similar approach is applied for calculating the overall uncertainty for the *in situ* $\delta^{26}Mg$ values relative to DSM-3:

$$2\,\sigma_{LA} = 2 \cdot \sqrt{(SD_{rs})^2 + (SD_{rl})^2}$$

(Eqn. I.6)

where SD_{rs} represents the standard deviation for the solution $\delta^{26}Mg$ value of the LAS used, and SD_{rl} is the standard deviation of all *in situ* $\delta^{26}Mg$ values determined for a certain sample. For all investigated reference glasses the difference between 2 σ_{LA} and the pure external reproducibility (2 SD_{rl}) of our *in situ* analyses is <0.025‰ for both $\delta^{56}Fe$ and $\delta^{26}Mg$ (see Tables I.2 and I.3).

I.3.4 Sample preparation for solution nebulization MC-ICP-MS analyses

Prior to the digestion in a mixture of concentrated HF-HNO_3 (3:1), the glass fragments with a weight between 3 mg and 50 mg were washed for 30 minutes in an ultrasonic bath containing Milli-Q water. The digestion was carried out in Savillex® teflon beakers at 140°C for a time interval of >24h. Prior to ion exchange chromatography, the dissolved samples were evaporated to dryness, repeatedly refluxed in HCl (8 mol l^{-1}) and HNO_3 (14.5 mol l^{-1}), and finally dissolved in HCl (6 mol l^{-1}).

Following the procedure described by Schoenberg and von Blanckenburg (2005), iron was purified by anion-exchange chromatography in 12-ml BioRad® Poly-Prep columns filled with 1.6 ml Dowex® 1-X8 (100-200 mesh) resin. Matrix elements (including Mg) were eluted with 8 ml HCl (6 mol l^{-1}) and collected in teflon beakers. This fraction contained quantitatively all Mg of the samples and was dried down and redissolved in HCl (0.4 mol l^{-1}) for subsequent Mg purification (see below). The Fe fraction was evaporated to dryness and redissolved in HCl (6 mol l^{-1}). After extensive resin cleaning the anion-exchange chromatography was repeated to obtain Fe fractions of high purity. These were dried down and a few drops of H_2O_2 (30% v/v) and concentrated HNO_3 were added to remove any organic compounds. After the last evaporation to dryness, the precipitates were dissolved in HNO_3 (0.5 mol l^{-1}) and diluted to ~7 µg ml^{-1} for mass spectrometry analyses. A 4 µg ml^{-1} Ni standard (NIST SRM 986) solution was added prior to analysis to each diluted sample for mass bias correction. In addition, we compared our Ni addition method with the commonly used Cu addition method for mass bias correction (see e.g., Sharma et al., 2001; Arnold et al., 2004b) with respect to accuracy and precision. A Cu solution (Alfa-Aesar Specpure®) with a natural $^{65}Cu/^{63}Cu$ of 0.4457 (calibrated against IRMM-014; Mansfeldt et al., 2012)

was added to a concentration of 4 µg ml^{-1} directly before the analyses to the sample solutions.

Magnesium purification by cation exchange chromatography was based on stage 2 of the procedure established by Wombacher et al. (2009) using 1.6 ml of Dowex® 50W-X8 (200-400 mesh) resin in 12-ml BioRad® Poly-Prep columns. Because Fe had already been separated in the previous purification procedure, the elution of Fe and Mn by acetone-HCl (see Wombacher et al., 2009) could be omitted. The eluted Mg fraction was evaporated to dryness and redissolved in HCl (0.4 mol l^{-1}). After extensive resin cleaning the cation-exchange chromatography was repeated to obtain sufficiently clean Mg solutions to minimize mass interferences. Nevertheless, we observed that the purification procedure did not quantitatively separate Ca and Mn from Mg. Depending on the original Mg-Ca and Mg-Mn ratios of the sample, a range of Mg/Ca and Mg/Mn between 12 and 150 and between 15 and 130, respectively, was determined (by analyses with a Varian Vista Pro ICP-OES). However, as solution nebulization Mg isotope analyses by MC-ICP-MS were carried out in high mass resolution mode, the isobaric interference of $^{48}Ca^{2+}$ on $^{24}Mg^{+}$ could be quantitatively resolved. A study by Huang et al. (2009) showed that the instrumental mass bias of Mg isotopes caused by the presence of Mn in the analyzed solution is not significant (<0.1‰) if the intensity ratio of $^{55}Mn/^{24}Mg$ is <0.2. We did not check the intensity ratio of $^{55}Mn/^{24}Mg$, but the solutions we analyzed have weight ratios of $^{55}Mn/^{24}Mg$ <0.08. Furthermore, in contrast to the study by Huang et al. (2009) our analyses were performed at "wet" plasma conditions which appear to be less susceptible to matrix effects than "dry" plasma conditions (e.g. Pogge von Strandmann et al., 2011; Teng et al., 2010). In summary, it appears unlikely that the low concentrations of Ca and Mn in the solutions we analyzed significantly affected the precision and accuracy of our Mg isotope measurements.

A potential effect of the Mg purification procedure on the isotope compositions of the samples was checked with two pure Mg solutions (including our in-house MgO standard and the widely used Cambridge-1 Mg solution; Galy et al., 2003) which were analyzed with and without chromatographic purification (Table I.3). Both fractions yielded identical results (see below). Subsequently, the samples were dried down in a mixture of H_2O_2 (30% v/v) and concentrated HNO_3 to remove any organic components that may have remained from the chromatographic purification. For isotope analyses, the precipitates were dissolved in HNO_3 (0.5 mol l^{-1}) and diluted to ~2 µg ml^{-1}.

I.3.5 Solution nebulization MC-ICP-MS

Iron and magnesium isotope analyses were carried out in high mass resolution mode using the standard-sample-standard bracketing protocol on a ThermoFinnigan Neptune MC-ICP-MS, which was equipped with a quartz glass spray chamber (double pass Scott design), an ESI PFA-ST nebulizer (uptake rate of 100 µl min^{-1}), and either a Ni H-type skimmer cone (for Fe isotope analyses) or a Ni X-type skimmer cone (for Mg isotope analyses). The X-type skimmer cones have higher transmission rates and were used for Mg isotope analyses as most samples investigated in this study have low Mg (relative to Fe) concentration, however they still yielded sufficiently high signals for high precision analyses (see section below).

For the Fe isotope analyses, the Faraday cup configuration (Table I.1b), interference correction and the instrumental mass discrimination correction were identical to that used for the *in situ* Fe isotope analyses. With this setup, a 20 V signal on ^{56}Fe was routinely achieved for a 7 µg ml^{-1} Fe solution. All samples were measured relative to the Fe standard IRMM-014. An individual measurement consisted of 20 cycles with a cycle integration time of ~11 s (5 integrations with an integration time of 2.1 seconds). The results are reported as $\delta^{x}Fe$ (Eqn. I.1) where x is either 56 or 57. The internal precision of a single analysis (2 SE; n = 20) is always better than 0.03‰ for the ^{56}Fe-^{54}Fe ratio. The reproducibility of $\delta^{56}Fe$ values, based on replicate analyses of individual samples during a single analytical session, is typically better than ±0.04‰ (2 SD; n = 4). The external reproducibility, including separate dissolutions and chemical purifications, is better than ±0.05‰ (2 SD; n = 8) for $\delta^{56}Fe$. Using Ni isotopes for instrumental mass bias correction resulted in similar external reproducibilities as previously achieved by using Cu isotopes (e.g., Weyer et al., 2005). Because the mass bias corrected interference correction for ^{58}Fe on ^{58}Ni also results in a small error (<0.01‰) on the measured $^{56}Fe/^{54}Fe$ (and $^{57}Fe/^{54}Fe$), the overall uncertainty (2 σ_{sol}) for the reported $\delta^{56}Fe$ values is calculated from the individual errors, as follows:

$$2\,\sigma_{sol} = 2 \cdot \sqrt{(SD_{rs})^2 + (\sigma_{ic})^2}$$

(Eqn. I.7)

where SD_{rs} represents the standard deviation of all $\delta^{56}Fe$ values determined for a certain sample, and σ_{ic} is the error introduced by the interference correction for ^{58}Fe on ^{58}Ni (0.01‰). The latter results from the fact that the ^{58}Fe-^{58}Ni ratio during solution nebulization analyses is not as high as for our laser ablation analyses (~200 instead of >500; see section

I.3.1 for details). The effect of this error propagation calculation is only minor, i.e. the difference between 2 σ_{sol} and the pure reproducibility (2 SD_{rs}) of the Fe isotope analyses by solution nebulization MC-ICP-MS is always <0.01‰ for δ^{56}Fe (see Table I.2).
For mass bias correction with the Cu addition method, a dynamic measurement protocol was implemented and the detector setup for Fe isotope analyses was slightly modified (see Table I.1b). The magnet settling time was 2.5 seconds, and the integration time for Cu analyses ~4 seconds (2 integrations with an integration time of 2.1 seconds).

For the Mg isotope analyses, the Faraday cup configuration was the same as that for the *in situ* Mg isotope analyses (Table I.1b). A 15 V signal on ^{24}Mg was usually achieved for a 2 µg ml^{-1} Mg solution. Samples were measured at least three times relative to the Mg standard DSM-3. An individual analysis consisted of 25 cycles with a cycle integration time of ~6.5 seconds (3 integrations with an integration time of 2.1 seconds). Results are reported in the delta notation:

$$\delta^{x}\mathrm{Mg} = \left[\frac{\left(\frac{^{x}\mathrm{Mg}}{^{24}\mathrm{Mg}}\right)_{\mathrm{sample}}}{\left(\frac{^{x}\mathrm{Mg}}{^{24}\mathrm{Mg}}\right)_{\mathrm{DSM\text{-}3}}} - 1\right] * 1000$$

(Eqn. I.8)

where x is either 25 or 26. Based on the replicate analyses of the individual samples during a single analytical session, the reproducibility (2 SD; n ≥ 3) is typically better than ±0.10‰ for δ^{26}Mg. Also, the external reproducibility, based on separate dissolutions and analyses of our in-house MgO standard, is better than ±0.10‰ (2 SD; n = 10) for δ^{26}Mg. The internal precision of a single analysis (2 SE; n = 25) is always better than ±0.03‰ for ^{26}Mg/^{24}Mg.

I.4 Results and Discussion

I.4.1 Solution nebulization MC-ICP-MS data

The measured δ^{56}Fe values for the USGS reference glasses BCR-2G, BIR-1G, and BHVO-2G are given in Table I.2. They are consistent with published δ^{56}Fe values of the respective rock powders (Fig. I.4a). Moreover, an excellent agreement is observed for data acquired using Ni and Cu for mass bias correction, respectively (Table I.2). The δ^{56}Fe values of the

six MPI-DING reference glasses range from -0.025±0.036‰ (GOR128-G) to 0.081±0.036‰ (KL2-G; Table I.2, Fig. I.5a). The Fe isotope compositions of the two reference glasses prepared from Gorgona Island komatiites (GOR128-G and GOR132-G) are in good agreement with δ^{56}Fe values reported by Hibbert et al. (2012). The two glasses prepared from Hawaiian tholeiitic basalts (ML3B-G and KL2-G) – as well as the USGS basaltic glasses – have δ^{56}Fe values that are consistent with the range in δ^{56}Fe defined by global basalts (Fig. I.5a; e.g., Schoenberg and von Blanckenburg, 2006; Weyer and Ionov, 2007; Teng et al., 2013).

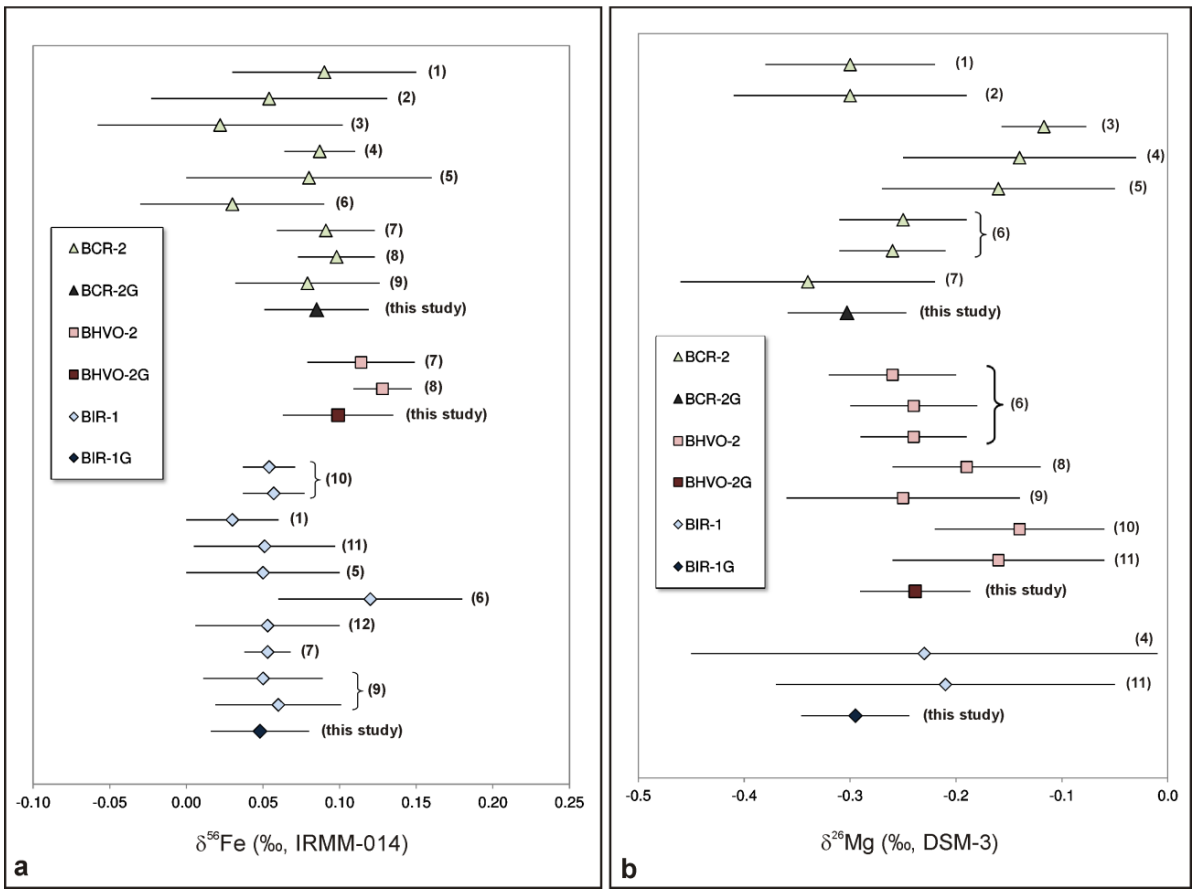

Figure I.4: (**a**) Fe and (**b**) Mg isotopic compositions of the three USGS reference glasses determined by solution nebulization MC-ICP-MS in this study and comparison with data for the respective rock powders analyzed in other studies. Literature data in (**a**) are from (1) Wombacher et al. (2009), (2) Dauphas et al. (2004), (3) Dauphas et al. (2007), (4) Dauphas et al. (2009), (5) Chapman et al. (2009), (6) Dideriksen et al. (2006), (7) Craddock and Dauphas (2011), (8) Millet et al. (2012), (9) Weyer et al. (2005), (10) Weyer and Ionov (2007), (11) Schoenberg and von Blanckenburg (2006), (12) Schuessler et al. (2009). Literature data in (**b**) are from (1) Teng et al. (2007), (2) Huang et al. (2009), (3) Bourdon et al. (2010), (4) Wombacher et al. (2009), (5) Tipper et al. (2008), (6) Pogge von Strandmann et al. (2011), (7) Huang et al. (2011), (8) Bizzarro et al. (2011), (9) Pogge von Strandmann (2008), (10) Wiechert and Halliday (2007), (11) Bizzarro et al. (2005). Error bars represent uncertainties as provided in the respective studies.

Identical Mg isotopic compositions have been analyzed for the unpurified Mg standards (in-house MgO and Cambridge-1) and the aliquots, which were subject to ion exchange chromatography (Table I.3). This demonstrates that the Mg purification procedure presented in this study does not fractionate Mg isotopes. The δ^{26}Mg values of the USGS reference glasses range from –0.303±0.056‰ (BCR-2G) to –0.239±0.052‰ (BHVO-2G), which is in good agreement with published δ^{26}Mg values of the respective rock powders BIR-1, BCR-2, and BHVO-2 (e.g. Pogge von Strandmann et al., 2011; Fig. I.4b, Table I.3). The six MPI-DING reference glasses analyzed in this study encompass a range of δ^{26}Mg values from –0.354±0.089‰ (StHs6/80-G) to –0.174±0.039‰ (GOR132-G; Fig. I.5b, Table I.3). All reference glasses agree well with published data for global oceanic island basalts (–0.26±0.08‰; Teng et al., 2010).

I.4.2 Laser ablation data

The variation of Mg and Fe isotope ratios monitored during line scans across the reference glasses is typically smaller than ±0.11‰ for both δ^{56}Fe and δ^{26}Mg (considering analyzed areas of ~50 µm x 200 µm). These variations are within the analytical uncertainties of the *in situ* isotope analyses of this study. Likewise, the laser ablation rasters used for the Mg and Fe isotope analyses were evenly distributed over an individual glass. Thus, any isotopic heterogeneity would have resulted in a poor reproducibility of the acquired δ values, which was not observed. Therefore all investigated reference glasses can be considered as isotopically homogeneous with respect to the analytical uncertainty (<0.13‰) and the spatial resolution (~50 µm x 200 µm). This is consistent with the findings by Jochum et al. (2006) who demonstrated that the MPI-DING reference glasses are isotopically homogeneous with respect to boron, lithium, and lead. One exception may be the basaltic glass ML3B-G which exhibits some small micro-heterogeneities in its Li isotopic composition (Jochum et al., 2006), and has slightly poorer reproducibilities in δ^{56}Fe and δ^{26}Mg values compared to the other glass reference materials (Tables I.2 and I.3). However, line scans did not reveal any significant isotopic heterogeneity for ML3B-G (Fig. A-I.4). All in all, both the USGS and the MPI-DING reference glasses analyzed in this study are suitable to serve as standards for further *in situ* isotope studies that aim for a similar level of analytical uncertainty (<0.13‰) and spatial resolution (~50 µm x 200 µm). In this regard, the use of glass reference materials as standards for *in situ* analyses is advantageous relative to the use of natural crystals which

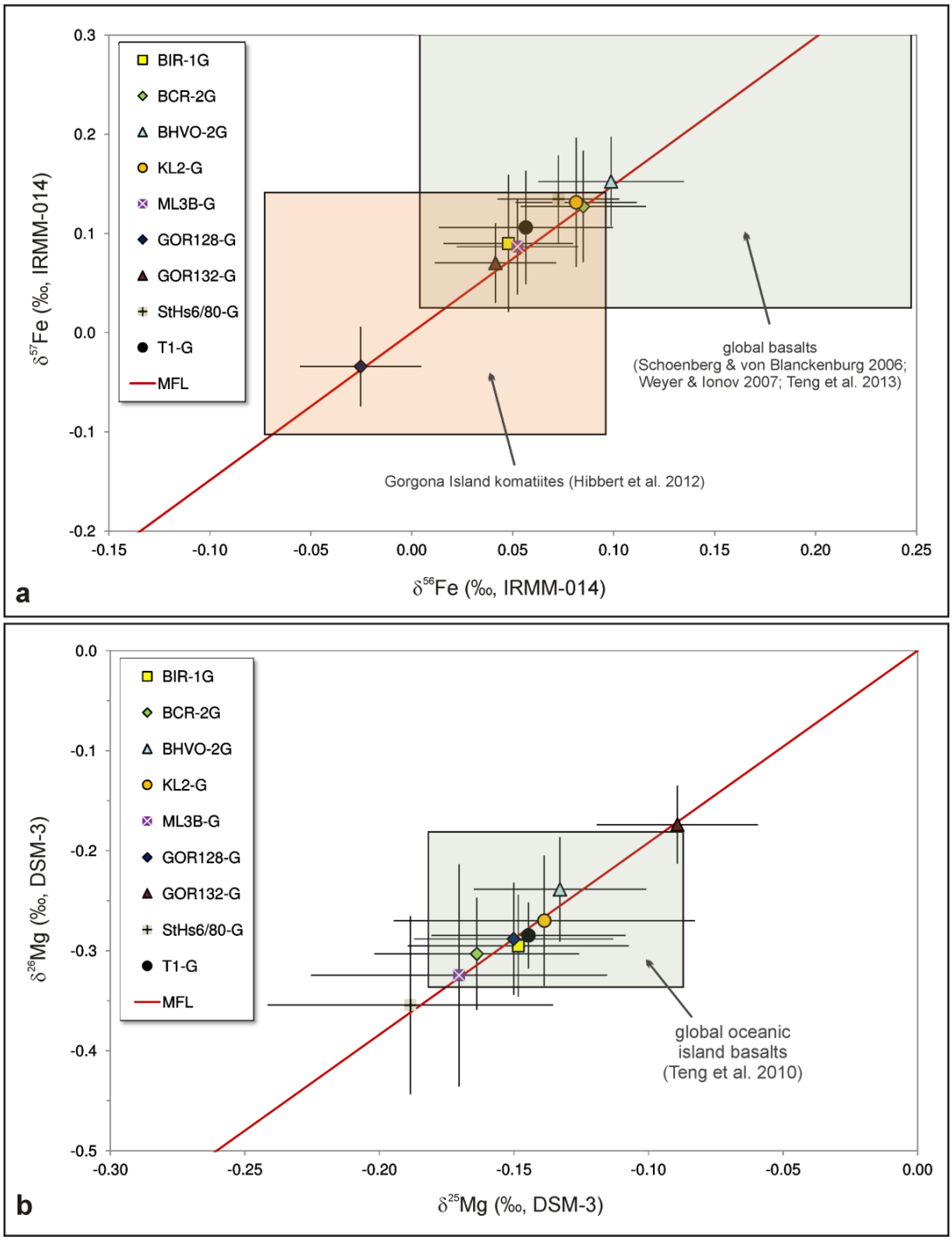

Figure I.5: Three-isotope plots for (**a**) Fe and (**b**) Mg for the MPI-DING and USGS reference glasses analyzed by solution nebulization MC-ICP-MS. Error bars are 2 standard deviations of replicate analyses. Data are from Tables I.2 and I.3. Ranges in Fe isotopic compositions of Gorgona Island komatiites analyzed by Hibbert et al. (2012) and of global basalts investigated by Schoenberg and von Blanckenburg (2006), Weyer and Ionov (2007) and Teng et al. (2013) are also shown in (**a**). MFL represents the mass-dependent fractionation line with a slope of 1.49 in (**a**) (Beard and Johnson, 2004; Steinhoefel et al., 2009a) and a slope of 1.92 in (**b**) (Young and Galy, 2004). (**b**) All glasses investigated in this study fall in the range in Mg isotopic compositions of global oceanic island basalts determined by Teng et al. (2010).

frequently show isotopic inhomogeneities, such as e.g. observed by Pearson et al. (2006) for a gem-quality San Carlos olivine.

The *in situ* isotope analyses of the three USGS reference glasses BIR-1G, BCR-2G and BHVO-2G reveal δ^{56}Fe values of -0.04±0.09‰, 0.10±0.12‰, and 0.06±0.13‰, respectively (Table I.2). The δ^{26}Mg values of these glasses range between -0.40±0.18‰ (BCR-2G) and -0.21±0.05‰ (BHVO-2G; Table I.3). *In situ* analyses of the five MPI-DING reference glasses show (within analytical uncertainties) indistinguishable δ^{56}Fe and δ^{26}Mg values. The δ^{56}Fe values range between -0.04±0.09‰ (GOR128-G) and 0.10±0.07‰ (T1-G; Table I.2), whereas δ^{26}Mg values show a slightly larger spread and vary between -0.31±0.12‰ (KL2-G) and -0.15±0.08‰ (GOR132-G; Table I.3). All *in situ* data agree with the δ^{56}Fe and δ^{26}Mg values determined by solution nebulization MC-ICP-MS (Fig. I.6), confirming that Fe and Mg isotope analyses by fs-LA-MC-ICP-MS are precise (2 SD <0.13‰ for δ^{56}Fe and δ^{26}Mg) *and* accurate. Furthermore, our in-house MgO standard yielded identical *in situ* and solution nebulization δ^{26}Mg values (-1.23±0.14‰ and -1.28±0.05‰, respectively). Given the large compositional diversity of the investigated reference glasses (Mg# between 0.33 and 0.83) and the MgO crystal, the good agreement between laser ablation and solution nebulization data indicates that there is no visible composition-dependent matrix effect (within our analytical precision) for *in situ* Mg isotope analyses by fs-LA-MC-ICP-MS. This is in contrast to observations of previous studies where an excimer nanosecond laser ablation MC-ICP-MS system was employed (Norman et al., 2006; Janney et al., 2011). Furthermore, this study confirms previous investigations (Horn and von Blanckenburg, 2007; Steinhoefel et al., 2009a) showing that largely matrix-independent *in situ* Fe isotope analyses can be performed by fs-LA-MC-ICP-MS.

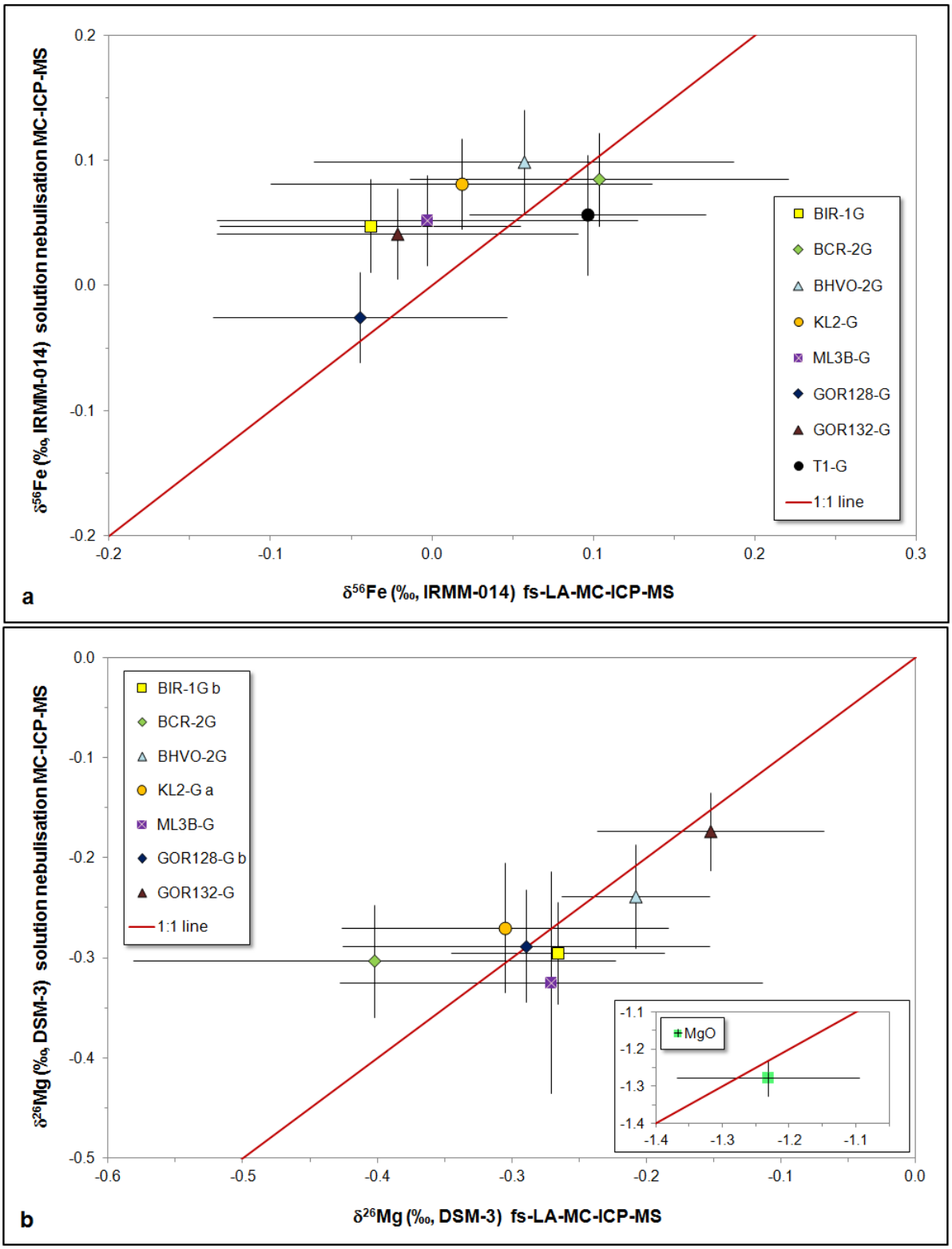

Figure I.6: Comparisons between (**a**) δ^{56}Fe values and (**b**) δ^{26}Mg values, respectively, obtained by solution nebulisation MC-ICP-MS with those determined *in situ* by fs-LA-MC-ICP-MS for the MPI-DING and USGS reference glasses. Inset in (**b**) shows the data for the in-house MgO standard. Error bars represent 95% confidence level (2 σ_{sol} and 2 σ_{LA} in **a**; 2 SD_{rs} and 2 σ_{LA} in **b**). Data are from Tables I.2 and I.3.

I.4.3 Application to chemically zoned olivines

Chemical zoning in minerals, such as Fe-Mg in olivine, can be the result of inter-diffusion driven by a chemical gradient between a mineral and the surrounding melt. Recent studies have shown that such chemical diffusion at magmatic temperatures generates Fe and Mg isotope fractionation in olivine that exceeds the potential equilibrium isotope fractionation by an order of magnitude (Teng et al., 2011; Weyer and Seitz, 2012; Sio et al., 2013). Accordingly, diffusion-generated compositional Fe-Mg zoning in olivine should be coupled with Fe-Mg isotopic zoning. In a recent study by Sio et al. (2013), *in situ* Fe and Mg isotope analyses of a large zoned olivine phenocryst from Hawaiian basalts have been performed by using micro-drilling followed by solution nebulization MC-ICP-MS, supporting a diffusion-driven origin of Fe and Mg isotopic zoning. In the same study, *in situ* Fe isotope analyses determined by conventional nanosecond LA-MC-ICP-MS and MC-SIMS relative to a matrix-matched olivine standard have been reported with a precision of ~0.2‰. The advantage of fs-LA-MC-ICP-MS analyses over micro-drilling is a significantly better spatial resolution (of ~50 µm compared to ~200 µm). Therefore, even short isotopic diffusion profiles can be analyzed by fs-LA-MC-ICP-MS. Compared to other *in situ* techniques such as MC-SIMS and nanosecond LA-MC-ICP-MS (Sio et al., 2013), fs-LA-MC-ICP-MS analyses yield considerably smaller analytical uncertainties (e.g. 0.12‰ for δ^{56}Fe compared to >0.2‰) and a matrix match between samples and standards is not essential. A similar precision is also obtained for Mg isotope analyses with fs-LA-MC-ICP-MS. Consequently, this technique allows resolution of diffusion-generated intra-mineral isotopic zoning of <100µm for both isotope systems.

In Figure I.7, an example of an olivine phenocryst with Fe-Mg chemical and isotopic zoning is shown. This olivine crystal reveals isotope fractionation of up to 1.1‰ in δ^{56}Fe and up to 0.5‰ in δ^{26}Mg. Chemical and isotopic zoning are strongly coupled, i.e., Fe and Mg isotopic zoning profiles are inversely correlated (Fig. I.7). As pointed out by Dauphas et al. (2010) and Teng et al. (2011) this negative correlation strongly indicates that the chemical zoning was generated by diffusion of Fe into and Mg out of the olivine, driven by the chemical gradient between crystal and melt. The observed diffusion-driven fractionation of Fe isotopes (1.1‰) is larger than that of Mg isotopes (0.5‰) in this Mg-rich olivine for mass balance reasons, i.e. the relative diffusion-driven change in Mg is larger than that in Fe. The fact that the core of the olivine does not show any chemical or isotopic zoning indicates that it was not affected by diffusion. These findings demonstrate that *in situ* Fe and Mg isotope

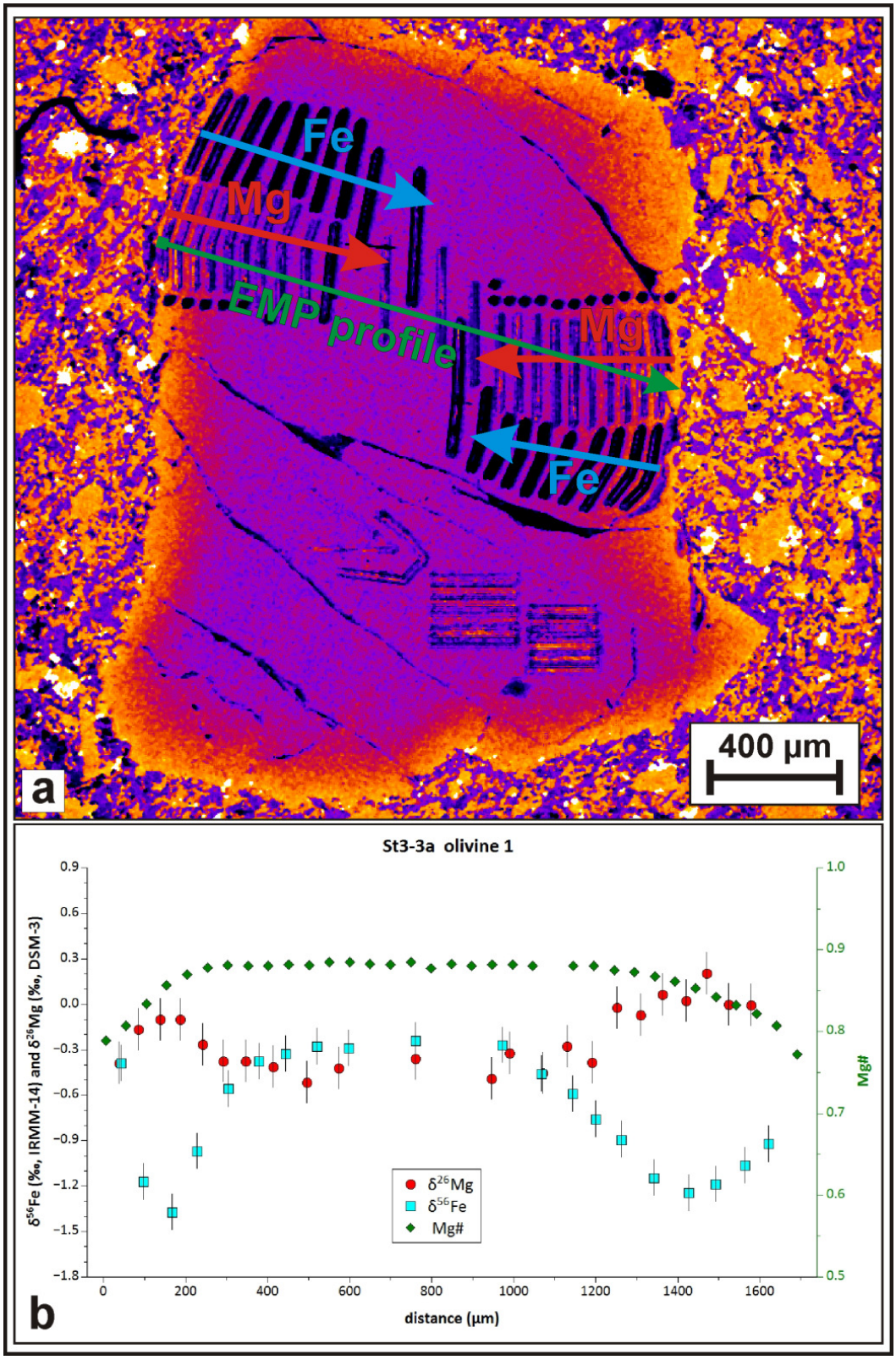

Figure I.7: Zoned olivine phenocryst in a basaltic rock from the Massif Central (France). (**a**) false-color BSE image of the olivine after analyses using femtosecond laser ablation MC-ICP-MS. Ablation of sample material was performed along lines parallel to the crystal rim. The green line represents the profile analyzed by electron microprobe (EMP). (**b**) Fe and Mg isotopic profiles as well as variation of Mg# across the olivine. Error bars represent 2 standard deviations.

analyses by femtosecond laser ablation MC-ICP-MS provide a powerful means to identify diffusive processes that occur on the mineral scale during magma differentiation. Such isotopic zoning may be used in addition to chemical zoning to constrain magma residence times of crystals by modeling such intra-mineral chemical gradients (e.g., Costa and Dungan, 2005; Kahl et al., 2011).

I.5 Conclusions

In this study, high precision Fe and Mg isotope ratios have been determined for MPI-DING and USGS reference glasses by conventional solution MC-ICP-MS and, for the first time, by *in situ* femtosecond laser ablation MC-ICP-MS. We demonstrate that *in situ* Fe and Mg isotope analyses of silicates by fs-LA-MC-ICP-MS can be performed with an external reproducibility of <0.13‰ (2 SD) for δ^{26}Mg and δ^{56}Fe values at a spatial resolution of about 50µm. All investigated glass reference materials are homogeneous with respect to their Fe and Mg isotopic signatures within our analytical uncertainties, and are thus suitable as reference materials for further *in situ* Fe-Mg isotope studies. The consistent results of bulk (highly precise solution nebulization MC-ICP-MS) and *in situ* (fs-LA-MC-ICP-MS) Fe and Mg isotope analyses provide robust reference values for these reference materials. These results also indicate that Fe and Mg isotope analyses by fs-LA-MC-ICP-MS are largely matrix-independent considering the variety of different glass compositions analyzed, including SiO_2-rich and SiO_2-poor glasses as well as a pure MgO crystal. Furthermore, the spatial resolution and precision of this technique is suitable to resolve small-scale isotopic variations in geological materials, such as diffusion-generated Fe-Mg isotopic zoning in magmatic olivines.

I.Tables

Table I.1a: Instrumental parameters for *in situ* Fe- and Mg isotope analyses

fs-LA system	
Spot diameter (µm)	40 — 50
Repition rate (Hz)	4 — 100
Pulse length (s)	~200 · 10^{-15}
Pulse energy output (mJ)	0.07
Pulse energy at sample (mJ)	0.015
Achievable energy density (J cm^{-2})	~2
Ablation cell volume (cm^3)	30
Neptune MC-ICP-MS	
Cool gas: Ar (l min^{-1})	14.6 — 15.0
Aux gas: Ar (l min^{-1})	0.7 — 0.9
Sample gas: Ar (l min^{-1})	0.88 — 0.94
Carrier gas: He (l min^{-1})	0.5 — 0.7
nebulizer uptake rate (µl min^{-1})	~100
RF generator power (W)	1200 — 1240
Acceleration voltage (V)	-10000
Extraction (V)	-1850 — -2000
Focus (V)	-590 — -680
routinely achieved signal intensity (V)	
for ^{56}Fe:	12 — 16
for ^{24}Mg:	6 — 10

Table I.1b: Faraday cup settings and types of cones used for the various analyses of this study

Method		Faraday cups, equipped with 10^{11} Ω resistors									sample cone	skimmer cone
		L4	L3	L2	L1	Center	H1	H2	H3	H4		
in situ and solution nebulization Mg isotope analyses		-	^{24}Mg	-	-	^{25}Mg	-	-	^{26}Mg	-	Ni	Ni, X-type
in situ Fe isotope analyses with Ni addition (static)		^{53}Cr	-	^{54}Fe	-	^{56}Fe	^{57}Fe	^{58}Ni	-	^{60}Ni	Ni	Ni, X-type
solution nebulization Fe isotope analyses with Ni addition (static)		^{53}Cr	-	^{54}Fe	-	^{56}Fe	^{57}Fe	^{58}Ni	-	^{60}Ni	Ni	Ni, H-type
solution nebulization Fe isotope analyses with Cu addition (dynamic)		^{53}Cr	-	^{54}Fe	-	^{56}Fe	^{57}Fe	^{58}Ni	-	^{60}Ni	Ni	Ni, H-type
	jump to	-	^{63}Cu	-	^{65}Cu	-	-	-	-	-		

Table I.2: Fe isotope compositions of MPI-DING and USGS reference glasses

	solution nebulization MC-ICP-MS							Provider [d]	fs-LA-MC-ICP-MS									
sample	δ^{56}Fe (‰, IRMM-014)	2 SD_{rs} [a]	2 σ_{sol} [b]	δ^{57}Fe (‰, IRMM-014)	2 SD_{rs} [a]	2 σ_{sol} [b]	n [c]		δ^{56}Fe (‰, IRMM-014)	2 σ_{LA} [e]	δ^{57}Fe (‰, IRMM-014)	2 σ_{LA} [e]	δ^{56}Fe (‰, LAS)	2 SD_{rl} [f]	δ^{57}Fe (‰, LAS)	2 SD_{rl} [f]	n [c]	primary standard used
^{60}Ni/^{58}Ni as instrumental mass bias monitor																		
BCR-2G	0.085	0.031	0.037	0.127	0.056	0.059	4	USGS	0.10	0.12	0.16	0.12	0.10	0.11	0.16	0.11	5	IRMM-014
BHVO-2G	0.099	0.036	0.042	0.152	0.045	0.049	4	USGS	0.06	0.13	0.09	0.20	-0.03	0.12	-0.04	0.18	17	BCR-2G
BIR-1G	0.048	0.032	0.037	0.090	0.069	0.072	4	USGS	-0.04	0.09	-0.05	0.15	-0.12	0.07	-0.17	0.13	18	BCR-2G
ML3B-G	0.052	0.030	0.036	0.087	0.048	0.052	4	MPI	0.00	0.13	-0.01	0.26	-0.09	0.12	-0.14	0.25	10	BCR-2G
KL2-G	0.081	0.030	0.036	0.131	0.065	0.068	4	MPI	0.02	0.12	0.02	0.21	-0.07	0.10	-0.10	0.20	14	BCR-2G
GOR128-G	-0.025	0.030	0.036	-0.034	0.040	0.045	4	MPI	-0.04	0.09	-0.06	0.16	-0.13	0.07	-0.19	0.14	12	BCR-2G
GOR132-G	0.041	0.030	0.036	0.070	0.040	0.045	4	MPI	-0.02	0.11	-0.01	0.17	-0.11	0.10	-0.14	0.15	10	BCR-2G
T1-G	0.056	0.043	0.048	0.106	0.057	0.060	4	MPI	0.10	0.07	0.16	0.13	0.01	0.05	0.04	0.11	4	BCR-2G
StHs6/80-G	0.073	0.030	0.036	0.135	0.044	0.048	4	MPI										
^{65}Cu/^{63}Cu as instrumental mass bias monitor																		
BCR-2G	0.091	0.037		0.130	0.046		4	USGS										
BHVO-2G	0.100	0.043		0.150	0.072		4	USGS										
BIR-1G	0.051	0.038		0.089	0.081		4	USGS										

[a] 2 SD_{rs} represents the reproducibility of the δ-values, based on replicate analyses of individual samples during a single analytical session.

[b] 2 σ_{sol} represents the overall uncertainty (95% confidence level) for the reported solution δ-value, according to Eqn. I.7.

[c] n represents number of analyses.

[d] USGS is the United States Geological Survey in Denver (USA); MPI represents Max-Planck-Institut in Mainz (Germany).

[e] 2 σ_{LA} represents the overall uncertainty (95% confidence level) for the reported *in situ* δ-value relative to IRMM-014, according to Eqn. I.5.

[f] 2 SD_{rl} represents the external reproducibility of the δ-values relative to a primary laser ablation standard (LAS), based on repeated analyses over a period of 12 months.

Table I.3: Mg isotope compositions of MPI-DING and USGS reference glasses

	Solution nebulization MC-ICP-MS						Provider [c]	fs-LA-MC-ICP-MS										
sample	δ^{25}Mg (‰, DSM-3)	2 SD_{rs} [a]	δ^{26}Mg (‰, DSM-3)	2 SD_{rs} [a]	n [b]	Comment		δ^{25}Mg (‰, DSM-3)	2 σ_{LA} [d]	δ^{26}Mg (‰, DSM-3)	2 σ_{LA} [d]	δ^{25}Mg (‰, LAS)	2 SD_{rl} [e]	δ^{26}Mg (‰, LAS)	2 SD_{rl} [e]	n [b]	primary standard used	Suffix in Fig. I.6
BHVO-2G	-0.133	0.032	-0.239	0.052	5		USGS	-0.10	0.04	-0.21	0.05	0.55	0.04	1.07	0.04	3	MgO	
BIR-1G	-0.148	0.041	-0.295	0.051	4		USGS	-0.14	0.06	-0.26	0.07	0.51	0.06	1.02	0.05	3	MgO	a
								-0.14	0.07	-0.27	0.08	-0.01	0.06	-0.03	0.06	12	BHVO-2G	b
BCR-2G	-0.164	0.038	-0.303	0.056	4		USGS	-0.21	0.09	-0.40	0.18	-0.08	0.08	-0.16	0.17	7	BHVO-2G	
ML3B-G	-0.170	0.055	-0.324	0.111	4		MPI	-0.14	0.07	-0.27	0.16	-0.01	0.07	-0.03	0.15	5	BHVO-2G	
KL2-G	-0.139	0.056	-0.270	0.065	4		MPI	-0.17	0.05	-0.31	0.12	0.48	0.04	0.97	0.11	8	MgO	a
								-0.15	0.05	-0.26	0.14	-0.02	0.04	-0.02	0.13	4	BHVO-2G	b
GOR128-G	-0.150	0.037	-0.288	0.056	4		MPI	-0.12	0.05	-0.23	0.10	0.01	0.04	0.01	0.08	5	BHVO-2G	a
								-0.15	0.05	-0.29	0.14	-0.06	0.05	-0.12	0.11	23	GOR132-G	b
GOR132-G	-0.089	0.030	-0.174	0.039	4		MPI	-0.09	0.06	-0.15	0.08	0.04	0.05	0.09	0.07	7	BHVO-2G	
StHs6/80-G	-0.189	0.053	-0.354	0.089	3		MPI											
T1-G	-0.145	0.036	-0.285	0.033	4		MPI											
MgO	-0.659	0.046	-1.276	0.100	4		SPI	-0.62	0.08	-1.23	0.14	-0.53	0.07	-1.06	0.11	5	GOR132-G	
	-0.654	0.030	-1.279	0.048	3	no ion exchange chromatography												
Cambridge-1	-1.355	0.034	-2.596	0.086	3													
	-1.342	0.033	-2.612	0.032	4	no ion exchange chromatography												

[a] 2 SD_{rs} represents the reproducibility of the δ-values, based on replicate analyses of individual samples during a single analytical session.

[b] n represents number of analyses.

[c] USGS is the United States Geological Survey in Denver (USA); MPI represents Max-Planck-Institut in Mainz (Germany); SPI represents SPI Supplies, Inc. (USA).

[d] 2 σ_{LA} represents the overall uncertainty (95% confidence level) for the reported *in situ* δ-value relative to DSM-3, according to Eqn. I.6.

[e] 2 SD_{rl} represents the measurement reproducibility of the δ-values relative to a primary laser ablation standard (LAS), based on repeated analyses over a period of 12 months.

Chapter II: Processes and time scales of magmatic evolution as revealed by Fe-Mg chemical and isotopic zoning in natural olivines*

* A modified version of Chapter II has been published as: Oeser M., Dohmen R., Horn I., Schuth S., Weyer S. (in press) Processes and time scales of magmatic evolution as revealed by Fe-Mg chemical and isotopic zoning in natural olivines. *Geochimica et Cosmochimica Acta*, DOI: 10.1016/j.gca.2015.01.025

II.Abstract

In this study, we applied high-precision *in situ* Fe and Mg isotope analyses by femtosecond laser ablation (fs-LA) MC-ICP-MS on chemically zoned olivine xeno- and phenocrysts from intra-plate volcanic regions in order to investigate the magnitude of Fe and Mg isotope fractionation and its suitability to gain information on magma evolution. Our results show that chemical zoning (i.e., Mg#) in magmatic olivines is commonly associated with significant zoning in δ^{56}Fe and δ^{26}Mg (up to 1.7‰ and 0.7‰, respectively). We explored different cases of kinetic fractionation of Fe and Mg isotopes by modeling diffusion in the melt or olivine and simultaneous growth or dissolution. Combining the information of chemical *and* isotopic zoning in olivine allows to distinguish between various processes that may occur during magma evolution, namely diffusive Fe-Mg exchange between olivine and melt, rapid crystal growth, and Fe-Mg inter-diffusion simultaneous to crystal dissolution or growth. Chemical diffusion in olivine appears to be the dominant process that drives isotope fractionation in magmatic olivine. Simplified modeling of Fe- and Mg diffusion is suitable to reproduce both the chemical and the isotopic zoning in most of the investigated olivines and, additionally, provides time information about magmatic processes. For the Massif Central (France), modeling of diffusive re-equilibration of mantle olivines in basanites revealed a short time span (<2 years) between the entrainment of a mantle xenolith in an intra-plate basaltic magma and the eruption of the magma. Furthermore, we determined high cooling rates (on the order of a few tens to hundreds of °C per year) for basanite samples from a single large outcrop in the Massif Central, which probably reflects the cooling of a massive lava flow after eruption. Results from the modeling of Fe- and Mg isotope fractionation in olivine point to a systematic difference between β_{Fe} and β_{Mg} (i.e., $\beta_{Fe}/\beta_{Mg} \approx 2$), implying that

the diffusivity ratio of ^{54}Fe and ^{56}Fe (i.e., D_{54Fe}/D_{56Fe}) is very similar to that of ^{24}Mg and ^{26}Mg, despite the smaller relative mass difference for the ^{54}Fe-^{56}Fe pair. This study demonstrates that a combined investigation of Fe-Mg chemical *and* isotopic zoning in olivine provides additional and more reliable information on magma evolution than chemical zoning alone.

II.1 Introduction

Chemical zoning, e.g., of Fe and Mg, is common for phenocrysts and xenocrysts in volcanic rocks. Possible end-member processes that can result in chemically zoned crystals, include (i) prolonged crystal growth in an evolving melt during magmatic differentiation without diffusive exchange between crystal and melt (further on described as "growth zoning"), and (ii) diffusion-controlled chemical exchange generated by a chemical gradient between crystal and melt (e.g., Teng et al., 2011). The latter has been used in several studies to obtain time information about the evolution of magmatic systems by the modeling of chemical gradients in magmatic minerals, such as plagioclase and olivine (e.g., Costa and Dungan, 2005; Kahl et al., 2011; Druitt et al., 2012). However, chemical zoning, generated by diffusion in the crystal, cannot always easily be distinguished from pure growth zoning that provides only limited time information.

The *in situ* analysis of stable metal isotope ratios in pheno- and xenocrysts provides a powerful tool to distinguish between these endmember processes (Sio et al., 2013). As light isotopes diffuse slightly faster than heavier isotopes, diffusive processes result in large kinetic isotope fractionations even at magmatic temperatures (e.g., Richter et al., 2003). In contrast, crystal growth (if slow and not limited by diffusion in the melt) is regarded to occur in equilibrium with the melt and accordingly, only small isotope effects are expected at magmatic temperatures (Polyakov and Mineev, 2000; Weyer and Ionov, 2007; Davidson et al., 2007; Teng et al., 2007; Schauble, 2011).

Recent studies have shown that chemical diffusion generates Fe and Mg isotope fractionation in olivine that exceeds potential equilibrium isotope fractionation by an order of magnitude (Teng et al., 2011; Weyer and Seitz, 2012; Sio et al., 2013). Accordingly, magmatic olivine crystals that show diffusion-generated Fe-Mg zoning may also be expected to show coupled Fe-Mg isotopic zoning. Moreover, Fe-Mg isotopic zoning in such olivine

may be used as evidence for the diffusion origin of their chemical zoning. Here, we analyzed Fe- and Mg isotope profiles for chemically zoned magmatic olivine crystals *in situ* by femtosecond laser ablation multi-collector ICP-MS (fs-LA-MC-ICP-MS) to address the following questions: (i) Do chemically zoned olivine crystals commonly show zoning in δ^{56}Fe and δ^{26}Mg? (ii) Can we use the isotopic zoning combined with the chemical zoning to gain information on magma evolution? In order to investigate this question we theoretically explore the effects of Fe-Mg inter-diffusion, crystal growth and crystal dissolution on chemical and isotopic zoning in olivine on the basis of different models. And finally, (iii) can we use simplified diffusion modeling to reproduce the chemical and isotopic zoning in magmatic olivine and thus gain information about the time scales of magma evolution?

II.2 Samples

We investigated olivine-bearing basaltic rocks from the Massif Central (France) and the Vogelsberg (Germany) volcanic regions, as well as from Tenerife (Canary Islands). Some of these samples also contain fresh mantle xenoliths, which are very suitable for studying diffusion-driven isotope fractionation because they were probably never in chemical equilibrium with their host melt (cf. Weyer and Seitz, 2012) and, hence, chemical re-equilibration by diffusive flux has very likely occurred.

Samples from the Massif Central comprise olivine-phyric basanites that were mainly taken (as solid rock) in a former quarry ("Roche Sauterre"; N45°54.858‘, E02°55.674‘) near the village of Sauterre. Basanites from Roche Sauterre (samples StR to StTop; Table II.1 in section II.Tables, Fig. II.1) erupted during the late Miocene to early Pliocene (Lorand et al. 2003; Nehlig et al. 2003). The Roche Sauterre may represent a large lava flow that merged in a paleo-topographic low, possibly forming a small lava lake (Richet, 2003). Sample BdOr is an olivine- and clinopyroxene-bearing basanite taken at the summit of the Banne d'Ordanche (N45°36.671‘, E02°46.355‘), which probably represents a relic of the north-west slope of a former strato-volcano (Richet, 2003). The sampled basanite itself erupted 710000 years ago. Sample LaTu (a 7000 years old olivine-bearing basanite) was taken at a road outcrop (N45°26.562', E02°55.281') near the village of Compains. The outcrop exposes a small lava flow from the volcano Montcineyre. Major element and trace element concentrations (determined by XRF and solution nebulization ICP-MS, respectively) of the Massif Central basanites are shown in Table II.1. See also Figure A-II.1 in Appendix II for a classification of these rocks according to alkali and silica contents (TAS diagram).

Sample TF-9 is an olivine-bearing basalt from Tenerife and Vog-13 is a nephelinite from the Vogelsberg volcanic region. Both samples have already been investigated by Weyer and Seitz (2012) for their Fe- and Li isotopic compositions and show large Fe- and Li isotope fractionation between olivine (mineral separates) and the basaltic matrix ($\Delta^{56}Fe_{ol\text{-}melt} \leq -0.19‰$ and $\Delta^{7}Li_{ol\text{-}melt} \leq -9.2‰$), indicating kinetic isotope fractionation due to diffusion of Fe and Li into olivine during magmatic differentiation (Weyer and Seitz, 2012).

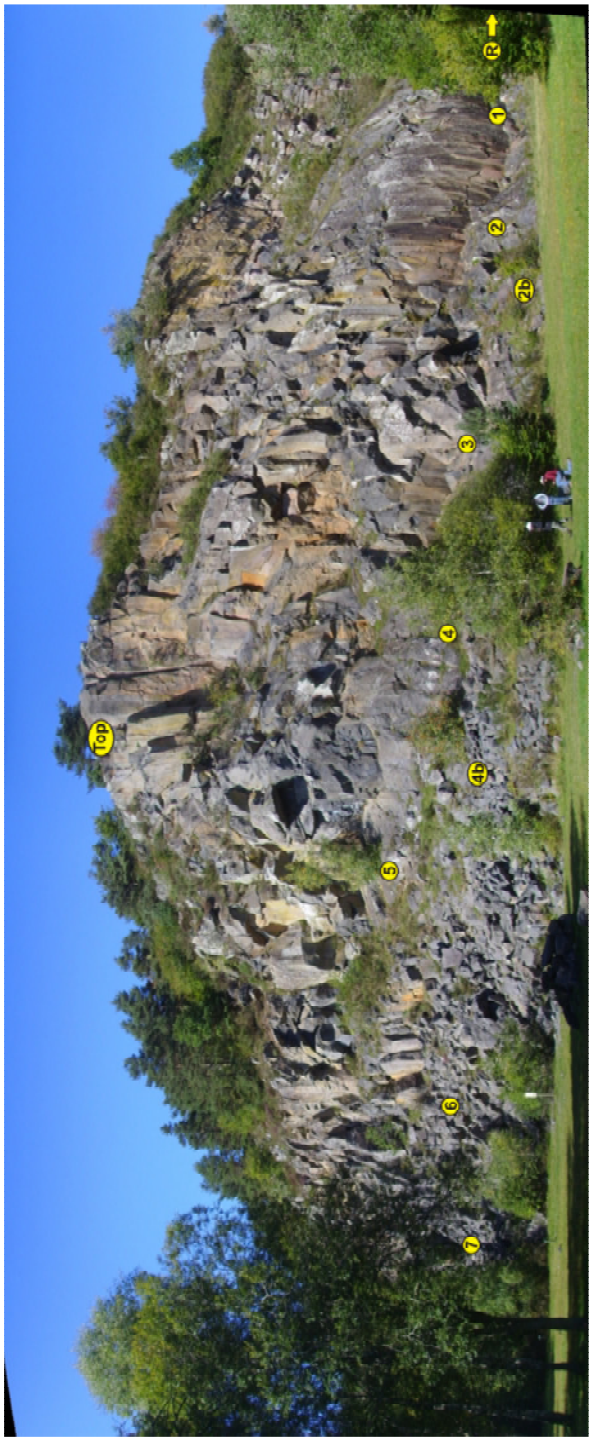

Figure II.1: The "Roche Sauterre" outcrop in the Chaîne de la Sioule (Massif Central, France). Locations where samples were taken are marked by yellow circles (with sample numbers).

II.3 Methods

II.3.1 Electron Microprobe Analyses

Major elements (Mg, Si, Ca, Mn, Fe, Ni) of selected olivine crystals were analyzed with a Cameca SX-100 electron microprobe (EPMA) at the Institut für Mineralogie of the Leibniz Universität Hannover (Germany). For all analyses an acceleration voltage of 15 kV, a beam current of 15 nA and a focused beam were used. Standard materials include synthetic MgO, NiO, Fe_2O_3, Mn_3O_4 as well as wollastonite (Si and Ca), and a Mg-rich olivine ("Jarosewich-Standard Fo90"; Jarosewich et al., 1980). Matrix corrections were performed using the PAP method (Pouchou and Pichoir, 1991). Counting times on peak and background were as follows: for Si, Mn: 10 seconds (s); Mg, Fe: 20 s; Ca: 40 s; Ni: 60 s.

II.3.2 *In situ* Fe- and Mg isotope analyses

In situ Fe- and Mg isotope analyses were carried out on olivine crystals, which show significant chemical zoning with respect to their Mg# and Ni contents. Iron and magnesium isotope analyses were performed by femtosecond laser ablation MC-ICP-MS (employing a Spectra-Physics Solstice fs-LA system and a Thermo-Finnigan Neptune®) in high mass resolution mode with sample-standard bracketing at the Institut für Mineralogie of the Leibniz Universität Hannover (Germany). For Fe isotope analyses, instrumental mass bias was monitored by simultaneous analyses of Ni isotopes (Poitrasson and Freydier 2005) of a Ni standard solution (NIST SRM 986, 5 µg ml^{-1}), which was added through ESI PFA-ST nebulizer into a quartz glass spray chamber (double pass Scott design) and then introduced into the plasma along with the ablation aerosol. Further details of the analytical procedure used in this study is given in section I.3. The long-term reproducibility that can routinely be achieved is better than ±0.13‰ (2 SD) for both δ^{56}Fe and δ^{26}Mg, based on replicate analyses of glass standards (e.g., BIR-1G, BCR-2G) over a period of 20 months. The reproducibility of δ^{56}Fe and δ^{26}Mg values for these standards during one analytical session (one day) is always better than ±0.09‰ and ±0.10‰ (2 SD) for δ^{56}Fe and δ^{26}Mg, respectively. This precision is probably more appropriate for defining the uncertainties of the measured δ-values for a single isotopic profile across an olivine because all analyses for creating one isotopic profile were always performed within one analytical session (one day).

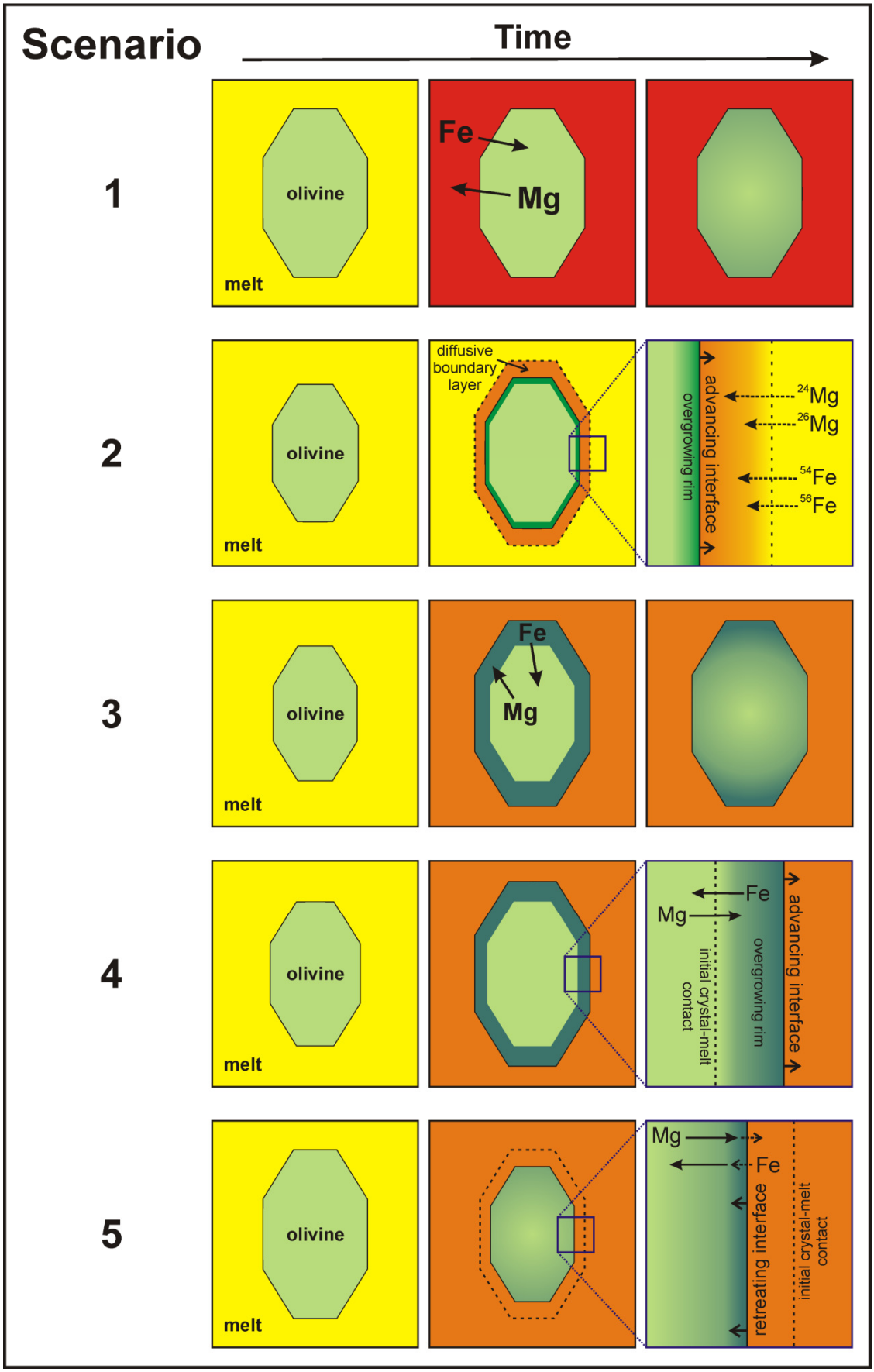

Figure II.2: Illustration of the five scenarios explored in this study in order to theoretically investigate the effects of Fe-Mg inter-diffusion, crystal growth and dissolution on chemical and isotopic zoning of olivines.

II.3.3 Modeling of chemical and isotopic zoning in olivines

II.3.3.1 Diffusion models

In order to illustrate which processes during magma evolution may be recorded by chemically and isotopically zoned olivines we simulated the effects of Fe-Mg inter-diffusion, crystal growth and crystal dissolution on chemical and isotopic zoning of olivines in general. The one-dimensional diffusion equation was solved for various boundary conditions corresponding to different scenarios (Fig. II.2) to equilibrate an initially homogenous olivine with the melt: (i) Pure Fe-Mg exchange of the olivine with the melt assuming a fixed rim composition and Fe-Mg inter-diffusion in olivine. Here we solved the diffusion equation numerically by the method of finite differences (e.g., see Costa et al. 2008). (ii) Diffusion-controlled growth of olivine in a melt on top of a homogeneous olivine core as a plane sheet. Diffusion in olivine was assumed to be negligible during this process since diffusion of Fe and Mg in the melt is several orders of magnitude faster. The analytical solution to the corresponding diffusion equation is given in Eqn. 3 of Watson and Müller (2009), originally derived by Smith et al. (1955). (iii) Internal homogenization of olivine after two growth episodes producing initially chemical step profiles but homogeneous Fe and Mg isotopic compositions across the olivine with a plane sheet geometry. Again the diffusion equation was solved numerically for this case. (iv) Growth or dissolution of olivine with a constant rim composition, C_{rim}, but simultaneous Fe-Mg inter-diffusion in the olivine considered to be here as a semi-infinite medium with an initially homogenous composition, C_0. An analytical solution for this moving boundary problem was derived by first applying the front-fixing method (Crank, 1975) to obtain a diffusion equation with a convection term characterized by the growth velocity, *R* (units m/s):

$$\frac{\partial C}{\partial t} = D\frac{\partial^2 C}{\partial t^2} + R\frac{\partial C}{\partial x}$$

(Eqn. II.1)

The analytical solution to Eqn. II.1 is, as follows:

$$C(x,t) = C_0 + \exp\left[\frac{R\left(x - \frac{Rt}{2}\right)}{2D}\right]\frac{1}{2}\exp(\lambda t)\left\{\exp\left(-x\sqrt{\frac{\lambda}{D}}\right)\mathrm{erfc}\left[\frac{x}{2\sqrt{Dt}} - \sqrt{\lambda t}\right] + \exp\left(x\sqrt{\frac{\lambda}{D}}\right)\mathrm{erfc}\left[\frac{x}{2\sqrt{Dt}} + \sqrt{\lambda t}\right]\right\}$$

(Eqn. II.2)

A detailed derivation of this solution is given in Appendix II.

For each of the above cases (i)-(iv) we simulated the kinetic fractionation of the Fe and Mg isotopes. For the individual diffusion coefficients we applied the empirical formula of Richter et al. (1999):

$$\frac{D_\mathrm{a}}{D_\mathrm{b}} = \left(\frac{M_\mathrm{b}}{M_\mathrm{a}}\right)^{\beta}$$

(Eqn. II.3)

where D represents the diffusion coefficient, a and b are isotopes of a certain element (e.g., ^{54}Fe and ^{56}Fe), and M is the atomic mass in a.m.u. The exponent β is considered as an empirical constant, which is usually smaller than 0.5 and depends, in general, on the diffusion medium (e.g., Richter et al., 2009b). The value of β can be estimated by fitting the observed extent of isotopic fractionation in the profiles. The profiles of the Mg and Fe isotopes were modeled independently although the chemical diffusion process is controlled by one chemical Fe-Mg inter-diffusion coefficient (e.g., Chakraborty, 1997). However, according to Eqn. II.3, the effective diffusivities of the individual isotopes of Mg or Fe are very similar for typical values of $\beta < 0.5$, and hence for the modeling of the chemical diffusion profiles of Fe and Mg, the diffusivities of the individual isotopes do not need to be taken into account. Therefore, the diffusivities of the Mg and Fe isotopes used in our model are all very close to the Fe-Mg inter-diffusion coefficient but corrected slightly by a factor according to Eqn. II.3. The finally observed value for β is purely empirical and specific for the given modeled case. For the present study, diffusion of the individual Fe and Mg isotopes were modeled independently in order to check whether the observed intra-mineral concentration gradients and isotopic fractionations can be explained by a diffusive

fractionation mechanism, where light isotopes diffuse faster compared to heavy isotopes. The sign and magnitude of the fractionation for a given element is controlled by its chemical gradient between the crystal and the chemical environment, in this case the melt.

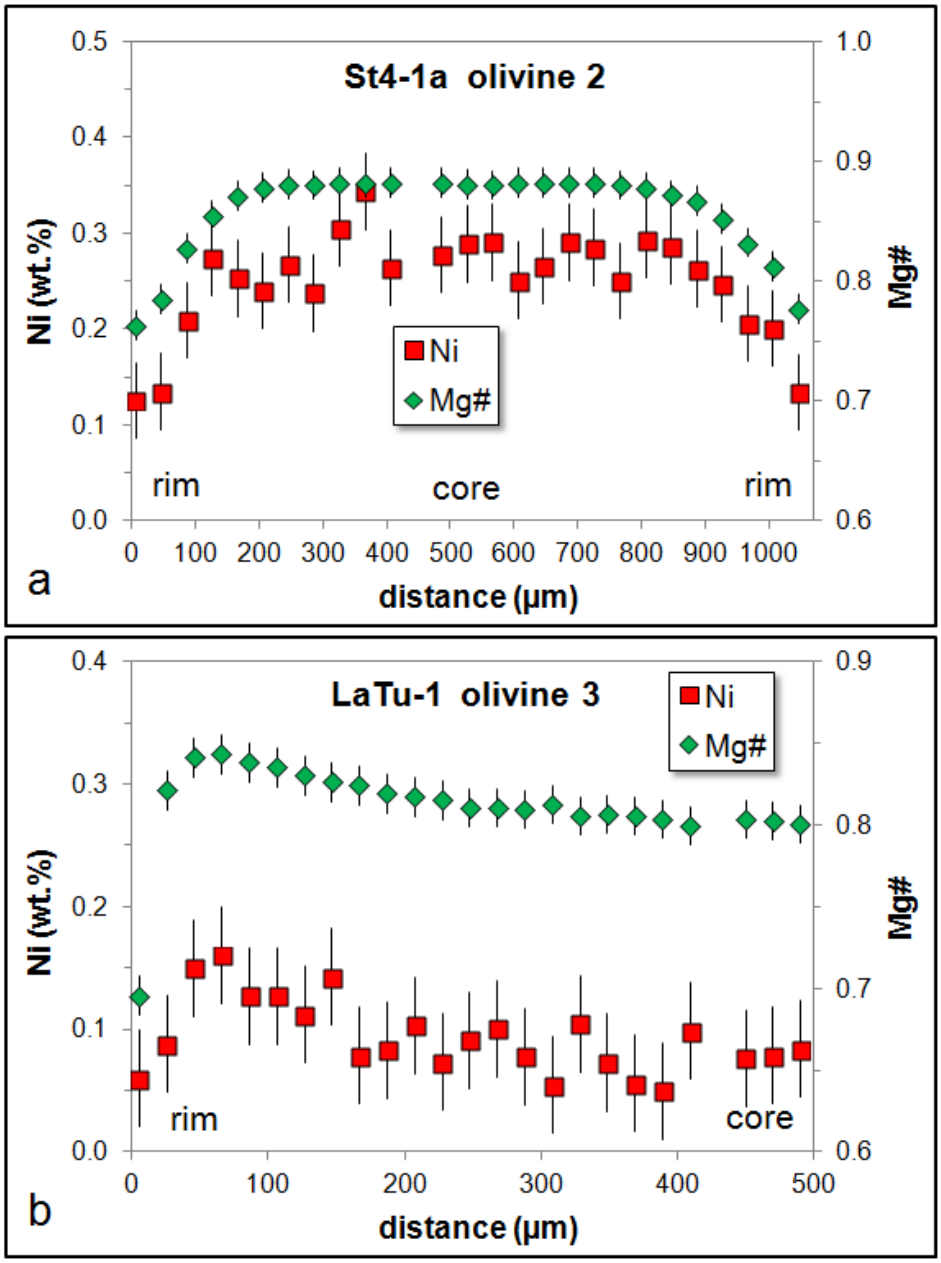

Figure II.3: Representative concentration profiles (Mg# and Ni) across (**a**) a normally zoned and (**b**) a multiply zoned olivine phenocryst in basanites from the Massif Central volcanic region (France) determined by EMP.

II.3.3.2 Determination of time scales

Chemical and isotopic zoning in olivines, which is mainly produced by Fe-Mg inter-diffusion (case (i) from above), can be used to estimate the time scales of diffusive re-equilibration which may represent magma residence times of these crystals (Costa et al., 2008). Here, we applied experimentally determined diffusion coefficients for Mg and Fe in olivine (e.g., Dohmen et al., 2007) to model the observed intra-mineral chemical and isotopic gradients. Throughout this study the diffusion coefficient for Fe-Mg diffusion in olivine was calculated following the parameterization of Dohmen and Chakraborty (2007). It depends on oxygen fugacity (fO_2), the mole fraction of the fayalite component (X_{Fe}), pressure (P), temperature (T), and the crystallographic orientation. A diffusion coefficient for a given profile direction can be calculated when the orientation of this profile relative to the crystallographic axes of the olivine is known (e.g., Costa et al., 2008). The crystallographic orientation of the individual olivine crystals was analyzed by electron backscatter diffraction (EBSD). These analyses were performed at the Institut für Geologie, Mineralogie und Geophysik of the Ruhr-Universität Bochum. Instrumental details for the EBSD system in Bochum are given in Table II.2.

Durations of the diffusive processes were estimated at isothermal conditions following the simplification outlined by Ganguly (2002), which is based on a "characteristic temperature" (T_{ch}) defined as $T_{ch} = 0.97 \cdot T_{peak}$, where T is in K. We have used the MELTS algorithm (Ghiorso and Sack, 1995; Asimow and Ghiorso, 1998) in order to constrain temperature, pressure, and fO_2 conditions for the basanites from the Roche Sauterre. The mineralogy of these samples (large olivines as the dominating phenocryst phase with core and rim compositions of Fo_{89} and Fo_{79}, respectively) is most closely reproduced at $P \leq 50$MPa and $fO_2 \approx$ NNO-2, yielding liquidus temperatures of ~1330°C and closure temperatures of ~1150°C. Hence, based on our modeling using MELTS and on thermometry data from Werling and Altherr (1997) and Faure et al. (2001) T_{peak} was assumed to be ~1295°C for Massif Central basanites (MCBs).

Chemical and isotopic zoning in olivines can be used to estimate cooling rates for the investigated samples, following the method described by Ganguly (2002), where T_{peak} and Q (the activation energy of diffusion) have to be known. Q was assumed to be 201 kJ/mol (Dohmen and Chakraborty, 2007) and "asymptotic" cooling was assumed (Ganguly, 2002). Further parameters that define our model for Fe-Mg inter-diffusion in olivine are as follows:

- The oxygen fugacity was taken to be $\Delta\log fO_2(NNO) = -2$, and its absolute value can be calculated at any temperature following the parameterizations of Schwab and Küstner (1981) and Herd (2008).
- The diffusion anisotropy in olivine was considered and the diffusion coefficient along any analytical profile can be calculated according to the approach presented in Costa and Chakraborty (2004; for an example see also Fig. A-II.2 in Appendix II).
- X_{Fe} was assumed to be constant and to be the mean of X_{Fe} in the core of the crystal and X_{Fe} at the very rim. Due to the limited compositional difference between core and rim (<0.2 in X_{Fe}) the uncertainty introduced by this simplification is negligible (see Fig. II.15).
- The pressure was taken to be invariable at 50 MPa.

Finally to solve the diffusion equation, the boundary conditions have to be defined. The core of the olivine represents a no-flux boundary while the magma around the crystal acts as an infinite reservoir (case i from above). Thus, Fe and Mg concentrations were assumed to be fixed at the contact of the olivine with the magma and to be equal to the Fe and Mg concentrations measured by EMP at the crystal rim. We also tested a diffusion model with changing Fe and Mg concentrations at the olivine-melt contact, i.e. the concentration of Fe increases while that of Mg decreases linearly with time (and temperature). However, especially the observed isotopic profiles could be reproduced much better with a model where Fe and Mg concentrations are assumed to be fixed.

II.4 Results

II.4.1 Fe-Mg chemical and isotopic zoning in natural "intra-plate" olivines

Line analyses by electron microprobe across more than 40 chemically zoned olivines from intra-plate volcanic rocks revealed that the vast majority have Fe-rich rims and Mg- and Ni-rich cores which we further on denote as "normally" zoned (Fig. II.3a). The difference in Mg# (molar Mg/[Mg+Fe]) between core and rim can be as large as 0.2, while the width of the Mg# zoning varies between ~50 µm and >400 µm. Olivine crystals of mantle xenoliths which were in contact with the basaltic host melt (further on denoted as "xenocrysts") exhibit always "normal" zoning at the rim and high Mg# paired with high Ni contents (in most cases >0.895 and >2800 µg g^{-1}, respectively) in the core. Only in a few samples, olivine shows complex zoning, i.e., sigmoidal pattern with low Mg# at the outermost rim, intermediate Mg# in the core and high Mg# in a zone in between (e.g., LaTu-1 ol3; Fig. II.3b). *In situ* Fe- (and Mg) isotope analyses can help to determine whether such zoning is diffusion- or growth-controlled, or a combination of both processes, as will be shown in section II.5.1.

Several of the investigated olivines show significant Fe-Mg isotopic zoning (up to 1.7‰ in δ^{56}Fe and 0.7‰ in δ^{26}Mg) that is coupled with the chemical zoning expressed as Mg#. The most common case is a normally zoned olivine where light Fe- and heavy Mg isotopes are relatively enriched in a zone near the Fe-rich crystal's rims, while the core does not show any chemical or isotopic zoning (Fig. II.4, Table II.3). Those olivines, which show multiple chemical zoning, correspondingly exhibit a complex isotopic zoning (Fig. II.5a), and a few olivines show normal chemical zoning, but still complex isotopic zoning, which appears to be decoupled from the chemical zoning (Fig. II.5b).

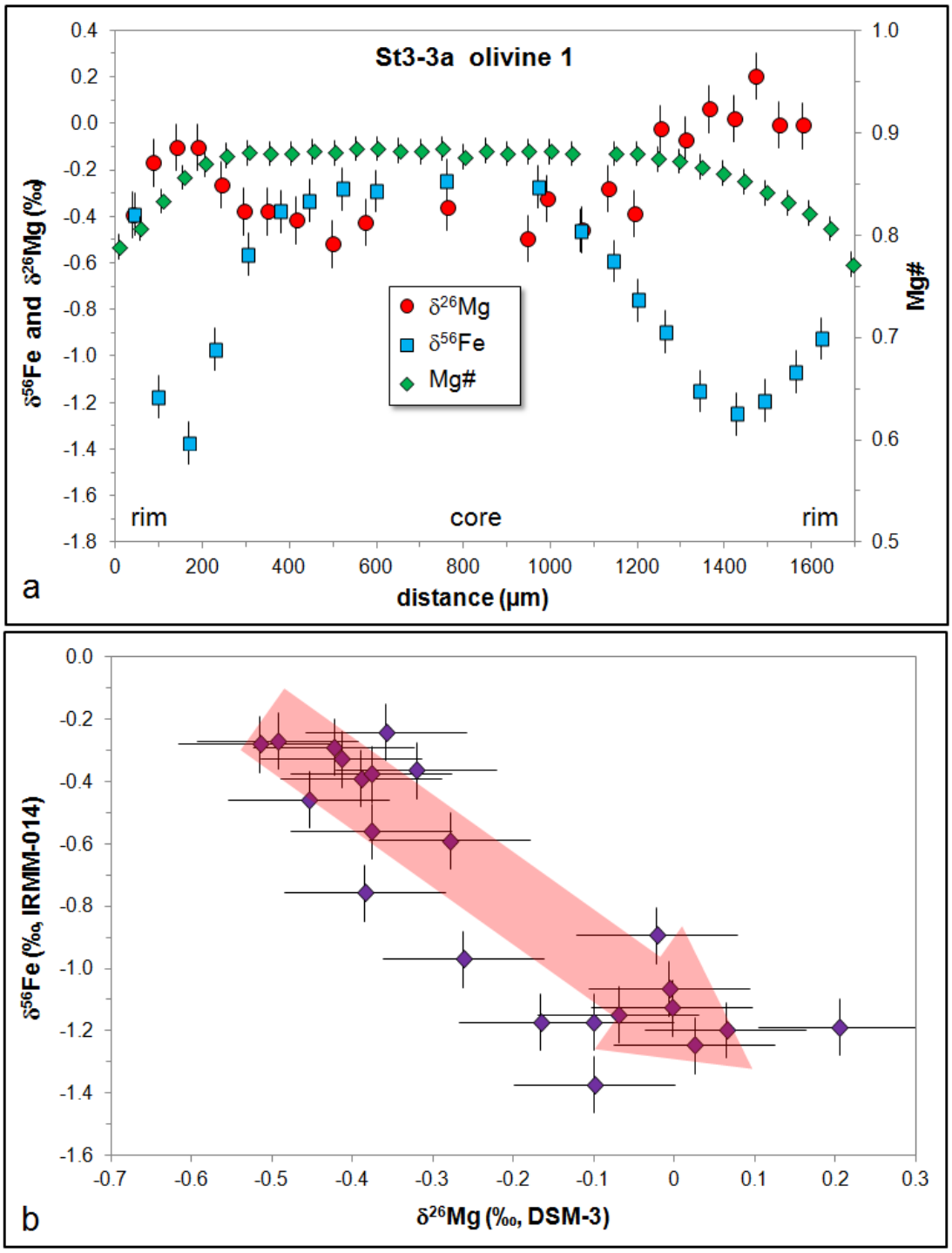

Figure II.4: (**a**) Fe-Mg chemical and isotopic profiles across a normally zoned olivine phenocryst (St3-3a olivine 1) from the Massif Central determined by fs-LA-MC-ICP-MS; Fe and Mg isotopic compositions are reported relative to IRMM-014 and DSM-3, respectively. (**b**) shows the negative correlation of δ^{56}Fe- and δ^{26}Mg-values that is characteristic of Fe-Mg inter-diffusion. Error bars represent the analytical uncertainty (2 SD) during one analytical session. Data are from Table II.3.

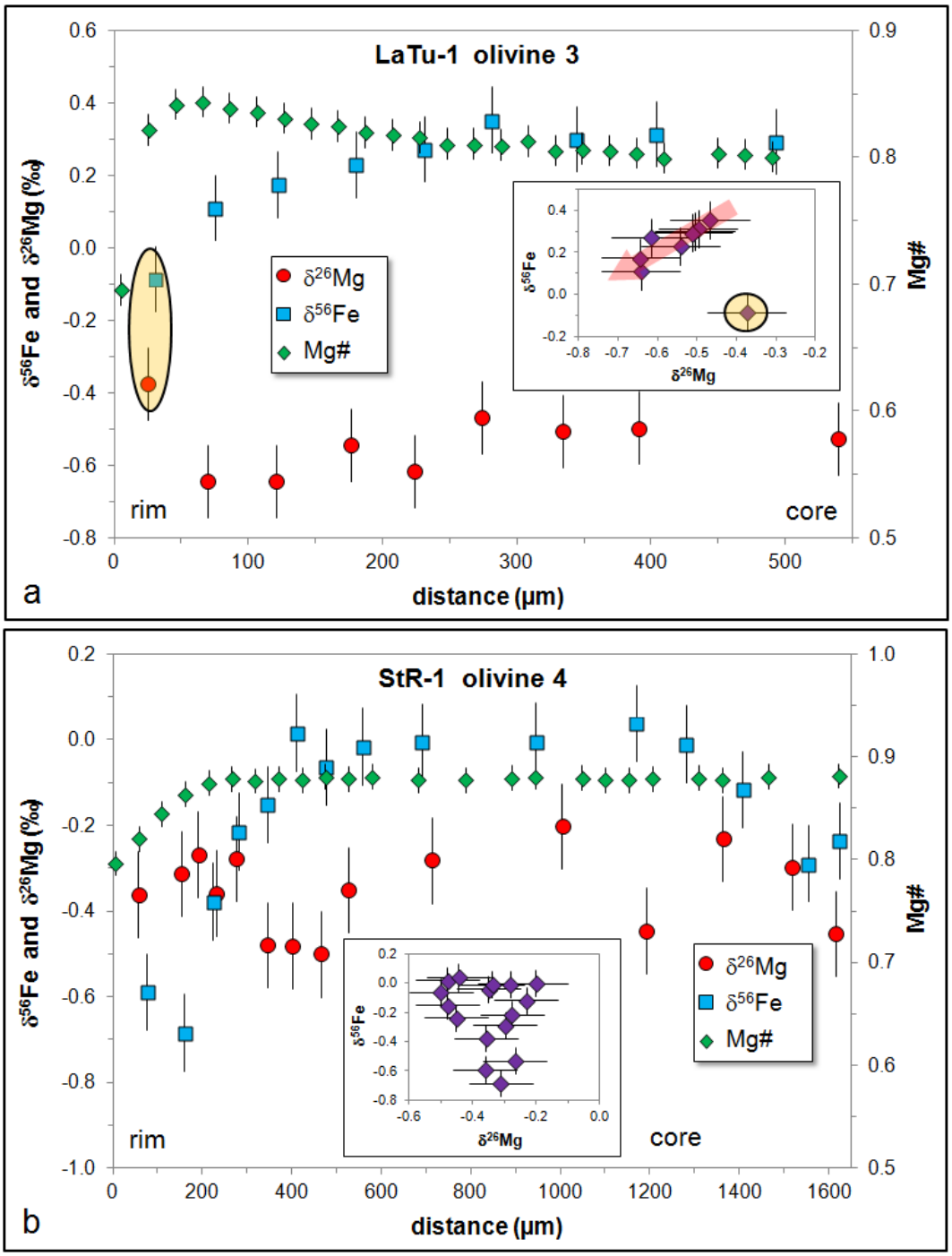

Figure II.5: Fe-Mg chemical and isotopic profiles across (**a**) a multiply zoned (LaTu-1 olivine 3) and (**b**) a normally zoned olivine phenocryst from the Massif Central; Fe and Mg isotopic compositions are reported relative to IRMM-014 and DSM-3, respectively. Insets in (a) and (b) show the relations of δ^{56}Fe- and δ^{26}Mg-values for these two olivines. Error bars represent the typical analytical uncertainty (2 SD) during one analytical session.

II.5 Discussion

II.5.1 Isotope effects in olivine during magma evolution

There are various processes potentially occurring during magma evolution which may generate and/or modify chemical and isotopic zoning in natural olivines, such as Fe-Mg inter-diffusion or rapid crystal growth. In the following section, we want to theoretically investigate the effects of five such scenarios (see Fig. II.2) on the chemical and isotopic compositions of olivines in order to provide a model-based framework for interpreting Fe-Mg chemical and isotopic profiles (determined *in situ*) and bulk Fe-Mg isotope data for olivines.

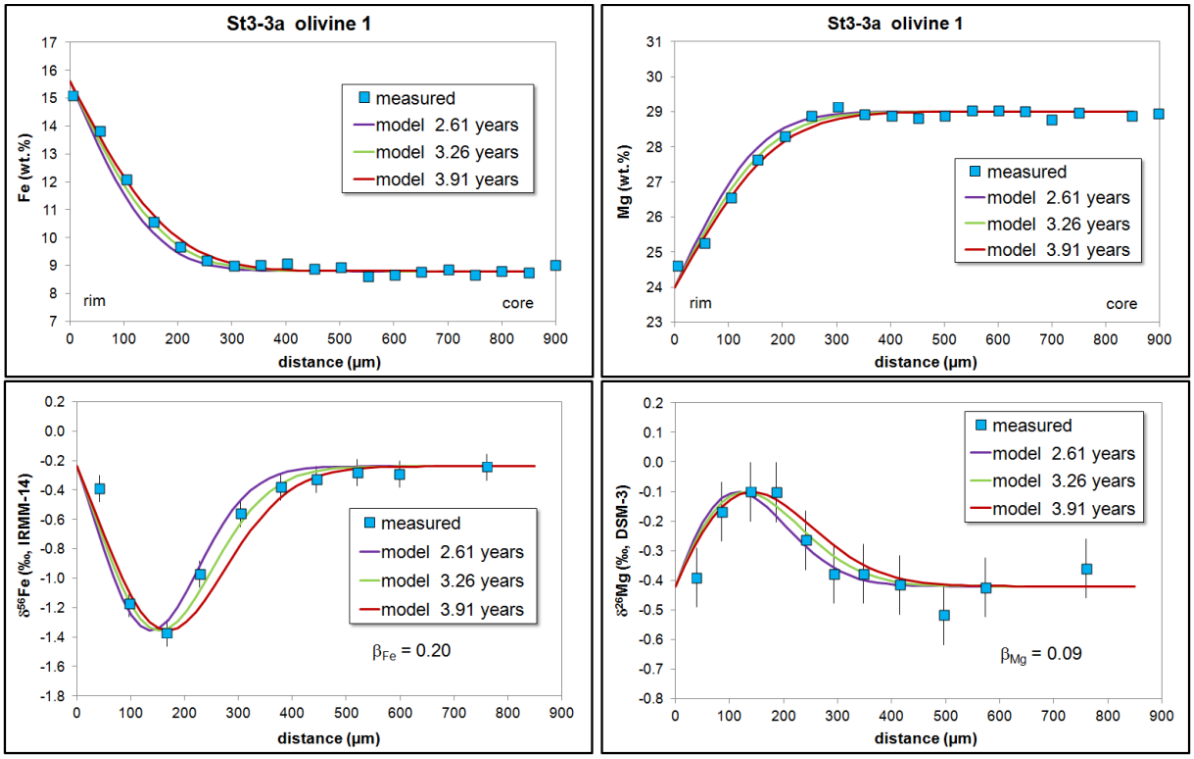

Figure II.6: Simplified modeling of Fe-Mg chemical and isotopic diffusion profiles for the Massif Central olivine shown in Fig. II.4. The diffusion coefficient D for Fe-Mg diffusion in olivine was calculated according to the parameterization of Dohmen and Chakraborty (2007). Model parameters: T = 1250°C (constant; corresponding to $0.97 \cdot T_{peak}$ and T_{peak} = 1570 K = 1297°C); X_{Fe} = 0.165 (constant); fO_2 at NNO-2; P = 50 MPa; we assumed fixed boundary concentrations; the dependency of the diffusion on the crystallographic orientation of the analyzed profiles, as determined by EBSD, was considered. We show modeling results for three time spans (2.61, 3.26 and 3.91 years) in order to illustrate the change of the profiles' lengths and shapes with time.

1) **Pure Fe-Mg inter-diffusion:** diffusive Fe-Mg exchange between olivine and melt is driven by a chemical gradient between crystal and melt. Such a chemical disequilibrium would certainly be expected if mantle xenoliths are entrained into a basaltic magma, but it may also develop between melt and olivine phenocrysts if the melt composition changed due to either magma mixing or magma differentiation. Previous studies have shown that Fe-Mg inter-diffusion results in chemical zoning coupled with inversely correlated Fe-Mg isotope signatures, either by modeling (Dauphas et al., 2010), the analyses of bulk olivine crystals and olivine fragments (Teng et al., 2011) or by *in situ* analyses of a single large olivine grain (Sio et al., 2013). The *in situ* analyses and modeling results for zoned olivines investigated in the present study corroborate these findings (Fig. II.6 and Fig. II.7). According to Dauphas et al. (2010) the observable δ^{56}Fe-δ^{26}Mg ratio depends on the β_{Fe}-β_{Mg} ratio and forsterite contents (X_{Fo}), as follows:

$$\frac{\delta^{56}\mathrm{Fe}}{\delta^{26}\mathrm{Mg}} = -\frac{\beta_{\mathrm{Fe}}}{\beta_{\mathrm{Mg}}} \times \frac{\left({}^{M_{56\mathrm{Fe}}}/_{M_{54\mathrm{Fe}}} - 1\right)}{\left({}^{M_{26\mathrm{Mg}}}/_{M_{24\mathrm{Mg}}} - 1\right)} \times \frac{X_{\mathrm{Fo}}}{1 - X_{\mathrm{Fo}}}$$

(Eqn. II.4)

We have used this equation to calculate possible δ^{56}Fe-δ^{26}Mg ratios for different X_{Fo} and assuming $\beta_{Fe}/\beta_{Mg} = 2$ (Sio et al., 2013; and our own estimations of β-values, see section II.5.3.2). The slopes of the correlations between δ^{56}Fe and δ^{26}Mg vary between -2.1 for $X_{Fo} = 0.7$ and -8.0 for $X_{Fo} = 0.9$ (Fig. II.8), underlining the mass balance effect on the diffusion-driven fractionation of Fe- and Mg isotopes in olivine (Sio et al., 2013; see also section I.4.3).

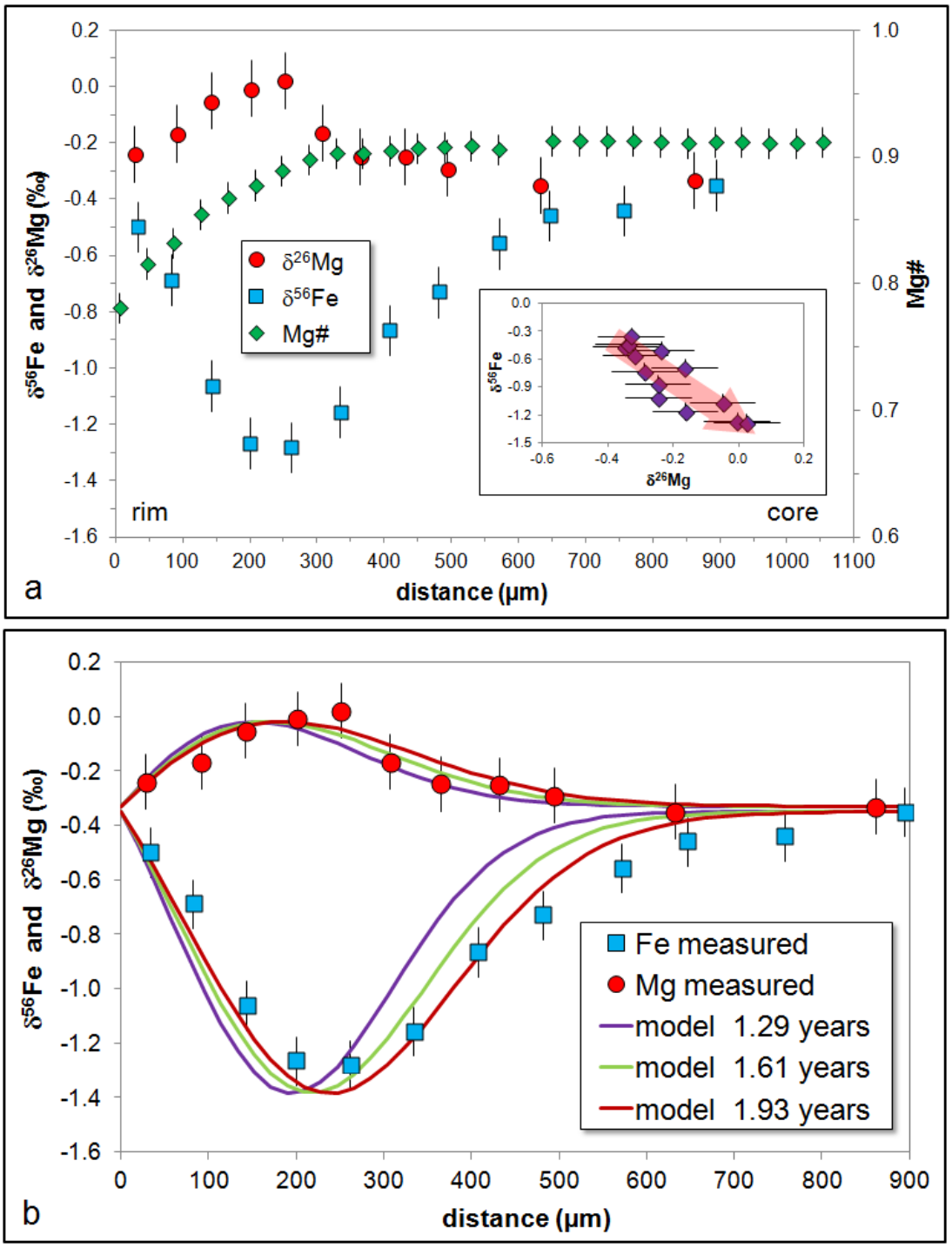

Figure II.7: (**a**) Fe-Mg chemical and isotopic profiles across a normally zoned olivine xenocryst from the Massif Central determined by fs-LA-MC-ICP-MS; Fe and Mg isotopic compositions are reported relative to IRMM-014 and DSM-3, respectively; inset in (a) shows the negative correlation of δ^{56}Fe- and δ^{26}Mg-values that is characteristic of Fe-Mg inter-diffusion. (**b**) Simplified modeling of Fe-Mg isotopic diffusion profiles for this olivine. Model parameters: T = 1250°C (constant; corresponding to $0.97 \cdot T_{peak}$ and T_{peak} = 1570 K = 1297°C); X_{Fe} = 0.155 (constant); fO_2 at NNO-2; P = 50 MPa; we assumed fixed boundary concentrations; the dependency of the diffusion on the crystallographic orientation of the analyzed profiles, as determined by EBSD, was considered; β_{Fe} = 0.120, β_{Mg} = 0.075. We show modeling results for three time spans (1.29, 1.61 and 1.93 years) in order to illustrate the change of the profiles' lengths and shapes with time.

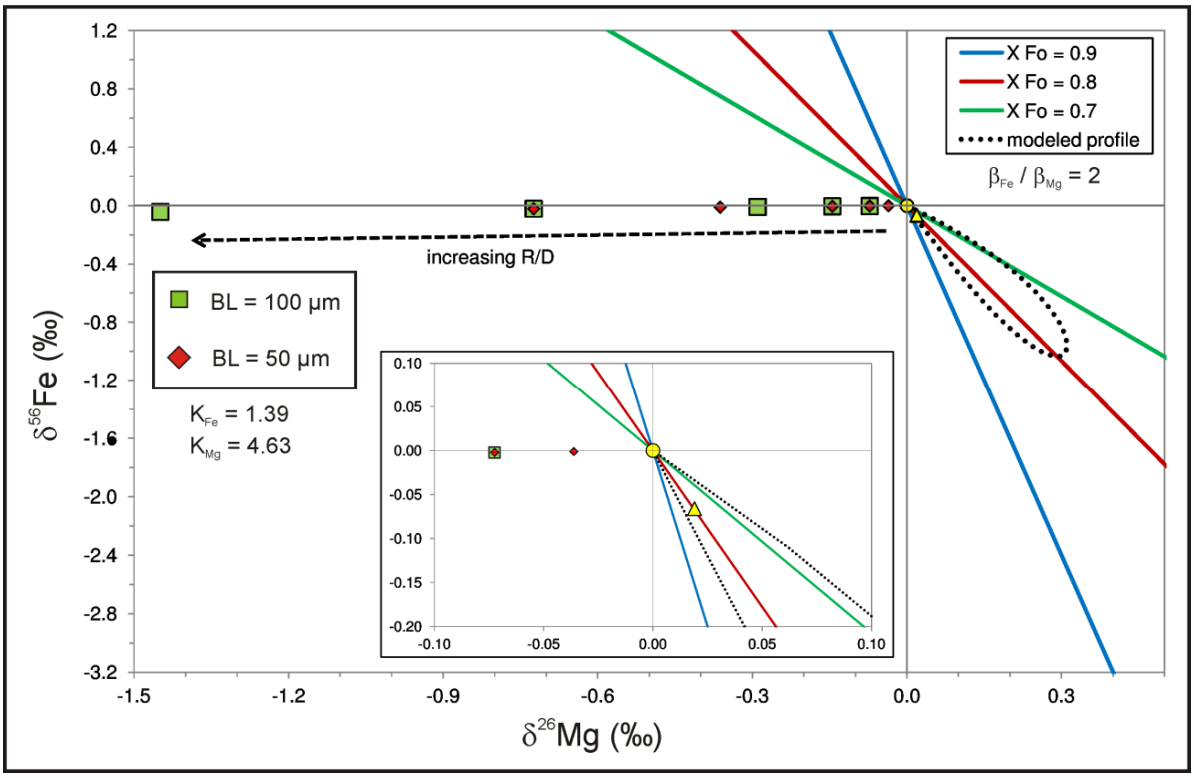

Figure II.8: Possible deviation from isotopic equilibrium in δ^{56}Fe and δ^{26}Mg observable in chemically zoned olivines. The effect of Fe-Mg inter-diffusion (scenarios 1, 3, 4, 5 in section II.5.1) is illustrated by the three lines with a negative slope which depends on the forsterite contents (X Fo) and the β_{Fe}-β_{Mg} ratio. δ^{56}Fe and δ^{26}Mg values of a modeled Fe-Mg isotopic profile across a normally zoned olivine xenocryst (St3-3a ol-xen1; Fig. II.7) are also shown as the dotted line. The β_{Fe}-β_{Mg} ratio for this olivine is 1.6.
The inset gives an enlarged view of the area around the origin. The yellow symbols represent the bulk isotopic compositions of (i) an olivine that is affected by intra-mineral Fe-Mg inter-diffusion after two growth episodes (scenario 3; yellow circle), and (ii) an olivine that is modified by crystal growth and simultaneous Fe-Mg inter-diffusion (scenario 4; yellow triangle).
The effect of rapid (diffusion-limited) crystal growth is illustrated by the squares and diamonds and it was calculated using Eqn. 11 presented in Watson & Müller (2009). Data were calculated for the following R/D values (in cm^{-1}): 0.5, 1, 2, 5, 10. See section II.5.1 and Appendix II for further details.

2) **Rapid crystal growth (producing a diffusive boundary layer around the growing crystal):** As pointed out by a number of studies (e.g., Watson and Müller, 2009; Goel et al., 2012) isotope fractionation can also occur during rapid (diffusion-limited) crystal growth if the growth rate is faster than diffusion of certain elements in the surrounding melt. Regarding compatible elements, such as Mg, the fast-growing olivine crystal would generate a depletion halo in the liquid near the crystal's rim (termed as "boundary

layer" by Watson and Müller, 2009). As Mg is much more compatible than Fe at temperatures around 1250°C and pressures around 50 MPa (i.e., $K_{Mg}^{ol\text{-}basalt} = C_{Mg}^{ol} / C_{Mg}^{basalt} \approx 4.6$; $K_{Fe}^{ol\text{-}basalt} \approx 1.4$; Ulmer, 1989) and the diffusivities of Fe and Mg appear to be similar in basaltic melts (Zhang et al., 2010, and references therein), the boundary layer would be strongly depleted in Mg and only slightly depleted in Fe. Accordingly, such fast diffusion-limited crystal growth would generate a similar chemical zoning in the olivine crystals (Mg-poor crystal rims) as Fe-Mg exchange between crystals and melt. However, combined *in situ* Fe and Mg isotope ratios can be used to distinguish between these two scenarios: since light isotopes generally diffuse faster than heavy isotopes, the diffusion of Mg and Fe from the infinite melt reservoir toward the growing crystal would produce an isotopically light boundary layer. We have used Eqn. 11 presented in Watson and Müller (2009; see Appendix II for details) to calculate the possible fractionation of Mg- and Fe isotopes due to rapid crystal growth at 1250°C and 50 MPa depending on the thickness of the boundary layer and the ratio of growth rate and diffusion rate (*R*/*D* in cm^{-1};Watson and Müller, 2009). Because the olivine-basalt partition coefficient K for Fe is near 1 at the assumed temperature and pressure conditions (Ulmer, 1989), the fractionation of Fe isotopes in the boundary layer would be expected to be very small (<0.1‰ even with a thick boundary layer and high *R*/*D*; Fig. II.9a). In contrast, as Mg is highly compatible in olivine (i.e., $K_{Mg}^{ol\text{-}basalt} >> 1$; Ulmer, 1989), significant fractionation of Mg isotopes would be expected in the boundary layer, resulting in $\delta^{26}Mg$ on the order of -1‰ (Fig. II.9b). As this characteristic isotope signature (highly negative $\delta^{26}Mg$, unaffected $\delta^{56}Fe$) would be incorporated into the growing olivine crystal, this would result in uncorrelated Fe-Mg isotope signature (see horizontal dashed line in Fig. II.8), in contrast to the negative isotopic correlation generated by chemical Fe-Mg exchange.

In addition to these considerations, we modeled Fe-Mg concentrations and isotopic profiles across an initially homogeneous olivine crystal (500 µm radius) assuming this olivine was rapidly overgrown by a ~100 µm thick rim (associated with a diffusive boundary layer; Fig. II.10). Model parameters of such a possible scenario are given in the figure caption of Fig. II.10. Even at a moderate *R*/*D* of 1.5 cm^{-1} the overgrowth rim will be depleted in Mg and enriched in Fe and will show an extremely light Mg isotopic composition. In contrast to Mg, the isotopic composition of Fe in the overgrowth rim would be identical within analytical uncertainties to that of the homogeneous core. The pronounced Mg isotopic zoning can be reliably resolved by *in situ* Mg isotope analyses

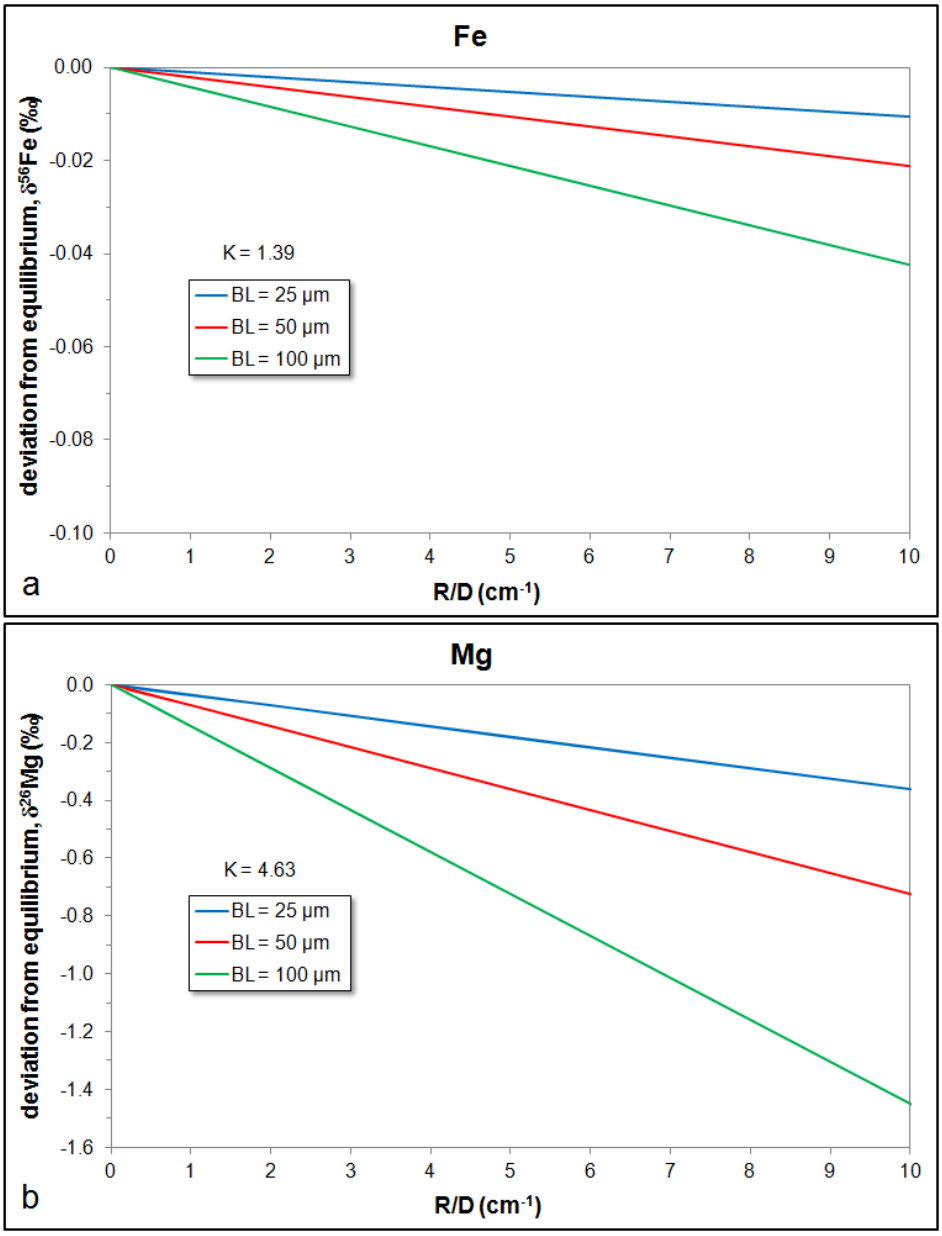

Figure II.9: Effect of rapid crystal growth on the maximum isotope fractionation of (**a**) Fe and (**b**) Mg in the boundary layer around a growing crystal, calculated according to Eqn. 11 in Watson & Müller (2009); see section II.5.1 and Appendix II for further details. The growing crystal would incorporate the characteristic isotope signature of the boundary layer, resulting in pronounced Mg isotopic zoning and essentially no variations in Fe isotope composition.

using fs-LA-MC-ICP-MS. The average Mg isotopic composition of this "model olivine" would also be shifted by -0.20‰ in δ^{26}Mg relative to the initial (equilibrium) Mg isotopic composition. Hence, even bulk analyses of such olivine grains (by solution nebulization MC-ICP-MS) may also be suitable to detect Mg isotope fractionation that

was generated by rapid crystal growth, given the currently achievable analytical uncertainty of ≤0.10‰ (2 SD) for δ^{26}Mg (e.g., Pogge von Strandmann et al., 2011; see also section I.3.5).

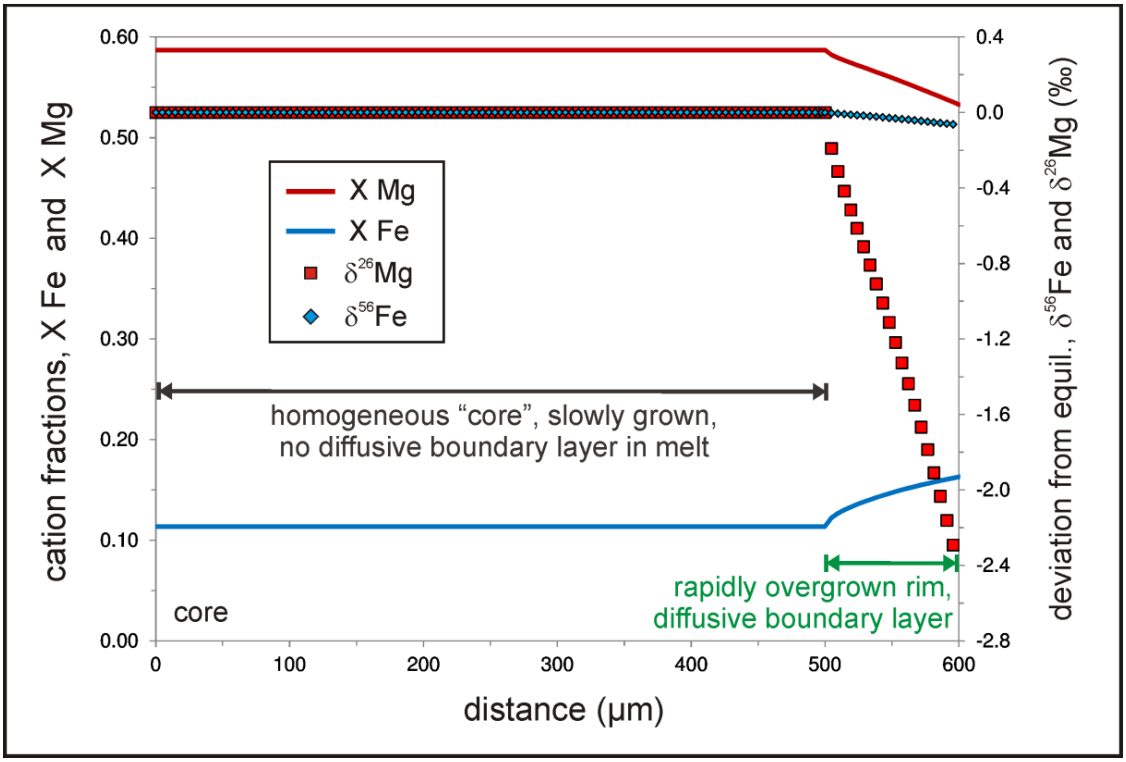

Figure II.10: Modeled core-to-rim traverses for Fe-Mg cation fractions (lines) and isotopic compositions (squares and diamonds) across an olivine (initial radius: 500 µm) that is rapidly overgrown by a 100 µm thick rim (associated with diffusive boundary layer). Cation fractions and isotopic compositions were calculated using Eqn. 3 presented in Watson & Müller (2009). Model parameters: T = 1250°C (constant); $D_{Mg} = D_{Fe} = 8.86 \cdot 10^{(-8)}$ cm²/s (Zhang et al., 2010, and references therein); R/D = 1.5 cm^{-1}. The cation partitioning coefficients for Mg and Fe, i.e. $Kd_{Mg}^{ol\text{-}melt}$ and $Kd_{Fe}^{ol\text{-}melt}$, depend on the cation fraction of Mg in the melt (Ulmer, 1989), which changes as the olivine grows. Hence, the change of Kd_{Mg} and Kd_{Fe} with continuing olivine growth was considered in the model. Initial cation fractions of Mg and Fe in the melt were assumed to be 0.151 and 0.0994, respectively (corresponding to 9.7 wt.% MgO and 11.4 wt.% FeO_t in a basanitic melt). D_{26Mg}/D_{24Mg} and D_{56Fe}/D_{54Fe} were taken to be 0.996 and 0.999, respectively (Richter et al., 2009b).

3) **Fe-Mg inter-diffusion after two crystal growth episodes (without a diffusive boundary layer):** studies by Kahl et al. (2011) and Longpré et al. (2014) have shown that natural olivines can also record two episodes of crystal growth that generated a step function in the Fo content traverses across such olivines (see e.g., Fig. 4c in Longpré et al.. 2014). These steps in the concentrations of Fe and Mg appear to be smoothed out by subsequent Fe-Mg inter-diffusion. We have used the Fe-Mg concentration traverses across an olivine phenocryst (EH_31-10-11_OL9) presented in the study by Longpré et al. (2014) in order to model the effect of such Fe-Mg inter-diffusion on the Fe-Mg isotopic profiles (Fig. II.11). Model parameters are the same as the ones used by Longpré et al. (2014), who modeled only the chemical zoning, and are given in the figure caption of Fig. II.11. Similar to diffusive Fe-Mg exchange between crystal and melt (scenario 1; Fig. II.6), the Fe and Mg isotopes are inversely correlated, however, the intra-mineral isotopic zoning is more complex. Especially the Fe isotopic zoning would be resolvable by *in situ* Fe isotope analyses using fs-LA-MC-ICP-MS (see section I.3.1) or MC-SIMS (Sio et al., 2013). Notably, a bulk analysis of such an olivine (by solution nebulization MC-ICP-MS) would not reveal any Fe-Mg isotope fractionation, as no diffusive flux into or out of the crystal is assumed in this scenario.

4) **Olivine growth (without a diffusive boundary layer) and simultaneous Fe-Mg inter-diffusion:** In theory, the growth of a rim around a homogeneous olivine crystal can also be associated with simultaneous Fe-Mg inter-diffusion. The effect of these processes (crystal growth + Fe-Mg inter-diffusion) on the chemical and isotopic gradients within the crystal strongly depend on the ratio of crystal growth rate (R in m/s) and diffusion coefficient (D in m²/s). Using Eqn. II.2 we present here possible rim-to-core traverses across an initially homogeneous olivine (with 10 wt.% Fe and 28 wt.% Mg, radius = 400 µm) that is overgrown with a rim of different composition (i.e., 16 wt.% Fe and 24 wt.% Mg) at a constant rate of $5.0 \cdot 10^{-11}$ m/s. This rate is at the lower boundary of crystal growth rates reported for natural olivines (e.g., Donaldson, 1975; Armienti et al., 1991; Jambon et al., 1992), because it has to be low enough in order to not generate a diffusive boundary layer around the growing crystal (see scenario 2 for details). Further model parameters are given in the figure caption of Fig. II.12.

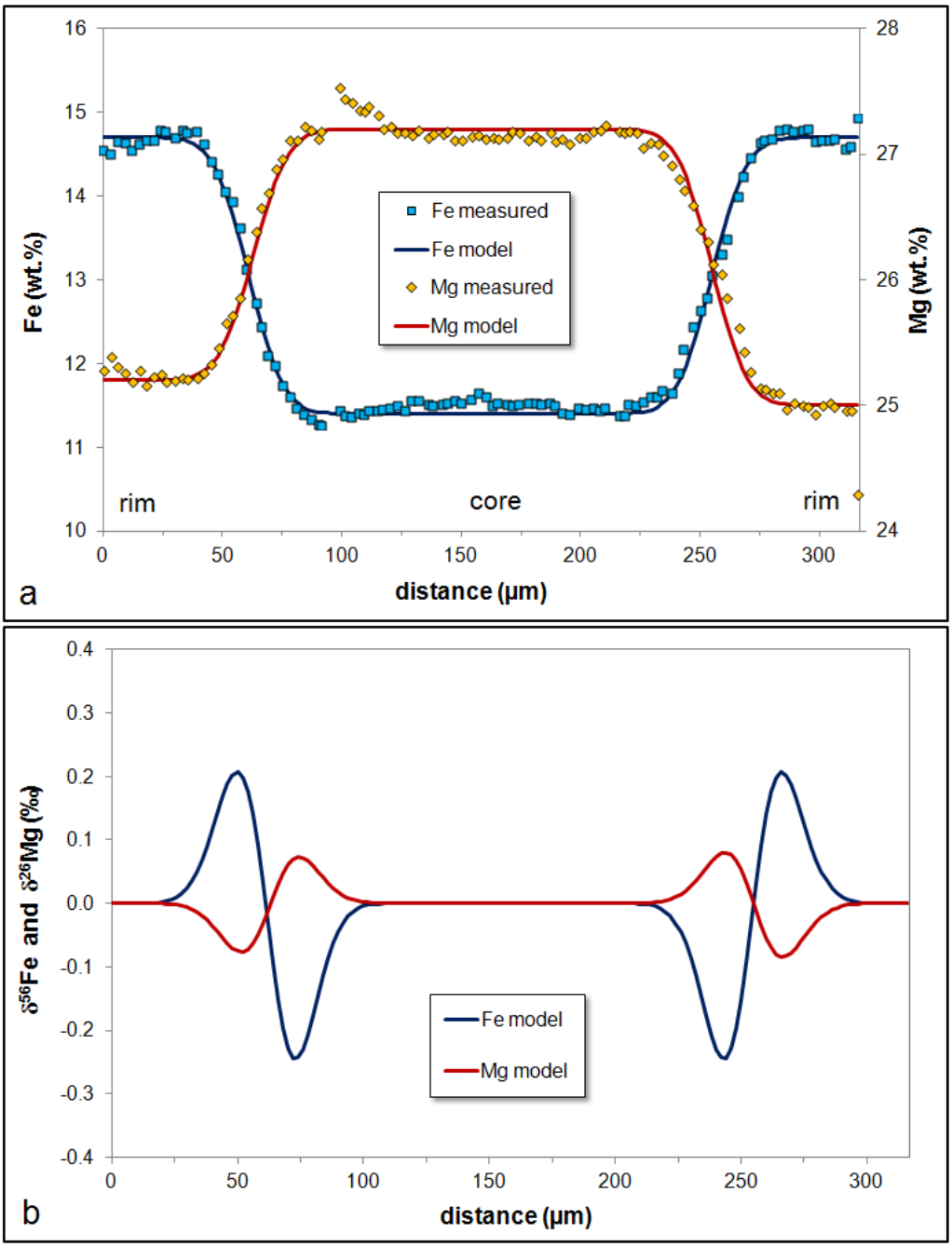

Figure II.11: (**a**) Fe- and Mg concentration profiles across an olivine phenocryst (EH_31-10-11_OL9) investigated by Longpré et al. (2014) and results of our diffusion modeling for this olivine. (**b**) inferred Fe-Mg isotopic profiles across this olivine deduced from modeling the diffusion-generated chemical zoning. Model parameters (as outlined in Longpré et al., 2014): T = 1150°C (constant); X_{Fe} = 0.2 (constant); fO_2 = 0.01 Pa; P = 600 MPa; diffusion along the crystallographic c-axis; β_{Fe} = 0.2; β_{Mg} = 0.1. In (b) the y-axis gives the deviation from equilibrium in δ^{56}Fe and δ^{26}Mg (analogous to Figures II.8-II.10). Fe- and Mg concentration data are from Table DR4 in Longpré et al. (2014).

As expected and similar to scenarios 1 and 3, the Fe-Mg isotopic profiles are inversely correlated (Fig. II.12). However, the intra-mineral isotopic zoning is even more complex than that observed for scenario 3), i.e., if Fe-Mg inter-diffusion occurred only *after* two growth episodes (Fig. II.11). Because of the moving boundary, the isotopic profiles of Fe and Mg are asymmetric, i.e., the isotope fractionation is always higher in the initial part of the olivine than in the newly formed rim (Fig. II.12). Consequently, this olivine would not be in isotopic equilibrium with the surrounding melt. For example, δ^{56}Fe and δ^{26}Mg values of a bulk olivine with an initial radius of 400 µm that was overgrown by a 65 µm thick rim (which would take 15 days in our model) would be shifted from equilibrium isotope compositions by -0.066‰ and 0.019‰, respectively.

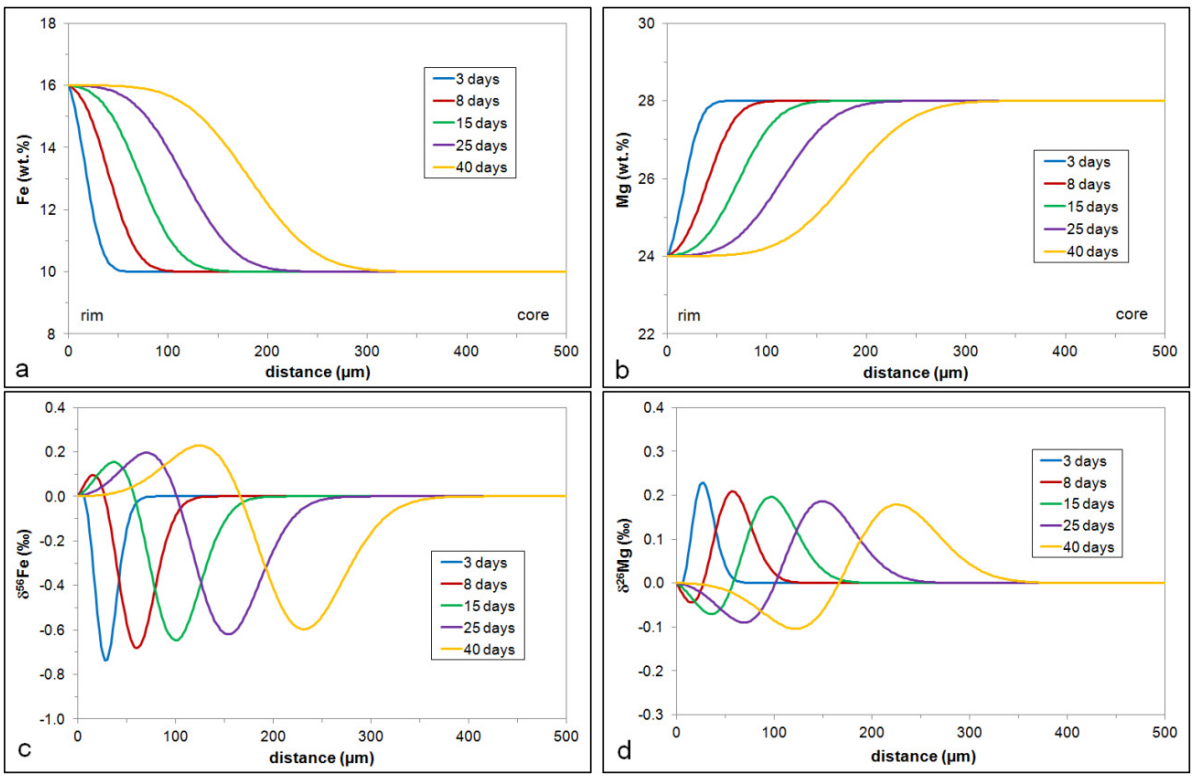

Figure II.12: Modeled Fe-Mg chemical (a and b) and isotopic (c and d) rim-to-core profiles for an olivine (radius = 400 µm) that is overgrown with a rim of different composition. The growth is associated with simultaneous Fe-Mg inter-diffusion. Model parameters: T = 1250°C; X_{Fe} = 0.18; fO_2 at NNO-2; P = 50 MPa; diffusion along the crystallographic c-axis; $D_{Fe\text{-}Mg} = 4.1 \cdot 10^{-16}$ m²/s; β_{Fe} = 0.2; β_{Mg} = 0.1. We assume that the overgrowing rim has the same Fe-Mg isotopic composition as the core. In (c) and (d) the y-axis gives the deviation from equilibrium in δ^{56}Fe and δ^{26}Mg (analogous to Figures II.8-II.11).

5) **Olivine dissolution and simultaneous Fe-Mg inter-diffusion:** similar to scenario 4), Fe-Mg inter-diffusion may also simultaneously occur during olivine dissolution. This case is most likely relevant if there is a strong chemical disequilibrium between olivine and its environment, e.g., if a mantle xenolith is entrained into a hot (>1200°C) basaltic or andesitic melt (Brearley and Scarfe, 1986; Donaldson, 1990). We use the same model (Eqn. II.2) as described in the previous section and work with a negative growth rate (*R* in m/s) in order to simulate crystal dissolution. The dissolution rate is assumed to be $6.0 \cdot 10^{-11}$ m/s, which is within the range of, but also at the lower boundary of experimentally determined dissolution rates for olivine in basaltic melts at temperatures around 1250°C (Brearley and Scarfe, 1986; Donaldson, 1985, 1990; Edwards and Russell, 1996). We assume an initially homogeneous olivine crystal (radius = 300 µm) with 7 wt.% Fe and 30 wt.% Mg; Fe and Mg concentrations at the olivine-melt interface are 16 wt.% and 24 wt.%, respectively. Further model parameters are given in the figure caption of Fig. II.13.

Using the above described model parameters, two key observations can be made: 1) After a few days the system reaches a steady state, i.e., the shapes of the chemical and isotopic profiles do not significantly change anymore although crystal dissolution and Fe-Mg inter-diffusion continue. Hence, after the system has reached this steady state, neither the chemical nor the isotopic profiles provide any time information. 2) Only the outermost ~30 µm of the crystal appear to be affected by Fe-Mg inter-diffusion, which is a consequence of the dissolution rate used in this model. Such short diffusion profiles can hardly be resolved by laser ablation analyses, given a spatial resolution of ~30 µm. If a much lower dissolution rate is assumed (i.e., $R \ll 6.0 \cdot 10^{-11}$ m/s), the lengths of the obtained chemical and isotopic diffusion profiles would approach those generated by pure diffusive Fe-Mg exchange between olivine and melt (scenario 1; Fig. II.6).

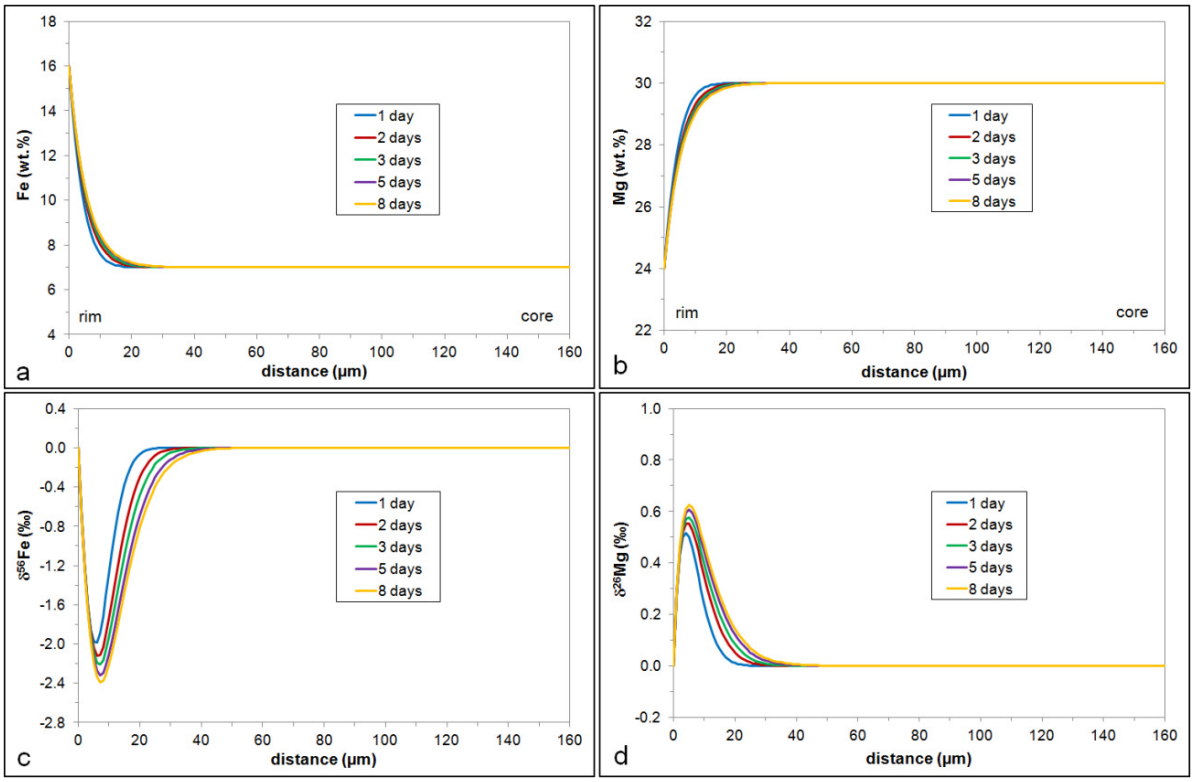

Figure II.13: Modeled Fe-Mg chemical (a and b) and isotopic (c and d) rim-to-core profiles for an olivine (initial radius = 300 µm) that is affected by dissolution associated with simultaneous Fe-Mg inter-diffusion. Model parameters: T = 1250°C; X_{Fe} = 0.15; fO_2 at NNO-2; P = 50 MPa; diffusion along the crystallographic c-axis; $D_{Fe\text{-}Mg} = 3.4 \cdot 10^{-16}$ m²/s; β_{Fe} = 0.2; β_{Mg} = 0.1. In (c) and (d) the y-axis gives the deviation from equilibrium in δ^{56}Fe and δ^{26}Mg (analogous to Figures II.8-II.12).

II.5.2 Origin of the chemical and isotopic zoning in "intra-plate" olivines

With this theoretical framework we aim to interpret the observed chemical and isotopic zoning in intra-plate olivines investigated in this study. As illustrated above, a negative correlation between δ^{26}Mg and δ^{56}Fe values strongly indicates that isotopic (and chemical) zoning in an olivine is mainly generated by Fe-Mg inter-diffusion driven either by a chemical gradient between crystal and melt (scenarios 1 and 5), or by an intra-mineral chemical gradient (scenarios 3 and 4). The majority of the olivines (both pheno- and xenocrysts) investigated in our study exhibit normal chemical zoning coupled with inversely correlated Fe-Mg isotopic profiles (Fig. II.4 and Fig. II.7), which strongly points to diffusion of Fe into and Mg out of these crystals. Sigmoidal shapes of Fe-Mg isotopic traverses coupled with intra-mineral growth zones as presented in Fig. II.11 and Fig. II.12 were not observed in our sample suite. As a consequence, there is no evidence of crystal growth episodes followed by or associated with simultaneous Fe-Mg inter-diffusion. Similarly,

because the fractionation of Fe isotopes is much higher than that of Mg isotopes in most of the investigated olivines, rapid (diffusion-limited) crystal growth (scenario 2) is unlikely to be the reason for the observed zoning in Mg#, δ^{26}Mg and δ^{56}Fe. Interestingly, olivine xenocrysts, which seem to be especially susceptible to dissolution if entrained into a hot basaltic melt, show long (>150 µm), pronounced Fe-Mg chemical and isotopic diffusion profiles. This indicates that xenocryst dissolution played only a minor role in modifying the chemical and isotopic zoning of olivines in our sample suite. According to these findings, simple diffusion of Fe into and Mg out of natural intra-plate olivines appears to be (i) the governing mechanism for generating chemically zoned olivines and (ii) a common process during the evolution of intra-plate magmas. The fact that – in most cases – the olivines' cores do not show any chemical or isotopic zoning indicates that they were apparently not affected by diffusion, though in theory, they may have become entirely re-equilibrated during a previous prolonged diffusion event. This is different to the observation by Sio et al. (2013) for a ca 2x4 mm large zoned olivine phenocryst from the Hawaiian Kilauea Iki lava lake, whose Fe-Mg isotopic profile indicates that diffusive Fe-Mg exchange already modified the chemical and isotopic composition of the core of this olivine. This implies that the olivine crystals of the intra-plate volcanic rocks investigated in our study experienced a shorter time span of diffusive re-equilibration than the Hawaiian olivine, investigated by Sio et al. (2013), assuming that these samples experienced similar peak temperatures (around 1250°C). In addition to such relative time constraints deduced from the different shapes of the coupled chemical and isotopic profiles in olivines, quantitative time information about magma evolution can be obtained by modeling both the chemical and isotopic zoning of such crystals, as discussed in section II.5.3.1.

Multiple chemical zoning coupled with complex isotopic zoning found in two olivines indicates that diffusion of Fe and Mg was the dominant process that modified the chemical and isotopic compositions of these olivines as well. Olivine 4b of sample TF-9 from Tenerife shows a negative correlation between δ^{26}Mg and δ^{56}Fe that is characteristic of Fe-Mg inter-diffusion (Fig. II.14a). Light Mg and heavy Fe isotopes appear to be relatively enriched in a zone near the rim where Mg may have diffused from the melt into the olivine (and Fe in the opposite direction) during a first diffusion episode. This process could be triggered if the olivine came into contact with a hotter, more primitive melt compared to the one it had grown in. Interestingly, the outermost rim of the crystal has a light Fe isotopic composition and a heavy Mg isotopic composition, indicating diffusion of Fe from the melt into this

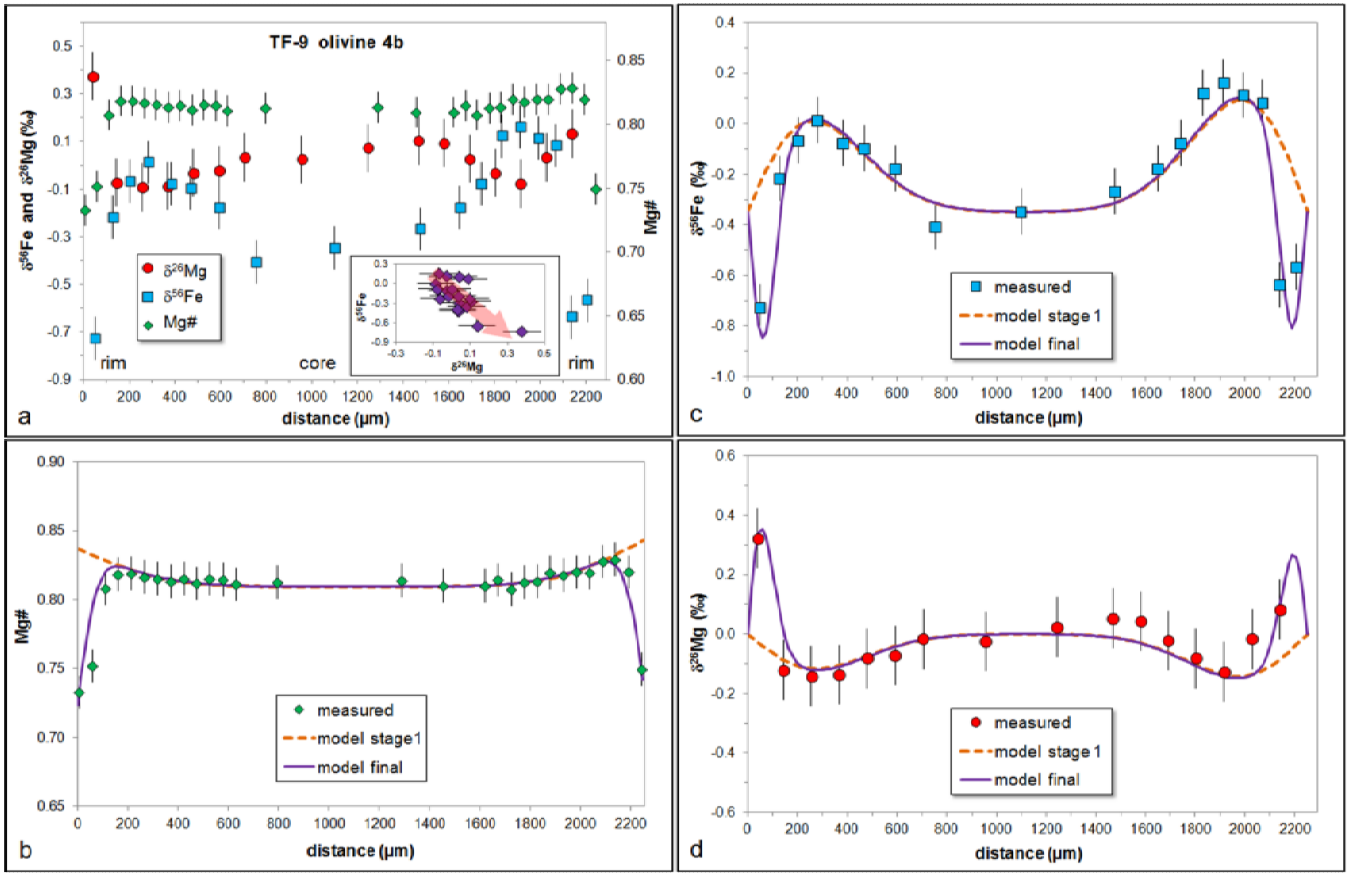

Figure II.14: (**a**) Fe-Mg chemical and isotopic profiles across a multiply zoned olivine phenocryst from Tenerife determined by fs-LA-MC-ICP-MS; inset in (a) shows the negative correlation of δ^{56}Fe- and δ^{26}Mg-values that is characteristic of Fe-Mg inter-diffusion. **(b)-(d)** Simplified modeling of Fe-Mg chemical (b) and isotopic (c and d) diffusion profiles for this olivine. The model includes two stages: during the first stage (lasting 10.4 years at 1250°C) Mg diffuses from the crystal's rim towards the core while Fe diffuses in the opposite direction (e.g. after magma mixing with a more primitive melt); the modeled chemical and isotopic profiles at the end of stage 1 are shown as a dashed line. In the second stage (lasting 1.15 years at 1200°C) Fe diffuses from the melt into the olivine while Mg diffuses out of the olivine (e.g. due to cooling and differentiation of the host magma, potentially after eruption). Other model parameters are as follows: X_{Fe} = 0.14 (constant); fO_2 at the NNO-buffer; P = 200 MPa (e.g. Neumann et al., 1999); we assumed fixed boundary concentrations for each stage; the dependency of the diffusion on the crystallographic orientation of the analyzed profiles, as determined by EBSD, was considered; during first stage: β_{Fe} = 0.30, β_{Mg} = 0.12; during second stage: β_{Fe} = 0.16, β_{Mg} = 0.09. In (a) and (d) the Mg isotopic composition of the core is set at 0‰, because the Mg isotopic profile was obtained by running a line scan from one rim to the core to the opposing rim.

domain (and diffusion of Mg in the opposite direction) during a second, shorter diffusion episode. This may be explained by a chemical gradient that was generated due to cooling and differentiation of the host magma, potentially after eruption. Hence, we have tried to reproduce the chemical and isotopic zoning of this olivine using a two-stage model (see section II.5.3.1).

The other multiply zoned olivine (LaTu-1 ol3; in a basanite from the Massif Central) at first sight exhibits positively correlated δ^{26}Mg and δ^{56}Fe values, although barely resolvable outside analytical uncertainties. Only the outermost δ^{26}Mg-δ^{56}Fe pair clearly deviates from this apparent trend (Fig. II.5a). This δ^{26}Mg-δ^{56}Fe pair was measured near the olivine's rim (distance <60µm), i.e., in a domain that appears to be normally zoned (Fig. II.5a). This observation may indicate that the crystal rim was affected by diffusion of Fe into and Mg out of the olivine ("normal" Fe-Mg inter-diffusion) for a short time interval, e.g., during cooling of the magma after eruption. The weak positive correlation of δ^{26}Mg and δ^{56}Fe values may point to Fe-Mg diffusion driven by a thermal gradient (Soret diffusion; e.g., Richter et al., 2009a; Huang et al., 2010) which is, however, an unlikely process on a mineral scale. Potentially, this olivine grain was part of a more massive cool crystal mush and became remixed into the magma prior to eruption.

Apart from the positive correlation of Mg and Fe isotopes possibly recorded in LaTu-1 olivine 3, the core of this olivine shows relatively heavy Fe and light Mg isotopic compositions (Fig. II.5a). The δ^{56}Fe value of the core is even 0.14‰ higher than that of the surrounding basaltic matrix (Table II.1), opposite in direction to what would be expected for equilibrium Fe isotope fractionation between olivine and melt (Weyer and Ionov, 2007; Dauphas et al., 2009; Schuessler et al., 2009). Potentially, the relatively heavy Fe and light Mg isotope compositions of this olivine's core were affected by Mg diffusion into and Fe diffusion out of the olivine, potentially after a magma mixing event with a hotter, more primitive melt (cf. the scenario described above for TF-9 olivine 4b). This would also be consistent with the decrease in Mg# from the domain near the rim (at distance 65 µm: Mg# = 0.84) towards the core (Mg# = 0.80). These findings show that multiply zoned olivines may record various episodes of Fe-Mg inter-diffusion (e.g., after magma mixing events) which may be elucidated by the combined study of chemical and isotopic profiles.

A few olivines exhibit normal chemical zoning, but a complex isotopic zoning with non-correlated δ^{26}Mg and δ^{56}Fe values (Fig. II.5b). These findings indicate a more complex history of crystal growth and diffusive processes and imply that for these samples the

chemical zoning is not generated by Fe-Mg inter-diffusion alone. Intra-mineral isotopic zoning that is decoupled from any chemical zoning (e.g., in a domain where the Mg# profile is flat) may be inherited from processes that occurred much earlier than the final process modifying the chemical and isotopic compositions of the olivine's rim. Interestingly, our findings suggest that isotopic profiles may still record such early (diffusion-controlled) events while chemical gradients have already been homogenized. Such contrasting behavior between chemical and isotopic fractionation has also recently been observed for the diffusion of Li into clinopyroxene (Richter et al., 2014); the findings of this experimental study indicate that diffusion-generated Li isotopic fractionation homogenized more slowly than the Li concentration in clinopyroxenes. Alternatively, in our study cutting effects associated with the sample preparation may result in distorted isotopic profiles. In this case, Fe-Mg inter-diffusion in the direction perpendicular to the plane of the thin section could strongly affect the isotopic (and chemical) composition of the apparent core of the olivine (e.g., Costa and Chakraborty, 2004). In any case, chemical zoning of olivines with uncorrelated Fe-Mg isotopic profiles should not be used for modeling the time scales of diffusive re-equilibration since the chemical zoning cannot be the result of simple Fe-Mg inter-diffusion or may be disturbed by diffusion in the third dimension.

II.5.3 Diffusion modeling

II.5.3.1 Estimation of time scales

If the chemical zoning in olivine crystals is mainly generated by Fe-Mg inter-diffusion, as proven by e.g., inverse Fe-Mg isotopic zoning, both the chemical and isotopic profiles can be used to estimate the time scales of diffusive re-equilibration of these crystals (e.g., Costa et al., 2008; Teng et al., 2011; Sio et al., 2013). With our simplified diffusion modeling at isothermal conditions both the chemical and the isotopic profiles of the investigated intra-plate olivines can be fitted well (Fig. II.6 and Fig. II.7b). The time scales obtained with our diffusion modeling range from a few months to ~11 years (Table II.4), which is similar to the short time scales determined by diffusion modeling of chemical gradients in olivines hosted in basaltic lava flows from the Chilean Andes and Mt. Etna (Costa and Dungan, 2005; Kahl et al., 2011).

In particular, the longest time span is recorded by a large, multiply zoned (chemically and isotopically) olivine phenocryst from Tenerife (Fig. II.14). Such complexly zoned phenocrysts have frequently been interpreted to be the result of magma mixing processes beneath the Canary Islands (e.g., Neumann et al., 1999; Stroncik et al., 2008; Longpré et al.,

2014). The Fe- and Mg isotopic profiles obtained in our study provide further evidence for the diffusive re-equilibration of phenocrysts after such mixing events (see section II.5.2). We applied a two-stage model in order to reproduce the chemical and isotopic zoning of TF-9 olivine 4b. Due to a chemical gradient between crystal and host melt (after a mixing event) Mg diffuses from a Mg-rich melt into the olivine, while Fe diffuses out of the olivine crystal. According to our model, this diffusion lasted for 10.4 years at 1250°C. During the second stage (lasting 1.15 years at 1200°C) Fe diffuses from the melt into the olivine while Mg diffuses out of the olivine (e.g., due to cooling and differentiation of the host magma, in a magma chamber or after eruption). Hence, the results of our diffusion modeling combined with the findings of Longpré et al. (2014), indicate that the time span between a mixing event and eruption is highly variable, i.e., between a few weeks (Longpré et al., 2014) and a couple of years (this study).

Our modeling results for three olivine xenocrysts in Massif Central basanites point to diffusion times of <2 years assuming diffusion at around 1250°C. This period may represent the time span between the entrainment of the xenocrysts (mantle xenolith) in the basanitic host magma and the quenching of the system at a temperature where the diffusive flux effectively froze. According to our model, this implies that the entrainment of mantle xenoliths in an intra-plate basanitic magma and the following eruption may occur within a few years or less. Werling and Altherr (1997) investigated mantle xenoliths in a variety of volcanic rocks from the Massif Central as well and found similar or somewhat longer time scales of partial re-equilibration of mantle xenoliths (a few days to 11 years) based on Ca zoning patterns of olivines. This is also largely consistent with the findings of other studies which estimated the residence time of mantle xenoliths in intra-plate basaltic magmas, based on Fe-Mg diffusion modeling in olivine, to be on the order of a few years (Shaw, 2004; Shaw et al., 2006). Note that time scales estimated with our model probably represent minimum time scales for the following reasons: 1) We assume a fixed "characteristic" temperature of 1250°C, corresponding to $T_{ch} = 0.97 \cdot T_{peak}$ and $T_{peak} = 1570$ K = 1297°C (Ganguly, 2002). However, $T_{ch} = 0.95 \cdot T_{peak}$ may also be an adequate approximation (Costa et al., 2008). In this case, T_{ch} would be 1219°C. Because diffusion rates strongly depend on temperature, assuming a high temperature for the diffusion model results in short durations of diffusive flux in order to reproduce a given chemical gradient. The effect of temperature on the calculated time scales for sample St3-3a-ol1 is illustrated in Fig. II.15a. 2) Assuming fixed concentrations at the contact of the olivine with the melt also results in shorter time

scales than those calculated if concentrations at the crystal rim changed with time, as outlined by Costa et al. (2008). In particular, if at the beginning of the model the chemical gradient between melt and olivine is small, the diffusive flux of Fe into and Mg out of the olivine will be minor. If the magma then cools and differentiates (i.e., Fe/Mg in the melt increases), the chemical disequilibrium between olivine and melt will continuously increase and, hence, expedite Fe-Mg inter-diffusion. Such a model would result in longer diffusion times compared to a model where a strong chemical gradient between olivine and melt is already assumed at the start of the simulation.

Further uncertainties of the modeled time scales arise from possible errors in estimating pressure and oxygen fugacity (Fig. II.15c and d) and from the assumption of a fixed fayalite component (X_{Fe}; Fig. II.15b); however, uncertainties associated with these parameters are relatively small (maximum a factor of 2) compared to those arising from incorrect temperature estimations. Given these uncertainties the time spans of diffusive re-equilibration estimated for our Massif Central mantle xenoliths may certainly overlap with the somewhat longer time scales determined by Werling and Altherr (1997), Shaw (2004) and Shaw et al. (2006) for their respective sample suites.

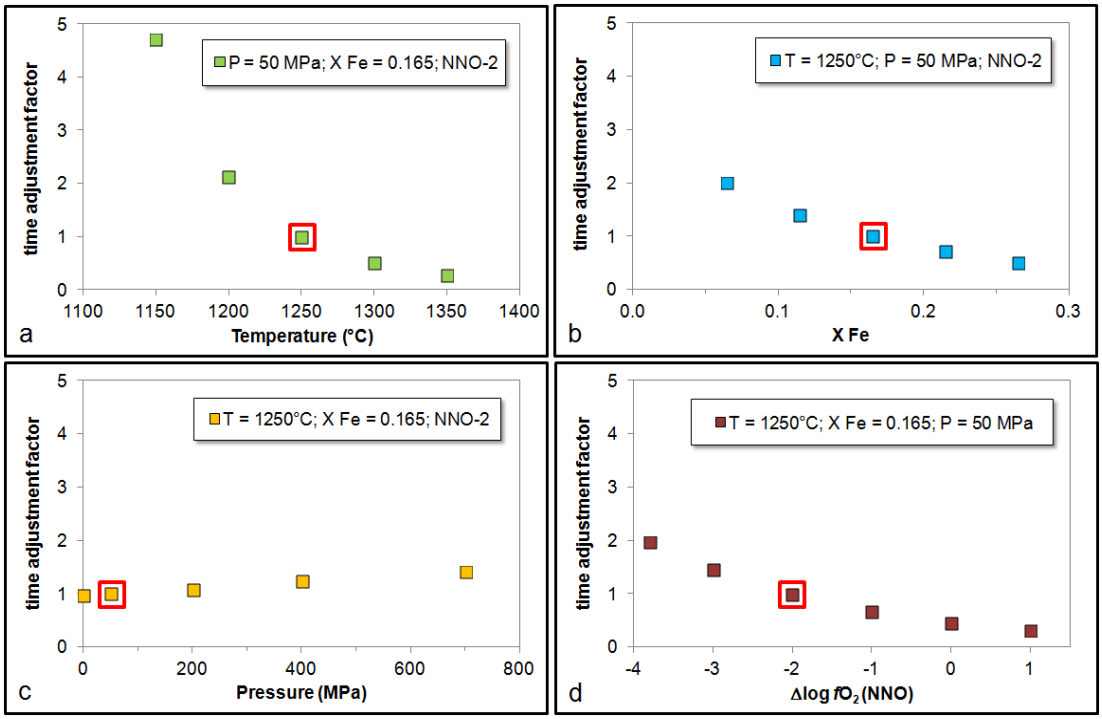

Figure II.15: Dependence of the calculated time scales obtained with our diffusion modeling on (**a**) temperature, (**b**) chemical composition, (**c**) pressure, (**d**) oxygen fugacity. The y-axes show the factor by which the modeled time scales have to be corrected, if the various parameters are different from what was assumed for the diffusion model (marked by red squares).

Cooling rates for basanites from the Roche Sauterre (Massif Central) were estimated by modeling the chemical and isotopic gradients in normally zoned olivine pheno- and xenocrysts (see section II.3.3). As with diffusion modeling at isothermal conditions (see above), both the chemical and the isotopic profiles can be fitted quite well (Fig. II.16). The obtained cooling rates for samples from the Roche Sauterre range from 50°C/year to >1000°C/year at T_{peak} (1297°C) (Table II.4). Note that, analogous to the minimum time scales provided by our diffusion modeling, these estimated cooling rates represent maximum cooling rates. If we assume a lower peak temperature (1250°C), the range of calculated cooling rates changes to 28-504°C/year (Table II.4). Interestingly, samples that were taken near the center of the outcrop show lower cooling rates than the ones taken near the rim or at the top of the outcrop. This may indicate that the Roche Sauterre outcrop represents a large lava body that cooled faster at its margins (due to contact with country rock) and slower near its center. These findings together with the relatively high cooling rates may indicate that the chemical disequilibrium between olivines and melt developed during subaerial cooling of the lava flow after eruption.

II.5.3.2 Estimation of β-values

Because the observed fractionation of Fe and Mg isotopes is particularly pronounced in the Massif Central olivines, they may be used to obtain constraints for the empirical parameter β (see section II.3.3). This parameter was determined experimentally for diffusion of Fe and Mg in silicate melts to be β_{Fe} =0.03 and β_{Mg}=0.05 (Richter et al., 2008, 2009b)., however, it is unknown for diffusion in olivine. In a recent study, Sio et al. (2013) observed diffusion-generated Fe-Mg chemical and isotopic zoning in an olivine phenocryst from the Hawaiian Kilauea Iki lava lake and fitted the isotopic profiles using β_{Fe} = 0.27±0.04 and β_{Mg} = 0.16±0.05. In agreement with these findings, our modeling results reveal that β_{Fe} appears to be consistently larger than β_{Mg} in olivine (i.e., mean of β_{Fe}: 0.161; mean of β_{Mg}: 0.084; Table II.4, Fig. II.17). If we calculate the ratio of diffusion coefficients for two isotopes of interest (i.e., D_{54Fe}/D_{56Fe} and D_{24Mg}/D_{26Mg}; see Eqn. II.3) using our estimated values for β_{Fe} and β_{Mg}, we find that D_{54Fe}/D_{56Fe} and D_{24Mg}/D_{26Mg} are nearly identical (i.e., they differ by less than 0.2%) for all investigated olivines. This is an intriguing finding given the larger relative mass difference of ^{24}Mg and ^{26}Mg compared to that of ^{56}Fe and ^{54}Fe (by a factor of ≈ 2). Furthermore, the investigations of diffusion-driven isotope fractionation in silicate melts (Richter et al., 2003, 2008, 2009b) rather indicates an increase of the diffusivity ratio of two

isotopes with increasing relative mass differences of these isotopes. Potentially, the similar diffusivity ratio of Fe isotopes and Mg isotopes in olivine is a result of the coupled diffusion process. Alternatively, the relatively high fractionation of Fe isotopes compared to Mg isotopes during diffusion in olivine may be related to the higher tracer diffusion of Fe relative to that of Mg (Chakraborty, 2010).

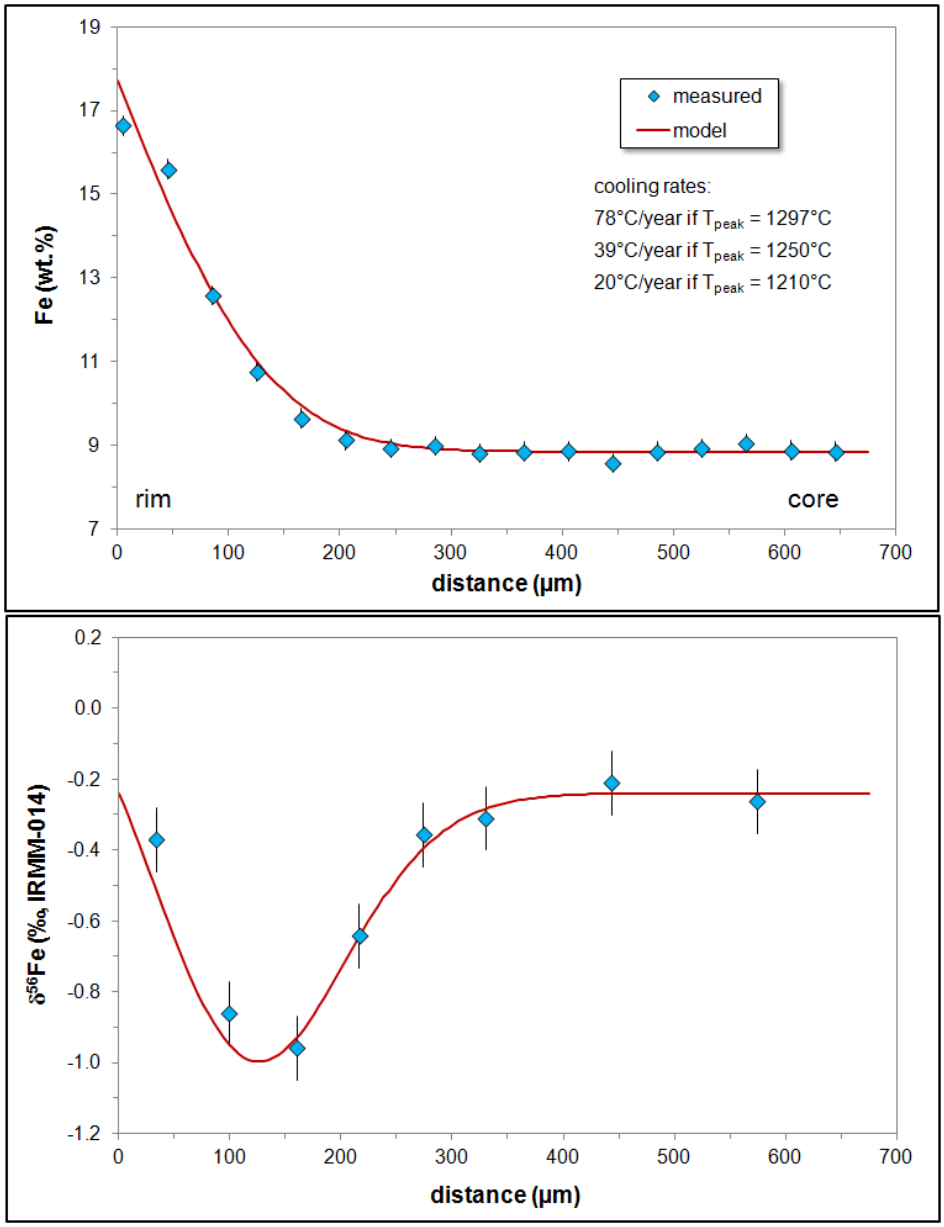

Figure II.16: Simplified modeling of chemical and isotopic diffusion profiles of Fe for a Massif Central olivine (St4-1a olivine 2), based on the method described by Ganguly (2002) which yields cooling rates for the investigated sample.

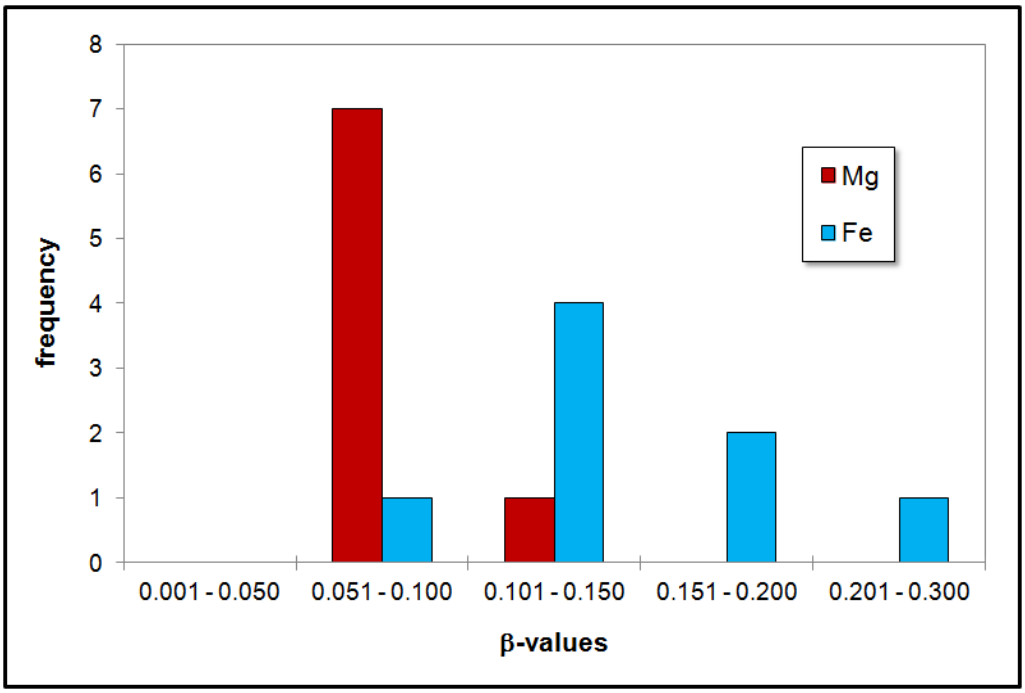

Figure II.17: Histogram of estimated β-values for Fe and Mg based on the modeling of diffusion-generated isotopic zoning in olivines from the Massif Central volcanic region and Tenerife. See also Fig. A-III.1 in Appendix III for a histogram of all β-values for Fe and Mg obtained in this doctoral research study.

We note that the absolute values for β_{Fe} and β_{Mg} determined in this study differ from those found by Sio et al. (2013). As pointed out by these authors, β-values depend on the boundary conditions used in the modeling. Hence, the discrepancy between the findings of Sio et al. (2013) and our results may simply arise from the fact that Sio et al. (2013) used changing boundary conditions in their model, while we worked with fixed boundary conditions. In addition, related to the coupling of the atomic jumps, the value of β, as an empirical constant, can also be a function of the olivine composition (i.e., the fayalite content). As mentioned in section II.3.3.2, we have also tried to fit the observed chemical and isotopic profiles using a model with changing Fe and Mg concentrations at the olivine-melt contact. In such a simulation, considerably higher β-values are indeed required to obtain a reasonably good fit for the Fe-Mg isotopic profiles (which is, however, still worse than the fit obtained by using a model with fixed Fe and Mg concentrations; Fig. A-II.3 in Appendix II). In any case, we can confirm the observations made by Sio et al. (2013) that β_{Fe} in olivine is higher than that

determined for basalt-rhyolite melt couples (Richter et al., 2009b) and that β-values, in general, appear to be higher for crystalline materials than for liquids. It has to be noted that β-values only represent a fitting parameter for the extent of isotope fractionation, while time scales or cooling rates are essentially expressed by the length of chemical and isotopic zoning. Fig. II.18 illustrates how a change of the β-values modifies the modeled isotopic profiles if all other parameters of the diffusion model (i.e., T, P, fO_2, t, boundary conditions) remain fixed.

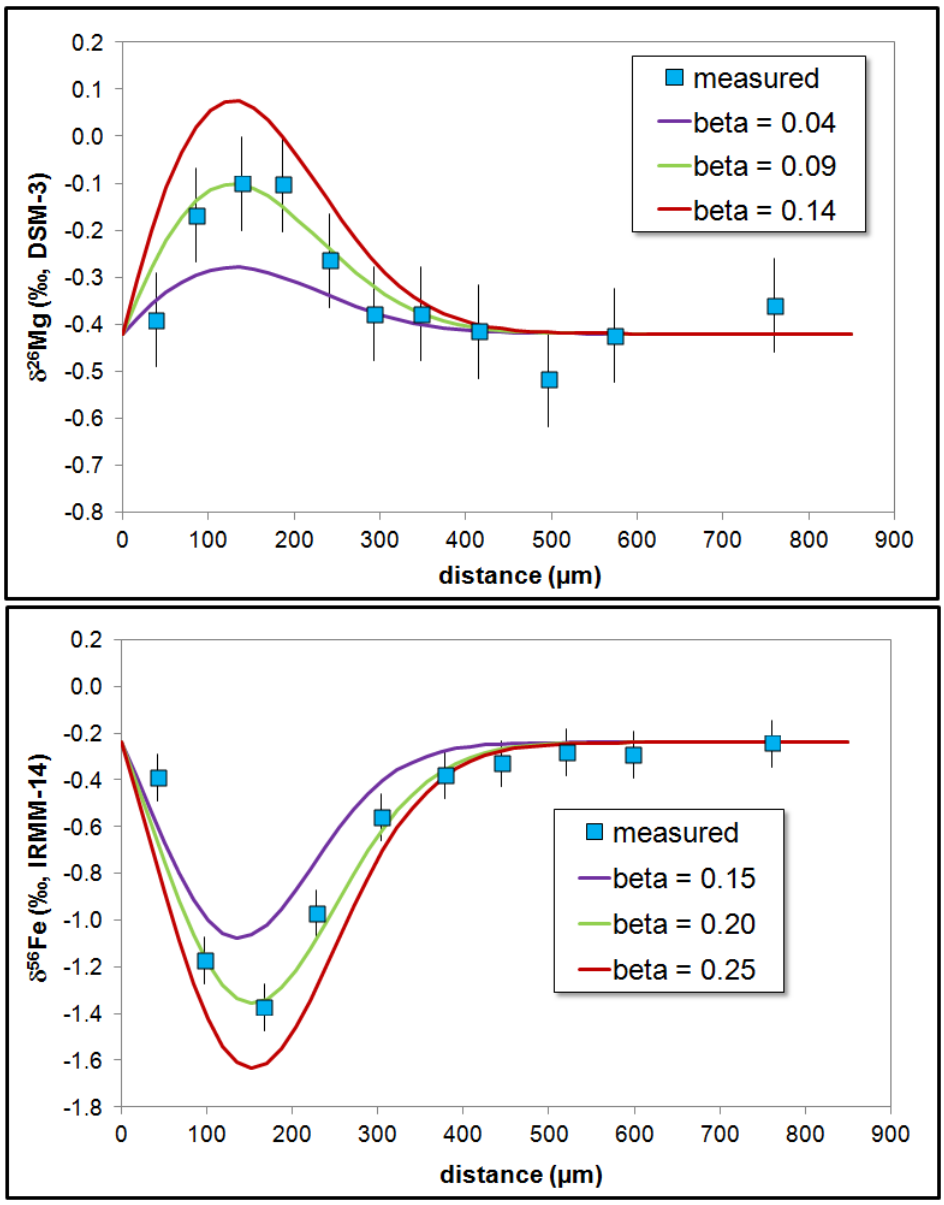

Figure II.18: Effect of using different β-values in the modeling of Fe- and Mg isotope fractionation in olivine phenocryst St3-3a olivine 1 (Fig. II.6).

II.6 Conclusions

The results of this study show that Fe and Mg isotopic zoning, related to Fe-Mg inter-diffusion (i.e., with chemical zoning coupled with inversely correlated Fe-Mg isotopic profiles), is common in olivine crystals of intra-plate volcanic rocks. *In situ* analyses of Fe and Mg isotope ratios in natural olivines provide a powerful tool to trace diffusive processes that occur on the mineral scale during magma evolution (Sio et al., 2013). As shown by theoretical modeling, chemical and isotopic zoning in olivine may also be the result of combined Fe-Mg inter-diffusion, crystal growth and dissolution. However, most of the observed isotopic zoning patterns of the investigated olivine crystals (pheno- and xenocrysts) can be well explained with simple Fe-Mg inter-diffusion.

Simplified modeling of the observed Fe-Mg chemical *and* isotopic diffusion profiles yields short residence times (mostly <3 years) for olivine phenocrysts and mantle xenoliths in intra-plate basanitic host magmas. Notably, the high cooling rates obtained by our diffusion modeling for samples from a large lava flow indicate that Fe-Mg diffusion profiles in olivine may simply be the result of cooling after eruption. Uncertainties of the modeled time scales and cooling rates are mainly based on the uncertainty of the magmatic temperature (and to a second order on oxygen fugacity).

Some of the investigated olivine crystals displayed multiple isotopic zoning, indicating a complex diffusion history (e.g., during magma mixing and other processes in the magma chamber) that was only indistinctly recorded by the chemical zoning.

Finally, our modeling suggests a systematic difference in the β-values for Fe and Mg isotopes, i.e., for our sample suite $\beta_{Fe}/\beta_{Mg} = 2.05 \pm 0.45$ (1 SD, n = 7). As a consequence, we observe surprisingly similar diffusivity ratios for Fe- and Mg isotopes (i.e., $D_{54Fe}/D_{56Fe} \approx D_{24Mg}/D_{26Mg}$), despite the contrast in relative mass difference between the isotopes.

II. Tables

Table II.1: Major and trace element concentrations and iron isotopic compositions of Massif Central samples

sample	StR	St1	St2b	St3	St4	St6	St7	StTop	BdOr	LaTu
location	Roche Sauterre	Roche Sauterre	Roche Sauterre	Roche Sauterre	Roche Sauterre	Roche Sauterre	Roche Sauterre	Roche Sauterre	Banne d'Ordanche	road outcrop
Latitude (°N)	45° 54.815'	45° 54.816'	45° 54.804'	45° 54.805'	45° 54.798'	45° 54.803'	45° 54.815'	45° 54.817'	45° 36.671'	45° 26.562'
Longitude (°E)	02° 55.722'	02° 55.689'	02° 55.675'	02° 55.669'	02° 55.659'	02° 55.622'	02° 55.612'	02° 55.650'	02° 46.355'	02° 55.281'
WR δ^{56}Fe (‰, IRMM-014)	0.15 ± 0.06	0.15 ± 0.06	0.14 ± 0.03	0.14 ± 0.03	0.14 ± 0.03	0.14 ± 0.03	0.14 ± 0.03	0.14 ± 0.03	0.13 ± 0.04	0.17 ± 0.03
matrix δ^{56}Fe (‰, IRMM-014)	0.13 ± 0.06	0.15 ± 0.04	0.14 ± 0.03	0.17 ± 0.03	0.14 ± 0.03	0.17 ± 0.04	0.13 ± 0.03	0.13 ± 0.05	0.14 ± 0.03	0.18 ± 0.03
SiO_2	42.3	42.3	42.5	42.6	42.6	42.2	42.9	42.6	42.7	43.5
TiO_2	3.20	3.26	3.18	3.14	3.20	3.21	3.54	3.26	3.34	2.96
Al_2O_3	12.2	12.0	12.2	12.1	12.3	12.0	13.8	12.3	14.3	13.6
Fe_2O_3	12.6	12.7	12.7	12.5	12.7	12.6	12.7	12.8	13.7	12.1
CaO	10.6	10.7	10.5	10.5	10.6	10.4	11.4	10.8	11.6	10.4
MgO	12.7	13.0	12.7	12.8	12.6	13.0	9.0	12.4	8.1	11.0
MnO	0.18	0.18	0.18	0.18	0.19	0.19	0.18	0.18	0.18	0.16
K_2O	1.78	1.69	1.87	1.86	1.66	1.92	1.83	1.40	1.45	1.56
Na_2O	2.98	2.88	2.87	2.93	2.94	2.96	3.26	2.92	3.20	3.23
P_2O_5	0.65	0.65	0.65	0.64	0.66	0.66	0.67	0.68	0.62	0.61
L.O.I.	0.34	0.19	0.12	0.29	0.03	0.36	0.30	0.19	0.27	0.40
Li	5.9	5.6	5.8	5.7	5.5	5.8	7.4	4.4	6.1	7.7
Be	1.67	1.66	1.70	1.67	1.74	1.65	1.96	1.74	1.59	1.61
Sc	27.9	27.9	28.1	27.2	27.3	27.1	32.8	28.0	30.0	28.8
V	326	330	345	320	329	321	393	331	388	318
Cr	579	582	619	605	587	672	355	556	243	439
Mn	1431	1505	1618	1468	1508	1471	1555	1440	1526	1347
Co	60	63	62	62	62	60	54	59	53	57
Ni	384	412	416	409	422	391	152	358	102	228
Cu	72	69	69	64	54	62	74	61	68	62
Zn	92	100	117	94	104	96	107	115	113	99
Sr	716	722	720	709	758	718	803	738	787	772
Y	22.6	22.4	23.1	22.7	23.3	22.2	25.7	22.8	25.8	23.1
Zr	280	278	288	281	288	282	311	287	247	247
Nb	73	73	76	75	76	74	80	76	65	64
Ba	463	470	474	453	487	472	519	477	491	491
La	51	50	52	52	53	52	54	53	45	47
Ce	100	99	102	101	104	100	108	102	90.2	90
Pr	11.6	11.5	11.8	11.6	11.9	11.6	12.5	11.7	10.7	10.3
Nd	45	45	46	45	46	45	48	46	43	40
Sm	8.3	8.4	8.5	8.4	8.7	8.3	9.2	8.5	8.6	7.9
Eu	2.56	2.55	2.60	2.54	2.61	2.50	2.83	2.61	2.62	2.50
Gd	7.0	7.1	7.5	7.3	7.4	7.1	8.1	7.2	7.4	6.9
Tb	1.07	1.08	1.10	1.08	1.12	1.07	1.17	1.08	1.15	1.06
Dy	5.1	5.2	5.2	5.2	5.3	5.1	5.7	5.2	5.7	5.2
Ho	0.92	0.91	0.93	0.92	0.94	0.90	1.01	0.92	1.02	0.93
Er	2.42	2.44	2.49	2.41	2.50	2.37	2.70	2.44	2.70	2.45
Tm	0.32	0.30	0.30	0.30	0.31	0.29	0.33	0.30	0.33	0.30
Yb	1.87	1.86	1.89	1.86	1.93	1.83	2.07	1.87	2.07	1.86
Lu	0.28	0.27	0.27	0.27	0.28	0.26	0.29	0.27	0.28	0.26
Hf	6.2	6.2	6.3	6.2	6.4	6.2	6.7	6.3	5.4	5.4
Th	5.8	5.6	5.8	5.8	5.9	5.9	6.1	6.0	4.9	5.5
Total	99.84	99.84	99.85	99.84	99.85	99.85	99.82	99.84	99.79	99.81

Oxides and L.O.I. in wt.%, others in ppm. Oxides+L.O.I. normalized to 99.5 wt.%.

Table II.2: Instrumental details of the EBSD system at the Ruhr-Universität Bochum

SEM	Zeiss LEO 1530 Gemini Field Emission SEM
Acceleration voltage (kV)	20
EBSD detector	Nordlys
Tilt angle	70°
Working distance (mm)	25
Acquisition program	Oxford Channel 5

Table II.3: Electron microprobe data and Mg- and Fe isotope data determined by femtosecond-LA-MC-ICP-MS for the profile across a Massif Central olivine phenocryst (St3-3a ol1; Fig. II.4)

EMP			fs-LA-MC-ICP-MS					
distance (µm)	Ni (wt.%)	Mg#	distance (µm)	δ^{26}Mg (‰, DSM-3)	2 SD	distance (µm)	δ^{56}Fe (‰, IRMM-014)	2 SD
5	0.132	0.789	38	-0.39	0.10	42	-0.39	0.09
55	0.174	0.807	85	-0.17	0.10	97	-1.17	0.09
104	0.265	0.834	138	-0.10	0.10	167	-1.37	0.09
154	0.268	0.857	186	-0.10	0.10	228	-0.97	0.09
203	0.281	0.870	241	-0.26	0.10	304	-0.56	0.09
253	0.316	0.878	292	-0.38	0.10	378	-0.38	0.09
303	0.297	0.881	347	-0.38	0.10	444	-0.33	0.09
352	0.272	0.880	414	-0.41	0.10	520	-0.28	0.09
402	0.273	0.880	496	-0.52	0.10	598	-0.29	0.09
451	0.267	0.882	573	-0.42	0.10	760	-0.24	0.09
501	0.305	0.881	760	-0.36	0.10	971	-0.27	0.09
551	0.294	0.885	946	-0.49	0.10	1068	-0.46	0.09
600	0.273	0.885	990	-0.32	0.10	1144	-0.59	0.09
650	0.273	0.883	1071	-0.45	0.10	1200	-0.76	0.09
699	0.299	0.882	1130	-0.28	0.10	1263	-0.89	0.09
749	0.266	0.885	1191	-0.39	0.10	1342	-1.15	0.09
799	0.310	0.877	1251	-0.02	0.10	1427	-1.25	0.09
848	0.261	0.883	1310	-0.07	0.10	1492	-1.19	0.09
898	0.262	0.880	1363	0.06	0.10	1564	-1.06	0.09
947	0.264	0.882	1421	0.03	0.10	1622	-0.92	0.09
997	0.268	0.882	1471	0.21	0.10			
1047	0.299	0.880	1524	0.00	0.10			
1146	0.310	0.880	1579	-0.01	0.10			
1195	0.282	0.880						
1245	0.300	0.875						
1295	0.291	0.873						
1344	0.245	0.867						
1394	0.257	0.861						
1443	0.299	0.853						
1493	0.257	0.842						
1543	0.238	0.832						
1592	0.215	0.822						
1642	0.188	0.807						
1691	0.104	0.772						

Table II.4: Estimation of time scales of diffusive re-equilibration, cooling rates and β-values based on diffusion modeling for intra-plate olivines with clearly coupled Fe-Mg chemical and isotopic profiles

volcanic region	location	sample	olivine type	time scale	cooling rates (°C/yr) if T_{peak} = 1297°C	if T_{peak} = 1250°C	if T_{peak} = 1210°C	β_{Fe}	β_{Mg}	D_{54Fe}/D_{56Fe}	D_{24Mg}/D_{26Mg}
Massif Central	Banne d'Ordanche	BdOr-1 ol2	xenocryst	239 days	341	168	88	0.200	0.075	1.0073	1.0060
Massif Central	Banne d'Ordanche	BdOr-1 ol-xen2	xenocryst	252 days	261	129	68	-	0.090	-	1.0072
Massif Central	Roche Sauterre	St3-3a ol-xen1	xenocryst	1.61 years	118	58	31	0.120	0.075	1.0044	1.0060
Massif Central	Roche Sauterre	St3-3a ol1	phenocryst	3.26 years	57	28	15	0.200	0.090	1.0073	1.0072
Massif Central	Roche Sauterre	St4-1a ol2	phenocryst	2.40 years	78	39	20	0.115	0.055	1.0042	1.0044
Massif Central	Roche Sauterre	StR-1 ol2	phenocryst	98 days	669	330	174	0.120	0.080	1.0044	1.0064
Massif Central	Roche Sauterre	StTop-2 ol4-2	phenocryst	70 days	1023	504	265	0.075	-	1.0027	-
Canary Islands	Tenerife	TF-9 ol4b	phenocryst	~11.5 years [a]	-	-	-	0.30 , 0.16 [b]	0.12 , 0.09 [b]	1.0110 , 1.0058 [b]	1.0096 , 1.0072 [b]

[a] includes two stages: stage 1 lasts 10.4 years, stage 2 lasts 1.15 years

[b] first value refers to stage 1, second value refers to stage 2

Chapter III: Fe-Mg chemical and isotopic zoning in olivines from mid-ocean ridge basalts

III.Abstract

High-precision *in situ* Fe and Mg isotope analyses by fs-LA-MC-ICP-MS have been applied on chemically zoned olivine crystals from mid-ocean ridge basalts (MORBs). The aim was to search for diffusion-driven isotopic zoning, in order to obtain information on processes and time scales of magma evolution beneath mid-ocean ridges. In most cases, the observed Fe-Mg isotope fractionation in MORB olivines is relatively small (0.10-0.25‰ in δ^{56}Fe and δ^{26}Mg), which is in accordance with the limited intra-mineral chemical gradients (max. 0.045 in Mg#). Two multiply zoned olivines from the slow-spreading Mid-Atlantic Ridge and the intermediate-spreading Costa Rica Rift show more pronounced zoning in δ^{56}Fe and δ^{26}Mg (up to 0.7‰ and 0.3‰, respectively). The chemical and isotopic zoning of these olivines points to two diffusion episodes, which can be reliably reconstructed by modeling the chemical gradients and, in particular, the isotopic profiles. Such modeling provides information about the time scales of diffusive re-equilibration after magma mixing events beneath mid-ocean ridges. While normally zoned olivines record relatively short time spans of diffusive re-equilibration (in most cases <1.5 years), residence times of multiply zoned olivines in a magma chamber after a magma mixing event may be considerably longer (up to ~8 years). Based on the data obtained in this study and in previous studies on chemically zoned MORB olivines, a clear dependence of the magma residence times of olivines on the spreading rate of the ridge cannot be detected.

III.1 Introduction

As shown in the previous chapters, a combined investigation of Fe-Mg chemical *and* isotopic zoning in olivine provides reliable information on magma evolution, and modeling of this zoning yields constraints on the time scales of magma differentiation processes. Previous studies have used the chemical zoning of olivines in mid-ocean ridge basalts (MORBs) to estimate the magma residence time of these crystals (Nabeleck and Langmuir,

1986; Humler and Whitechurch, 1988; Pan and Batiza, 2002; Danyushevsky et al., 2002). Nabeleck and Langmuir (1986) and Humler and Whitechurch (1988), who modeled the diffusive re-equilibration of Ni in olivines from the slow-spreading Mid-Atlantic Ridge (MAR) and the intermediate-spreading Central Indian Ridge, respectively, interpreted their modeled diffusion times to represent the time interval between a magma mixing event and the eruption of the MORBs. Pan and Batiza (2002) used a similar assumption, based on Fe-Mg zoning in olivines from the fast-spreading East Pacific Rise (EPR). In contrast, the time interval obtained by modeling Fe-Mg zoning in melt inclusions and olivines from the EPR in the study by Danyushevsky et al. (2002) was interpreted to represent the time between olivine crystallization and eruption. Nevertheless, all of these studies point to rather short magma residence times of olivines in MORBs (i.e., between 1 day and 4 years), with shorter time intervals being prevalent. This is also consistent with the findings of Costa et al. (2010) who modeled diffusion-generated Mg zoning in plagioclase in MORBs from the MAR and the intermediate-spreading Costa Rica Rift (CRR) and found time spans of <1.5 years between magma mixing and eruption. However, as already explained in section II.1, diffusion-driven zoning may be difficult to distinguish from growth zoning and the latter provides only limited information on time scales. Hence, the developed technique of *in situ* Fe- and Mg isotope analyses has been applied herein to olivines in MORBs in order to reliably trace Fe-Mg inter-diffusion; then, modeling the clearly diffusion-generated zoning in MORB olivines can help to improve our knowledge about time scales of magma evolution at mid-ocean ridge settings.

III.2 Samples

Plagioclase-olivine phyric MORBs from the slow-spreading Mid-Atlantic Ridge (MAR) and the intermediate-spreading Costa Rica Rift (CRR) were investigated. These MORB samples were taken from Deep Sea Drilling Project (DSDP) drill cores from sites 332A and 396B near the MAR and from Ocean Drilling Project (ODP) drill cores from site 896A near the CRR. The IODP core repository in Bremen (Germany) provided the samples from sites 332A and 396B, the Gulf Coast Repository in College Station, Texas (USA), provided the samples from site 896A.

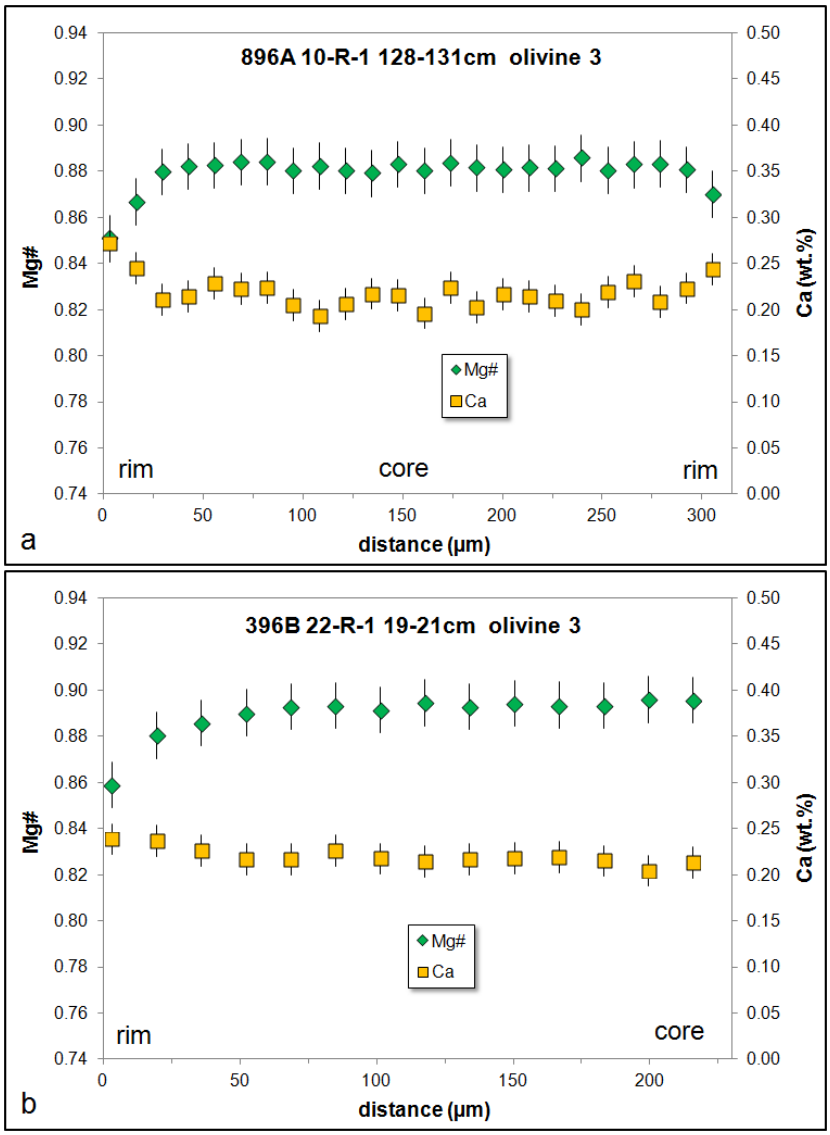

Figure III.1: Representative concentration profiles (Mg# and Ca) determined by EMP across normally zoned olivine phenocrysts in MORBs from (**a**) the intermediate-spreading Costa Rica Rift (ODP Hole 896A) and (**b**) the slow-spreading Mid-Atlantic Ridge (DSDP Hole 396B).

Electron microprobe analyses (see section III.3.1) were performed on two samples from site 332A (Table III.1), which is located 30 km west of the Mid-Atlantic Ridge axis at 36°52'N and where 330 m of acoustic basement (consisting of massive to pillowed basalt, basalt breccia, and interlayered sediments) was penetrated (Aumento et al., 1974). These samples ([332A 36-R-1 33-34cm and 72-73cm]; hereafter referred to as 332A-8 and 332A-9, respectively) are coarsely plagioclase-olivine phyric basalts from the second deepest level of Hole 332A at ~390 m below sea floor (mbsf; lithologic unit 6; Aumento et al., 1974). Details

about the geochemistry of the basalts from this lithologic unit are given in Flower et al. (1974; "magma group 332A-4").

Furthermore, electron microprobe (EMP) analyses were conducted on six samples from Hole 396B (see Table III.1 for details), which is located ~150 km east of the MAR axis at 22°59.1'N, 43°30.9'W and penetrated 255 m of basaltic basement. The analyzed samples are plagioclase-olivine porphyritic basalts from the middle section of this hole at ~300 mbsf (chemical unit B_2; Dmitriev et al., 1979). Major and trace element contents of basalts and phenocryst phases from this unit are provided by, e.g., Flower et al. (1976). A study by Sato et al. (1976) estimated eruption temperatures of basalts at site 396B to be 1190-1220°C, based on the temperature dependence of the MgO-FeO equilibrium between olivine and basaltic melt/glass (Roeder and Emslie, 1970).

Finally, three samples from site 896A were also analyzed by EMP (Table III.1). ODP Hole 896A is located ~200 km south of the intermediate-spreading Costa Rica Rift at 01°13.0'N, 83°43.4'W. It penetrated 290 m of acoustic basement consisting mainly of massive basalt flows and pillow lavas. Two samples (highly phyric plagioclase-olivine basalts) are from an intermediate unit at ~280 mbsf, where pillow basalts were cored. The third one is from a lower unit at ~387 mbsf, where massive lava flows were cored (Alt et al., 1993), and represents a moderately phyric plagioclase-clinopyroxene-olivine basalt. In a study by McNeill and Danyushevsky (1996), homogenization temperatures of glass inclusions in plagioclase and olivine in 896A basalts were determined to be 1190-1220°C, likely reflecting the crystallization temperature of relatively evolved melts at site 896A. High-MgO, primary melts, in equilibrium with $Fo_{91.6}$ olivine and with crystallization temperatures of ~1340°C, appear to have played an important role during the petrogenesis of those more evolved lavas (McNeill and Danyushevsky, 1996; Costa et al., 2010).

III.3 Methods

III.3.1 Electron microprobe and *in situ* Fe- and Mg isotope analyses

Electron microprobe and *in situ* Fe- and Mg isotope analyses were performed with the same setup as described in section II.3. Fe-Mg isotopic profiles were determined on olivines that show a distinct chemical zoning, i.e. with a width of >60 µm and variations in Mg# of >0.02.

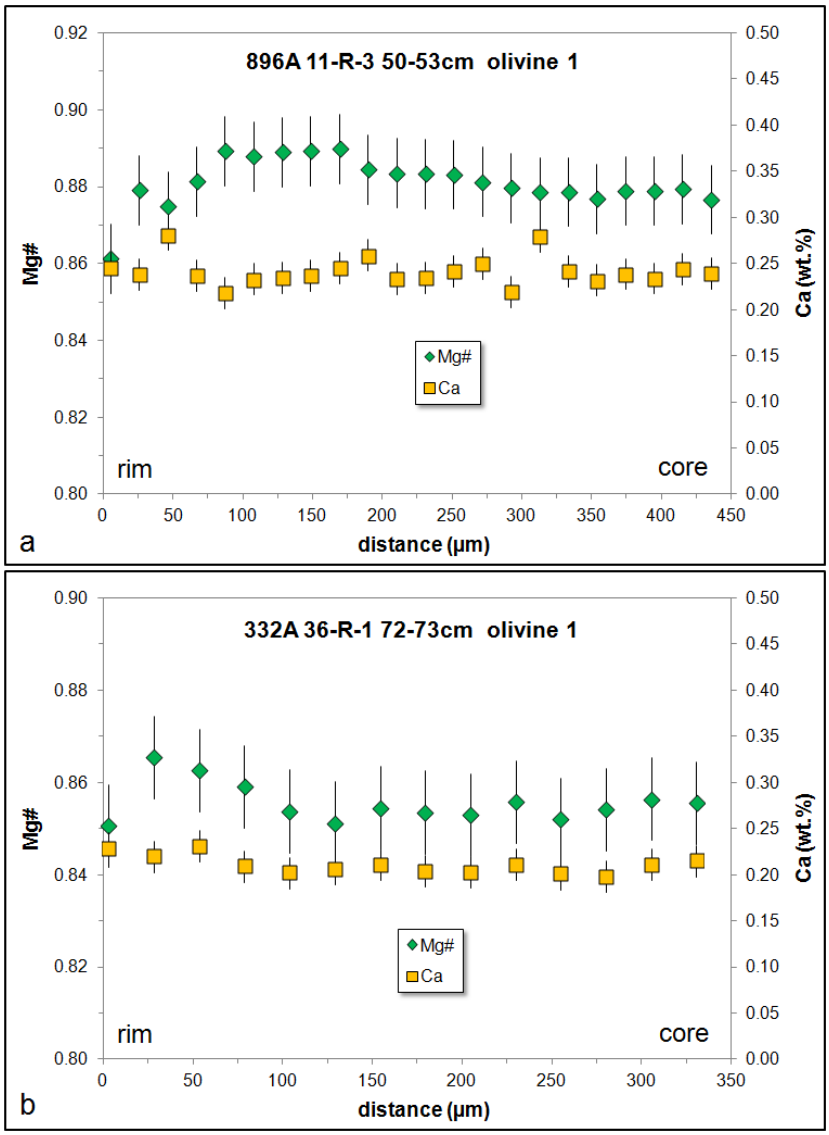

Figure III.2: Concentration profiles (Mg# and Ca) determined by EMP across multiply zoned olivines in MORBs from (**a**) the Costa Rica Rift (ODP Hole 896A) and (**b**) the Mid-Atlantic Ridge (DSDP Hole 332A).

III.3.2 Diffusion modeling and determination of time scales

In general, modeling of Fe-Mg inter-diffusion in MORB olivines follows the procedure described in section II.3.3. Pure Fe-Mg exchange of the olivine with the melt was simulated assuming a fixed rim composition and Fe-Mg inter-diffusion in olivine. Here, the diffusion equation was solved numerically by the method of finite differences (e.g., see Costa et al. 2008). For one multiply zoned olivine (896A-05b olivine 1) an internal homogenization of the crystal after two growth episodes was simulated with a plane sheet geometry in order to reproduce the observed chemical and isotopic zoning (see section III.4.2). These growth episodes initially produced a chemical step profile but homogeneous Fe and Mg isotopic

compositions across the olivine. As already mentioned in section II.3.3.2, the diffusion coefficient for Fe-Mg diffusion in olivine was calculated following the parameterization of Dohmen and Chakraborty (2007), and durations of the diffusive processes were estimated at isothermal conditions following the simplification illustrated by Ganguly (2002) where a peak-temperature has to be defined. As the maximum eruption temperatures of the MORBs investigated in this study appear to be 1220°C (see section III.2), T_{peak} was assumed to be 1220°C in most cases. Exceptions are multiply zoned olivines, which apparently have been in contact with a hotter melt during their magma residence time. Further parameters that define our model for Fe-Mg inter-diffusion in olivine are as follows:

- The oxygen fugacity was assumed to be at the FMQ-buffer (e.g., Cottrell and Kelley, 2011; Mallmann and O'Neill, 2009), and its temperature-dependence was calculated following the parameterizations of Schwab and Küstner (1981) and Herd (2008).
- The diffusion anisotropy in olivine was considered and the diffusion coefficient along any analytical profile was calculated according to the approach presented in Costa and Chakraborty (2004).
- X_{Fe} was assumed to be constant and to be the mean of X_{Fe} in the core of the crystal and X_{Fe} at the very rim. Due to the limited compositional difference between core and rim (<0.05 in X_{Fe}) the uncertainty introduced by this simplification is negligible.
- The pressure was taken to be invariable at 100 MPa.

Finally to solve the diffusion equation, the boundary conditions have to be defined. In our model, the core of the olivine represents a no-flux boundary while the magma around the crystal acts as an infinite reservoir. Thus, Fe and Mg concentrations were assumed to be fixed at the contact of the olivine with the magma and to be equal to the Fe and Mg concentrations measured by EMP at the crystal rim.

III.4 Results and Discussion

III.4.1 Fe-Mg chemical and isotopic zoning in MORB olivines

Of the 39 olivine phenocrysts in MORBs analyzed to date by EMP 22 do not show a clear zoning in terms of Mg# (or forsterite contents). 14 olivines exhibit normal zoning (up to 4.5 mole percent), i.e. the rim contains more Fe than the core (Fig. III.1); two crystals show multiple, i.e. both normal and reverse, zoning (Fig. III.2); one olivine exhibits only reverse zoning. As already observed in previous studies (Flower et al., 1976; Sato et al., 1976; McNeill and Danyushevsky, 1996; Pan and Batiza, 2002), within one thin section (or

sample) forsterite contents of olivine cores can vary significantly, in our samples up to 4 mole percent, possibly reflecting various olivine populations that were scavenged from diverse original magmas and mixed into one hybrid host magma which finally erupted. If a chemical disequilibrium existed between olivines and the new host, diffusive transport would generate chemical zoning in the crystals (cf. Pan and Batiza, 2002).

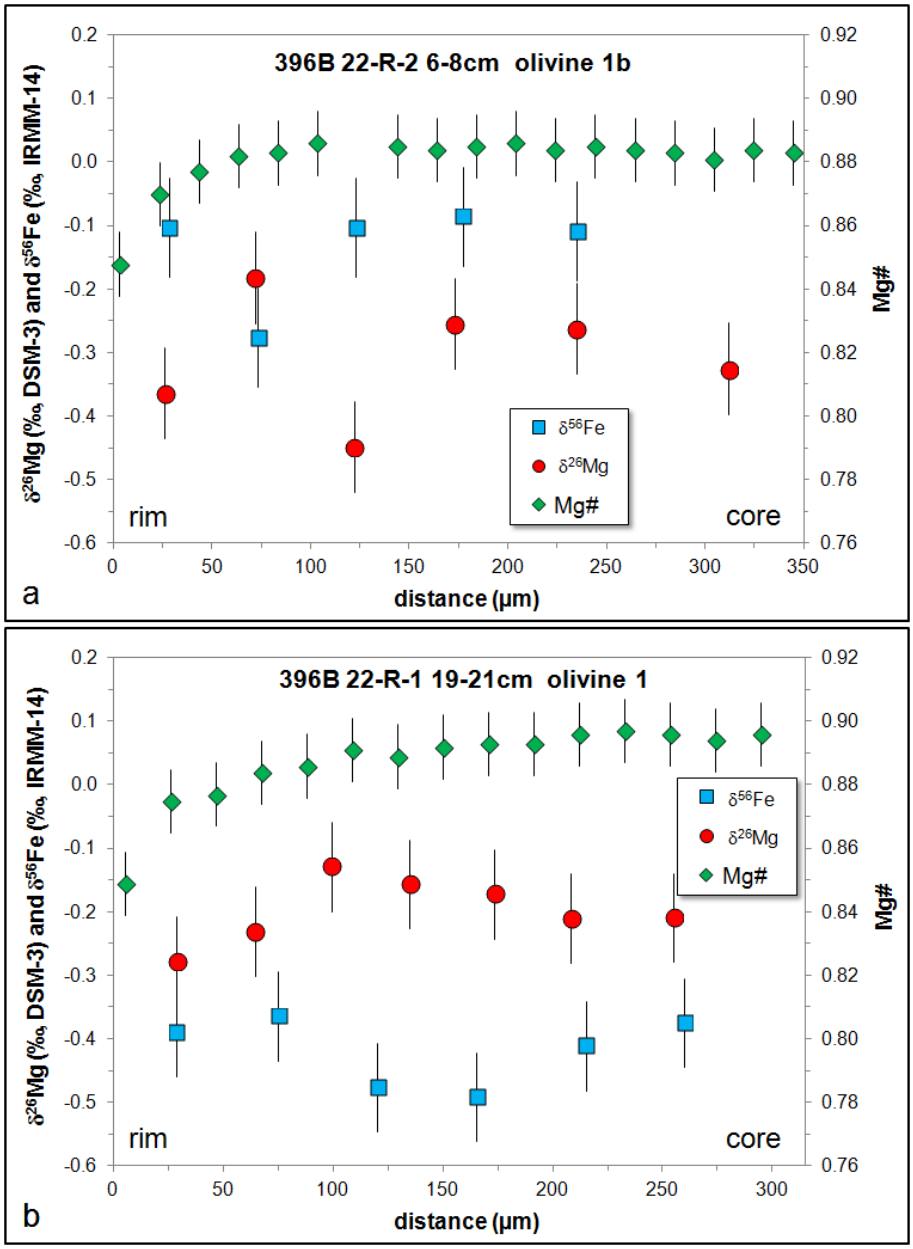

Figure III.3: Fe-Mg chemical and isotopic profiles across normally zoned olivines from the Mid-Atlantic Ridge determined by fs-LA-MC-ICP-MS. The inversely correlated Fe- and Mg isotope profiles indicate that the chemical zoning was mainly generated by Fe-Mg inter-diffusion. Error bars represent the analytical uncertainty (2 SD) during the analytical session.

Fe and Mg isotopic profiles that were determined by fs-LA-MC-ICP-MS for normally zoned olivine phenocrysts point to diffusion-generated chemical zoning as light iron and heavy magnesium isotopes are relatively enriched in a zone near the Fe-rich crystal rims (Fig. III.3), similar to the zoning observed for most of the investigated olivine grains from intra-plate volcanic rocks (see chapter II). However, in contrast to the latter, the investigated MORB olivines exhibit only narrow zoning profiles, indicating relatively short diffusion times. Furthermore, the isotopic variations were in some cases barely resolvable, given the analytical uncertainty of ~0.1‰ for δ^{56}Fe and δ^{26}Mg. Nevertheless, modeling of the chemical and isotopic zoning can provide information on the time scales of magma evolution beneath mid-ocean ridges (see section III.4.2).

Fe and Mg isotopic profiles were also obtained for the two multiply zoned olivines. In the olivine from the MAR (332A-9 olivine 1; Fig. III.4a), heavy Fe and light Mg isotopes appear to be relatively enriched in a zone where Mg may have diffused from the crystal's rim, i.e. from the melt, towards the core (and Fe in the opposite direction). This process could be triggered if the olivine came into contact with a more primitive melt (compared to the one it had grown in). Furthermore, the crystal rim has light Fe and heavy Mg isotopic compositions, indicating diffusion of Fe from the melt into this domain during a second, shorter diffusion event. This may be explained by a chemical gradient that was generated by magma differentiation during the magma ascent in dikes, or by a second mixing event with a more evolved magma (which finally also triggered the eruption).
The other multiply zoned olivine comes from the CRR (896A-05b olivine 1; Fig. III.4b). Its apparently homogeneous core (in terms of Mg#) shows a relatively heavy Fe isotopic composition (δ^{56}Fe ≈ 0.30‰ relative to IRMM-014), indicating that the core was affected by Mg diffusion into and Fe diffusion out of the olivine, potentially due to contact with a hotter, more primitive melt. The lightest Fe isotopic composition is observed near the Fe-rich crystal rim. This domain may also be characterized by a relatively heavy Mg isotopic composition, although the precision of the *in situ* analyses is not good enough to resolve Mg isotope variations unambiguously here. Nevertheless, the chemical and isotopic zoning of this olivine points to at least two diffusion episodes, analogous to the other multiply zoned olivine (332A-9 olivine 1). Hence, two-stage models were applied to simulate the observed chemical and isotopic zoning of these crystals (see section III.4.2).

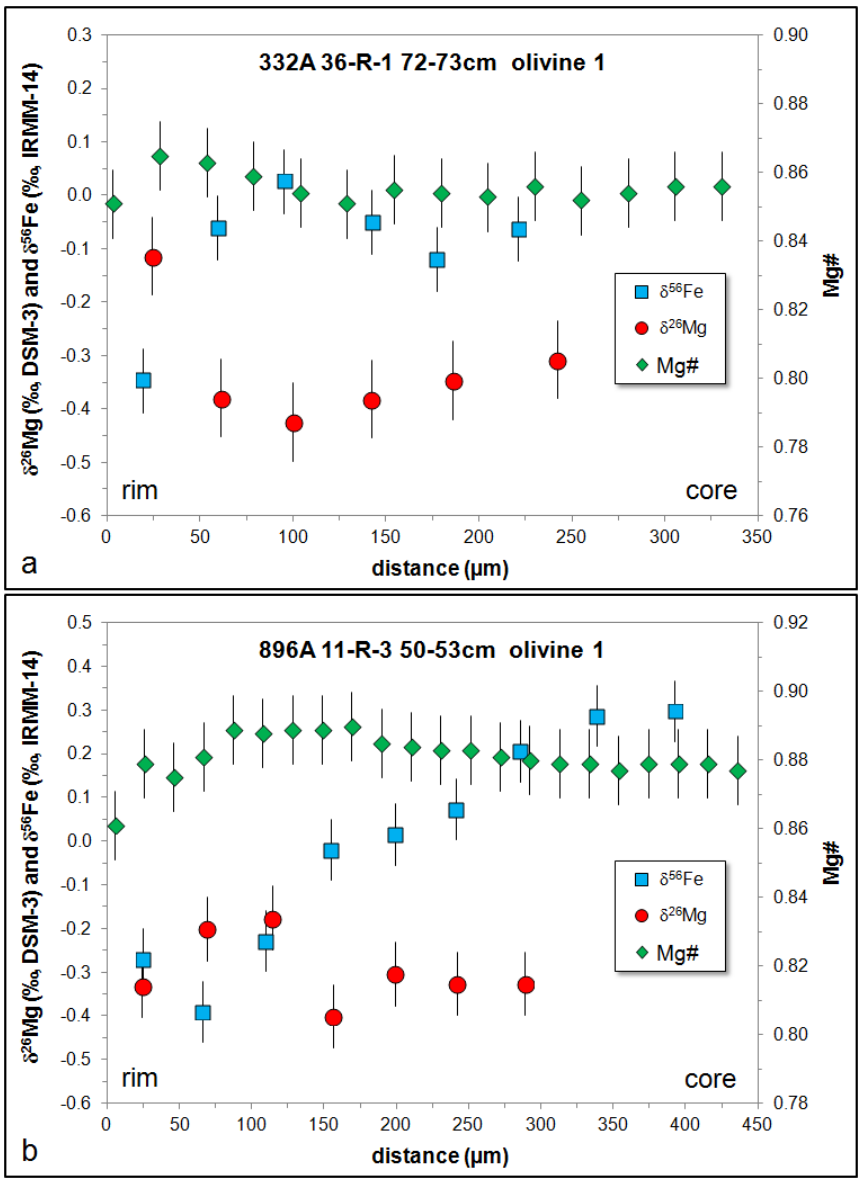

Figure III.4: Fe-Mg chemical and isotopic profiles across multiply zoned olivines from (**a**) the Mid-Atlantic Ridge and (**b**) the Costa Rica Rift. Error bars represent the analytical uncertainty (2 SD) during the analytical session.

As pointed out by Costa et al. (2010), repeated magma mixing events appear to be common during the petrogenesis of MORBs. The findings of this study support this hypothesis as olivines with complex chemical zoning patterns were found in MORB samples from both the MAR and the CRR. Additionally, isotopic zoning profiles – as obtained in this project – provide further evidence of diffusive re-equilibration of phenocrysts after magma mixing events or during magma cooling.

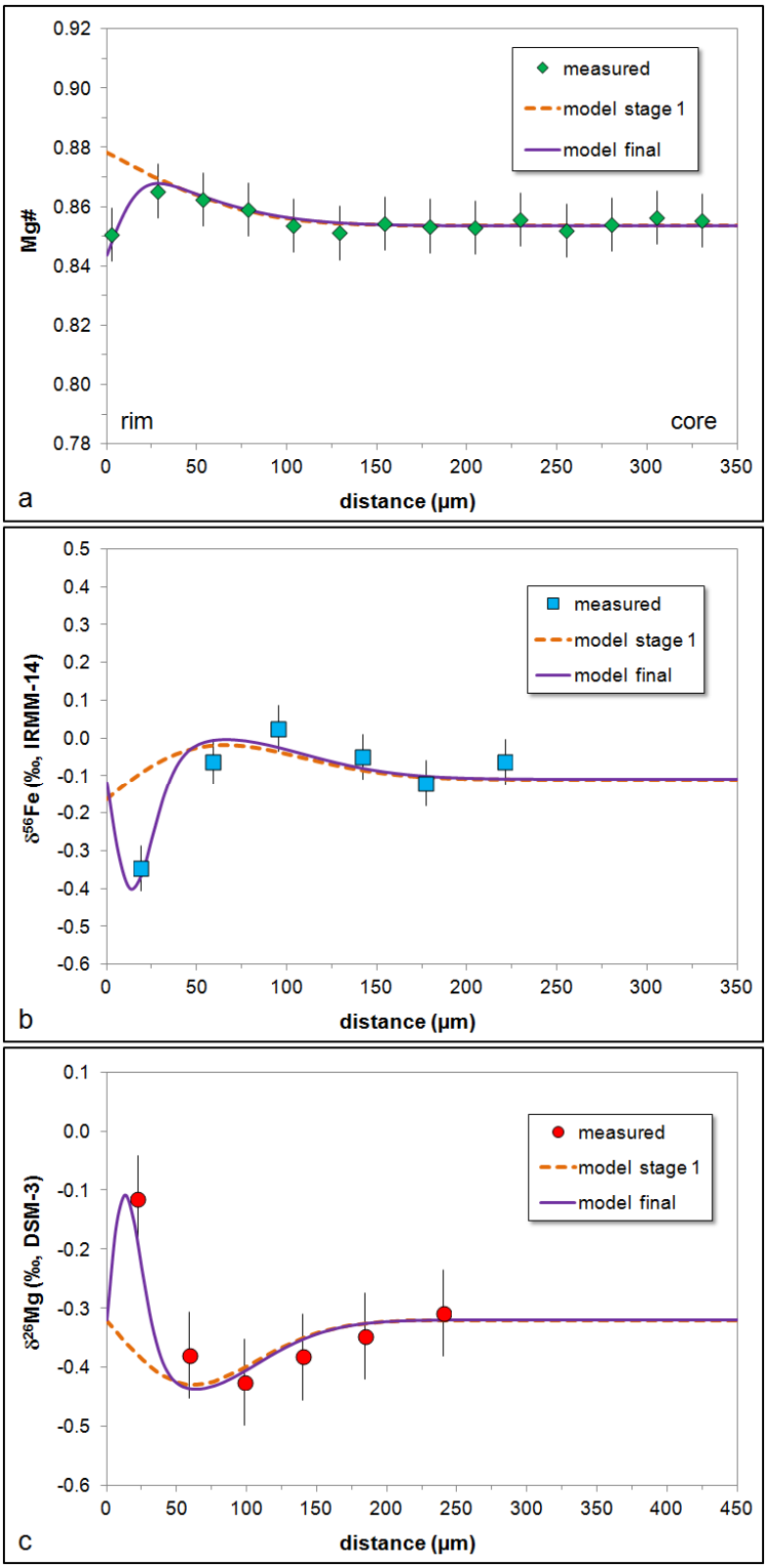

Figure III.5: Modeling of Fe-Mg chemical (**a**) and isotopic (**b,c**) diffusion profiles for the multiply zoned olivine shown in Fig. III.4a (in the text referred to as 332A-9 olivine 1). The model includes two stages: during the first stage (lasting ~490 days at 1205°C) Mg diffuses from the melt into the olivine while Fe diffuses in the opposite direction (e.g. after magma mixing with a more primitive melt); the modeled chemical and isotopic profiles at the end of stage 1 are shown as a dashed line. In the second stage (lasting 45 days at 1175°C) Fe diffuses from the melt into the olivine while Mg diffuses out of the olivine (e.g. due to cooling and differentiation of the host magma, potentially during magma ascent in dikes). During first stage: β_{Fe} = 0.08, β_{Mg} = 0.10; during second stage: β_{Fe} = 0.18, β_{Mg} = 0.15. See section III.3.2 for further model parameters. As outlined in section II.5.3.2, β-values depend on the boundary conditions used in the model (fixed vs. changing edge compositions). Assuming fixed Fe and Mg concentrations at the olivine-melt contact for both stages may not be entirely correct, which may explain the discrepancy of the β-values for stages 1 and 2.

III.4.2 Estimation of time scales by diffusion modeling

If zoning in olivine was dominantly produced by Fe-Mg inter-diffusion, which can be reliably traced by Fe-Mg isotopic zoning, modeling of its chemical and isotopic zoning may provide time information about (i) the residence time of these crystals in the magma and/or (ii) magma cooling rates (e.g., Costa et al., 2008; Teng et al., 2011; Sio et al., 2013). In general, the simplified diffusion modeling at isothermal conditions used in this study is suitable to reproduce both the chemical and the isotopic profiles of the investigated MORB olivines (Fig. III.5, III.7 and III.8). The time scales obtained with this diffusion modeling range from a few months to ~8 years (Table III.2), which is roughly within the range of reported magma residence times for MORB olivines (Nabeleck and Langmuir, 1986; Humler and Whitechurch, 1988; Pan and Batiza, 2002; Danyushevsky et al., 2002).

The longest time scale is documented by the multiply zoned olivine from the CRR (896A-05b olivine 1; Table III.2). As explained in section III.4.1, the complex chemical and isotopic zoning of this olivine points to two diffusion events. Hence, a two-stage model was applied to reproduce the chemical and isotopic zoning of this crystal. Simple diffusive Fe-Mg exchange between olivine and melt (scenario 1 in section II.5.1) is suitable to reproduce the chemical zoning (Fig. III.6a), if Mg diffuses into and Fe out of the olivine during a first diffusion episode, which is followed by second, shorter diffusion event where Fe diffuses into the olivine (and Mg in the opposite direction). However, such a scenario does not satisfactorily reproduce the observed isotopic zoning, especially for Fe (Fig. III.6b). Alternatively, a chemical step function may be assumed for the first diffusion episode, which may develop due to two episodes of crystal growth (scenario 3 in section II.5.1; see also Kahl et al., 2011; Longpré et al., 2014). These steps in the concentrations of Fe and Mg are subsequently smoothed out by intra-mineral Fe-Mg inter-diffusion resulting in Fe-Mg isotopic zoning (Fig. III.7). The second diffusion event is characterized by diffusion of Fe into and Mg out of the olivine due to magma differentiation / cooling. The time scales obtained with such a model (that adequately reproduces the chemical *and* isotopic zoning of this olivine) are 6.1 years for the first diffusion episode at ~1205°C and 2.1 years for the second one at ~1175°C (Table III.2). Note that the used model is not successful in simulating the very heavy Fe isotopic composition in the core of the olivine (Fig. III.7b). However, as outlined in section II.5.2, this isotopic composition may be inherited from diffusive processes that occurred even earlier in the crystal's history. Costa et al. (2010) investigated Mg zoning of plagioclase crystals in MORBs from ODP site 896A and estimated the time

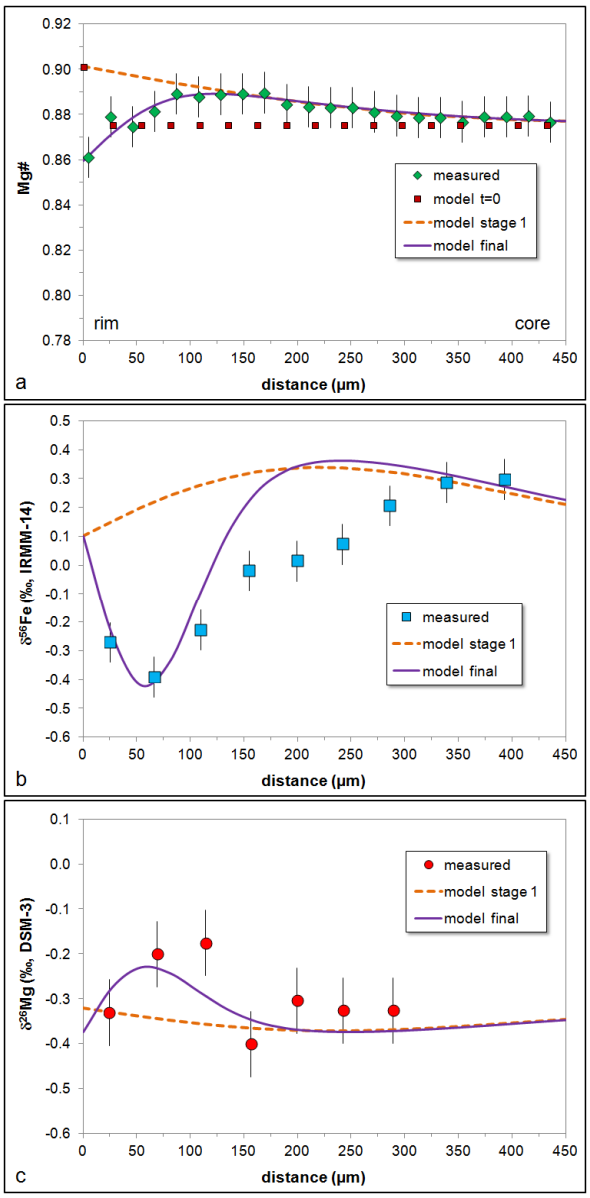

Figure III.6: Modeling of Fe-Mg chemical (**a**) and isotopic (**b,c**) diffusion profiles for the multiply zoned olivine shown in Fig. III.4b (in the text referred to as 896A-05b olivine 1). The model includes two stages and is similar to that described in the figure caption of Fig. III.5. During first stage: $\beta_{Fe} = 0.12$, $\beta_{Mg} = 0.11$; during second stage: $\beta_{Fe} = 0.22$, $\beta_{Mg} = 0.11$. See section III.3.2 for further model parameters. Note that this model does not satisfactorily reproduce the observed isotopic zoning, especially for Fe.

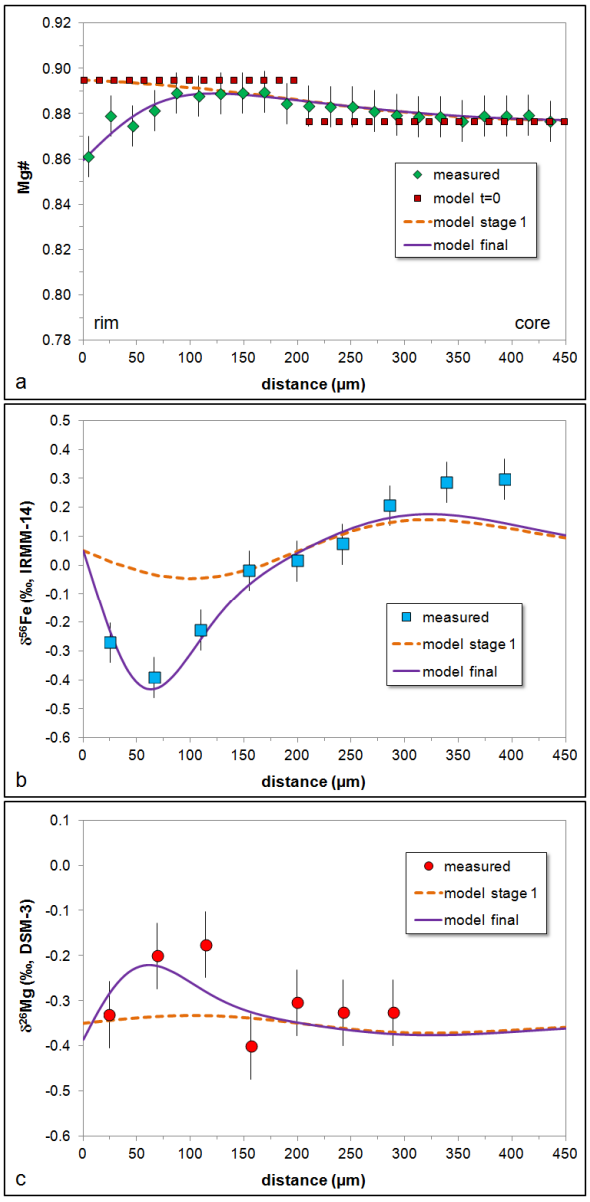

Figure III.7: Modeling of Fe-Mg chemical (**a**) and isotopic (**b,c**) diffusion profiles for the multiply zoned olivine shown in Fig. III.4b. The model includes two stages: prior to the first diffusion episode, a chemical step function (red squares in a) was established due to two episodes of crystal growth. Subsequent Fe-Mg inter-diffusion smoothes out this step; the modeled chemical and isotopic profiles at the end of stage 1 (lasting 6.1 years at 1205°C) are shown as a dashed line. In the second stage (lasting 2.1 years at 1175°C) Fe diffuses from the melt into the olivine while Mg diffuses out of the olivine (e.g. due to cooling and differentiation of the host magma). For both stages: $\beta_{Fe} = 0.16$, $\beta_{Mg} = 0.11$. See section III.3.2 for further model parameters. In addition to the better fit, the constant β-values for both stages indicate that this scenario is more realistic than the one presented in Fig. III.6.

span between magma mixing and eruption to be <1.5 years. In contrast, results of our diffusion modeling point to somewhat longer time scales of diffusive re-equilibration of olivines after a magma mixing event. An explanation for this discrepancy may be that olivine, because of its higher density, is more prone to remain in a crystal mush at the bottom of a magma chamber, leading to a longer magma residence time. In summary, the investigation of this multiply zoned olivine shows that a combined study of chemical *and* isotopic zoning in minerals is particularly suitable to reconstruct growth- and diffusion processes affecting a crystal and, thus, provide valuable information on magma evolution.

The other multiply zoned olivine found in a MORB from the MAR (332A-9 olivine 1) also implies two episodes of diffusive re-equilibration, although both chemical and isotopic zoning are less pronounced in this olivine than in the one from the CRR. A model with pure diffusive Fe-Mg exchange between olivine and melt in two stages is suitable to simulate the chemical zoning as well as the Fe-Mg isotopic zoning (Fig. III.5). The first stage lasts ~490 days at 1205°C, possibly representing the time span between a magma mixing event (with a primitive melt) and either a second mixing event with a more evolved magma or the start of the final magma ascent in dikes associated with cooling and differentiation of the magma. In the latter case, the second stage (lasting 45 days at 1175°C) could represent the duration of magma transfer from the magma chamber to the seafloor (Table III.2). As suggested in a study by Paonita and Martelli (2006), ascent rates of MORBs appear to be extremely variable, i.e. they range from 0.01 m/s up to 10 m/s, probably depending on the local stress conditions of the upper oceanic crust near the eruption site. Given these velocities, the time scale of ~45 days would be too long to reflect the duration of magma transfer from the magma chamber to the seafloor. Either, magma ascent at MORs may be slower than estimated by Paonita and Martelli (2006), in cases, or the time of 45 days may represent the time span between a mixing event with a more evolved magma and the eruption, following the reasoning of Pan and Batiza (2002; see section III.1).

Normally zoned olivines from DSDP Hole 396B at the slow-spreading MAR (Fig. III.8) exhibit relatively short time scales of diffusive re-equilibration, typically <1.2 years, except for olivine 1a in sample 396B-14-1 (Table III.2). Interestingly, these time scales are in good agreement with the time spans obtained by Pan and Batiza (2002; diffusion times between 1 day and ~1.5 years), who investigated and modeled Fe-Mg chemical zoning of olivines in MORBs from the fast-spreading East Pacific Rise. In the study by Pan and Batiza (2002),

however, the diffusion anisotropy in olivine was not considered, and Fe-Mg inter-diffusion coefficients in olivine were calculated for the crystallographic c-axis only. Hence, magma residence times of the EPR olivines may be somewhat longer than the duration estimated by Pan and Batiza (2002), if the measured chemical profiles have not been taken parallel to the crystallographic c-axis of the investigated olivine grains.

Combining the findings of previous studies (Nabeleck and Langmuir, 1986; Humler and Whitechurch, 1988; Pan and Batiza, 2002; Danyushevsky et al., 2002) with the results of this study suggests that magma residence times of olivines in MORBs do probably not depend on the spreading rate of the ridge, as variable time scales of diffusive re-equilibration (from a few days to a couple of years) were observed for both, slow- and fast spreading ridges. Nevertheless, short time intervals of <1.5 years between two mixing events or between a final mixing event and eruption are common. These findings indicate that, although slow-, intermediate- and fast-spreading ridges are characterized by the production of vastly different magma volumes, they display a similar pulsing of magmatic processes.

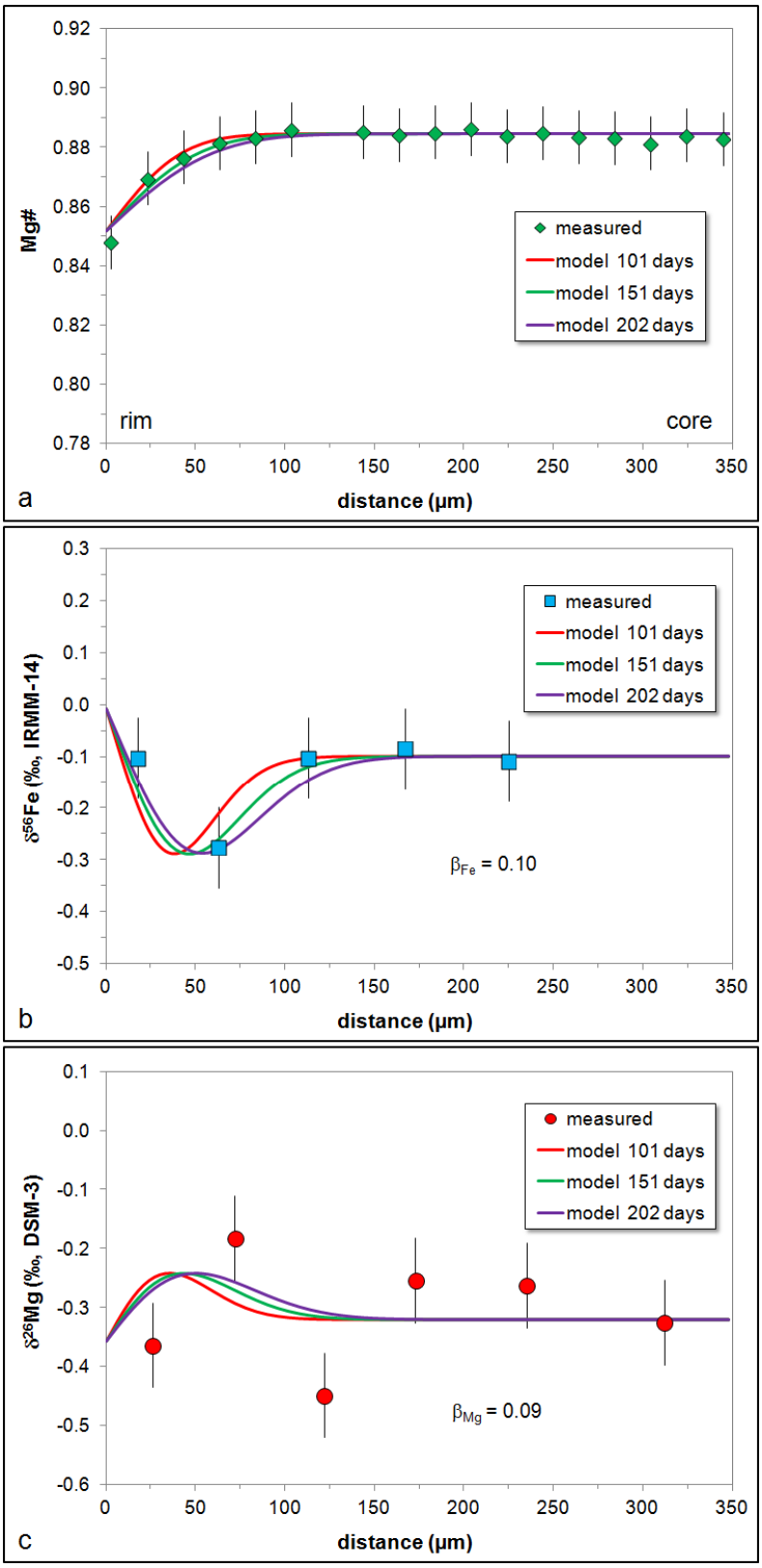

Figure III.8: Modeling of Fe-Mg chemical (**a**) and isotopic (**b** and **c**) diffusion profiles for the normally zoned olivine shown in Fig. III.3a. See section III.3.2 for details of the modeling and model parameters. Modeling results for three time spans (101, 151 and 202 days) are shown in order to illustrate the change of the profiles' lengths and shapes with time.

III.5 Conclusions

The main findings of this study on olivines in MORBs are:

- 50% of the crystals investigated herein do not show a clear chemical zoning (in terms of Mg#), indicating either that chemical disequilibrium between olivine and melt is not the common case in MORBs, or – if a disequilibrium did exist – that the time for diffusive re-equilibration of olivine was not sufficient. This is in contrast to the observations made for olivines in intra-plate volcanic rocks where almost every analyzed olivine shows pronounced Fe-Mg chemical (and isotopic) zoning (see section II.4.1).
- MORB olivines that are chemically zoned mostly show inversely correlated Fe-Mg isotopic profiles, pointing to diffusion-generated chemical and isotopic zoning. However, because the intra-mineral chemical gradients are rather small, the isotope fractionation is also small and in some cases barely resolvable given the analytical uncertainty of ~0.1‰ for δ^{56}Fe and δ^{26}Mg.
- The time scales obtained by modeling the observed Fe-Mg chemical and isotopic zoning are consistent with magma residence times of MORB olivines obtained in previous studies (e.g., Pan and Batiza, 2002), exhibiting relatively short time spans of diffusive re-equilibration for normally zoned crystals (in most cases <1.5 years) and somewhat longer time scales (up to ~8 years) for multiply zoned olivines. This is not too surprising as normally zoned olivines record only one (the last) diffusion episode, while multiply zoned olivines record at least two diffusion episodes (i.e. two magma mixing events). One may speculate that the rare occurrence of multiply zoned olivines in our sample suite indicates that a sub-ridge magma chamber is almost completely emptied during an eruption (possibly triggered by a new magma pulse), i.e. only a few olivines remain in the magma chamber where they can encounter a second magma pulse. Alternatively, multiply zoned olivines may simply record their transport from one (deep-level) magma chamber to another (high-level) magma chamber (cf. Kahl et al., 2011).

III. Tables

Table III.1: List of MORB samples analyzed by electron microprobe

ridge system	expedition / leg	site	hole	core	section	interval (cm) top	interval (cm) bottom	sample ID
MAR	DSDP 37	332	A	36	1	33	34	332A-8-1 & -2
MAR	DSDP 37	332	A	36	1	72	73	332A-9
MAR	DSDP 46	396	B	20	4	78	81	396B-7-1 & -2
MAR	DSDP 46	396	B	20	4	118	120	396B-8
MAR	DSDP 46	396	B	22	1	19	21	396B-9
MAR	DSDP 46	396	B	22	1	109	111	396B-11-1 & -2
MAR	DSDP 46	396	B	22	2	6	8	396B-12
MAR	DSDP 46	396	B	22	2	126	127	396B-14-1 & -2
CRR	ODP 148	896	A	10	1	128	131	896A-04
CRR	ODP 148	896	A	11	3	50	53	896A-05a & -05b
CRR	ODP 148	896	A	22	4	18.5	22.5	896A-17a & -17b

Table III.2: Estimation of time scales of diffusive re-equilibration and β-values based on diffusion modeling for MORB olivines with clearly coupled Fe-Mg chemical and isotopic profiles

ridge system	site	sample & olivine ID	type of zoning	time interval 1	T1 (°C)	time interval 2	T2 (°C)	β_{Fe}	β_{Mg}
MAR	332A	332A-9 ol1	multiple	490 days	1205	45 days	1175	0.08 , 0.18 [a]	0.10 , 0.15 [a]
MAR	396B	396B-9 ol3	normal	336 days	1175	28 days	1150	0.17 , 0.17 [a]	(0.08 , 0.08) [a,b]
MAR	396B	396B-11-1 ol1	normal	414 days	1175	-	-	0.120	x
MAR	396B	396B-12 ol1a	normal	168 days	1175	-	-	0.110	(0.050)
MAR	396B	396B-12 ol1b	normal	140 days	1175	-	-	0.100	(0.090)
MAR	396B	396B-14-1 ol1a	normal	3.0 years	1175	-	-	0.090	x
CRR	896A	896A-05b ol1	multiple	6.1 years	1205	2.1 years	1175	0.16 , 0.16 [a]	0.11 , 0.11 [a]

[a] First value refers to time interval 1, second value refers to time interval 2.

[b] Values in parentheses are poorly constrained, because the observed Mg isotope fractionation is relatively small.

dashes: not required

crosses: not determined

Chapter IV: Diffusion rates of minor and trace elements in natural olivines*

* 50% of the trace element analyses on olivines performed for this chapter were carried out by Nikolas Stehr. Raw data reduction as well as data evaluation and interpretation were done by myself.

IV.Abstract

Concentration profiles of 19 minor and trace elements across 17 chemically zoned (in terms of Mg#), natural olivines were acquired using femtosecond-laser ablation-sector field-ICP-MS. The concentration profiles of 11 elements could be used to estimate chemical diffusion coefficients of these elements relative to Fe-Mg. Our results indicate that the diffusion coefficients of the majority of the investigated cations in olivine (Li, Ca, Sc, Ti, V, Cr, Mn, Co, Ni, Y, Yb, Fe-Mg) are quite similar, i.e. the diffusion rates of the fastest (Li) and the slowest (Ti) elements differ by less than one order of magnitude. Still, the observed differences in the diffusion rates of these elements allow for proposing a common order of diffusivity in natural olivine which is from highest to lowest: Li > Fe-Mg > Mn > Cr ≈ Co ≈ V > Ni ≈ Sc > Y ≥ Yb > Ca ≈ Ti. These differences in diffusion rates are probably best explained by the ability of these elements to use different diffusion pathways in olivine, which in turn depends on charge and radius of their cations.

IV.1 Introduction

Studying minor and trace element contents in magmatic olivine provides a powerful tool to unravel igneous processes such as mantle melting or early crystallization of magmas (e.g., Foley et al., 2010, 2013). A number of geothermometers, such as the Ca-in-olivine thermometer (e.g., Köhler and Brey, 1990; Shejwalkar and Coogan, 2013), are also based on trace element concentrations in olivine, allowing to estimate equilibration temperatures of peridotites (e.g., De Hoog et al., 2010) or maximum crystallization temperatures of mantle

derived melts (e.g., Coogan et al., 2014). However, diffusive re-equilibration of olivine in a differentiating magma may modify trace element contents of the crystal significantly if diffusion of these elements through the crystal lattice is fast enough. Likewise, the composition of melt inclusions, which are trapped in the early crystallizing phase olivine and expected to record the composition of a primitive melt, may re-equilibrate by diffusion during the magma residence time of the host mineral (Spandler et al., 2007). Hence, knowledge of the diffusion rates of minor and trace elements in olivine is essential in order to evaluate the potential effects of diffusive re-equilibration. Previous experimental studies which examined diffusion rates of minor and trace elements in olivine reported contradicting results. For example, studies by Spandler et al. (2007) and Spandler and O'Neill (2010) investigating diffusion of various trace elements in a San Carlos olivine at 1300°C indicate that the diffusion rates of REE are very similar to that of Fe-Mg inter-diffusion. In contrast, Remmert et al. (2008) and Cherniak (2010) have found much lower diffusion coefficients for REE in olivine (~3 orders of magnitude lower than the data obtained by Spandler et al. (2007) and Spandler and O'Neill (2010)). Similarly, diffusion of Ca in olivine has been determined to be only slightly slower (by a factor of ~2-4; Jurewicz and Watson, 1988; Spandler and O'Neill, 2010; Qian et al., 2010) or, in other studies, to be significantly slower (by a factor of >10; Coogan et al., 2005) than Fe-Mg inter-diffusion. To our knowledge, only the study by Qian et al. (2010) used major and trace element profiles across a *natural*, large olivine xenocryst (included in dioritic magma) in order to determine diffusion coefficients for Li, Ca, Sc, Fe-Mg, Co, Ni, and Y relative to Mn in olivine. Here, we follow this approach by estimating diffusion coefficients relative to Fe-Mg (i.e. $D_M/D_{Fe\text{-}Mg}$) for Li, Ca, Sc, Ti, V, Cr, Mn, Co, Ni, Y, and Yb based on trace element profiles across 17 natural olivines in intra-plate basanites and in mid-ocean ridge basalts (MORBs) that are chemically zoned in terms of Mg#. For 9 of the 17 investigated olivines, a diffusion origin was proven by the coupling of the Fe-Mg chemical zoning with inversely correlated Fe-Mg isotopic zoning (see chapters II and III of this dissertation; Sio et al., 2013). The intention of this study is to provide diffusion rates of trace elements in olivine relative to the well-determined Fe-Mg exchange diffusion (Dohmen and Chakraborty, 2007; Dohmen et al., 2007), based on the investigation of well-selected natural olivines, and with that contributing to a better understanding on the parameters that control trace element diffusion in olivine.

IV.2 Samples

The investigated samples comprise various olivine-bearing basanites from the Massif Central volcanic region (France) as well as plagioclase-olivine phyric basalts from the Mid-Atlantic Ridge (MAR), which have already been described in section II.2 (Massif Central basanites) and in section III.2 (mid-ocean ridge basalts from the MAR).

IV.3 Methods

IV.3.1 Electron microprobe and *in situ* trace element analyses

Electron microprobe were carried out with the same setup as described in section II.3. Minor and trace element analyses were performed by femtosecond laser ablation ICP-MS (fs-LA-ICP-MS), using a fast scanning sector field ICP-MS (ThermoScientific Element XR®) that is connected to the fs-LA system described in section I.3.1. Note that major elements (i.e. Fe, Mg, Si) were also analyzed by fs-LA-ICP-MS (simultaneously to the trace element analyses; Table IV.1). Concentration data for Fe-Mg, Ca, Mn and Ni obtained by fs-LA-ICP-MS are identical to those acquired by EMP analyses within analytical uncertainties (Fig. A-IV.1 in Appendix IV). Sample ablation was performed by spot analyses with a spot diameter between 30 µm and 50 µm. Laser repetition rate was 8-10 Hz. Each analysis started with a 30 second background acquisition, followed by an ablation interval of 40-60 seconds. The Element XR® ICP-MS was equipped with a Ni "Jet" sample cone and either a Ni "X" or a Ni "H" skimmer cone and it was tuned to maintain low oxide production levels (<0.4% ThO); it was operated in "accuracy mode" setting the mass window to 25% with 20 samples per peak. With this acquisition protocol, one sweep for 22 elements (from ^{7}Li to ^{178}Hf, Table IV.1) takes ~1.5 s. Elements yielding high total count rates (i.e., 10^6 – 10^8 counts per second; Mg, Fe, Mn, Si) were analyzed in the Analog detection mode, elements yielding total count rates $<10^6$ cps were measured using the Counting detection mode of the Element XR®. External calibration of the acquired data was performed using the USGS reference glasses BCR-2G and BIR-1G with the preferred values reported in the GeoReM database (Jochum et al., 2005a), and ^{29}Si was used for internal standardization. Data reduction was performed with the Lotus-based spreadsheet program LAMTRACE (Jackson, 2008), which also automatically calculates the lower limit of detection (LLD) for each analysis using the algorithm developed by Longerich et al. (1996). Based on repeated analyses over a period of 1 year, the external reproducibility of the measured element concentrations in the basaltic reference glasses is typically better than 7% (relative standard deviation, n ≥ 83), except for

Li, Cr, Nb, Hf and the REE which have analytical uncertainties <20% (RSD; Table A-IV.2 in Appendix IV). However, during a single analytical session (1 day) the reproducibility of the measured element concentrations is usually much better (<3%, RSD), except for Li, Cr, Nb, Hf and the REE (<10%, RSD). These latter analytical uncertainties are probably more appropriate than the long term uncertainties to define the relative uncertainties of element concentration profiles across an olivine crystal, which always were performed within one analytical session (one day).

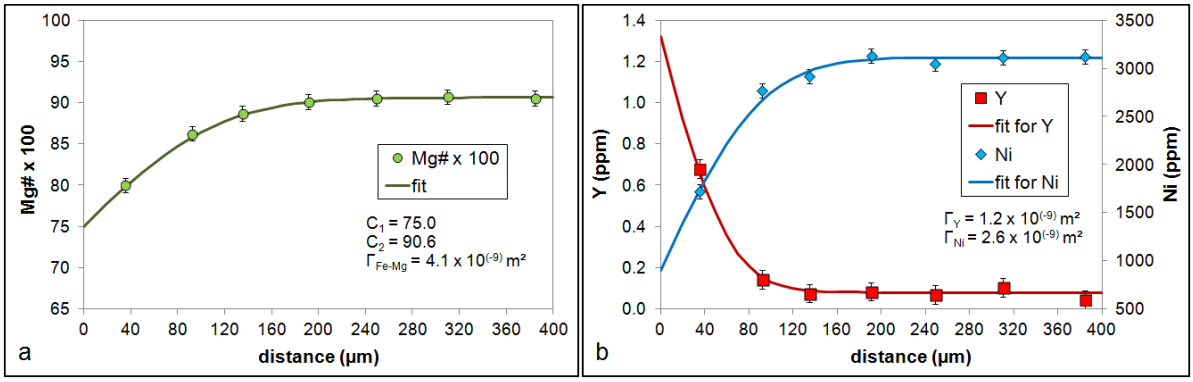

Figure IV.1: Examples of fitted diffusion profiles in an olivine xenocryst from the Massif Central (sample BdOr-1 olivine 2). Error bars represent 2 SD based on replicate analyses of basaltic reference glasses (BIR-1G and BCR-2G) during a single analytical session.

IV.3.2 Estimation of comparative diffusion coefficients in olivines

Similar to the approach used by Qian et al. (2010), we estimated diffusion coefficients of minor and trace elements relative to Fe-Mg in natural olivines, as follows. The Mg# of every analyzed spot was calculated based on the Fe and Mg concentrations measured by fs-LA-ICP-MS. Assuming one-dimensional diffusion into (or out of) a semi-infinite medium, the obtained Fe-Mg (i.e., Mg#) diffusion profile was reproduced using the following equation, which is based on Eqn. 3.13 in Crank (1975):

$$C = C_1 + (C_2 - C_1) \times \mathrm{erf}\left(\frac{x}{2 \times \sqrt{\Gamma}}\right)$$

(Eqn. IV.1)

where C_1 is the concentration (or Mg#) at the olivine surface, C_2 is the concentration in the olivine core, x is the distance in m, and Γ represents the product of diffusion coefficient and

time ($D{\cdot}t$; e.g. Ganguly, 2002). The observed Mg# diffusion profile is then fitted simply by adjusting C_1, C_2 and Γ (Fig. IV.1a). Hence, for each olivine investigated in this study, we receive a characteristic value for $\Gamma_{\text{Fe-Mg}}$, which ranges between $7.0{\cdot}10^{(-10)}$ m² and $1.7{\cdot}10^{(-8)}$ m² for our sample suite. In a next step, the diffusion profiles of trace elements are also fitted by using Eqn. 1 and adjusting C_1, C_2 and Γ (Fig. IV.1b), thus yielding values for Γ_{M} (where M is e.g. Y) for each investigated olivine. For a single olivine, we assume that the duration of the diffusive flux t is the same or very similar for all elements. Therefore, if $\Gamma = D{\cdot}t$, we can infer that

$$\frac{\Gamma_{\text{M}}}{\Gamma_{\text{Fe-Mg}}} \cong \frac{D_{\text{M}}}{D_{\text{Fe-Mg}}}$$

(Eqn. IV.2)

Thus, we receive diffusion rates of trace elements relative to that of Fe-Mg inter-diffusion in olivine (Table IV.2).

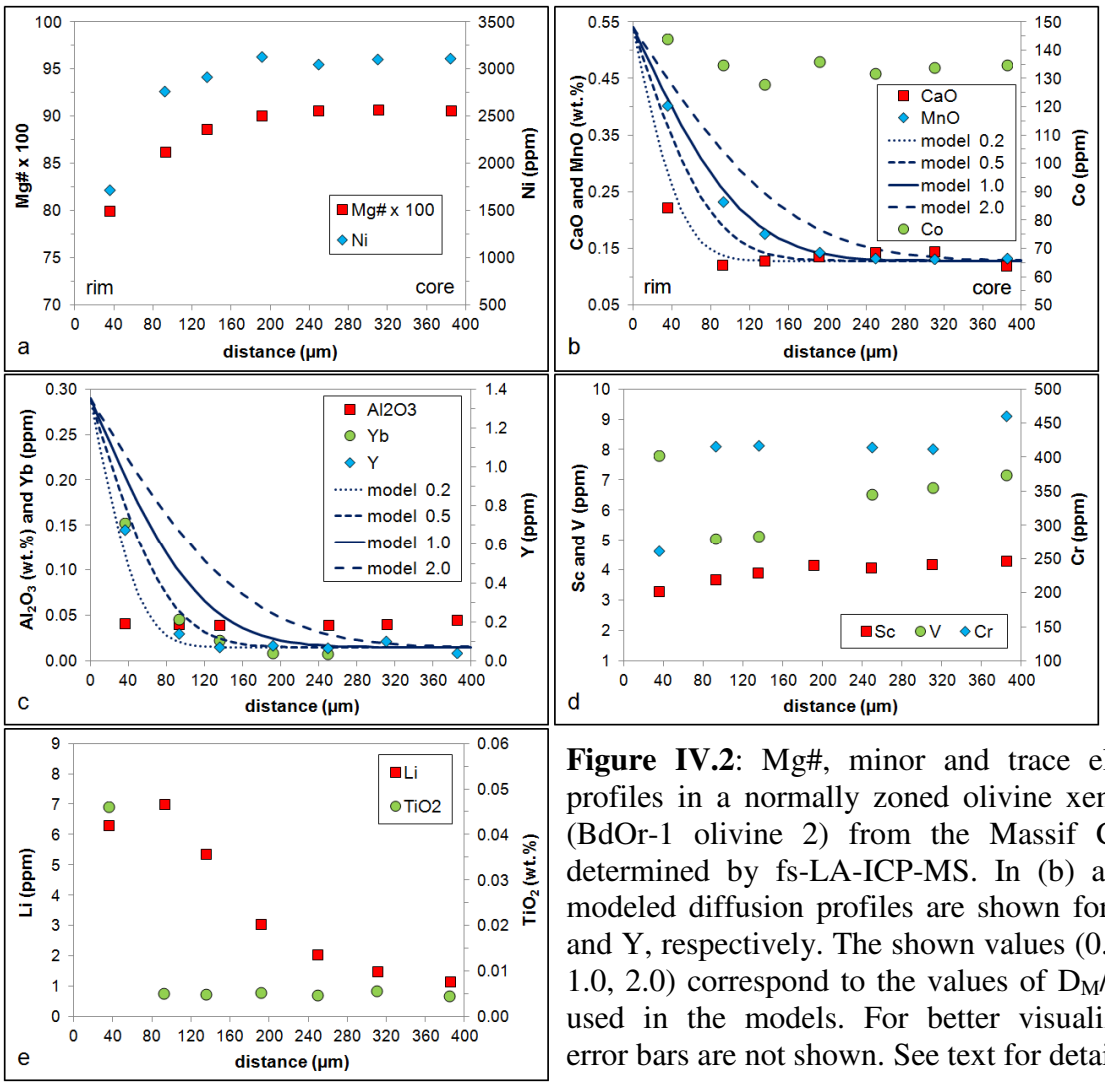

Figure IV.2: Mg#, minor and trace element profiles in a normally zoned olivine xenocryst (BdOr-1 olivine 2) from the Massif Central determined by fs-LA-ICP-MS. In (b) and (c) modeled diffusion profiles are shown for MnO and Y, respectively. The shown values (0.2, 0.5, 1.0, 2.0) correspond to the values of $D_M/D_{Fe\text{-}Mg}$ used in the models. For better visualization, error bars are not shown. See text for details.

IV.4 Results and Discussion

IV.4.1 Trace element profiles across natural olivines

Minor and trace element profiles were acquired for 17 olivine crystals (phenocrysts and xenocrysts in Massif Central basanites and phenocrysts in MORBs from the MAR) which mostly show normal zoning in Mg# based on previous EMP analyses. Only one olivine (332A-9 ol 1) exhibits reverse zoning in terms of Mg#. Similar to Mg#, the zoning of several minor and trace elements (e.g., Li, Ca, Sc, Cr, Mn, Ni, Y, Yb) is also quite pronounced, and for some elements general tendencies for the concentration gradients between core and rim of the crystals can be outlined. In most cases, the cores of the olivines show higher concentrations of Sc, Cr, Ni (and Mg) than the rims (Fig. IV.2 and IV.3), indicating that these elements have diffused out of olivine. Based on olivine/melt partition coefficients (K_M) acquired by Kennedy et al. (1993), Beattie (1994) and Spandler and O'Neill (2010) in experimental studies, Sc represents a moderately incompatible and Cr a slightly incompatible or even compatible element, while Mg and Ni are the most compatible elements in olivine (Fig. IV.4). Among the elements commonly occurring as trivalent cations, Sc and Cr represent the most compatible ones in olivine. The relatively good compatibility of Sc^{3+} and Cr^{3+} is likely a consequence of their ionic radii, i.e. Sc^{3+} (effective ionic radius of 0.745 Å in sixfold coordination; Shannon, 1976) is only slightly larger than Mg^{2+} (0.72 Å), while Cr^{3+} (0.615 Å) is somewhat smaller than Ni^{2+} (0.69 Å, Table IV.1). Furthermore, Cr can also occur as Cr^{2+} with an effective ionic radius of 0.80 Å (Shannon, 1976) which is similar to that of the divalent Fe cation (0.78 Å). Thus, the polyvalence of Cr may potentially contribute to the relatively good compatibility of Cr in olivine.

The diffusion of Cr, Ni and Mg out of olivine is consistent with a relative depletion of these elements in the basaltic / basanitic melt during magma differentiation, e.g., by (fractional) crystallization of olivine, clinopyroxene (cpx), and spinel group minerals (SGMs) as Cr, Ni and Mg are regarded as compatible elements in these phases. The diffusion of Sc out of olivine is less clear, given the moderately incompatible nature of Sc. However, Sc is reported to be compatible in clinopyroxene and in magnetite (Gallahan and Nielsen, 1992; Hart and Dunn, 1993; Nielsen et al., 1994). Thus, crystallization of SGMs, especially of the magnetite series, along with clinopyroxene and olivine may lead to a relative depletion of Sc in the melt during magma differentiation, which may cause diffusion of Sc from olivine into the melt. Alternatively, the incorporation of Sc^{3+} and Cr^{3+} into olivine may be coupled as a $(Fe,Mg)ScCrO_4$ component (cf. Qian et al., 2010). This would imply (i) a correlation of Sc

and Cr contents (which is true for only 2 of the 17 investigated olivines) and (ii) that the diffusion rates of both elements are very similar (which is, however, not the case; see section IV.4.2 and Table IV.2).

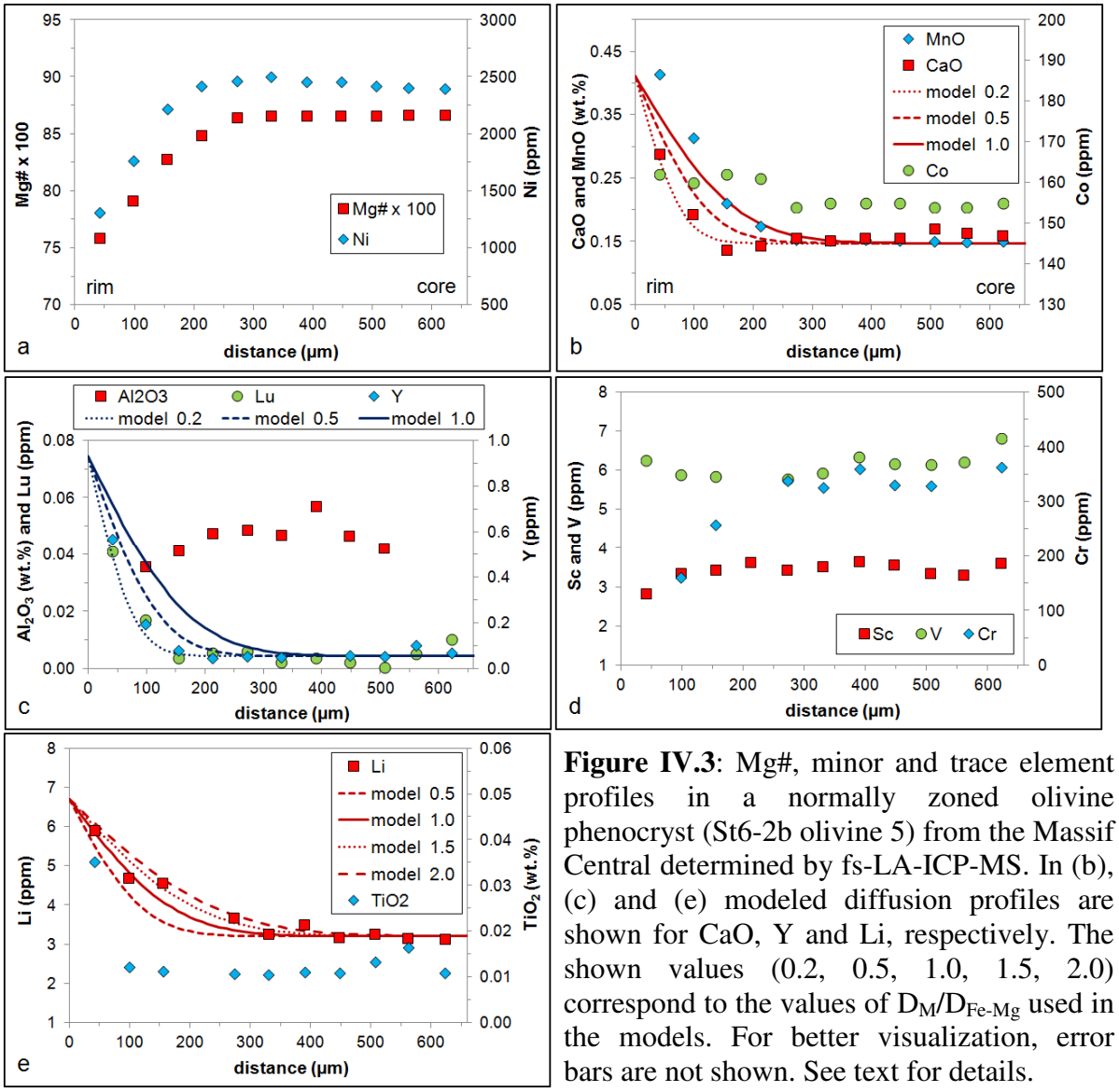

Figure IV.3: Mg#, minor and trace element profiles in a normally zoned olivine phenocryst (St6-2b olivine 5) from the Massif Central determined by fs-LA-ICP-MS. In (b), (c) and (e) modeled diffusion profiles are shown for CaO, Y and Li, respectively. The shown values (0.2, 0.5, 1.0, 1.5, 2.0) correspond to the values of $D_M/D_{Fe\text{-}Mg}$ used in the models. For better visualization, error bars are not shown. See text for details.

The rims of the olivines usually have higher concentrations of Li, Ca, Ti, Mn, Co, Y, Yb (and Fe) than the cores (Fig. IV.2 and IV.3), indicating that these elements have diffused into olivine. Because of its large ionic radius (1.00 Å, Table IV.1) Ca^{2+} is highly incompatible in olivine, i.e. $10^{-2} < K_{Ca} < 10^{-1}$ (Fig. IV.4; e.g., Beattie, 1994; Kennedy et al., 1993; Spandler

and O'Neill, 2010), in contrast to the other divalent cations of this group, i.e., Mn, Co, Fe which are either only slightly incompatible (Mn, $K_{Mn} \approx 0.8$) or compatible (Fe and Co, $1 < K_M < 4$, Fig. IV.4). The trivalent cations of Y and Yb have large ionic radii (0.90 Å and 0.87 Å, respectively) and are highly incompatible (Fig. IV.4). Of the two octahedral sites (M1 and M2) in the olivine structure, only the larger M2 site appears to be suitable to accommodate such large cations (e.g., Brown, 1982). In contrast, medium-sized and more compatible cations, such as Mn and Co, can be distributed over both octahedral sites (Spandler and O'Neill, 2010, and references therein). Likewise, Li is only moderately incompatible, probably due to the ionic radius of Li^{1+} (0.76 Å) which is very similar to that of Co^{2+} (0.745 Å). Finally, Ti is usually incorporated into a crystal structure as Ti^{4+}, which has relatively small ionic radii of 0.605 Å in sixfold coordination and of 0.42 Å in fourfold coordination (Shannon, 1976). As pointed out in previous studies (e.g., Berry et al., 2007; Hermann et al., 2005; Spandler and O'Neill, 2010), Ti (as Ti^{4+}) may substitute for Si in the tetrahedral site of the olivine structure, and it can occupy an octahedral site (i) as Ti^{3+} if another trivalent cation (e.g. Al^{3+}) substitutes for Si^{4+} in the tetrahedral site or (ii) as Ti^{4+} if it is charge-balanced by a vacancy in an octahedral site. Despite these potential, multiple substitution mechanisms, Ti appears to be a highly incompatible element in olivine (Fig. IV.4).

The diffusion of incompatible elements such as Li, Ca, Ti, Mn, Y, Yb into olivine is consistent with a relative enrichment of these elements in the basaltic / basanitic melt during magma differentiation. Likewise, the strong chemical disequilibrium between mantle olivines (xenocrysts) and the basanitic host melt likely generated a diffusive flux of incompatible elements from the melt into these olivines. Interestingly, the element Co, commonly considered as compatible in olivine (e.g., Beattie, 1994), also shows small enrichment in the rims of olivine crystals compared to their cores (up to 10% in phenocrysts and between 16% and 35% in xenocrysts), indicating diffusion of Co into olivine during magma differentiation or upon the entrainment of mantle olivines. Thus, Co was apparently enriched during magma evolution in most investigated basalts to a comparable extent as Fe.

For other elements investigated in this study general tendencies cannot be derived, either because the concentrations in olivine are beneath or close to the detection limit (e.g. for the extremely incompatible elements Zr, Hf, Nb, Gd), or because the profile shapes of individual elements vary considerably from one olivine to another (e.g. Al, V), i.e. we observed flat concentration profiles as well as ambiguous intra-mineral variations, but in some cases also apparently diffusion-generated zoning (especially for V). The ambiguous intra-mineral

variations in Al concentration may be the result of hitting small melt inclusions in olivine during the laser ablation analyses. For V, variable directions of diffusion (or even flat concentration profiles) are likely related to the occurrence of V in variable oxidation states (V^{2+}, V^{3+}, V^{4+} and V^{5+}). Hence, the compatibility of V in olivine – as well as its diffusion rate (see section IV.4.2) – is probably strongly redox-controlled. The variability in the profile shapes of Al probably results from the very low diffusion rate of Al in olivine, which was determined to be orders of magnitude lower than that of Fe-Mg (Spandler et al., 2007; Spandler and O'Neill, 2010). Evans et al. (2008) suggested that the incorporation of Al^{3+} into olivine is coupled as a $(Fe,Mg)Al^{[IV]}Al^{[VI]}O_4$ component with a high degree of short-range order between tetrahedral and octahedral Al. In this case, the slow diffusion of Al in olivine would essentially be the result of the slow diffusion in tetrahedral sites (Spandler and O'Neill, 2010). Therefore, if intra-mineral variations of Al contents are observed, these likely reflect the preservation of igneous zoning (Spandler et al., 2007).

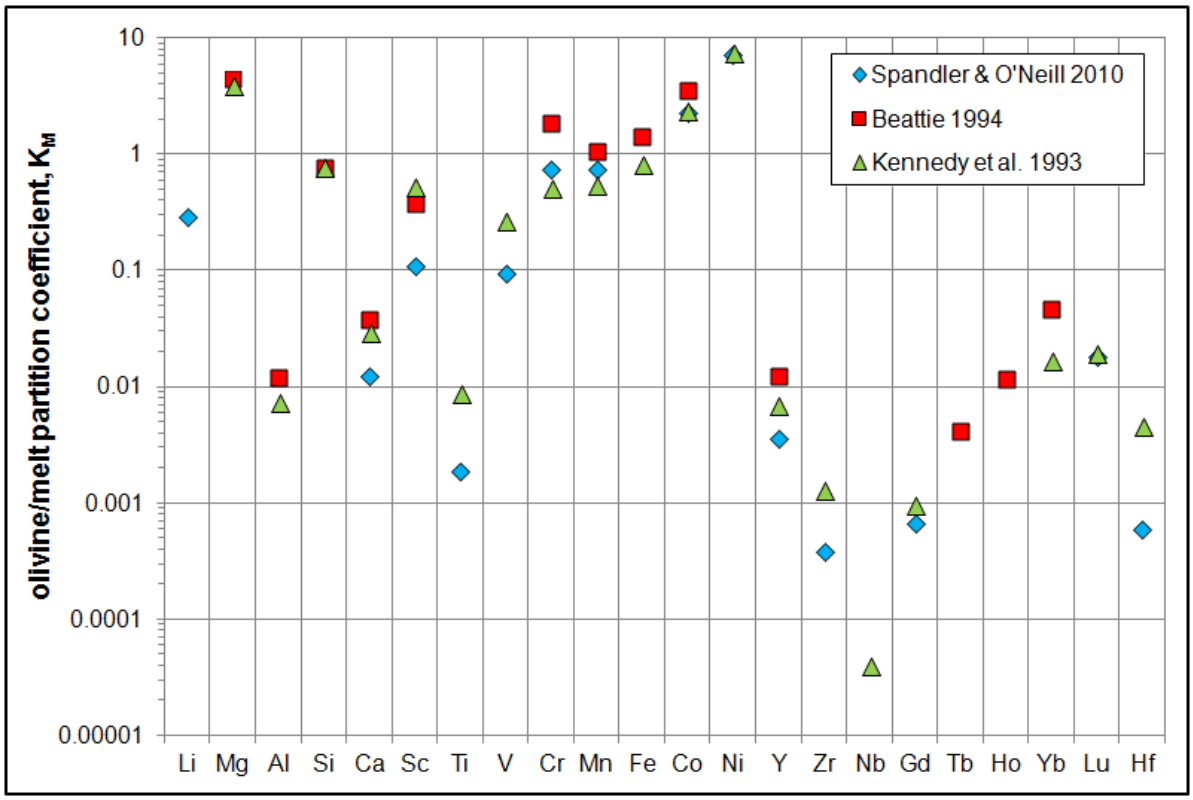

Figure IV.4: Experimentally determined olivine / silicate melt partition coefficients for major and trace elements reported in the literature. We show data (i) for experimental run "BO 67" with a minimum temperature of 1200°C as reported in Kennedy et al. (1993), and (ii) for experiment "B7" conducted at 1250°C as reported in Beattie (1994). Experiments by Spandler and O'Neill (2010) were performed at 1300°C.

IV.4.2 Diffusion rates of trace elements relative to Fe-Mg

In 9 out of the 17 olivines investigated in this study, the Fe-Mg chemical zoning was mainly generated by chemical diffusion, as deduced from Fe-Mg isotopic profiles and a negative correlation between δ^{26}Mg and δ^{56}Fe (see chapters II and III). Hence, it is likely that the observed zoning of many trace elements in these olivines was also essentially generated by diffusive processes. For the other 8 olivines Fe-Mg isotopic profiles have not been acquired; therefore, direct evidence for diffusion-controlled chemical zoning is lacking. One of these olivines is a xenocryst which was very likely affected by diffusive re-equilibration as it was probably never in chemical equilibrium with its host melt. Furthermore, as the majority of zoned olivines from our sample suite shows clear signatures of Fe-Mg inter-diffusion, it may be assumed that chemical diffusion represents the governing process for generating the trace element zoning in most cases.

In general, our estimations of the relative diffusion coefficients for Li, Ca, Sc, Mn, Co, Ni, and Y in olivine are consistent with the findings of the studies by Qian et al. (2010) and Spandler and O'Neill (2010). Results are given in Table IV.2 and Figure IV.5.

Li appears to diffuse faster than Fe-Mg (by a factor of ~1.7). The diffusion of Li in olivine has been investigated experimentally by Dohmen et al. (2010), who showed that two diffusion mechanisms may operate simultaneously for Li. As summarized by e.g. Chakraborty (2010), Li appears to be incorporated in olivine in vacant octahedral sites as well as in interstitial sites. The diffusion within interstitial sites is >5 orders of magnitude faster than Fe-Mg diffusion in olivine; however, it is an unlikely mechanism for most natural systems (Dohmen et al., 2010) because rather unusual boundary conditions (e.g., high fO_2, very high Li concentration at the olivine surface) are needed to activate this mechanism. Hence, the diffusion rate of Li in natural olivine is mainly controlled by the slower mechanism (in the octahedral sites), which may be up to three orders of magnitude faster than Fe-Mg inter-diffusion (Dohmen et al., 2010).

Average diffusion rates of **Mn** and **Co** appear to be quite similar and they are somewhat smaller (by a factor of ~1.25) than that of Fe-Mg; however, the estimated relative diffusion coefficients of Co show strong variations (RSD ≈ 60%, n = 10). The similarity in diffusion rates of Mn, Co, Fe and Mg is not surprising as these divalent cations are more or less randomly distributed over both octahedral sites (M1 and M2) in the olivine structure, due to their similar ionic radii (Fig. IV.5; cf. Spandler and O'Neill, 2010).

Ni seems to diffuse slower than Fe-Mg (by a factor of ~1.6), which is consistent with the results presented in Petry et al. (2004), Qian et al. (2010) and Spandler and O'Neill (2010).

The latter have attributed this finding to the ordering of Ni^{2+} preferentially into the smaller M1 site. It has been postulated that the density of diffusion pathways through a crystal (and thus the diffusion rate of a certain element) is reduced by a high degree of ordering (Spandler and O'Neill, 2010).

$\mathbf{D_{Ca}}$ and $\mathbf{D_{Sc}}$ are distinctly smaller than $D_{Fe\text{-}Mg}$ (by a factor of ~2-4). **Y** and **Yb** appear to have very similar diffusion rates, which are also considerably lower (by a factor of 2-3) than that of Fe-Mg, but still much faster than those determined for REE in olivine by Cherniak (2010) and Remmert et al. (2008). The relatively low diffusion coefficients of Ca, Y and Yb determined in our study is likely caused by the preference of their relatively large cations for the larger M2 site. As mentioned above, such high degree of ordering probably limits the diffusion rate of an element. In contrast to Ca^{2+} and Y^{3+}, Sc^{3+} is probably small enough to be evenly distributed over both octahedral sites (e.g., Evans et al., 2008), thus facilitating a faster diffusion of Sc in olivine (Fig. IV.5). In general, the incorporation of any trivalent cation in olivine has to be charge-balanced. As described in previous studies (e.g., Evans et al., 2008; Nielsen et al., 1992), this charge balance is very likely achieved by the incorporation of vacancies in octahedral sites, with the following endmembers, for example: $Y[Mg_{1/2}vac_{1/2}]SiO_4$ or $(Sc_{2/3}vac_{1/3})_2SiO_4$. If such a substitution mechanism typically operates, the diffusion rate of trivalent cations in olivine would be mainly controlled by the diffusion of vacancies (which is very fast; e.g., Chakraborty, 2010) and/or by the diffusion rate of the two major divalent cations in olivine, Fe^{2+} and Mg^{2+}. This may be an explanation for the overall similarity in diffusion rates of trivalent and divalent cations observed in this study, which is in contrast to some previous studies where trivalent cations (e.g., Cr, REE) have been found to diffuse orders of magnitude slower than Fe-Mg (Ito and Ganguly, 2006; Remmert et al., 2008; Cherniak, 2010).

Furthermore, our investigations provide relative diffusion coefficients for Ti, V and Cr (Table IV.2, Fig. IV.5). V and Cr appear to have similar diffusion rates and diffuse slightly slower than Fe-Mg (by a factor of ~1.3). For **V**, this is in some contrast to the findings of previous studies where D_V was calculated to be equal to $D_{Fe\text{-}Mg}$ (along the crystallographic a- and b-axes; Spandler and O'Neill, 2010) or even one order of magnitude higher than $D_{Fe\text{-}Mg}$ (along the c-axis; Qian et al., 2010; Spandler and O'Neill, 2010). We note that our estimated relative diffusion coefficients for V are quite variable (RSD ≈ 65%, n = 10). However, there is no systematic dependence of $D_V/D_{Fe\text{-}Mg}$ upon the crystallographic orientation of the analyzed profiles (see below). As already pointed out by Spandler and O'Neill (2010),

investigating the diffusive behavior of V is rather complicated as the latter can occur in various redox states (V^{2+}, V^{3+}, V^{4+} and V^{5+}). As element diffusivity in olivine appears to be controlled by various parameters (e.g., T, P, fO_2, vacancy concentration; e.g., Chakraborty, 2010), the diffusion rate of V may be strongly redox-controlled, i.e. depend on the oxidation state of V dominating at the respective redox conditions. Hence, it is not surprising that there are some discrepancies between the different studies investigating diffusion rates of V in olivine. For example, Spandler and O'Neill (2010) performed their diffusion experiments at FMQ-1 and found diffusion rates of V that are more or less comparable to those of Fe-Mg. In contrast, for the natural olivine xenocryst investigated by Qian et al. (2010), fO_2 was assumed to be at FMQ+1 and D_V was estimated to be orders magnitude larger than $D_{Fe\text{-}Mg}$.

For **Cr**, Qian et al. (2010) postulated a coupled substitution of Cr^{3+} and Al^{3+} for M^{2+} and Si^{4+} (where M is Mg or Fe) in the olivine structure. We have not found any clear evidence for this substitution mechanism in our sample suite, as the concentration profiles of Cr and Al are not correlated with each other in most cases and Al appears to diffuse much slower than Cr. The relatively fast diffusion rate of Cr observed in this study may be attributed to its polyvalence, allowing its cations to occupy both octahedral sites in the olivine structure: the relatively small Cr^{3+} likely prefers the smaller M1 site, while Cr^{2+} (similar to Fe^{2+}) may occupy both M1 and M2. Thus, the density of possible diffusion pathways for Cr is increased, expediting the diffusion of Cr through olivine (cf., Spandler and O'Neill, 2010). Note that, as shown by Spandler and O'Neill (2010), at FMQ-1 Cr may be present in olivine as 40% Cr^{2+} and 60% Cr^{3+}.

Ti represents a slowly diffusing element in olivine (compared to most other trace elements investigated herein) as the average diffusion coefficient of Ti (relative to Fe-Mg) was estimated to be 0.27. If Ti is mainly incorporated into olivine as Ti^{4+} on the tetrahedral site, its diffusion would be controlled by the slow diffusion of Si^{4+} in olivine, which is orders of magnitude slower than Fe-Mg inter-diffusion (e.g., Chakraborty, 2010; Dohmen et al., 2002). Although we observe relatively slow diffusion of Ti in our olivines, the obtained relative diffusion coefficients $D_{Ti}/D_{Fe\text{-}Mg}$ are too large to be simply explained by diffusion of Ti^{4+} from one tetrahedral site to another. As mentioned in section IV.4.1 and already described in Spandler and O'Neill (2010), Ti^{3+} may substitute for a divalent cation in the octahedral site if another trivalent cation (e.g. Al^{3+}) substitutes for Si^{4+} in the tetrahedral site, thus opening another diffusion pathway for Ti in olivine. This may be an explanation for the here observed relatively high diffusion rate of Ti compared to what is expected for Si. Alternatively, if Ti^{4+} substitutes into an octahedral site (charge-balanced by a vacancy in the

other octahedral site), its diffusion behavior (and rate) may be similar to that of trivalent cations.

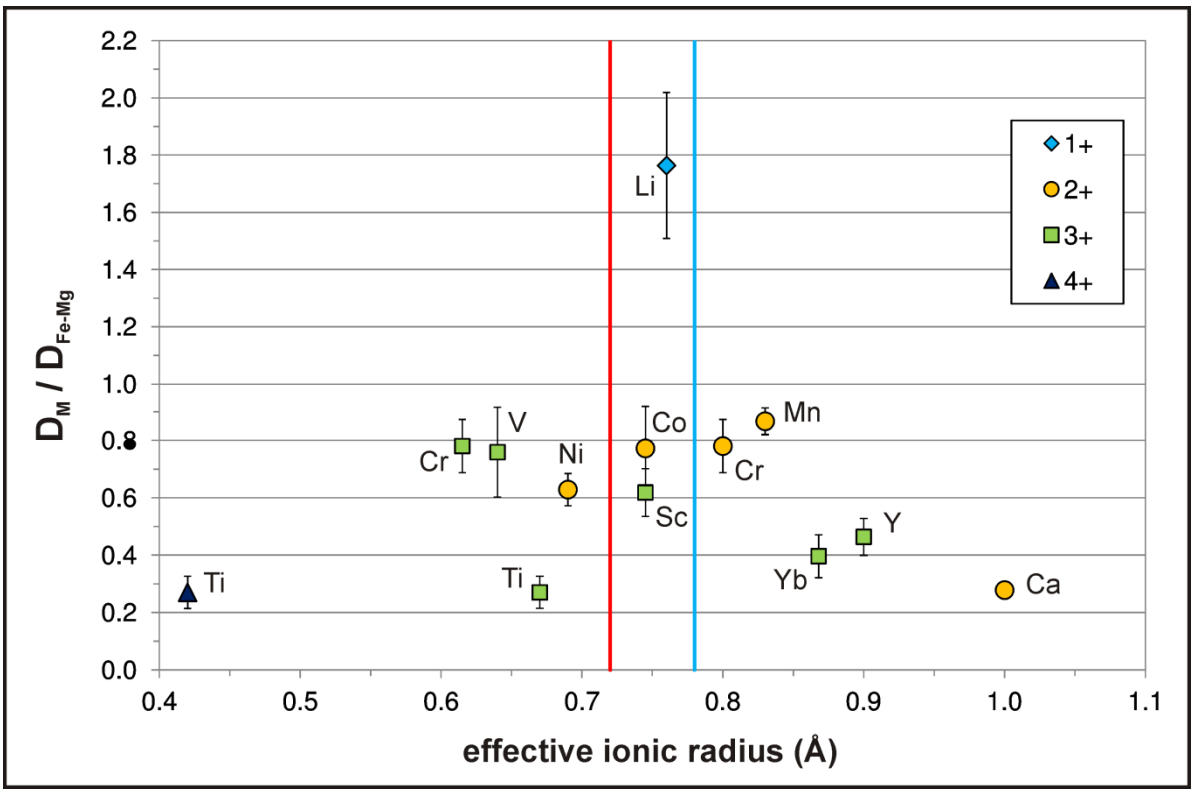

Figure IV.5: Diffusion coefficients of minor and trace elements relative to that of Fe-Mg inter-diffusion versus effective ionic radius. Ionic radii are given for sixfold coordination, except for Ti^{4+} (fourfold coordination), as reported in Shannon (1976). Error bars represent one standard error, based on 7-17 measurements of the D_M/D_{Fe-Mg} value for each element. The blue line and the red line show the effective ionic radii of Fe^{2+} and Mg^{2+} (sixfold coordination), respectively.

Similar to Qian et al. (2010) we have also checked whether there is any dependence of D_M/D_{Fe-Mg} upon the orientation of the analyzed profile relative to the crystallographic axes of the olivines. Such a dependence would be expected for an element whose diffusion behavior is different from that of Fe-Mg, e.g. findings of the study by Spandler and O'Neill (2010) indicate that the diffusion of REE in olivine is isotropic while that of Fe-Mg (and many other elements; e.g., Chakraborty, 2010) is anisotropic. However, in contrast to the observations made by Qian et al. (2010) for D_M/D_{Mn}, we cannot find any systematic dependence of D_M/D_{Fe-Mg} upon the crystallographic orientation of the analyzed profiles, given the uncertainties of the D_M/D_{Fe-Mg}-values determined in this study (RSE 5-21%, Table IV.2).

IV.5 Conclusions

In this study, comparative diffusion coefficients of 11 minor and trace elements relative to Fe-Mg in olivine were determined, based on concentration profiles of these elements across 17 natural, chemically zoned olivine pheno- and xenocrysts. Our findings indicate that many cations diffuse through olivine at similar rates. Although differences in the diffusion rates of the fastest (Li, Fe-Mg) and the slowest (Ti, Ca) elements certainly exist, this variation does not exceed one order of magnitude. Exceptions may be Al and other small cations, such as Si^{4+} or P^{5+}, that are preferably incorporated into tetrahedral sites in olivine (Spandler and O'Neill, 2010). Finally, this study confirms that diffusion rates of trace elements in olivine determined in experimental studies (e.g., Dohmen et al., 2010; Petry et al., 2004; Spandler and O'Neill, 2010) are comparable to those observed for olivines in natural samples (Qian et al., 2010; and this study).

IV. Tables

Table IV.1: List of elements analyzed in this study with common oxidation states, ionic radii, and literature data of olivine/melt partition coefficients (K_M)

element	isotopic mass analyzed	common oxidation state(s)	oxidation state assumed	coordination number	effective ionic radius (Å) [a]	K_M Spandler & O'Neill 2010 (1300°C)	K_M Beattie 1994 "B7" (1250°C)	K_M Kennedy et al. 1993 "BO 67" (1200°C)
Li	7	1	1	6	0.760	2.9E-01		
Mg	25	2	2	6	0.720		4.4E+00	4.0E+00
Al	27	3	3	4, 6	0.390, 0.535		1.2E-02	7.4E-03
Si	29	4	4	4	0.260		7.7E-01	7.8E-01
Ca	43	2	2	6	1.000	1.3E-02	3.8E-02	3.0E-02
Sc	45	3	3	6	0.745	1.1E-01	3.8E-01	5.3E-01
Ti	47	3, 4	4	4	0.420	1.9E-03		9.0E-03
V	51	2-5	3	6	0.640	9.4E-02		2.7E-01
Cr	53	2, 3	3	6	0.615	7.5E-01	1.9E+00	5.2E-01
Mn	55	2, 3, 4	2	6	0.830	7.5E-01	1.1E+00	5.5E-01
Fe	57	2, 3	2	6	0.780		1.4E+00	8.4E-01
Co	59	2, 3	2	6	0.745	2.3E+00	3.6E+00	2.4E+00
Ni	60	2, 3	2	6	0.690	7.2E+00		7.6E+00
Y	89	3	3	6	0.900	3.6E-03	1.3E-02	7.0E-03
Zr	90	4	4	4, 6	0.590, 0.720	3.8E-04		1.3E-03
Nb	93	3, 5	5	4, 6	0.480, 0.640			4.1E-05
Gd	157	3	3	6	0.938	6.7E-04		9.9E-04
Tb	159	3, 4	3	6	0.923		4.2E-03	
Ho	165	3	3	6	0.901		1.2E-02	
Yb	172	2, 3	3	6	0.868		4.7E-02	1.7E-02
Lu	175	3	3	6	0.861	1.8E-02		2.0E-02
Hf	178	4	4	4, 6	0.580, 0.710	6.0E-04		4.6E-03

[a] effective ionic radii are from Shannon (1976)

Table IV.2: Comparative diffusion coefficients relative to Fe-Mg (i.e., $D_M/D_{Fe\text{-}Mg}$)

location	sample	olivine	type	Li	Ca	Sc	Ti	V	Cr	Mn	Co	Ni	Y	Yb (or Lu)	evidence of Fe-Mg inter-diffusion?	$(\cos\gamma)^2$ [b]
Massif Central	BdOr-1	ol 2	xenocryst	2.07	0.22	0.80	0.17	-	0.24	0.85	0.44	0.63	0.29	0.54	yes	0.70
Massif Central	BdOr-1	olxen 1	xenocryst	0.53	0.26	-	-	-	0.86	0.53	0.66	0.99	0.43	-	yes	0.96
Massif Central	BdOr-1	olxen 2	xenocryst	1.06	0.26	-	-	0.75	0.75	0.81	0.75	0.50	0.40	-	yes	0.04
Massif Central	St3-3a	ol 1	phenocryst	2.78	0.39	0.56	-	0.22	0.89	0.78	-	0.67	0.44	-	yes	0.11
Massif Central	St3-3a	olxen 1	xenocryst	-	-	-	-	1.19	-	0.75	0.75	0.63	0.50	0.63	yes	0.89
Massif Central	St4-1a	ol 2	phenocryst	1.52	0.24	0.28	0.20	-	-	0.80	-	0.96	0.44	0.24	yes	0.75
MAR [a]	332A-9	ol 1	phenocryst	-	0.19	0.38	0.54	1.04	0.40	1.04	0.75	0.46	-	0.63	yes	0.00
MAR	396B-9	ol 1	phenocryst	-	-	-	0.44	-	-	1.12	0.85	0.22	1.22	-	yes	0.86
MAR	396B-9	ol 3	phenocryst	-	-	-	0.12	0.38	0.96	0.87	0.69	0.90	-	-	yes	0.49
MAR	396B-12	ol 1b	phenocryst	-	-	-	0.36	-	1.29	-	-	0.43	0.71	-	yes	0.25
MAR	396B-14-1	ol 2	phenocryst	2.00	-	0.93	-	0.23	-	1.30	-	0.53	0.20	-	no	0.00
Massif Central	BdOr-1	ol 1	phenocryst	1.61	0.32	0.97	-	0.81	-	0.97	-	0.65	0.58	-	no	0.00
Massif Central	St3-3a	ol 2	phenocryst	2.89	0.24	0.56	-	1.78	0.67	0.89	2.00	0.44	0.51	0.18	no	0.03
Massif Central	St3-3b	ol 2	xenocryst	-	0.29	-	-	-	-	0.71	0.50	0.97	0.35	0.21	no	-
Massif Central	St6-2b	ol 4a	phenocryst	-	0.21	0.71	-	0.86	-	1.00	-	0.29	0.30	-	no	0.64
Massif Central	St6-2b	ol 4b	phenocryst	-	0.44	-	0.22	0.33	0.89	0.72	0.33	0.72	0.29	0.37	no	0.04
Massif Central	St6-2b	ol 5	phenocryst	1.41	0.26	0.38	0.12	-	0.87	0.74	-	0.71	0.28	-	no	0.88
			mean	**1.76**	**0.28**	**0.62**	**0.27**	**0.76**	**0.78**	**0.87**	**0.77**	**0.63**	**0.46**	**0.40**		
			RSD (%)	43.3	26.8	40.6	58.2	65.1	37.6	21.5	59.7	36.9	53.4	49.7		
			RSE (%)	14.4	7.7	13.5	20.6	20.6	11.9	5.4	18.9	8.9	13.8	18.8		
			median	1.61	0.26	0.56	0.21	0.78	0.86	0.83	0.72	0.63	0.43	0.37		

[a] MAR represents Mid-Atlantic Ridge

[b] γ represents the angle between the orientation of the measured profile relative to the c-axis of the olivine (Costa & Chakraborty, 2004); therefore, if $(\cos\gamma)^2=1$, the profile runs perfectly parallel to the c-axis.

dashes: not determined

References

Alt J. C., Kinoshita H., Stokking L. B. and et al. (1993) 3. Site 896. *Proc. Ocean Drill. Program, Initial Reports* **148**, 123–192.

Anbar A. D. and Rouxel O. (2007) Metal Stable Isotopes in Paleoceanography. *Annu. Rev. Earth Planet. Sci.* **35**, 717–746.

Armienti P., Innocenti F., Pareschi M. T., Pompilio M. and Rocchi S. (1991) Crystal Population Density in not Stationary Volcanic Systems: Estimate of Olivine Growth Rate in Basalts of Lanzarote (Canary Islands). *Mineral. Petrol.* **44**, 181–196.

Arnold G. L., Anbar A. D., Barling J. and Lyons T. W. (2004a) Molybdenum isotope evidence for widespread anoxia in mid-Proterozoic oceans. *Science* **304**, 87–90.

Arnold G. L., Weyer S. and Anbar A. D. (2004b) Fe isotope variations in natural materials measured using high mass resolution multiple collector ICPMS. *Anal. Chem.* **76**, 322–327.

Asimow P. D. and Ghiorso M. S. (1998) Algorithmic modifications extending MELTS to calculate subsolidus phase relations. *Am. Mineral.* **83**, 1127–1132.

Aumento F., Melson W., Bougault H., Dmitriev L., Fischer J., Flower M., Hall J., Howe R., Hyndman R., Miles G., Robinson P. and Wright T. (1974) 2. Site 332. *Deep Sea Drill. Proj. - Initial Reports* **37**, 15–199.

Beard B. L. and Johnson C. M. (2004) Fe Isotope Variations in the Modern and Ancient Earth and Other Planetary Bodies. *Rev. Mineral. Geochemistry* **55**, 319–357.

Beattie P. (1994) Systematics and energetics of trace-element partitioning between olivine and silicate melts: Implications for the nature of mineral/melt partitioning. *Chem. Geol.* **117**, 57–71.

Berry A. J., Walker A. M., Hermann J., O'Neill H. S. C., Foran G. J. and Gale J. D. (2007) Titanium substitution mechanisms in forsterite. *Chem. Geol.* **242**, 176–186.

Bizzarro M., Baker J. A., Haack H. and Lundgaard K. L. (2005) Rapid Timescales for Accretion and Melting of Differentiated Planetesimals inferred from ^{26}Al-^{26}Mg Chronometry. *Astrophys. J.* **632**, L41–L44.

Bizzarro M., Paton C., Larsen K., Schiller M., Trinquier A. and Ulfbeck D. (2011) High-precision Mg-isotope measurements of terrestrial and extraterrestrial material by HR-MC-ICPMS—implications for the relative and absolute Mg-isotope composition of the bulk silicate Earth. *J. Anal. At. Spectrom.* **26**, 565-577.

Bourdon B., Tipper E. T., Fitoussi C. and Stracke A. (2010) Chondritic Mg isotope composition of the Earth. *Geochim. Cosmochim. Acta* **74**, 5069–5083.

Brearley M. and Scarfe C. M. (1986) Dissolution Rates of Upper Mantle Minerals in an Alkali Basalt Melt at High Pressure: An Experimental Study and Implications for Ultramafic Xenolith Survival. *J. Petrol.* **27**, 1157–1182.

Brown G. E. (1982) Olivines and Silicate Spinels. *Rev. Mineral.* **5**, 275–381.

Chakraborty S. (1997) Rates and mechanisms of Fe-Mg interdiffusion in olivine at 980°–1300°C. *J. Geophys. Res.* **102**, 12317–12331.

Chakraborty S. (2010) Diffusion Coefficients in Olivine, Wadsleyite and Ringwoodite. *Rev. Mineral. Geochemistry* **72**, 603–639.

Chapman J. B., Weiss D. J., Shan Y. and Lemburger M. (2009) Iron isotope fractionation during leaching of granite and basalt by hydrochloric and oxalic acids. *Geochim. Cosmochim. Acta* **73**, 1312–1324.

Cherniak D. J. (2010) REE diffusion in olivine. *Am. Mineral.* **95**, 362–368.

Coogan L. A., Hain A., Stahl S. and Chakraborty S. (2005) Experimental determination of the diffusion coefficient for calcium in olivine between 900°C and 1500°C. *Geochim. Cosmochim. Acta* **69**, 3683–3694.

Coogan L. A., Saunders A. D. and Wilson R. N. (2014) Aluminum-in-olivine thermometry of primitive basalts: Evidence of an anomalously hot mantle source for large igneous provinces. *Chem. Geol.* **368**, 1–10.

Costa F. and Chakraborty S. (2004) Decadal time gaps between mafic intrusion and silicic eruption obtained from chemical zoning patterns in olivine. *Earth Planet. Sci. Lett.* **227**, 517–530.

Costa F. and Dungan M. (2005) Short time scales of magmatic assimilation from diffusion modeling of multiple elements in olivine. *Geology* **33**, 837–840.

Costa F., Dohmen R. and Chakraborty S. (2008) Time Scales of Magmatic Processes from Modeling the Zoning Patterns of Crystals. *Rev. Mineral. Geochemistry* **69**, 545–594.

Costa F., Coogan L. A. and Chakraborty S. (2010) The time scales of magma mixing and mingling involving primitive melts and melt–mush interaction at mid-ocean ridges. *Contrib. to Mineral. Petrol.* **159**, 371–387.

Cottrell E. and Kelley K. A. (2011) The oxidation state of Fe in MORB glasses and the oxygen fugacity of the upper mantle. *Earth Planet. Sci. Lett.* **305**, 270–282.

Craddock P. R. and Dauphas N. (2011) Iron Isotopic Compositions of Geological Reference Materials and Chondrites. *Geostand. Geoanalytical Res.* **35**, 101–123.

Craddock P. R., Warren J. M. and Dauphas N. (2013) Abyssal peridotites reveal the near-chondritic Fe isotopic composition of the Earth. *Earth Planet. Sci. Lett.* **365**, 63–76.

Crank J. (1975) *The Mathematics of Diffusion*. second edi., Clarendon Press, Oxford.

Danyushevsky L. V, Sokolov S. and Falloon T. J. (2002) Melt Inclusions in Olivine Phenocrysts: Using Diffusive Re-equilibration to Determine the Cooling History of a Crystal, with Implications for the Origin of Olivine-phyric Volcanic Rocks. *J. Petrol.* **43**, 1651–1671.

Dauphas N., Janney P. E., Mendybaev R. A., Wadhwa M., Richter F. M., Davis A. M., van Zuilen M., Hines R. and Foley C. N. (2004) Chromatographic Separation and Multicollection-ICPMS Analysis of Iron. Investigating Mass-Dependent and –Independent Isotope Effects. *Anal. Chem.* **76**, 5855–5863.

Dauphas N., Cates N. L., Mojzsis S. J. and Busigny V. (2007) Identification of chemical sedimentary protoliths using iron isotopes in the >3750 Ma Nuvvuagittuq supracrustal belt, Canada. *Earth Planet. Sci. Lett.* **254**, 358–376.

Dauphas N., Cook D. L., Sacarabany A., Fröhlich C., Davis A. M., Wadhwa M., Pourmand A., Rauscher T. and Gallino R. (2008) Iron 60 Evidence for Early Injection and Efficient Mixing of Stellar Debris in the Protosolar Nebula. *Astrophys. J.* **686**, 560–569.

Dauphas N., Craddock P. R., Asimow P. D., Bennett V. C., Nutman A. P. and Ohnenstetter D. (2009) Iron isotopes may reveal the redox conditions of mantle melting from Archean to Present. *Earth Planet. Sci. Lett.* **288**, 255–267.

Dauphas N., Teng F.-Z. and Arndt N. T. (2010) Magnesium and iron isotopes in 2.7 Ga Alexo komatiites: Mantle signatures, no evidence for Soret diffusion, and identification of diffusive transport in zoned olivine. *Geochim. Cosmochim. Acta* **74**, 3274–3291.

Dauphas N., Roskosz M., Alp E. E., Neuville D. R., Hu M. Y., Sio C. K., Tissot F. L. H., Zhao J., Tissandier L., Médard E. and Cordier C. (2014) Magma redox and structural controls on iron isotope variations in Earth's mantle and crust. *Earth Planet. Sci. Lett.* **398**, 127–140.

Davidson J. P., Morgan D. J., Charlier B. L. A., Harlou R. and Hora J. M. (2007) Microsampling and Isotopic Analysis of Igneous Rocks: Implications for the Study of Magmatic Systems. *Annu. Rev. Earth Planet. Sci.* **35**, 273–311.

Deer W. A., Howie R. A. and Zussman J. (1992) *An Introduction to the Rock-forming Minerals*. second edi., Pearson Prentice Hall, Harlow, England.

Dideriksen K., Baker J. A. and Stipp S. L. S. (2006) Iron isotopes in natural carbonate minerals determined by MC-ICP-MS with a ^{58}Fe-^{54}Fe double spike. *Geochim. Cosmochim. Acta* **70**, 118–132.

Dmitriev L., Heirtzler J., Kirkpatrick J., Matthews D., Petersen N., Cambon P., Honnorez J., Ohnenstetter D., Sato H., Schmincke H., Dick H., Dungan M., Hodges F. N., Erickson A. and Aguilar R. (1979) 2. Holes 396A and 396B. *Deep Sea Drill. Proj. - Initial Reports* **46**, 15–86.

Dohmen R., Chakraborty S. and Becker H.-W. (2002) Si and O diffusion in olivine and implications for characterizing plastic flow in the mantle. *Geophys. Res. Lett.* **29**, 26–1 – 26–4.

Dohmen R., Becker H.-W. and Chakraborty S. (2007) Fe–Mg diffusion in olivine I: experimental determination between 700 and 1,200°C as a function of composition, crystal orientation and oxygen fugacity. *Phys. Chem. Miner.* **34**, 389–407.

Dohmen R. and Chakraborty S. (2007) Fe-Mg diffusion in olivine II: Point defect chemistry, change of diffusion mechanisms and a model for calculation of coefficients in natural olivine. *Phys. Chem. Miner.* **34**, 409–430.

Dohmen R., Kasemann S. A., Coogan L. and Chakraborty S. (2010) Diffusion of Li in olivine. Part I: Experimental observations and a multi species diffusion model. *Geochim. Cosmochim. Acta* **74**, 274–292.

Donaldson C. H. (1975) Calculated diffusion coefficients and the growth rate of olivine in a basalt magma. *Lithos* **8**, 163–174.

Donaldson C. H. (1985) The Rates of Dissolution of Olivine, Plagioclase, and Quartz in a Basalt Melt. *Mineral. Mag.* **49**, 683–693.

Donaldson C. H. (1990) Forsterite dissolution in superheated basaltic, andesitic and rhyolitic melts. *Mineral. Mag.* **54**, 67–74.

Druitt T. H., Costa F., Deloule E., Dungan M. and Scaillet B. (2012) Decadal to monthly timescales of magma transfer and reservoir growth at a caldera volcano. *Nature* **482**, 77–80.

Edwards B. R. and Russell J. K. (1996) A review and analysis of silicate mineral dissolution experiments in natural silicate melts. *Chem. Geol.* **130**, 233–245.

Evans T. M., O'Neill H. St. and Tuff J. (2008) The influence of melt composition on the partitioning of REEs, Y, Sc, Zr and Al between forsterite and melt in the system CMAS. *Geochim. Cosmochim. Acta* **72**, 5708–5721.

Faure F., Trolliard G., Montel J.-M. and Nicollet C. (2001) Nano-petrographic investigation of a mafic xenolith (maar de Beaunit, Massif Central, France). *Eur. J. Mineral.* **13**, 27–40.

Flower M., Robinson P., Schmincke H. and Ohnmacht W. (1974) 51. Petrology and Geochemistry of igneous rocks, DSDP Leg 37. *Deep Sea Drill. Proj. - Initial Reports* **37**, 653–679.

Flower M. F. J., Ohnmacht W., Schmincke H., Gibson I. L., Robinson P. T. and Parker R. (1976) 8. Petrology and Geochemistry of Basalts from Hole 396B, Leg 46. *Deep Sea Drill. Proj. - Initial Reports* **46**, 179–213.

Foley S. F., Jacob D. E. and O'Neill H. S. C. (2010) Trace element variations in olivine phenocrysts from Ugandan potassic rocks as clues to the chemical characteristics of parental magmas. *Contrib. to Mineral. Petrol.* **162**, 1–20.

Foley S. F., Prelevic D., Rehfeldt T. and Jacob D. E. (2013) Minor and trace elements in olivines as probes into early igneous and mantle melting processes. *Earth Planet. Sci. Lett.* **363**, 181–191.

Gallahan W. and Nielsen R. (1992) The partitioning of Sc, Y, and the rare earth elements between high-Ca pyroxene and natural mafic to intermediate lavas at 1 atmosphere. *Geochim. Cosmochim. Acta* **56**, 2387–2404.

Galy A., Yoffe O., Janney P. E., Williams R. W., Cloquet C., Alard O., Halicz L., Wadhwa M., Hutcheon I. D., Ramon E. and Carignan J. (2003) Magnesium isotope heterogeneity of the isotopic standard SRM980 and new reference materials for magnesium-isotope-ratio measurements. *J. Anal. At. Spectrom.* **18**, 1352–1356.

Ganguly J. (2002) Diffusion kinetics in minerals: Principles and applications to tectono-metamorphic processes. *EMU Notes Mineral.* **4**, 271–309.

Gao S., Liu X., Yuan H., Hattendorf B., Günther D., Chen L. and Hu S. (2002) Determination of Forty Two Major and Trace Elements in USGS and NIST SRM Glasses by Laser Ablation-Inductively Coupled Plasma-Mass Spectrometry. *Geostand. Geoanalytical Res.* **26**, 181–196.

Ghiorso M. S. and Sack R. O. (1995) Chemical mass transfer in magmatic processes IV. A revised and internally consistent thermodynamic model for the interpolation and extrapolation of liquid-solid equilibria in magmatic systems at elevated temperatures and pressures. *Contrib. to Mineral. Petrol.* **119**, 197–212.

Goel G., Zhang L., Lacks D. J. and Van Orman J. (2012) Isotope fractionation by diffusion in silicate melts: Insights from molecular dynamics simulations. *Geochim. Cosmochim. Acta* **93**, 205–213.

Gramlich J. W., Machlan L. A., Barnes I. L. and Paulsen P. J. (1989) Absolute isotopic abundance ratios and atomic weight of a reference sample of nickel. *J. Res. Natl. Inst. Stand. Technol.* **94**, 347–356.

Gueguen B., Rouxel O., Ponzevera E., Bekker A. and Fouquet Y. (2013) Nickel Isotope Variations in Terrestrial Silicate Rocks and Geological Reference Materials Measured by MC-ICP-MS. *Geostand. Geoanalytical Res.* **37**, 297–317.

Hart S. R. and Dunn T. (1993) Experimental cpx/melt partitioning of 24 trace elements. *Contrib. to Mineral. Petrol.* **113**, 1–8.

Herd C. D. K. (2008) Basalts as Probes of Planetary Interior Redox State. *Rev. Mineral. Geochemistry* **68**, 527–553.

Hermann J., O'Neill H. S. C. and Berry A. J. (2005) Titanium solubility in olivine in the system TiO2–MgO–SiO2: no evidence for an ultra-deep origin of Ti-bearing olivine. *Contrib. to Mineral. Petrol.* **148**, 746–760.

Hibbert K. E. J., Williams H. M., Kerr a. C. and Puchtel I. S. (2012) Iron isotopes in ancient and modern komatiites: Evidence in support of an oxidised mantle from Archean to present. *Earth Planet. Sci. Lett.* **321-322**, 198–207.

De Hoog J. C. M., Gall L. and Cornell D. H. (2010) Trace-element geochemistry of mantle olivine and application to mantle petrogenesis and geothermobarometry. *Chem. Geol.* **270**, 196–215.

Horn I. and von Blanckenburg F. (2007) Investigation on elemental and isotopic fractionation during 196 nm femtosecond laser ablation multiple collector inductively coupled plasma mass spectrometry. *Spectrochim. Acta Part B At. Spectrosc.* **62**, 410–422.

Horn I., Von Blanckenburg F., Schoenberg R., Steinhoefel G. and Markl G. (2006) In situ iron isotope ratio determination using UV-femtosecond laser ablation with application to hydrothermal ore formation processes. *Geochim. Cosmochim. Acta* **70**, 3677–3688.

Huang F., Glessner J., Ianno A., Lundstrom C. and Zhang Z. (2009) Magnesium isotopic composition of igneous rock standards measured by MC-ICP-MS. *Chem. Geol.* **268**, 15–23.

Huang F., Chakraborty P., Lundstrom C. C., Holmden C., Glessner J. J. G., Kieffer S. W. and Lesher C. E. (2010) Isotope fractionation in silicate melts by thermal diffusion. *Nature* **464**, 396–400.

Huang F., Zhang Z., Lundstrom C. C. and Zhi X. (2011) Iron and magnesium isotopic compositions of peridotite xenoliths from Eastern China. *Geochim. Cosmochim. Acta* **75**, 3318–3334.

Humler E. and Whitechurch H. (1988) Petrology of basalts from the Central Indian Ridge (lat. 25°23′S, long. 70°04′E): estimates of frequencies and fractional volumes of magma injections in a two-layered reservoir. *Earth Planet. Sci. Lett.* **88**, 169–181.

Ito M. and Ganguly J. (2006) Diffusion kinetics of Cr in olivine and 53Mn–53Cr thermochronology of early solar system objects. *Geochim. Cosmochim. Acta* **70**, 799–809.

Jackson S. (2008) LAMTRACE Data Reduction Software for LA-ICP-MS. In *Laser Ablation ICP-MS in the Earth Sciences: Current Practices and Outstanding Issues, Mineralogical Association of Canada Short Course Series, vol. 40* (ed. P. Sylvester). Mineralogical Association of Canada. pp. 305–307.

Jambon A., Lussiez P., Clocchiatti R., Weisz J. and Hernandez J. (1992) Olivine growth rates in a tholeiitic basalt: An experimental study of melt inclusions in plagioclase. *Chem. Geol.* **96**, 277–287.

Janney P. E., Richter F. M., Mendybaev R. A., Wadhwa M., Georg R. B., Watson E. B. and Hines R. R. (2011) Matrix effects in the analysis of Mg and Si isotope ratios in natural and synthetic glasses by laser ablation-multicollector ICPMS: A comparison of single- and double-focusing mass spectrometers. *Chem. Geol.* **281**, 26–40.

Jarosewich E., Nelen J. A. and Norberg J. A. (1980) Reference Samples for Electron Microprobe Analysis. *Geostand. Newsl.* **4**, 43–47.

Jeffcoate A., Elliott T., Kasemann S., Ionov D., Cooper K. and Brooker R. (2007) Li isotope fractionation in peridotites and mafic melts. *Geochim. Cosmochim. Acta* **71**, 202–218.

Jochum K. P., Dingwell D. B., Rocholl A., Stoll B., Hofmann A. W. and et al. (2000) The Preparation and Preliminary Characterisation of Eight Geological MPI-DING Reference Glasses for In-Situ Microanalysis. *Geostand. Newsl.* **24**, 87–133.

Jochum K. P., Nohl U., Herwig K., Lammel E., Stoll B. and Hofmann A. W. (2005a) GeoReM: A New Geochemical Database for Reference Materials and Isotopic Standards. *Geostand. Geoanalytical Res.* **29**, 333–338.

Jochum K. P., Willbold M., Raczek I., Stoll B. and Herwig K. (2005b) Chemical Characterisation of the USGS Reference Glasses GSA-1G, GSC-1G, GSD-1G, GSE-1G, BCR-2G, BHVO-2G and BIR-1G Using EPMA , ID-TIMS , ID-ICP-MS and LA-ICP-MS. *Geostand. Geoanalytical Res.* **29**, 285–302.

Jochum K. P., Stoll B., Herwig K., Willbold M., Hofmann A. W., Amini M., Aarburg S., Abouchami W., Hellebrand E., Mocek B., Raczek I., Stracke A., Alard O., Bouman C., Becker S., Dücking M., Brätz H., Klemd R., de Bruin D., Canil D., Cornell D., de Hoog C.-J., Dalpé C., Danyushevsky L., Eisenhauer A., Gao Y., Snow J. E., Groschopf N., Günther D., Latkoczy C., Guillong M., Hauri E. H., Höfer H. E., Lahaye Y., Horz K., Jacob D. E., Kasemann S. a., Kent A. J. R., Ludwig T., Zack T., Mason P. R. D., Meixner A., Rosner M., Misawa K., Nash B. P., Pfänder J., Premo W. R., Sun W. D., Tiepolo M., Vannucci R., Vennemann T., Wayne D. and Woodhead J. D. (2006) MPI-DING reference glasses for in situ microanalysis: New reference values for element concentrations and isotope ratios. *Geochemistry Geophys. Geosystems* **7**, Q02008.

Jochum K. P., Wilson S. A., Abouchami W., Amini M., Chmeleff J., Eisenhauer A., Hegner E., Iaccheri L. M., Kieffer B., Krause J., McDonough W. F., Mertz-Kraus R., Raczek I., Rudnick R. L., Scholz D., Steinhoefel G., Stoll B., Stracke A., Tonarini S., Weis D., Weis U. and Woodhead J. D. (2011) GSD-1G and MPI-DING Reference Glasses for In Situ and Bulk Isotopic Determination. *Geostand. Geoanalytical Res.* **35**, 193–226.

Jurewicz A. J. G. and Watson E. B. (1988) Cations in olivine, Part 2: Diffusion in olivine xenocrysts, with applications to petrology and mineral physics. *Contrib. to Mineral. Petrol.* **99**, 186–201.

Kahl M., Chakraborty S., Costa F. and Pompilio M. (2011) Dynamic plumbing system beneath volcanoes revealed by kinetic modeling, and the connection to monitoring data: An example from Mt. Etna. *Earth Planet. Sci. Lett.* **308**, 11–22.

Kennedy A. K., Lofgren G. E. and Wasserburg G. J. (1993) An experimental study of trace element partitioning between olivine, orthopyroxene and melt in chondrules: equilibrium values and kinetic effects. *Earth Planet. Sci. Lett.* **115**, 177–195.

Köhler T. P. and Brey G. P. (1990) Calcium exchange between olivine and clinopyroxene calibrated as a geothermobarometer for natural peridotites from 2 to 60 kb with applications. *Geochim. Cosmochim. Acta* **54**, 2375–2388.

Longerich H. P., Jackson S. E. and Günther D. (1996) Laser Ablation Inductively Coupled Plasma Mass Spectrometric Transient Signal Data Acquisition and Analyte Concentration Calculation. *J. Anal. At. Spectrom.* **11**, 899–904.

Longpré M.-A., Klügel A., Diehl A. and Stix J. (2014) Mixing in mantle magma reservoirs prior to and during the 2011-2012 eruption at El Hierro, Canary Islands. *Geology* **42**, 315–318.

Lorand J., Alard O., Luguet A. and Keays R. R. (2003) Sulfur and selenium systematics of the subcontinental lithospheric mantle: Inferences from the Massif Central xenolith suite (France). *Geochim. Cosmochim. Acta* **67**, 4137–4151.

Mallmann G. and O'Neill H. S. C. (2009) The Crystal/Melt Partitioning of V during Mantle Melting as a Function of Oxygen Fugacity Compared with some other Elements (Al, P, Ca, Sc, Ti, Cr, Fe, Ga, Y, Zr and Nb). *J. Petrol.* **50**, 1765–1794.

Mansfeldt T., Schuth S., Häusler W., Wagner F. E., Kaufhold S. and Overesch M. (2012) Iron oxide mineralogy and stable iron isotope composition in a Gleysol with petrogleyic properties. *J. Soils Sediments* **12**, 97–114.

McNeill A. W. and Danyushevsky L. V (1996) 3. Composition and Crystallization Temperatures of primary melts from Hole 896A Basalts: Evidence from Melt Inclusion Studies. *Proc. Ocean Drill. Program, Sci. Results* **148**, 21–35.

Millet M.-A., Baker J. A. and Payne C. E. (2012) Ultra-precise stable Fe isotope measurements by high resolution multiple-collector inductively coupled plasma mass spectrometry with a 57Fe–58Fe double spike. *Chem. Geol.* **304-305**, 18–25.

Nabeleck P. I. and Langmuir C. H. (1986) The significance of unusual zoning in olivines from FAMOUS area basalt 527-1-1. *Contrib. to Mineral. Petrol.* **93**, 1–8.

Nehlig P., Boivin P., de Goër A., Mergoil J., Prouteau G., Sustrac G. and Thieblemont D. (2003) *Les volcans du Massif central*., Orléans.

Neumann E.-R., Wulff-Pedersen E., Simonsen S. L., Pearson N. J., Marti J. and Mitjavila J. (1999) Evidence for Fractional Crystallization of Periodically Refilled Magma Chambers in Tenerife, Canary Islands. *J. Petrol.* **40**, 1089–1123.

Nielsen R. L., Gallahan W. E. and Newberger F. (1992) Experimentally determined mineral-melt partition coefficients for Sc, Y and REE for olivine, orthopyroxene, pigeonite, magnetite and ilmenite. *Contrib. to Mineral. Petrol.* **110**, 488–499.

Nielsen R. L., Forsythe L. M., Gallahan W. E. and Fisk M. R. (1994) Major- and trace-element magnetite-melt equilibria. *Chem. Geol.* **117**, 167–191.

Norman M. D., McCulloch M. T., O'Neill H. S. C. and Yaxley G. M. (2006) Magnesium isotopic analysis of olivine by laser-ablation multi-collector ICP-MS: composition dependent matrix effects and a comparison of the Earth and Moon. *J. Anal. At. Spectrom.* **21**, 50–54.

O' Connor C., Sharp B. L. and Evans P. (2006) On-line additions of aqueous standards for calibration of laser ablation inductively coupled plasma mass spectrometry: theory and comparison of wet and dry plasma conditions. *J. Anal. At. Spectrom.* **21**, 556-565.

Pan Y. and Batiza R. (2002) Mid-ocean ridge magma chamber processes: Constraints from olivine zonation in lavas from the East Pacific Rise at 9°30'N and 10°30'N. *J. Geophys. Res. - Solid Earth* **107**, 9–13.

Paonita A. and Martelli M. (2006) Magma dynamics at mid-ocean ridges by noble gas kinetic fractionation: Assessment of magmatic ascent rates. *Earth Planet. Sci. Lett.* **241**, 138–158.

Pearson N., Griffin W., Alard O. and O'Reilly S. (2006) The isotopic composition of magnesium in mantle olivine: Records of depletion and metasomatism. *Chem. Geol.* **226**, 115–133.

Petry C., Chakraborty S. and Palme H. (2004) Experimental determination of Ni diffusion coefficients in olivine and their dependence on temperature, composition, oxygen fugacity, and crystallographic orientation. *Geochim. Cosmochim. Acta* **68**, 4179–4188.

Pogge von Strandmann P. (2008) Precise magnesium isotope measurements in core top planktic and benthic foraminifera. *Geochemistry, Geophys. Geosystems* **9**.

Pogge von Strandmann P. A. E., Elliott T., Marschall H. R., Coath C., Lai Y.-J., Jeffcoate A. B. and Ionov D. A. (2011) Variations of Li and Mg isotope ratios in bulk chondrites and mantle xenoliths. *Geochim. Cosmochim. Acta* **75**, 5247–5268.

Poitrasson F. and Freydier R. (2005) Heavy iron isotope composition of granites determined by high resolution MC-ICP-MS. *Chem. Geol.* **222**, 132–147.

Polyakov V. B. and Mineev S. D. (2000) The use of Mössbauer spectroscopy in stable isotope geochemistry. *Geochim. Cosmochim. Acta* **64**, 849–865.

Pouchou J. and Pichoir F. (1991) Quantitative analysis of homogeneous or stratified microvolumes applying the model "PAP". In *Electron Probe Quantification* (eds. K. Heinrich and D. Newbury). Plenum Press, New York. pp. 31–75.

Qian Q., O'Neill H. and Hermann J. (2010) Comparative diffusion coefficients of major and trace elements in olivine at ~950 °C from a xenocryst included in dioritic magma. *Geology* **38**, 331–334.

Remmert P., Dohmen R. and Chakraborty S. (2008) Diffusion of REE, Hf and Sr in Olivine. In *AGU Fall Meeting Abstracts* p. 1844.

Richet P. (2003) *Guide des Volcans de France*. 1st ed., BRGM, Belin, Paris.

Richter F. M., Liang Y. and Davis A. M. (1999) Isotope fractionation by diffusion in molten oxides. *Geochim. Cosmochim. Acta* **63**, 2853–2861.

Richter F. M., Davis A. M., DePaolo D. J. and Watson E. B. (2003) Isotope fractionation by chemical diffusion between molten basalt and rhyolite. *Geochim. Cosmochim. Acta* **67**, 3905–3923.

Richter F., Watson E., Mendybaev R., Teng F. and Janney P. (2008) Magnesium isotope fractionation in silicate melts by chemical and thermal diffusion. *Geochim. Cosmochim. Acta* **72**, 206–220.

Richter F. M., Dauphas N. and Teng F. (2009a) Non-traditional fractionation of non-traditional isotopes: Evaporation, chemical diffusion and Soret diffusion. *Chem. Geol.* **258**, 92–103.

Richter F. M., Watson E. B., Mendybaev R., Dauphas N., Georg B., Watkins J. and Valley J. (2009b) Isotopic fractionation of the major elements of molten basalt by chemical and thermal diffusion. *Geochim. Cosmochim. Acta* **73**, 4250–4263.

Richter F., Watson B., Chaussidon M., Mendybaev R. and Ruscitto D. (2014) Lithium isotope fractionation by diffusion in minerals. Part 1: Pyroxenes. *Geochim. Cosmochim. Acta* **126**, 352–370.

Roeder P. L. and Emslie R. F. (1970) Olivine-Liquid Equilibrium. *Contrib. to Mineral. Petrol.* **29**, 275–289.

Rouxel O. J., Bekker A. and Edwards K. J. (2005) Iron isotope constraints on the Archean and Paleoproterozoic ocean redox state. *Science* **307**, 1088–1091.

Sato H., Aoki K., Okamoto K. and Fujita B. (1976) 4. Petrology and Chemistry of Basaltic Rocks from Hole 396B, IPOD/DSDP Leg 46. *Deep Sea Drill. Proj. - Initial Reports* **46**, 115–141.

Schauble E. A. (2011) First-principles estimates of equilibrium magnesium isotope fractionation in silicate, oxide, carbonate and hexaaquamagnesium(2+) crystals. *Geochim. Cosmochim. Acta* **75**, 844–869.

Schneider C. A., Rasband W. S. and Eliceiri K. W. (2012) NIH Image to ImageJ: 25 years of image analysis. *Nat. Methods* **9**, 671–675.

Schoenberg R. and von Blanckenburg F. (2005) An assessment of the accuracy of stable Fe isotope ratio measurements on samples with organic and inorganic matrices by high-resolution multicollector ICP-MS. *Int. J. Mass Spectrom.* **242**, 257–272.

Schoenberg R. and Von Blanckenburg F. (2006) Modes of planetary-scale Fe isotope fractionation. *Earth Planet. Sci. Lett.* **252**, 342–359.

Schuessler J., Schoenberg R. and Sigmarsson O. (2009) Iron and lithium isotope systematics of the Hekla volcano, Iceland — Evidence for Fe isotope fractionation during magma differentiation. *Chem. Geol.* **258**, 78–91.

Schwab R. G. and Küstner D. (1981) The equilibrium fugacities of important oxygen buffers in technology and petrology. *Neues Jahrb. für Mineral.* **140**, 111–142.

Shahar A., Young E. D. and Manning C. E. (2008) Equilibrium high-temperature Fe isotope fractionation between fayalite and magnetite: An experimental calibration. *Earth Planet. Sci. Lett.* **268**, 330–338.

Shannon R. D. (1976) Revised Effective Ionic Radii and Systematic Studies of Interatomie Distances in Halides and Chaleogenides. *Acta Crystallogr.* **A32**, 751–767.

Sharma M., Polizzotto M. and Anbar a. D. (2001) Iron isotopes in hot springs along the Juan de Fuca Ridge. *Earth Planet. Sci. Lett.* **194**, 39–51.

Shaw C. S. J. (2004) The temporal evolution of three magmatic systems in the West Eifel volcanic field, Germany. *J. Volcanol. Geotherm. Res.* **131**, 213–240.

Shaw C. S. J., Heidelbach F. and Dingwell D. B. (2006) The origin of reaction textures in mantle peridotite xenoliths from Sal Island, Cape Verde: the case for "metasomatism" by the host lava. *Contrib. to Mineral. Petrol.* **151**, 681–697.

Shejwalkar A. and Coogan L. a. (2013) Experimental calibration of the roles of temperature and composition in the Ca-in-olivine geothermometer at 0.1MPa. *Lithos* **177**, 54–60.

Sio C. K. I., Dauphas N., Teng F.-Z., Chaussidon M., Helz R. T. and Roskosz M. (2013) Discerning crystal growth from diffusion profiles in zoned olivine by in situ Mg–Fe isotopic analyses. *Geochim. Cosmochim. Acta* **123**, 302–321.

Smith V. G., Tiller W. A. and Rutter J. W. (1955) A Mathematical Analyses of Solute Redistribution during Solidification. *Can. J. Phys.* **33**, 723–745.

Spandler C., O'Neill H. S. C. and Kamenetsky V. S. (2007) Survival times of anomalous melt inclusions from element diffusion in olivine and chromite. *Nature* **447**, 303–306.

Spandler C. and O'Neill H. S. C. (2010) Diffusion and partition coefficients of minor and trace elements in San Carlos olivine at 1,300°C with some geochemical implications. *Contrib. to Mineral. Petrol.* **159**, 791–818.

Steinhoefel G., Horn I. and von Blanckenburg F. (2009a) Matrix-independent Fe isotope ratio determination in silicates using UV femtosecond laser ablation. *Chem. Geol.* **268**, 67–73.

Steinhoefel G., Horn I. and von Blanckenburg F. (2009b) Micro-scale tracing of Fe and Si isotope signatures in banded iron formation using femtosecond laser ablation. *Geochim. Cosmochim. Acta* **73**, 5343–5360.

Stroncik N., Klügel A. and Hansteen T. H. (2008) The magmatic plumbing system beneath El Hierro (Canary Islands): constraints from phenocrysts and naturally quenched basaltic glasses in submarine rocks. *Contrib. to Mineral. Petrol.* **157**, 593–607.

Taylor P., Maeck R. and De Bievre P. (1992) Determination of the absolute isotopic composition and Atomic Weight of a reference sample of natural iron. *Int. J. Mass Spectrom. Ion Process.* **121**, 111–125.

Teng F., Wadhwa M. and Helz R. (2007) Investigation of magnesium isotope fractionation during basalt differentiation: Implications for a chondritic composition of the terrestrial mantle. *Earth Planet. Sci. Lett.* **261**, 84–92.

Teng F.-Z., Dauphas N. and Helz R. T. (2008) Iron Isotope Fractionation During Magmatic Differentiation in Kilauea Iki Lava Lake. *Science* **320**, 1620–1622.

Teng F.-Z., Li W.-Y., Ke S., Marty B., Dauphas N., Huang S., Wu F.-Y. and Pourmand A. (2010) Magnesium isotopic composition of the Earth and chondrites. *Geochim. Cosmochim. Acta* **74**, 4150–4166.

Teng F.-Z., Dauphas N., Helz R. T., Gao S. and Huang S. (2011) Diffusion-driven magnesium and iron isotope fractionation in Hawaiian olivine. *Earth Planet. Sci. Lett.* **308**, 317–324.

Teng F.-Z., Dauphas N., Huang S. and Marty B. (2013) Iron isotopic systematics of oceanic basalts. *Geochim. Cosmochim. Acta* **107**, 12–26.

Tipper E., Louvat P., Capmas F., Galy A. and Gaillardet J. (2008) Accuracy of stable Mg and Ca isotope data obtained by MC-ICP-MS using the standard addition method. *Chem. Geol.* **257**, 65–75.

Ulmer P. (1989) The dependence of the Fe^{2+}–Mg cation-partitioning between olivine and basaltic liquid on pressure, temperature and composition: An experimental study to 30 kbars. *Contrib. to Mineral. Petrol.* **101**, 261–273.

Völkening J. and Papanastassiou D. A. (1989) Iron Isotope Anomalies. *Astrophys. J.* **347**, L43–L46.

Wang K., Moynier F., Podosek F. and Foriel J. (2011) ^{58}Fe and ^{54}Cr in Early Solar System Materials. *Astrophys. J. Lett.* **739**, L58 (5pp).

Watson E. B. and Müller T. (2009) Non-equilibrium isotopic and elemental fractionation during diffusion-controlled crystal growth under static and dynamic conditions. *Chem. Geol.* **267**, 111–124.

Werling F. and Altherr R. (1997) Thermal evolution of the lithosphere beneath the French Massif Central as deduced from geothermobarometry on mantle xenoliths. *Tectonophysics* **275**, 119–141.

Weyer S. and Schwieters J. B. (2003) High precision Fe isotope measurements with high mass resolution MC-ICPMS. *Int. J. Mass Spectrom.* **226**, 355–368.

Weyer S., Anbar A. D., Brey G. P., Münker C., Mezger K. and Woodland A. B. (2005) Iron isotope fractionation during planetary differentiation. *Earth Planet. Sci. Lett.* **240**, 251–264.

Weyer S. and Ionov D. (2007) Partial melting and melt percolation in the mantle: The message from Fe isotopes. *Earth Planet. Sci. Lett.* **259**, 119–133.

Weyer S., Anbar A. D., Brey G. P., Münker K., Mezger K. and Woodland A. B. (2007) Fe-isotope fractionation during partial melting on Earth and the current view on the Fe-isotope budgets of the planets (reply to the comment of F. Poitrasson and to the comment of B.L. Beard and C.M. Johnson on "Iron isotope fractionation during

planetary differentiation" by S. Weyer, A.D. Anbar, G.P. Brey, K. Münker, K. Mezger, A.B. Woodland). *Earth Planet. Sci. Lett.* **256**, 638–646.

Weyer S. (2008) Geochemistry. What drives iron isotope fractionation in magma? *Science* **320**, 1600–1.

Weyer S. and Seitz H.-M. (2012) Coupled lithium- and iron isotope fractionation during magmatic differentiation. *Chem. Geol.* **294-295**, 42–50.

Wiechert U. and Halliday A. N. (2007) Non-chondritic magnesium and the origins of the inner terrestrial planets. *Earth Planet. Sci. Lett.* **256**, 360–371.

Williams H. M., Peslier A. H., McCammon C. A., Halliday, Levasseur S., Teutsch N. and Burg J. P. (2005) Systematic iron isotope variations in mantle rocks and minerals: The effect of partial melting and oxygen fugacity. *Earth Planet. Sci. Lett.* **235**, 435–452.

Wombacher F., Eisenhauer A., Heuser A. and Weyer S. (2009) Separation of Mg, Ca and Fe from geological reference materials for stable isotope ratio analyses by MC-ICP-MS and double-spike TIMS. *J. Anal. At. Spectrom.* **24**, 627–636.

Xie L.-W., Yin Q.-Z., Yang J.-H., Wu F.-Y. and Yang Y.-H. (2011) High precision analysis of Mg isotopic composition in olivine by laser ablation MC-ICP-MS. *J. Anal. At. Spectrom.* **26**, 1773–1780.

Yang W., Teng F.-Z. and Zhang H.-F. (2009) Chondritic magnesium isotopic composition of the terrestrial mantle: A case study of peridotite xenoliths from the North China craton. *Earth Planet. Sci. Lett.* **288**, 475–482.

Young E. D. and Galy A. (2004) The Isotope Geochemistry and Cosmochemistry of Magnesium. *Rev. Mineral. Geochemistry* **55**, 197–230.

Zhang Y., Ni H. and Chen Y. (2010) Diffusion Data in Silicate Melts. *Rev. Mineral. Geochemistry* **72**, 311–408.

Zhao X., Zhang H., Zhu X., Tang S. and Tang Y. (2010) Iron isotope variations in spinel peridotite xenoliths from North China Craton: implications for mantle metasomatism. *Contrib. to Mineral. Petrol.* **160**, 1–14.

Appendix I *

*corresponds to Chapter I of this dissertation

Supplementary Figures

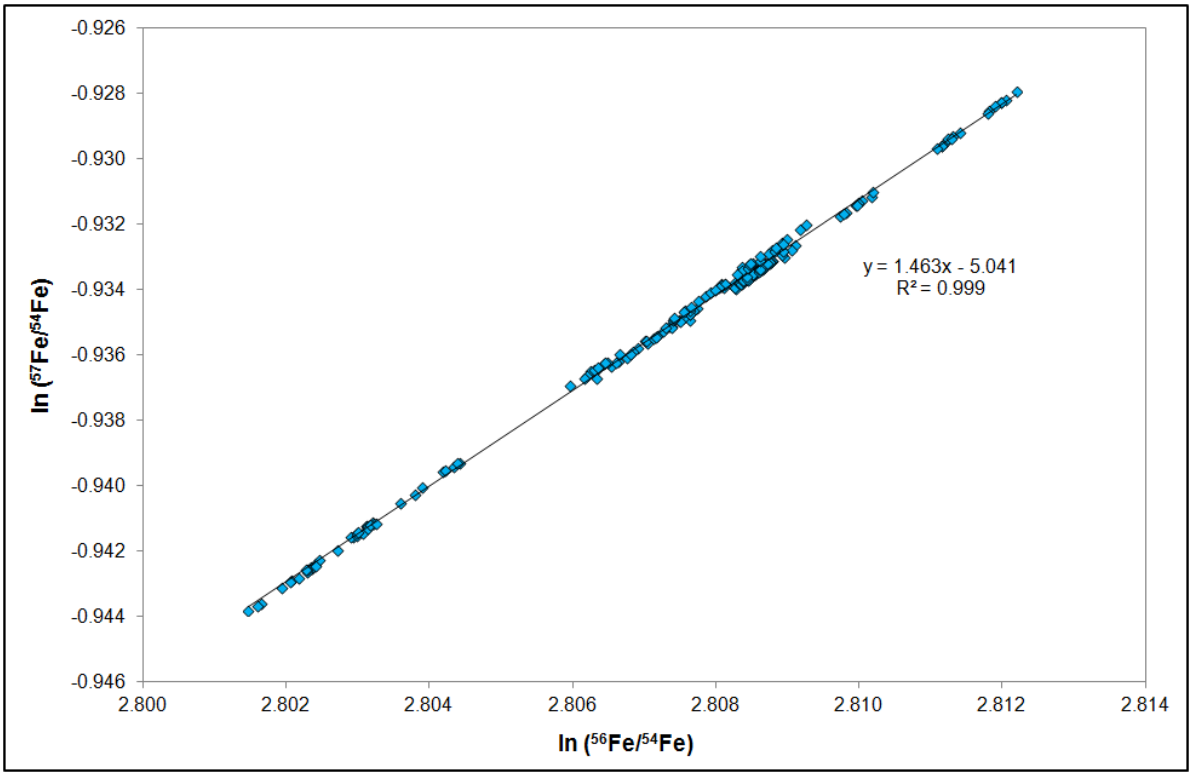

Figure A-I.1: Plot of the natural logarithms of the interference-corrected ^{57}Fe-^{54}Fe- and ^{56}Fe-^{54}Fe ratios determined by fs-LA-MC-ICP-MS (for all investigated reference glasses), which define a regression line with a slope that is almost identical to that of the mass-dependent fractionation line (~1.48; Beard and Johnson, 2004; Steinhoefel et al., 2009a). This shows that variations in the measured Fe isotope ratios are related only to instrumental mass discrimination, and not to interferences.

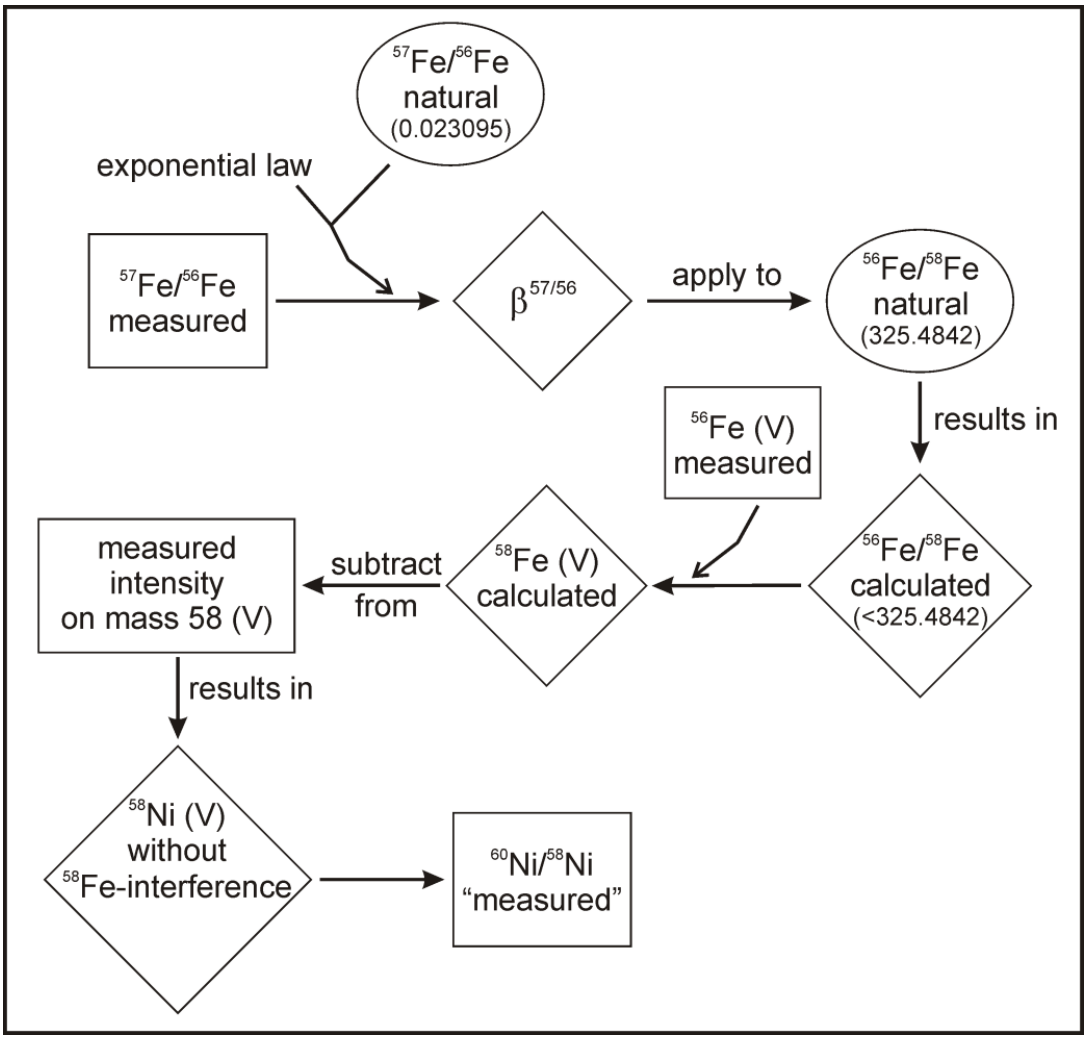

Figure A-I.2: Flow chart illustrating the mass bias corrected interference correction for ^{58}Fe on ^{58}Ni. Using the measured ^{57}Fe-^{56}Fe ratio, assuming a natural ratio of 0.023095 (Taylor *et al.* 1992) and applying the exponential law, the fractionation coefficient $\beta^{57/56}$ is calculated for every acquired cycle. Then a mass bias correction is applied to the natural ^{56}Fe-^{58}Fe ratio (325.4842; Taylor *et al.* 1992) using $\beta^{57/56}$ in order to calculate the ^{56}Fe-^{58}Fe ratio that the MC-ICP-MS would measure if mass 58 was interference-free. This calculated ^{56}Fe-^{58}Fe ratio is used to calculate the signal intensity of ^{58}Fe based on the measured intensity of the ^{56}Fe beam. Finally, the intensity of ^{58}Fe is subtracted from the measured signal intensity on mass 58 in order to obtain the true signal intensity of ^{58}Ni and to calculate an interference-corrected ^{60}Ni/^{58}Ni.

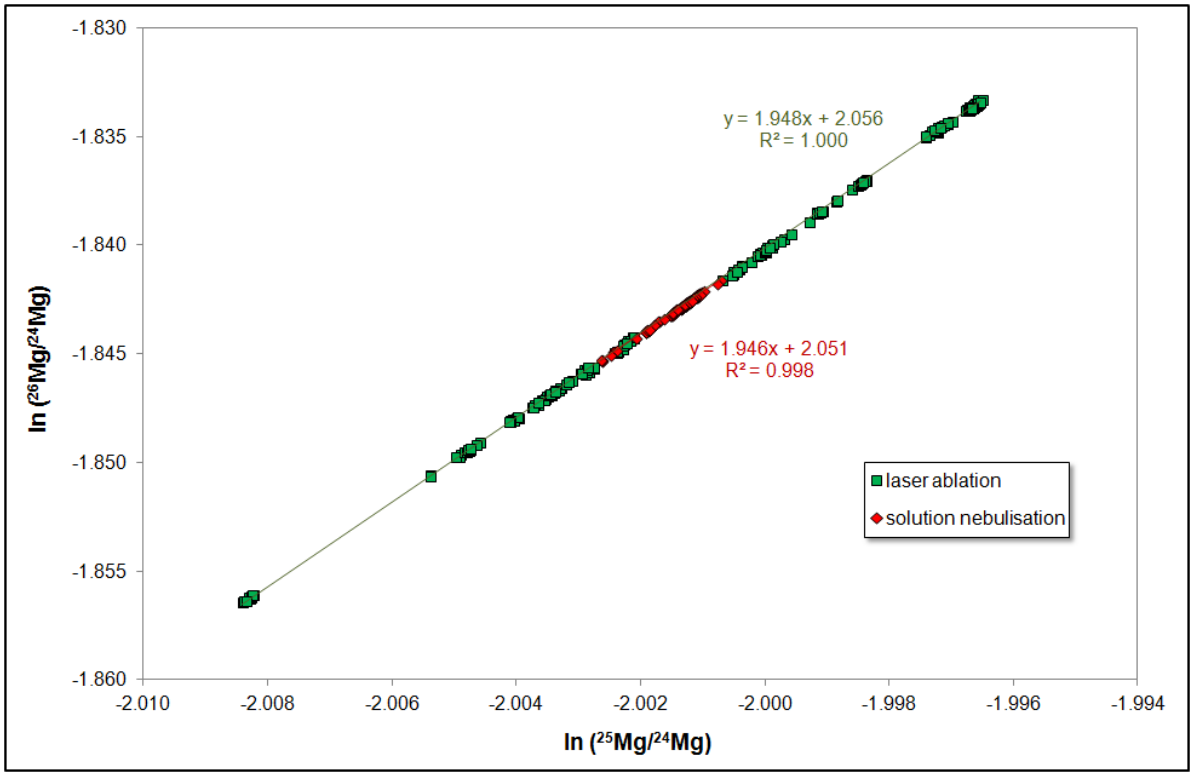

Figure A-I.3: Plot of the natural logarithms of the $^{26}Mg/^{24}Mg$- and $^{25}Mg/^{24}Mg$ ratios determined by fs-LA- and solution nebulisation MC-ICP-MS (for all investigated reference glasses), which define regression lines with a slope that is almost identical to that of the mass-dependent fractionation line (1.92; Young and Galy, 2004). This demonstrates that variations in the measured Mg isotope ratios are related only to instrumental mass discrimination, and not to interferences.

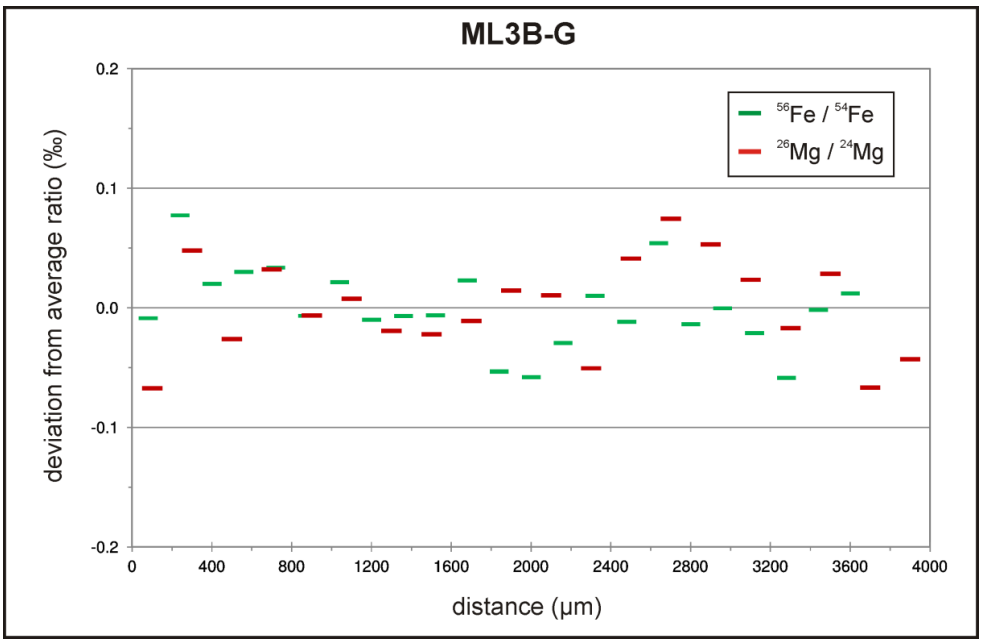

Figure A-I.4: Variation of Fe- and Mg isotope ratios during line scans across the MPI-DING reference glass ML3B-G. Average isotope ratios (0‰ on the y-axis) were calculated from all individual isotope ratios acquired during the line scans. Then, blocks of 10-20 cycles were used to calculate an average isotope ratio for an analyzed area of ~ 50 µm x 200 µm. The figure shows the deviation of these "local" isotopic compositions from the average isotopic composition, indicating that ML3B-G does not show any significant isotopic heterogeneities (for Fe and Mg).

The following plots show similar profiles for the basaltic and komatiitic reference glasses investigated in this study.

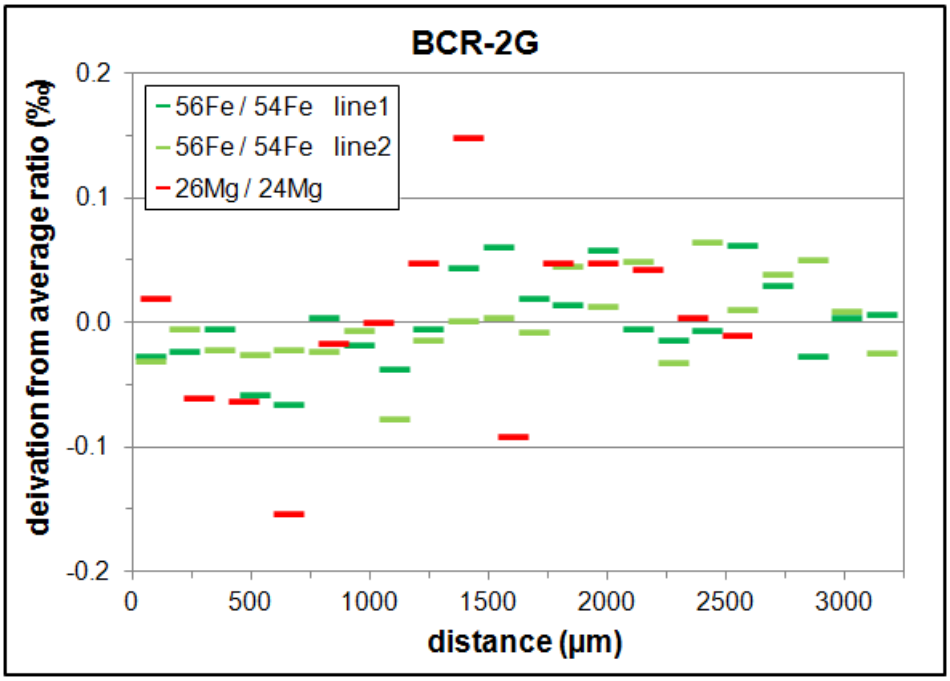

Figure A-I.5: Variation of Fe- and Mg isotope ratios during line scans across the USGS reference glass BCR-2G.

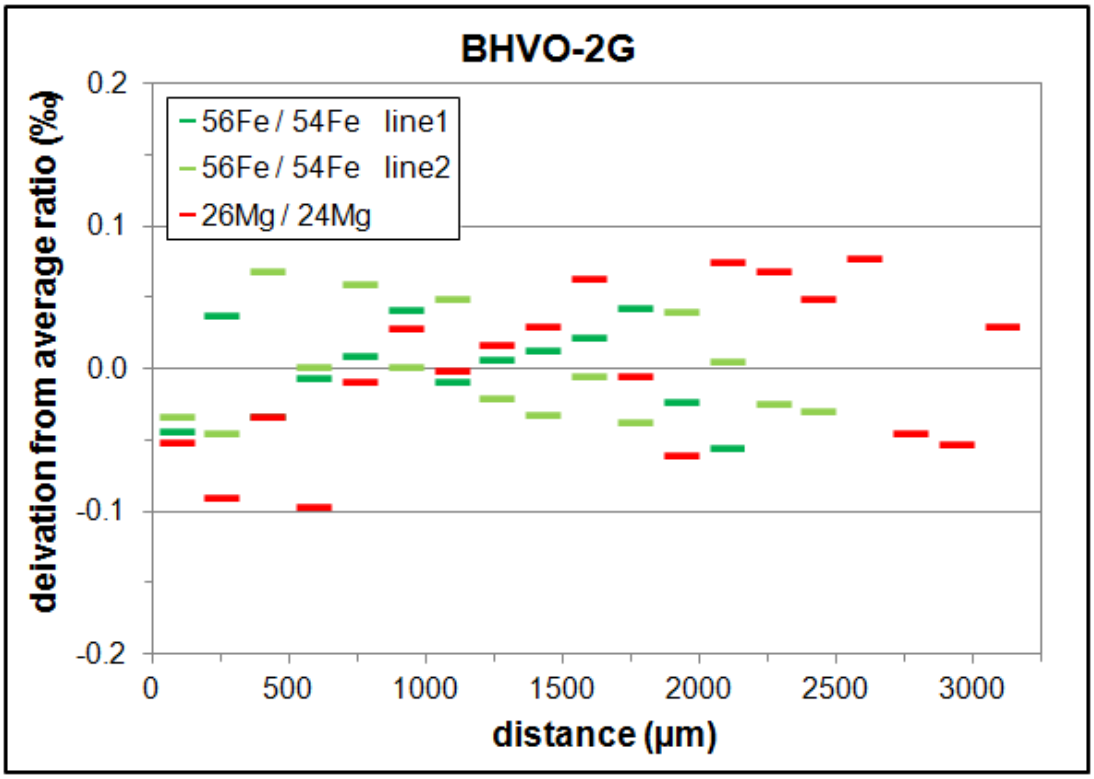

Figure A-I.6: Variation of Fe- and Mg isotope ratios during line scans across the USGS reference glass BHVO-2G.

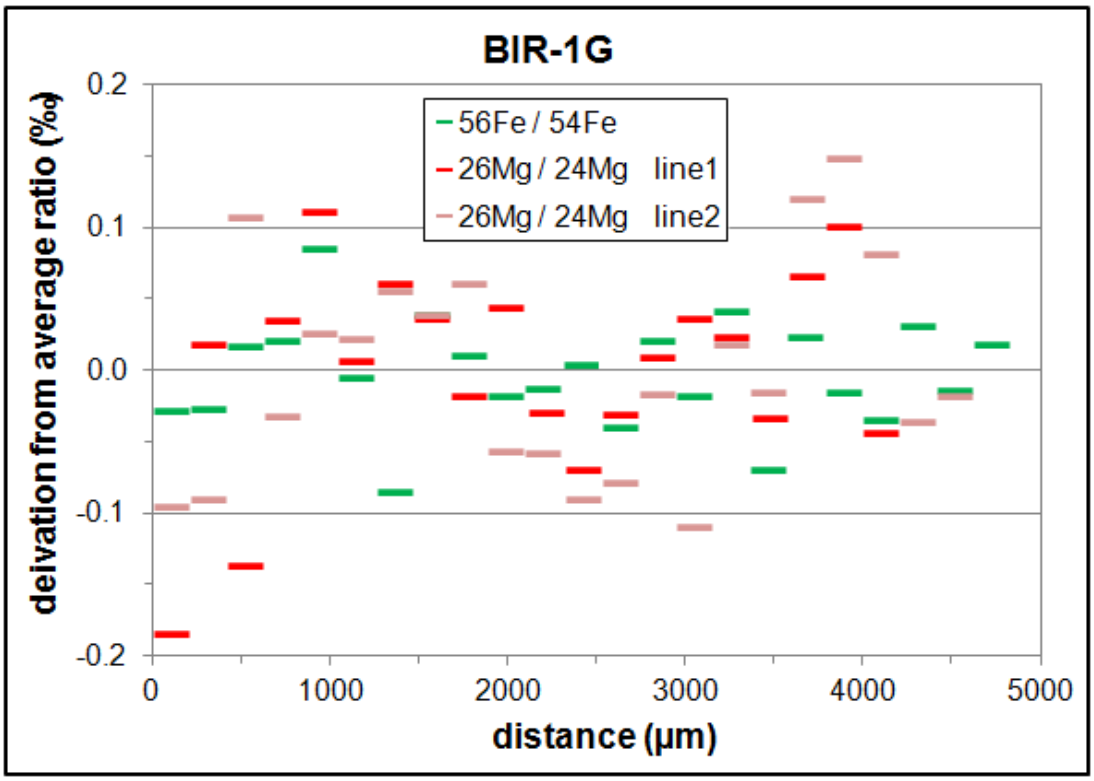

Figure A-I.7: Variation of Fe- and Mg isotope ratios during line scans across the USGS reference glass BIR-1G.

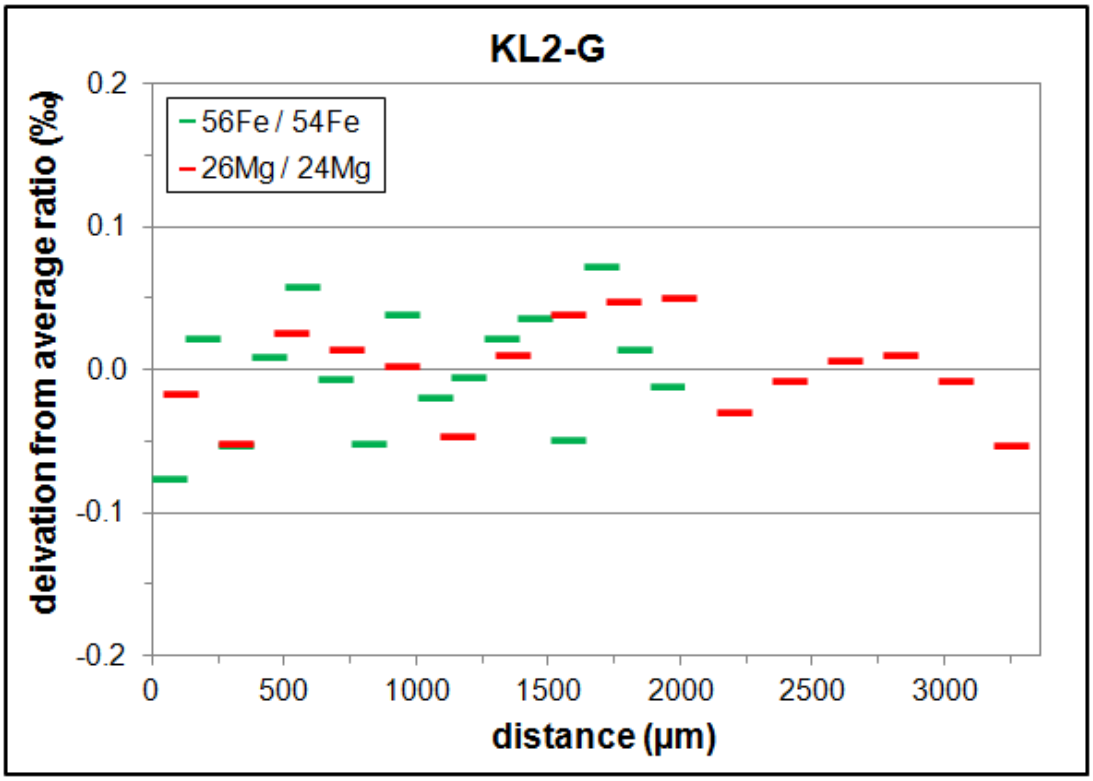

Figure A-I.8: Variation of Fe- and Mg isotope ratios during line scans across the MPI-DING reference glass KL2-G.

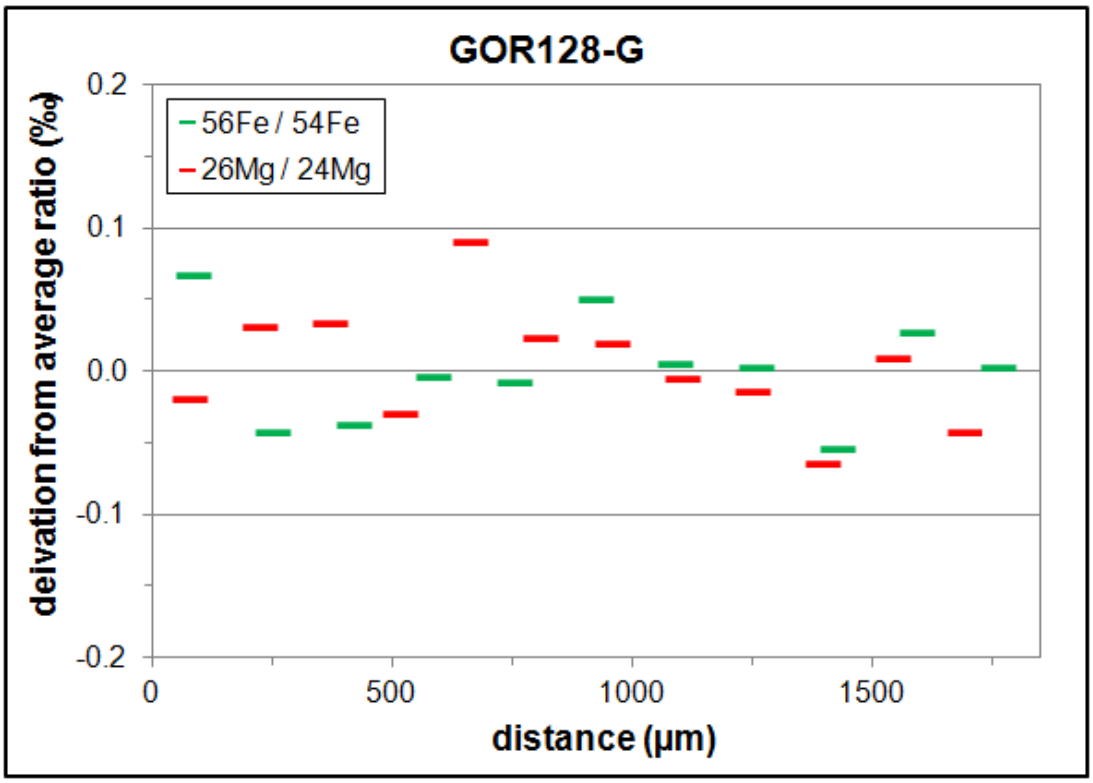

Figure A-I.9: Variation of Fe- and Mg isotope ratios during line scans across the MPI-DING reference glass GOR128-G.

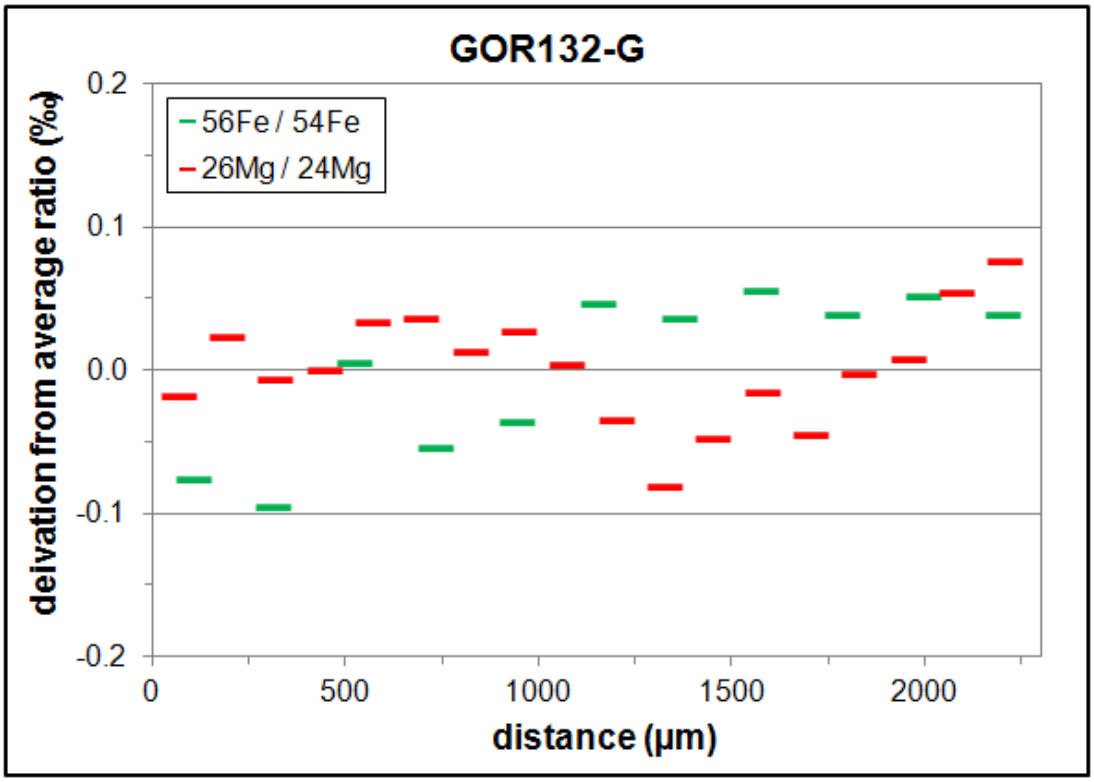

Figure A-I.10: Variation of Fe- and Mg isotope ratios during line scans across the MPI-DING reference glass GOR132-G.

Appendix II *

*corresponds to Chapter II of this dissertation

Supplementary information about modeling

Derivation of the analytical solution for the moving boundary problem (iv) in section II.3.3.1

We applied the front-fixing method (Crank, 1975) to obtain a diffusion equation with a convection term characterized by the growth velocity, R (units m/s):

$$\frac{\partial C}{\partial t} = D\frac{\partial^2 C}{\partial t^2} + R\frac{\partial C}{\partial x}$$

(Eqn. A-II.1)

The above equation is then transformed by making the ansatz:

$$C(x,t) - C_0 = \exp\left[\frac{R\left(x - \frac{Rt}{2}\right)}{2D}\right] w(x,t)$$

(Eqn. A-II.2)

and after substitution into Eqn. A-II.1, we obtain a partial differential equation for $w(x,t)$:

$$\frac{\partial w}{\partial t} = D\frac{\partial^2 w}{\partial t^2}$$

(Eqn. A-II.3)

with the transformed initial and boundary conditions, respectively:

$$w(x,0) = 0$$

$$w(0,t) = C_{rim}\exp\left(\frac{R^2 t}{4D}\right)$$

The corresponding analytical solution for $w(x,t)$ can be found in Crank (1975):

$$w(x,t) = \frac{1}{2}\exp(\lambda t)\left\{\exp\left(-x\sqrt{\frac{\lambda}{D}}\right)\operatorname{erfc}\left[\frac{x}{2\sqrt{Dt}} - \sqrt{\lambda t}\right]\right.$$

$$\left. + \exp\left(x\sqrt{\frac{\lambda}{D}}\right)\operatorname{erfc}\left[\frac{x}{2\sqrt{Dt}} + \sqrt{\lambda t}\right]\right\}$$

(Eqn. A-II.4)

After substitution of this formula for $w(x,t)$ into Eqn. A-II.2 the analytical solution to Eqn. A-II.1 finally is, as follows:

$$C(x,t) = C_0 + \exp\left[\frac{R\left(x - \frac{Rt}{2}\right)}{2D}\right]\frac{1}{2}\exp(\lambda t)\left\{\exp\left(-x\sqrt{\frac{\lambda}{D}}\right)\operatorname{erfc}\left[\frac{x}{2\sqrt{Dt}} - \sqrt{\lambda t}\right]\right.$$

$$\left. + \exp\left(x\sqrt{\frac{\lambda}{D}}\right)\operatorname{erfc}\left[\frac{x}{2\sqrt{Dt}} + \sqrt{\lambda t}\right]\right\}$$

(Eqn. A-II.5)

This derivation was performed by Dr. Ralf Dohmen (Ruhr-Universität Bochum) who also created an Excel-spreadsheet for modeling concentration profiles based on Eqn. A-II.5.

Modeling isotope fractionation due to rapid (diffusion-limited) crystal growth

Eqn. 11 presented in Watson & Müller (2009):

$$\delta(‰) = 1000\cdot(1-D_A/D_B)\cdot(R\cdot BL/D_A)\cdot(1-K)$$

where D represents the diffusion coefficient, A and B are isotopes of a certain element (e.g. ^{56}Fe and ^{54}Fe), R is the growth rate of the crystal, BL is the thickness of the boundary layer and K is the olivine-melt equilibrium partition coefficient for Fe or Mg, e.g. $K_{Mg} = C_{Mg}^{ol} / C_{Mg}^{melt}$. K_{Mg} and K_{Fe} were calculated for T =1250°C and P = 50 MPa following the parameterizations in Ulmer (1989). D_{26Mg}/D_{24Mg} and D_{56Fe}/D_{54Fe} were taken to be 0.996 and 0.999, respectively (Richter et al., 2009a).

Supplementary figures

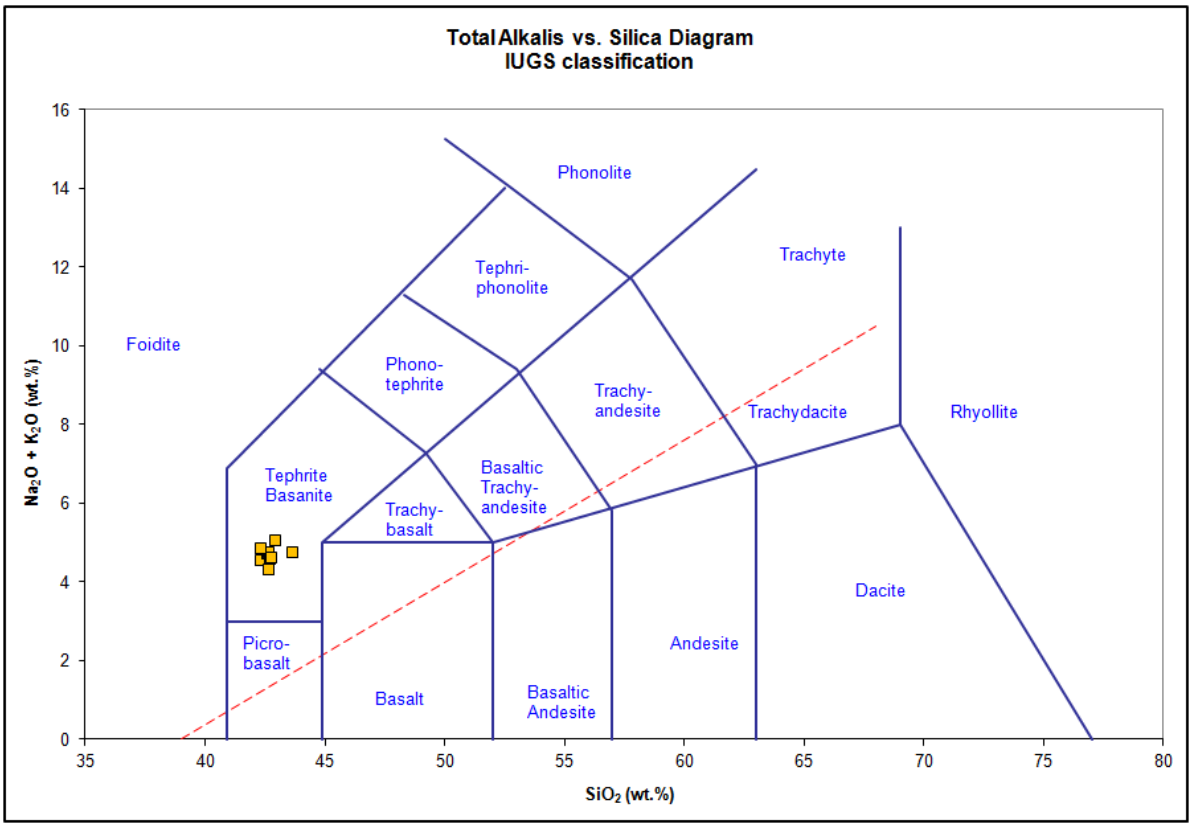

Figure A-II.1: TAS diagram with alkali and silica contents of samples from the Massif Central investigated in this study (orange squares). Data are from Table II.1. The dashed red line represents the alkaline-subalkaline dividing line.

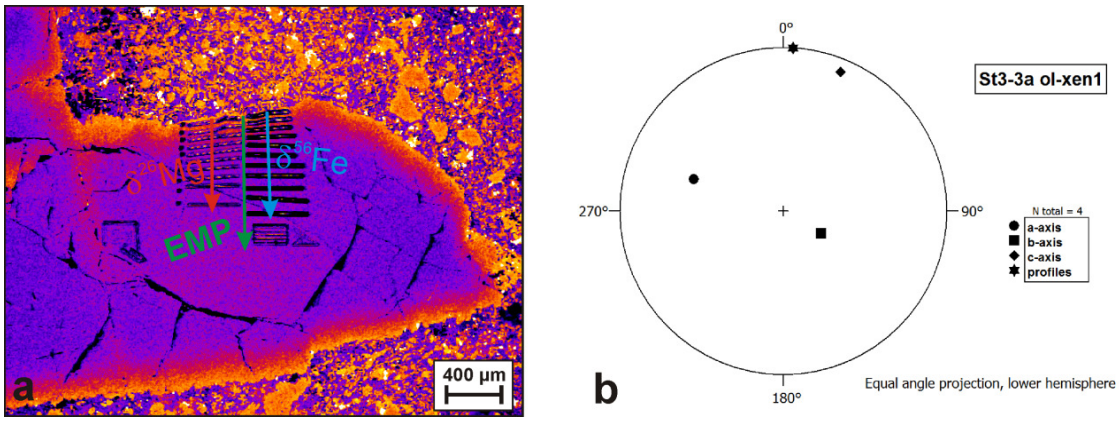

Figure A-II.2: (**a**) False-color BSE image of a zoned mantle olivine in a basanitic rock from the Massif Central (sample St3-3a ol-xen1) after analyses using electron microprobe (EMP) and femtosecond laser ablation MC-ICP-MS. (**b**) Stereographic plot obtained by EBSD analyses showing the angular relations between the crystallographic axes in olivine (a, b and c) and the direction of the analyzed profiles. The plot was generated by using Stereo32.

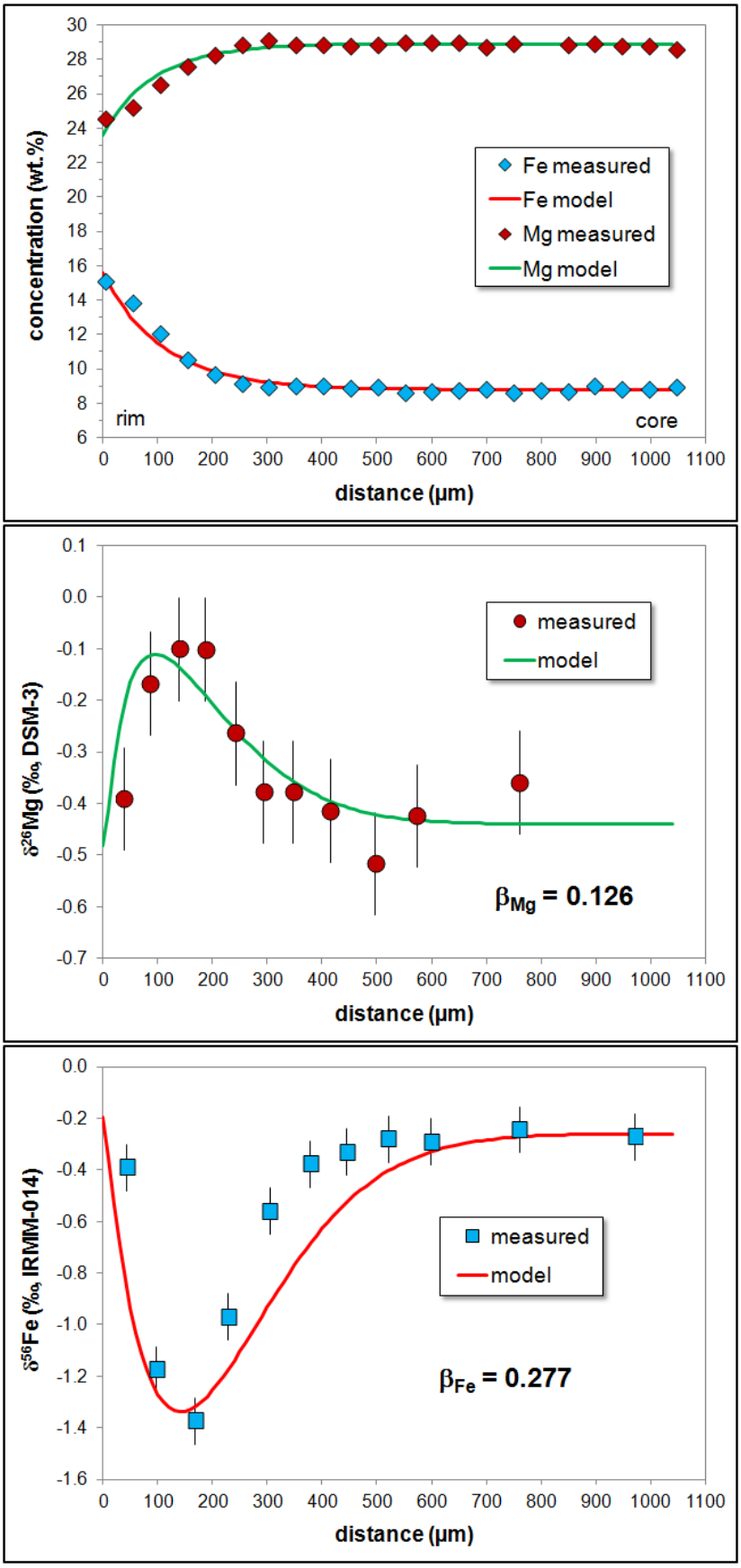

Figure A-II.3: Modeled Fe-Mg chemical and isotopic diffusion profiles for the Massif Central olivine shown in Fig. II.3 (St3-3a ol1), using a model with changing iron and magnesium concentrations at the olivine-melt contact. Modeling was performed by using the software MATLAB®. Model parameters: Linear cooling from 1300°C to 1150°C and with that linear change of the Fe and Mg concentrations at the olivine-melt contact; cooling rate ~110°C/year; P = 50 MPa; X_{Fe} = 0.165; fO_2 at the NNO-buffer. In such a model, higher β-values are required to obtain a reasonably good fit for the Fe-Mg isotopic profiles, which is, however, still worse than the fit obtained by using a model with fixed Fe and Mg concentrations (see Fig. II.6 for comparison).

The following plots show Fe-Mg chemical and isotopic profiles across "intra-plate" olivines investigated in this study. Data are from Table A-II.1 (see below).

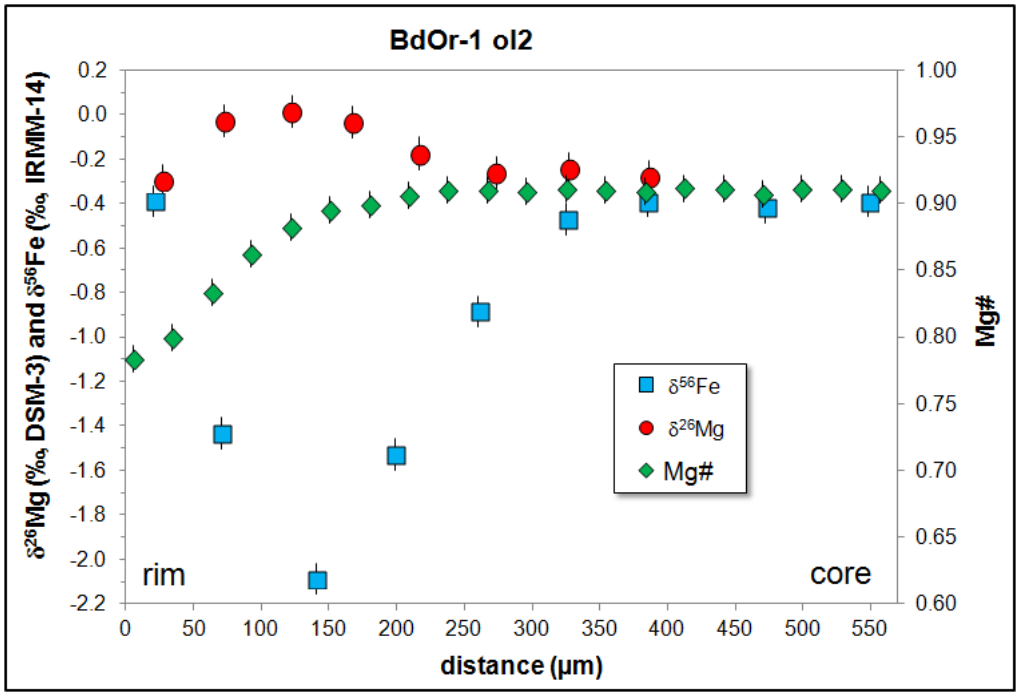

Figure A-II.4: Fe-Mg chemical and isotopic rim-to-core profiles for a normally zoned olivine xenocryst from the Massif Central.

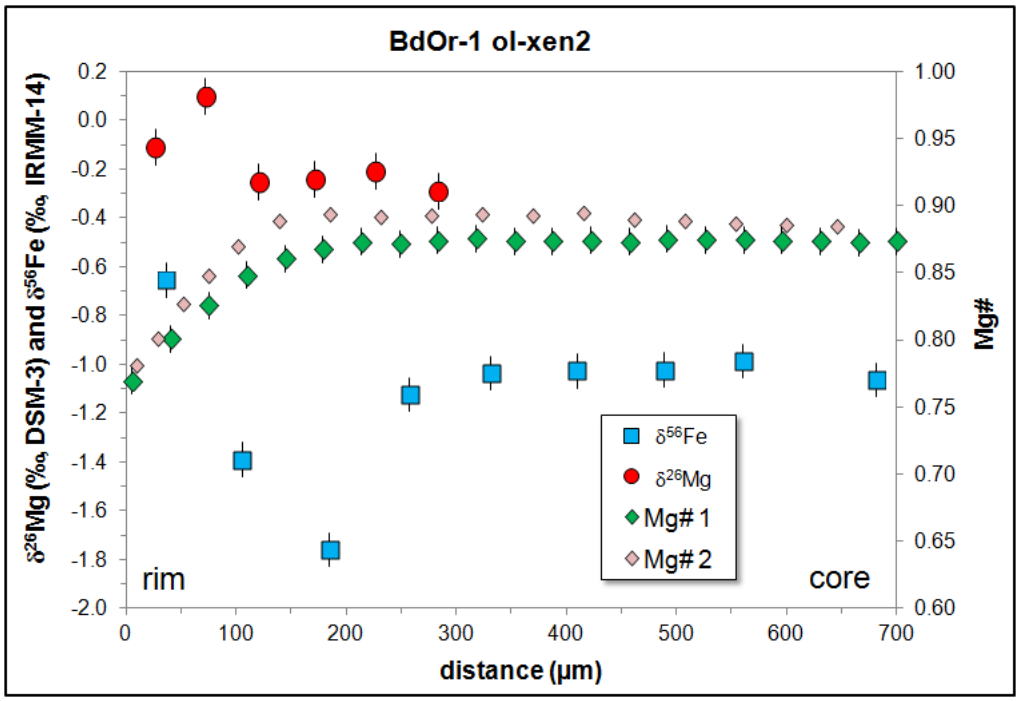

Figure A-II.5: Fe-Mg chemical and isotopic rim-to-core profiles for a normally zoned mantle olivine from the Massif Central. Note: Mg# 2 is the Fe-Mg chemical profile along the Mg isotopic traverse based on the analysis of a BSE image using the software ImageJ (e.g., Schneider et al., 2012).

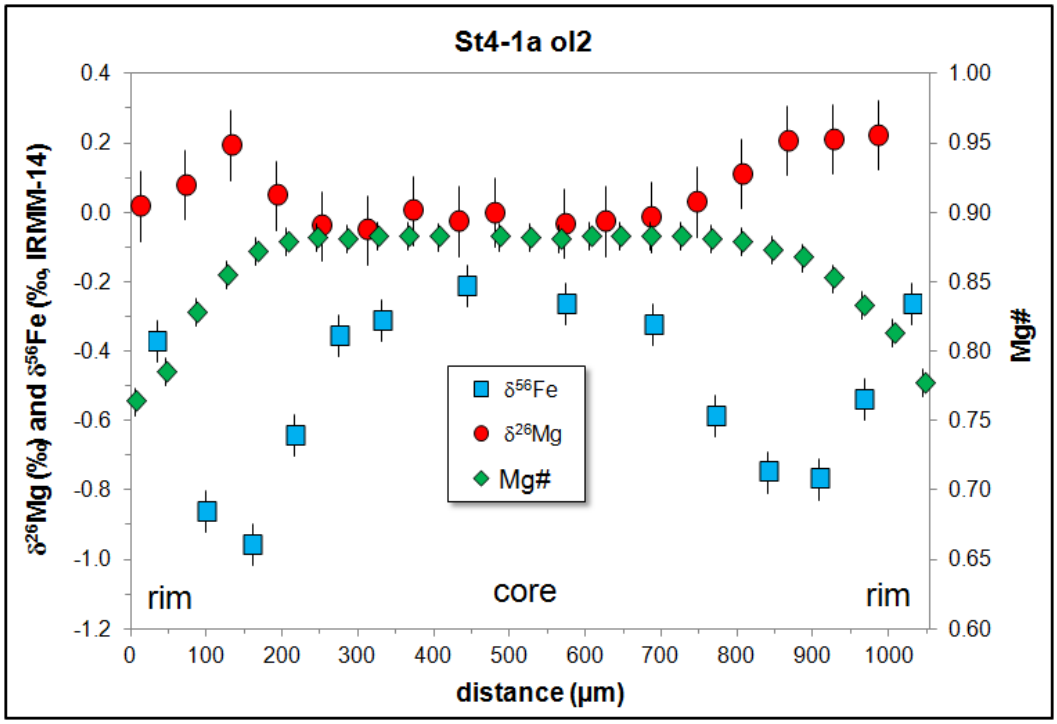

Figure A-II.6: Fe-Mg chemical and isotopic profiles across a normally zoned olivine phenocryst from the Massif Central. Note: the Mg isotopic composition of the core is set at 0‰, because the Mg isotopic profile was obtained by running a line scan from one rim to the core to the opposing rim.

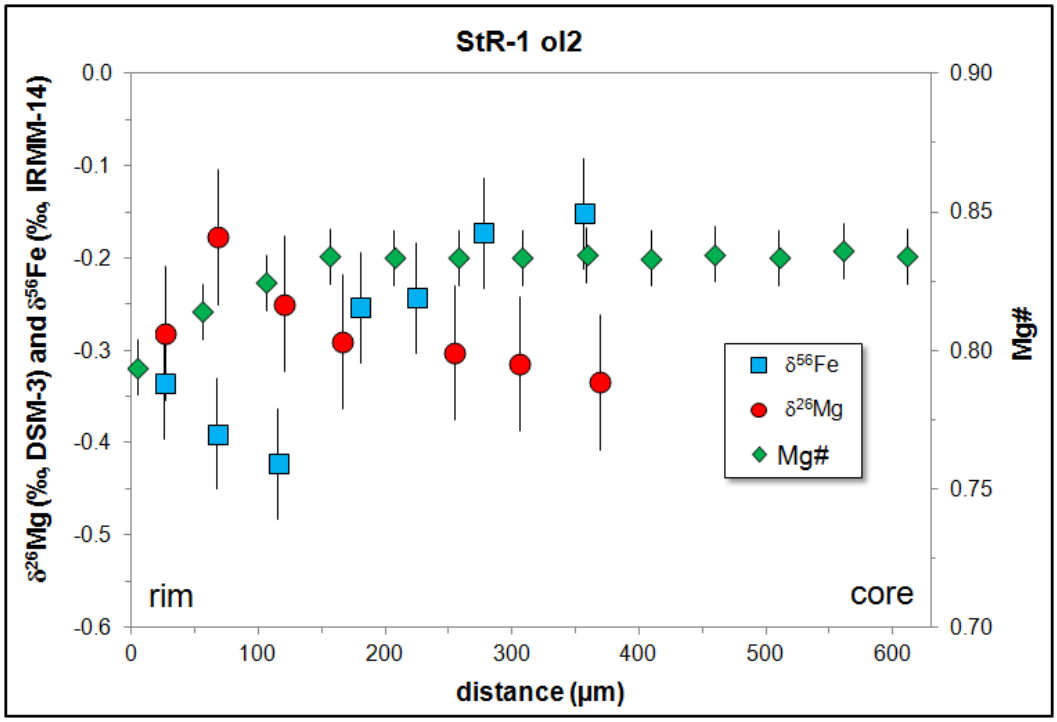

Figure A-II.7: Fe-Mg chemical and isotopic rim-to-core profiles for a normally zoned olivine phenocryst from the Massif Central. Error bars represent the analytical uncertainty (2 SD) during one analytical session.

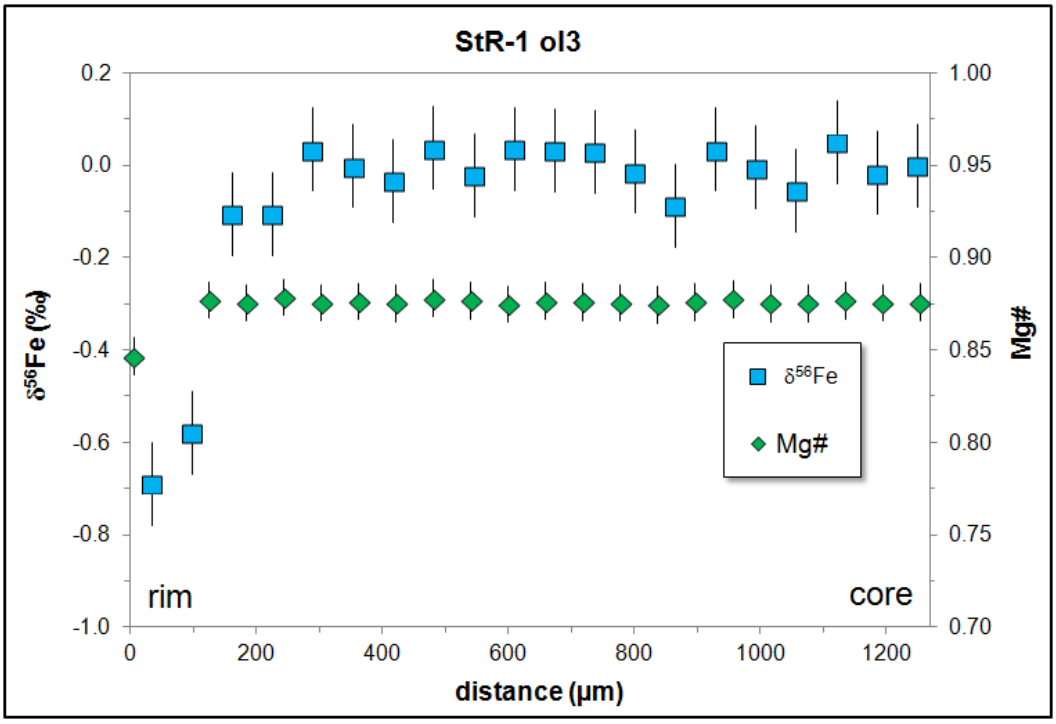

Figure A-II.8: Fe-Mg chemical and isotopic rim-to-core profiles for a normally zoned olivine phenocryst from the Massif Central. Note: the Fe isotopic composition of the core is set at 0‰, because the Fe isotopic profile was obtained by running a line scan from the rim to the core twice

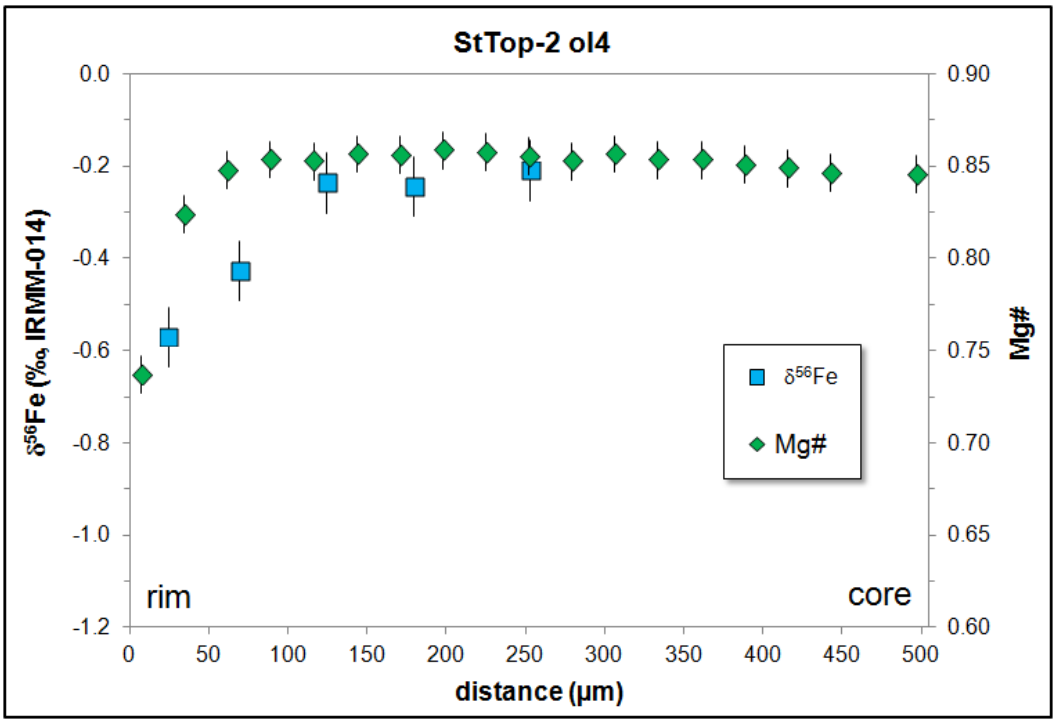

Figure A-II.9: Fe-Mg chemical and isotopic rim-to-core profiles for a normally zoned olivine phenocryst from the Massif Central. Error bars represent the analytical uncertainty (2 SD) during one analytical session.

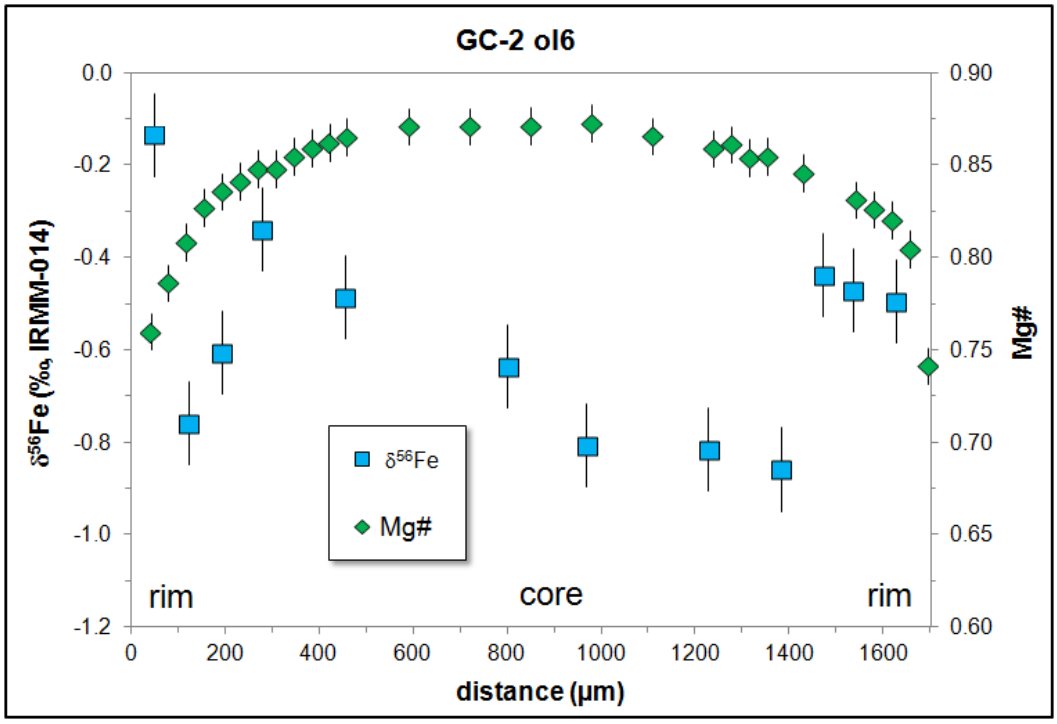

Figure A-II.10: Fe-Mg chemical and isotopic profiles across a normally zoned olivine phenocryst from Gran Canaria. Error bars represent the analytical uncertainty (2 SD) during one analytical session.

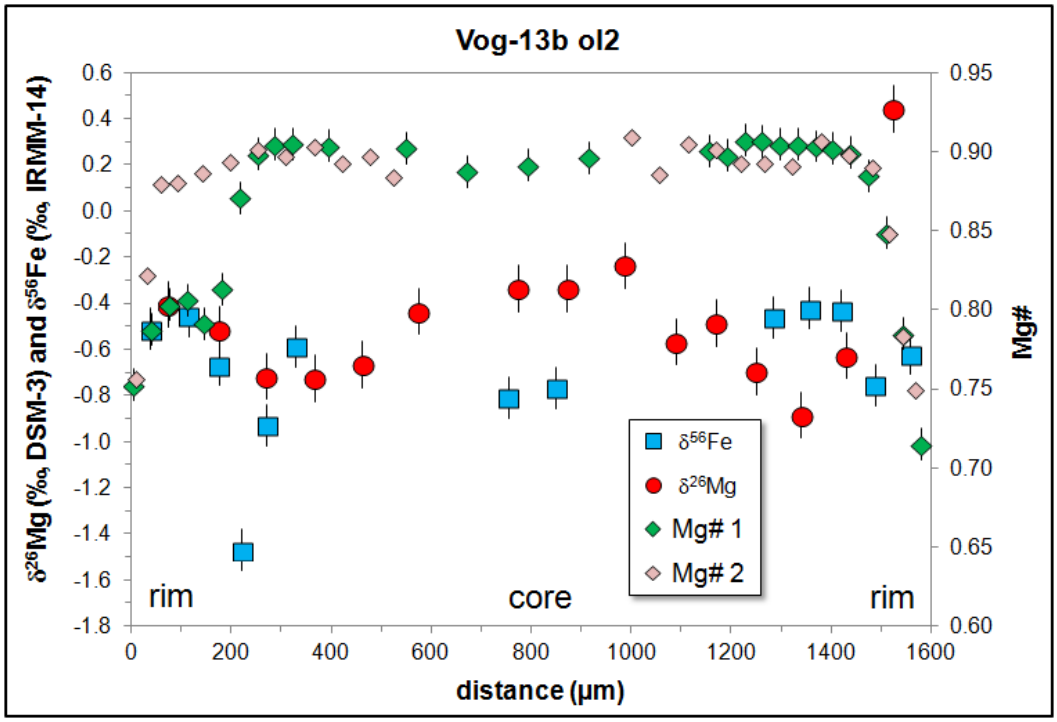

Figure A-II.11: Fe-Mg chemical and isotopic profiles across a normally zoned olivine xenocryst from the Vogelsberg volcanic region. Note: Mg# 2 is the Fe-Mg chemical profile along the Mg isotopic traverse based on the analysis of a BSE image using the software ImageJ (e.g., Schneider et al., 2012).

Supplementary Tables

For “intra-plate” olivines and clinopyroxenes investigated in this study, major element concentrations obtained by EMP analyses, Fe- and Mg isotope data acquired by fs-LA-MC-ICP-MS, and EBSD-data are given in Tables A-II.1 and A-II.2. These tables are attached as an electronic Excel-file (“Tables_in_Appendix.xlsx”).

Appendix III *

*corresponds to Chapter III of this dissertation

Supplementary Tables

For olivines, clinopyroxenes and basaltic glass in MORBs investigated in this study, major element concentrations obtained by EMP analyses, Fe- and Mg isotope data acquired by fs-LA-MC-ICP-MS, and EBSD-data are given in Tables A-III.1, A-III.2 and A-III.3. These tables are attached as an electronic Excel-file ("Tables_in_Appendix.xlsx").

Supplementary figures

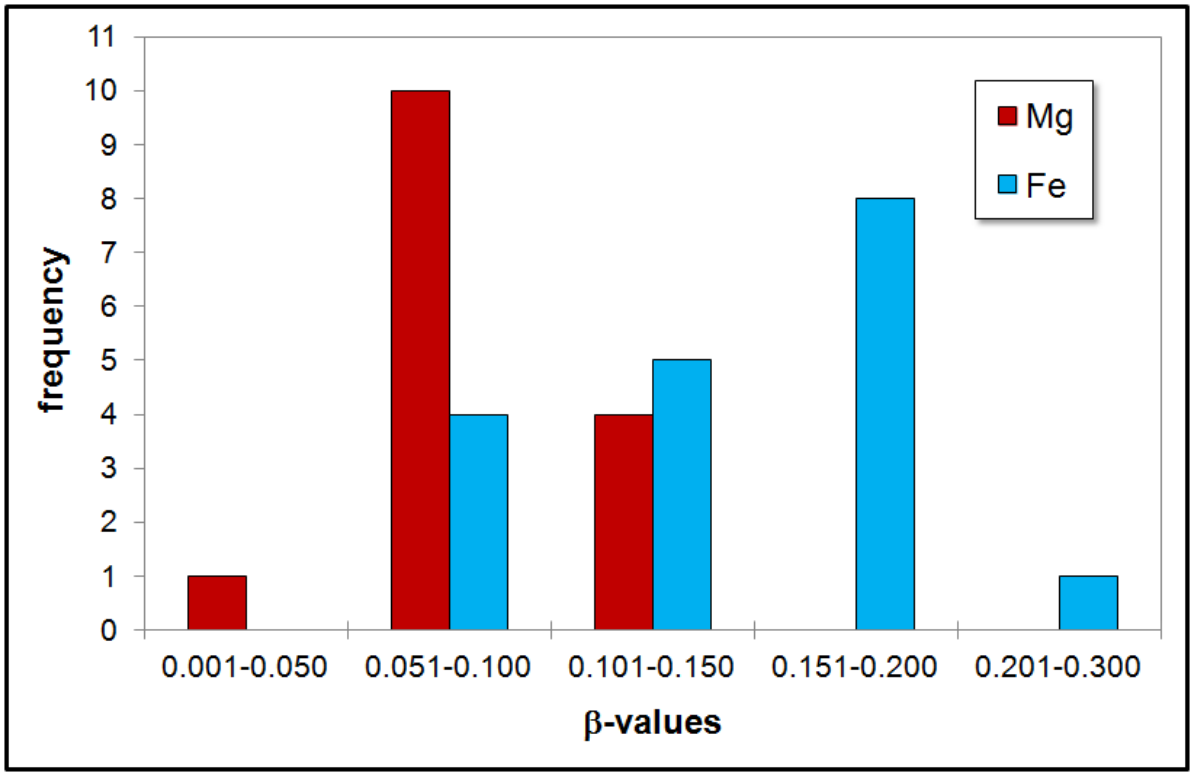

Figure A-III.1: Histogram of estimated β-values for Fe and Mg based on the modeling of diffusion-generated isotopic zoning in olivines from the Massif Central volcanic region, Tenerife, and mid-ocean ridges.

The following plots show Fe-Mg chemical and isotopic profiles across MORB olivines investigated in this study. Data are from Table A-III.1 (see above).

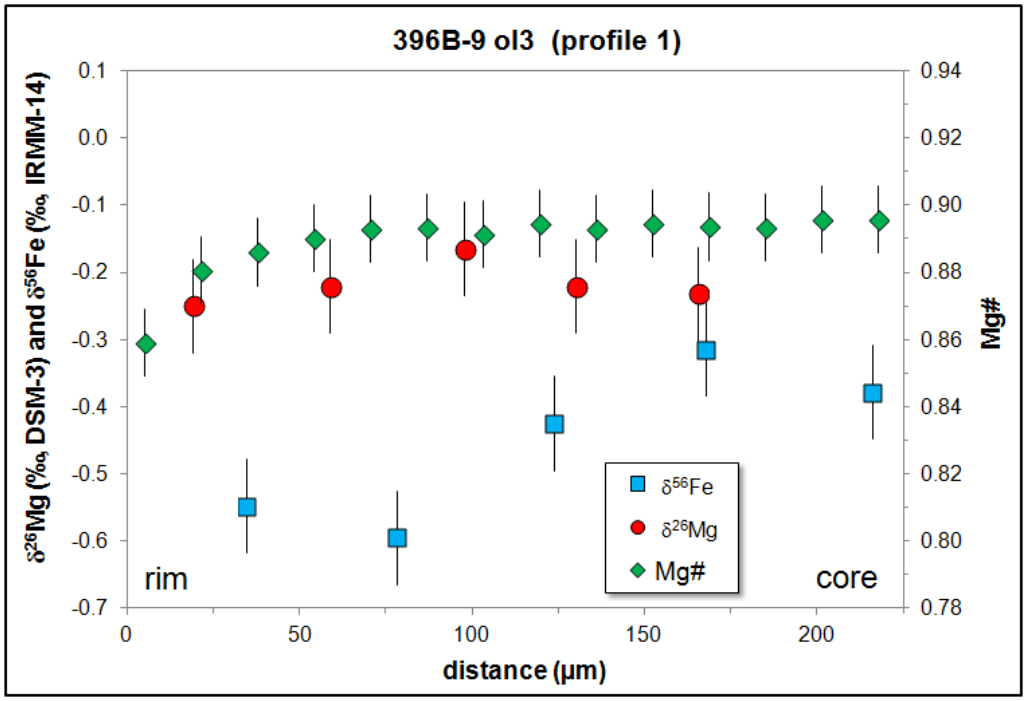

Figure A-III.2: Fe-Mg chemical and isotopic rim-to-core profiles for a normally zoned olivine from the MAR (sample 396B 22-R-1 19-21cm). Error bars represent the analytical uncertainty (2 SD) during one analytical session.

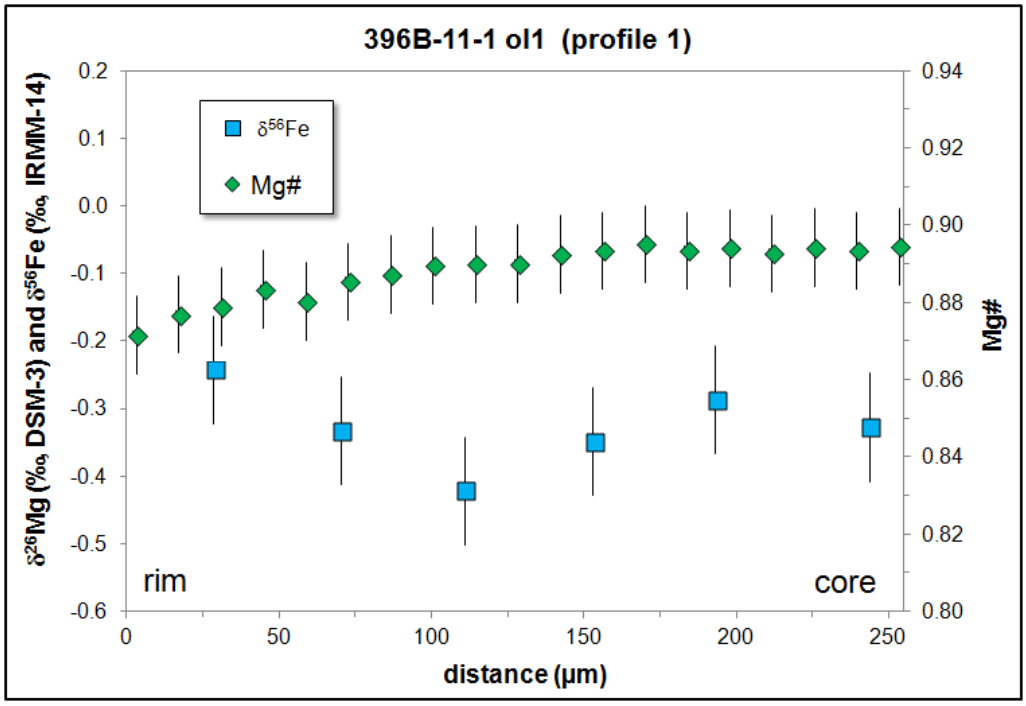

Figure A-III.3: Fe-Mg chemical and isotopic rim-to-core profiles for a normally zoned olivine from the MAR (sample 396B 22-R-1 109-111cm).

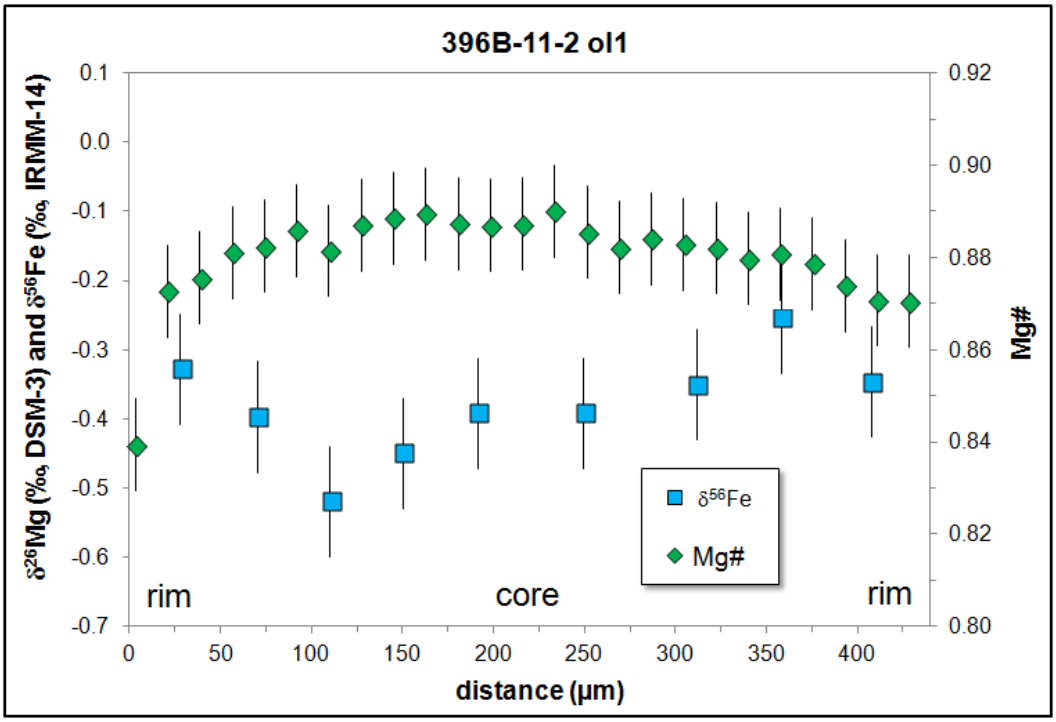

Figure A-III.4: Fe-Mg chemical and isotopic profiles across a normally zoned olivine from the MAR (sample 396B 22-R-1 109-111cm). Error bars represent the analytical uncertainty (2 SD) during one analytical session.

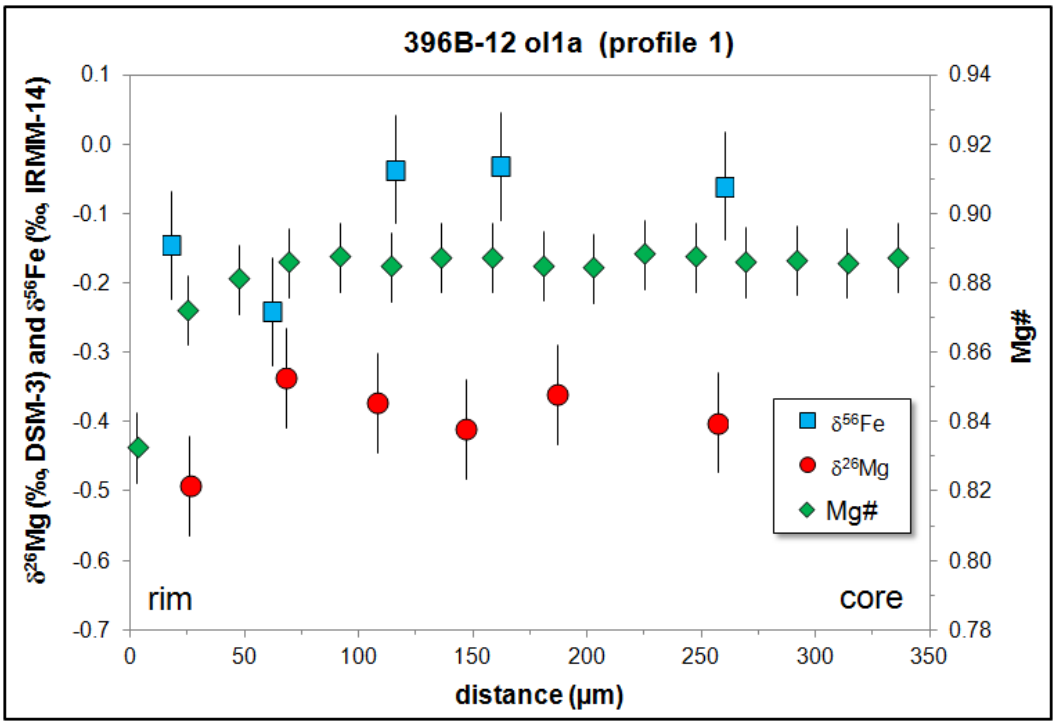

Figure A-III.5: Fe-Mg chemical and isotopic rim-to-core profiles for a normally zoned olivine from the MAR (sample 396B 22-R-2 6-8cm). Error bars represent the analytical uncertainty (2 SD) during one analytical session.

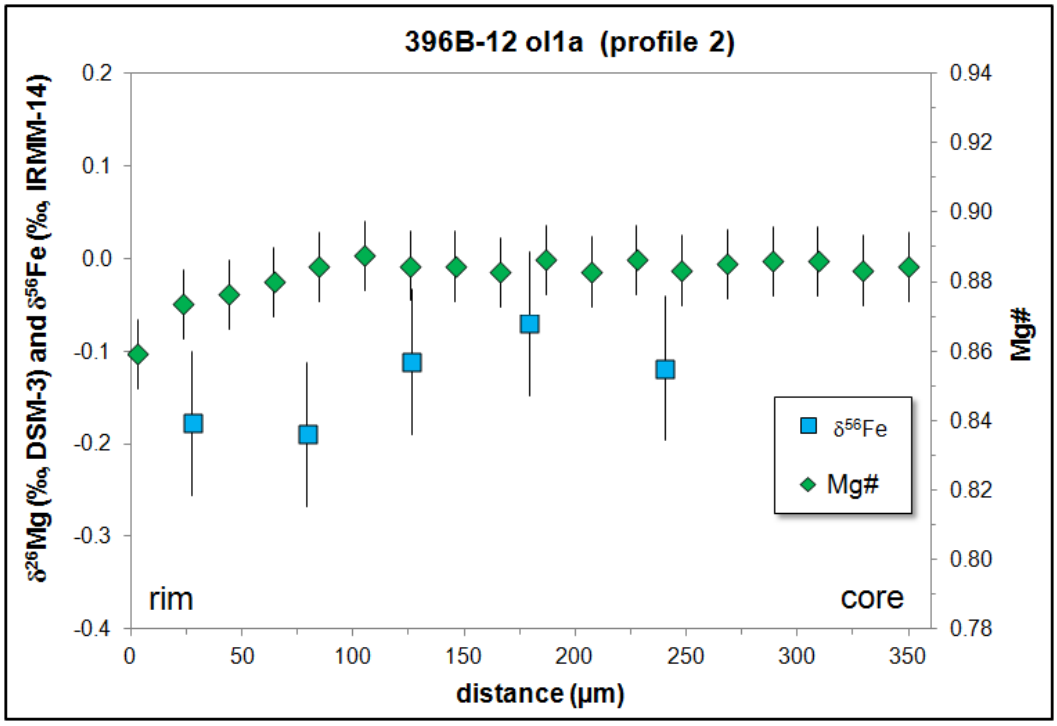

Figure A-III.6: Fe-Mg chemical and isotopic rim-to-core profiles for a normally zoned olivine from the MAR (sample 396B 22-R-2 6-8cm). Error bars represent the analytical uncertainty (2 SD) during one analytical session.

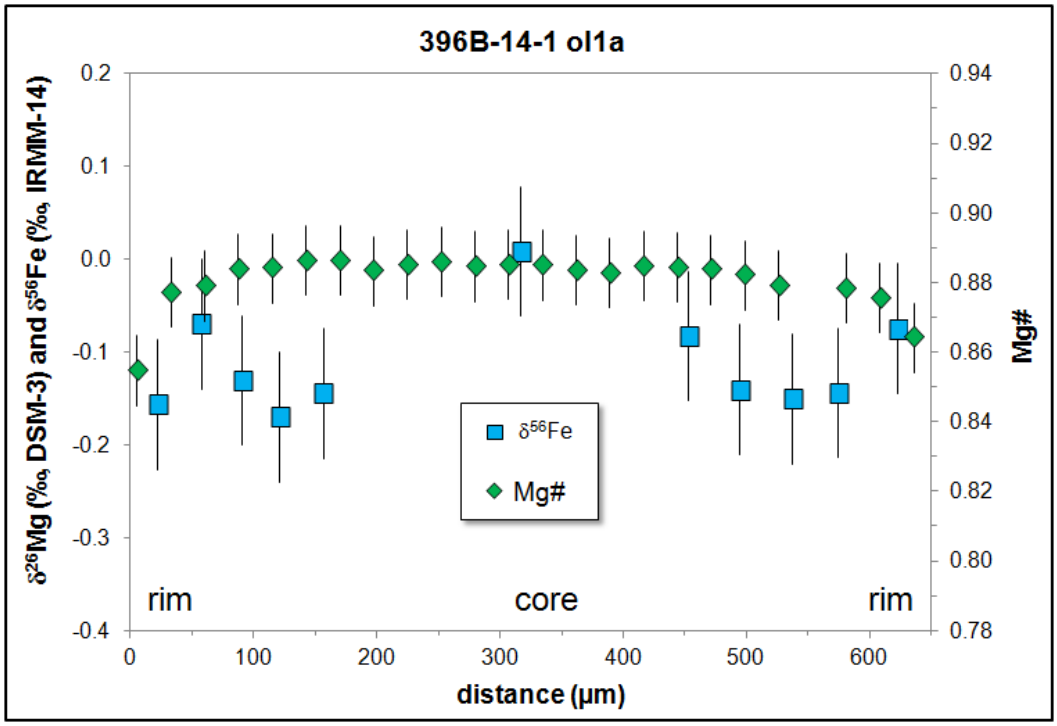

Figure A-III.7: Fe-Mg chemical and isotopic profiles across a normally zoned olivine from the MAR (sample 396B 22-R-2 126-127cm). Error bars represent the analytical uncertainty (2 SD) during one analytical session.

Appendix IV *

*corresponds to Chapter IV of this dissertation

Supplementary Tables

Major and trace element concentrations acquired by fs-LA-ICP-MS for olivines and basaltic reference glasses (BIR-1G and BCR-2G) are given in Tables A-IV.1 and A-IV.2. These tables are attached as an electronic Excel-file ("Tables_in_Appendix.xlsx").

Supplementary figures

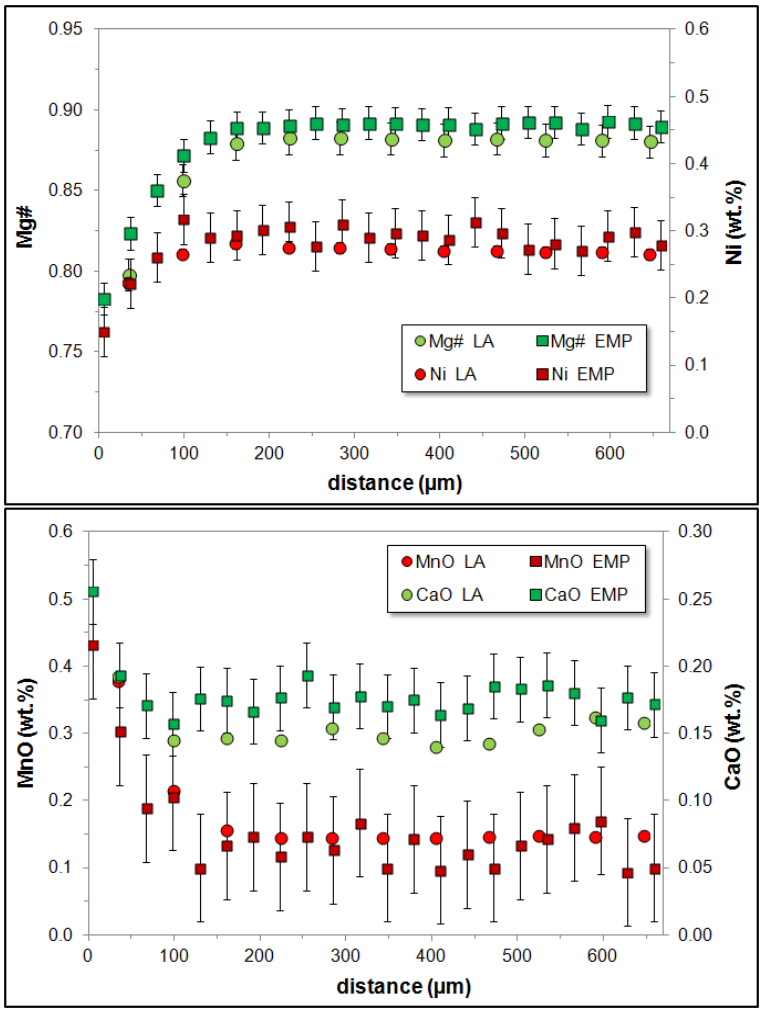

Figure A-IV.1: Representative concentration profiles for Fe-Mg (Mg#), Ni, MnO and CaO obtained by fs-LA-ICP-MS (LA) and by electron microprobe analyses (EMP), showing that the measured concentrations are identical (within analytical uncertainties) irrespective of which method was used. Error bars represent 2σ uncertainties and may be smaller than the symbol size.

The following plots show major and trace element profiles – obtained by fs-LA-sector field-ICP-MS – across MORB- and "intra-plate" olivines investigated in this study. The analytical uncertainties of the measured element concentrations is usually <3% (RSD), except for Li, Cr and the REE (<10%, RSD). Data are from Table A-IV.1 (see above).

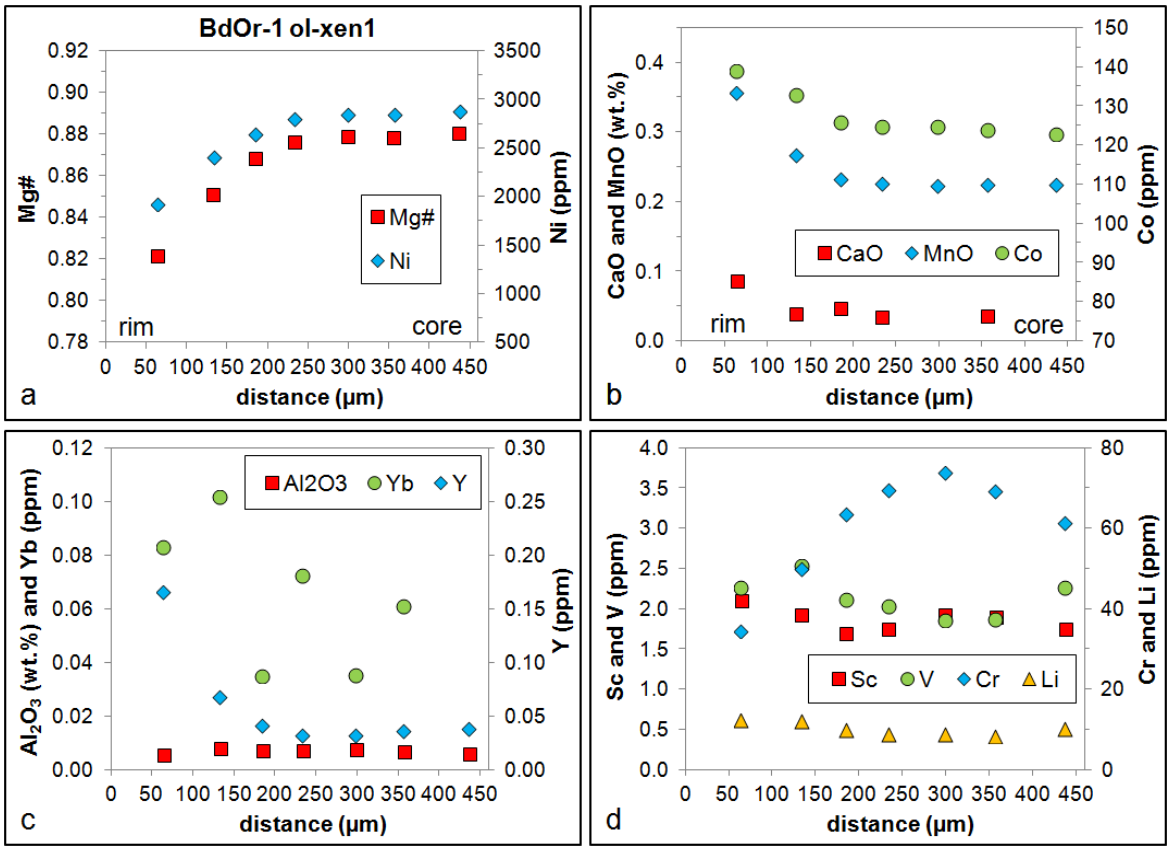

Figure A-IV.2: Mg#, minor and trace element rim-to-core profiles for a normally zoned mantle olivine from the Massif Central.

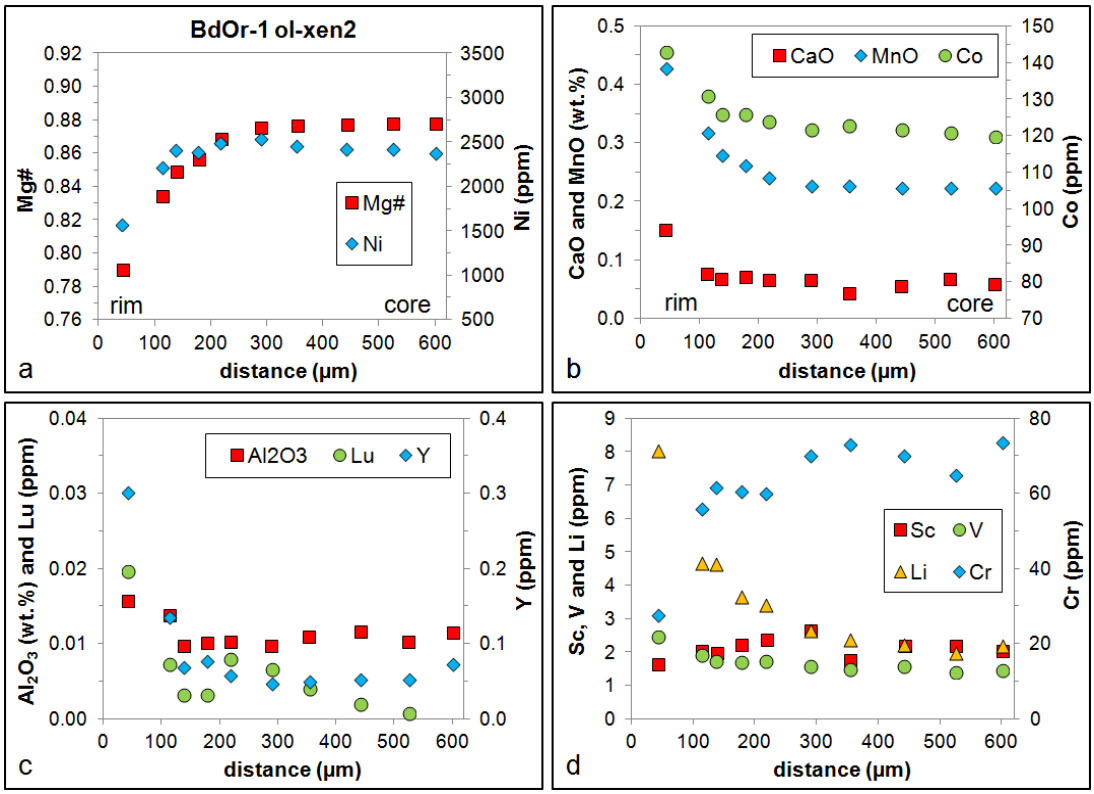

Figure A-IV.3: Mg#, minor and trace element rim-to-core profiles for a normally zoned mantle olivine from the Massif Central.

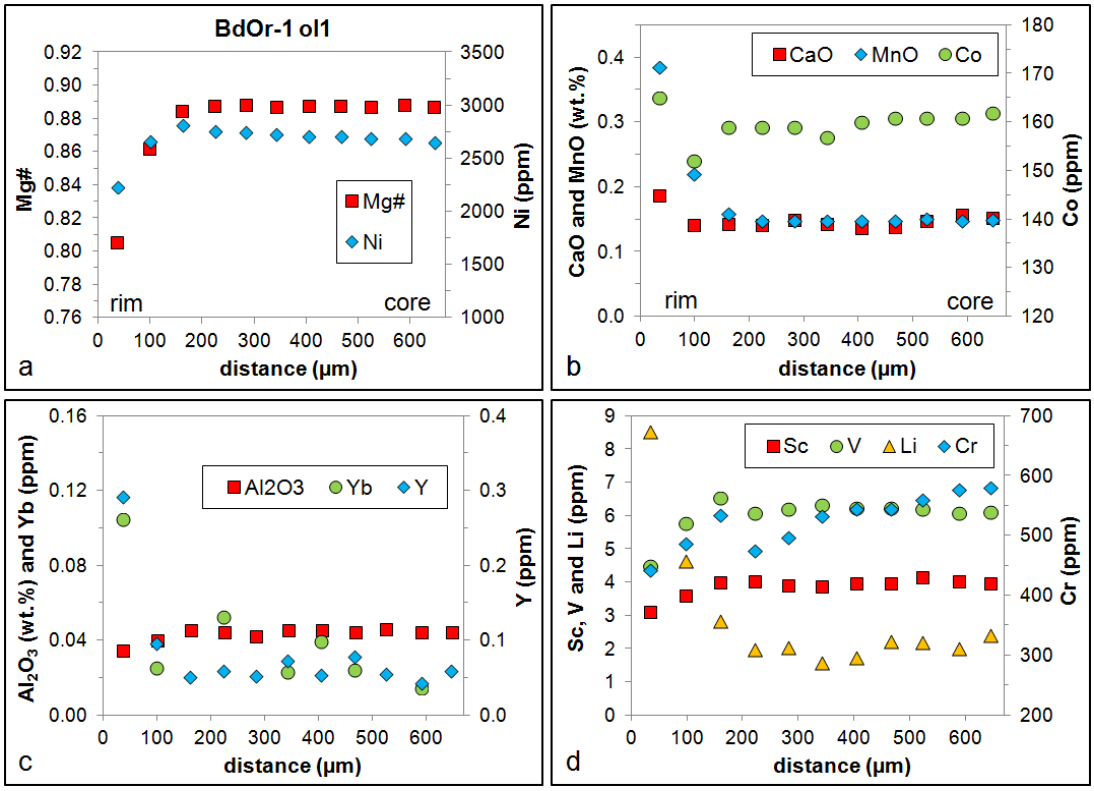

Figure A-IV.4: Mg#, minor and trace element rim-to-core profiles for a normally zoned olivine phenocryst from the Massif Central.

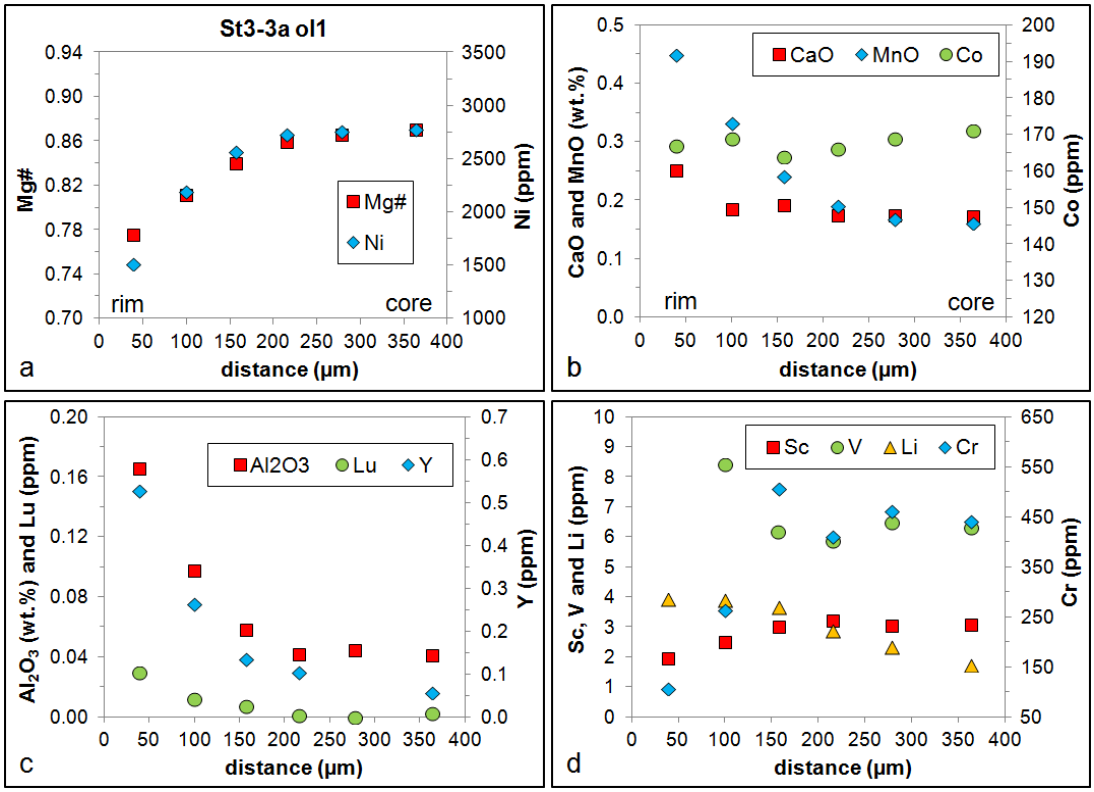

Figure A-IV.5: Mg#, minor and trace element rim-to-core profiles for a normally zoned olivine phenocryst from the Massif Central.

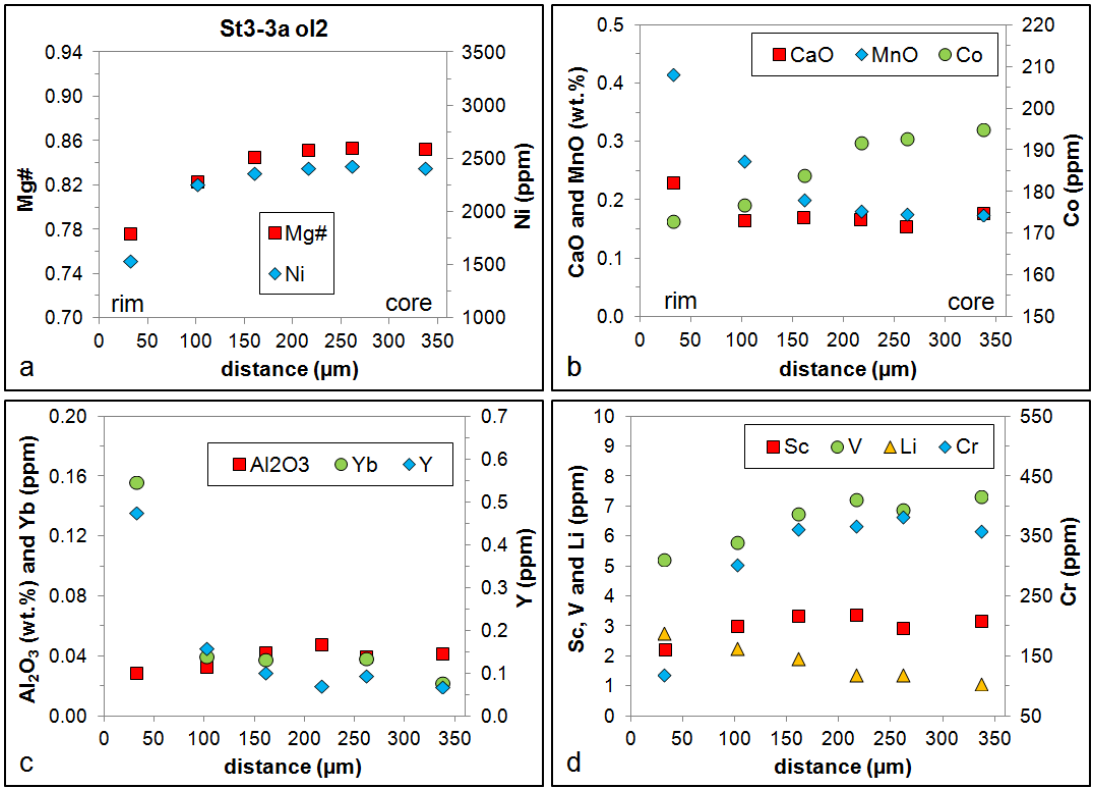

Figure A-IV.6: Mg#, minor and trace element rim-to-core profiles for a normally zoned olivine phenocryst from the Massif Central.

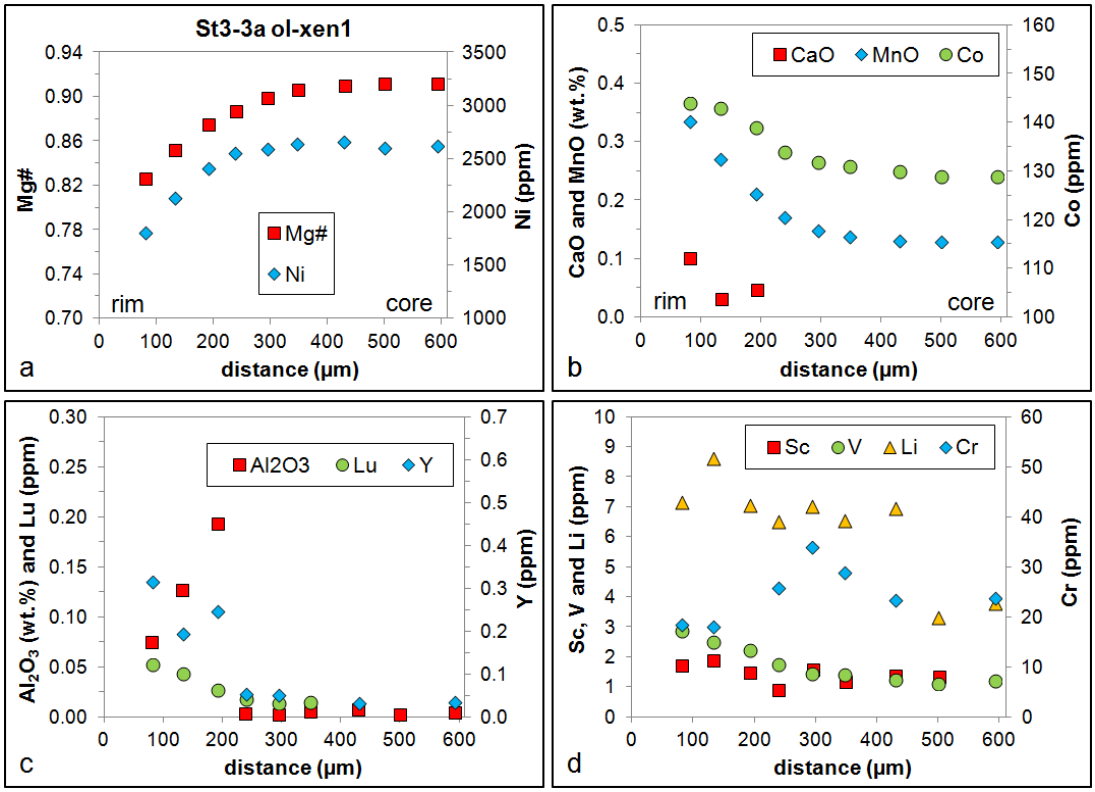

Figure A-IV.7: Mg#, minor and trace element rim-to-core profiles for a normally zoned mantle olivine from the Massif Central.

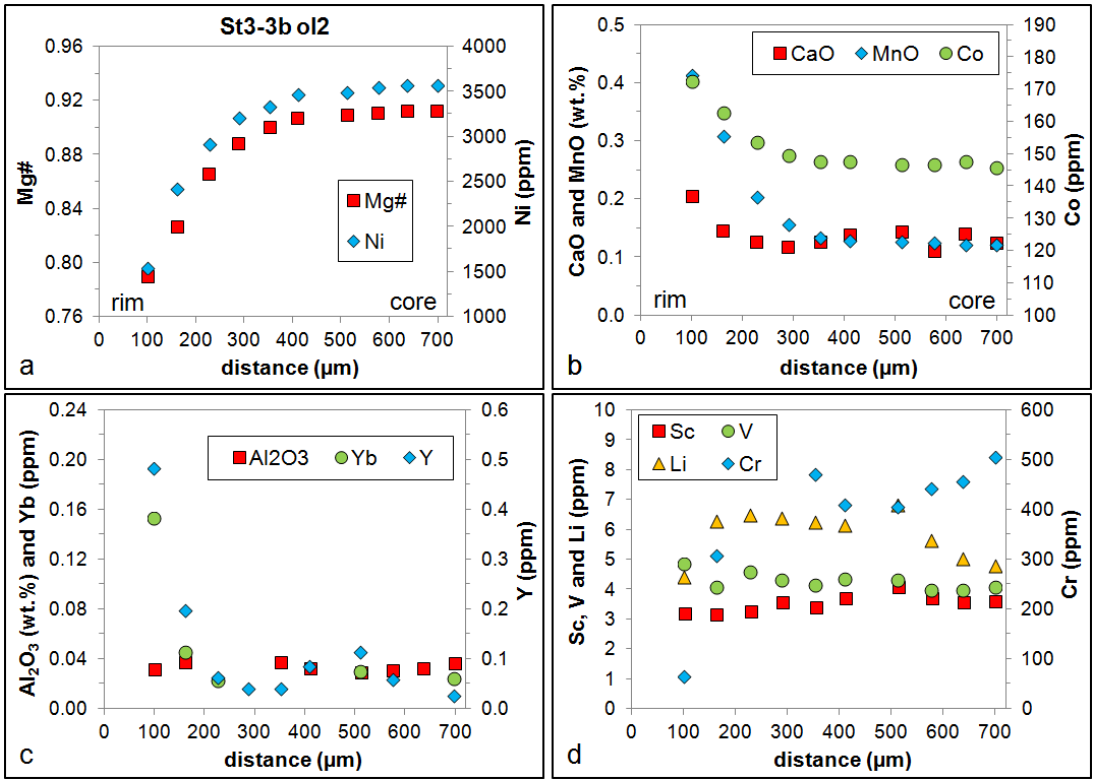

Figure A-IV.8: Mg#, minor and trace element rim-to-core profiles for a normally zoned olivine xenocryst from the Massif Central.

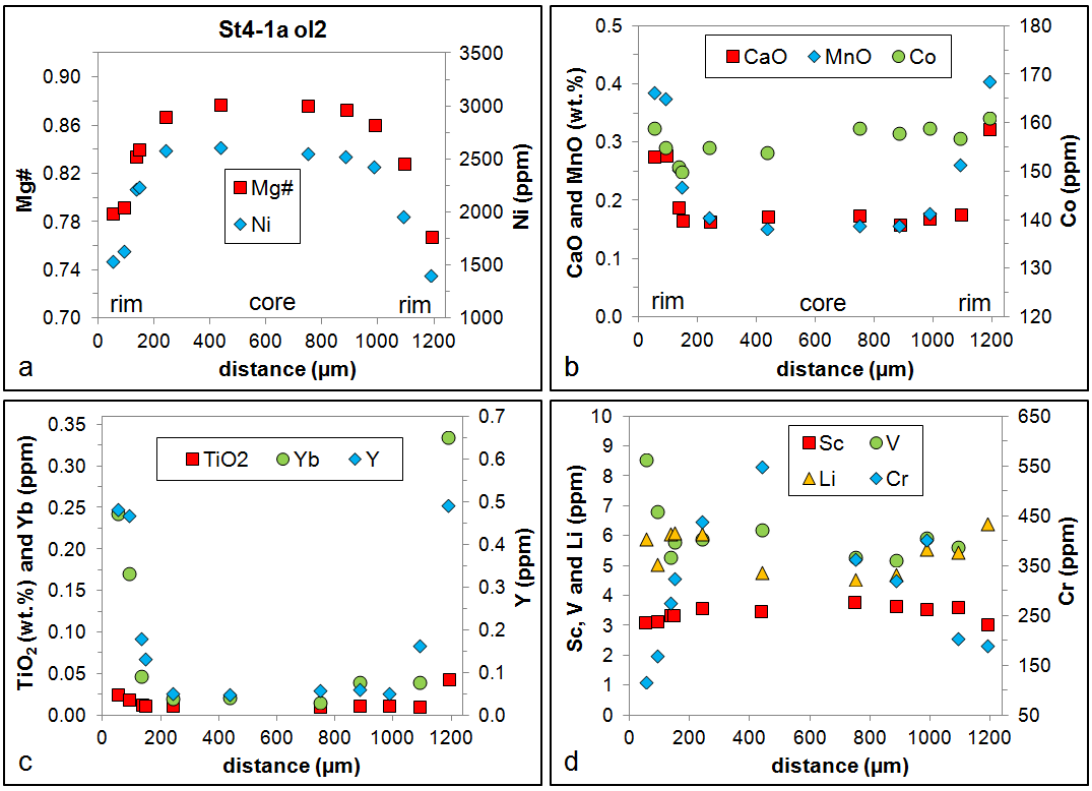

Figure A-IV.9: Mg#, minor and trace element profiles across a normally zoned olivine phenocryst from the Massif Central.

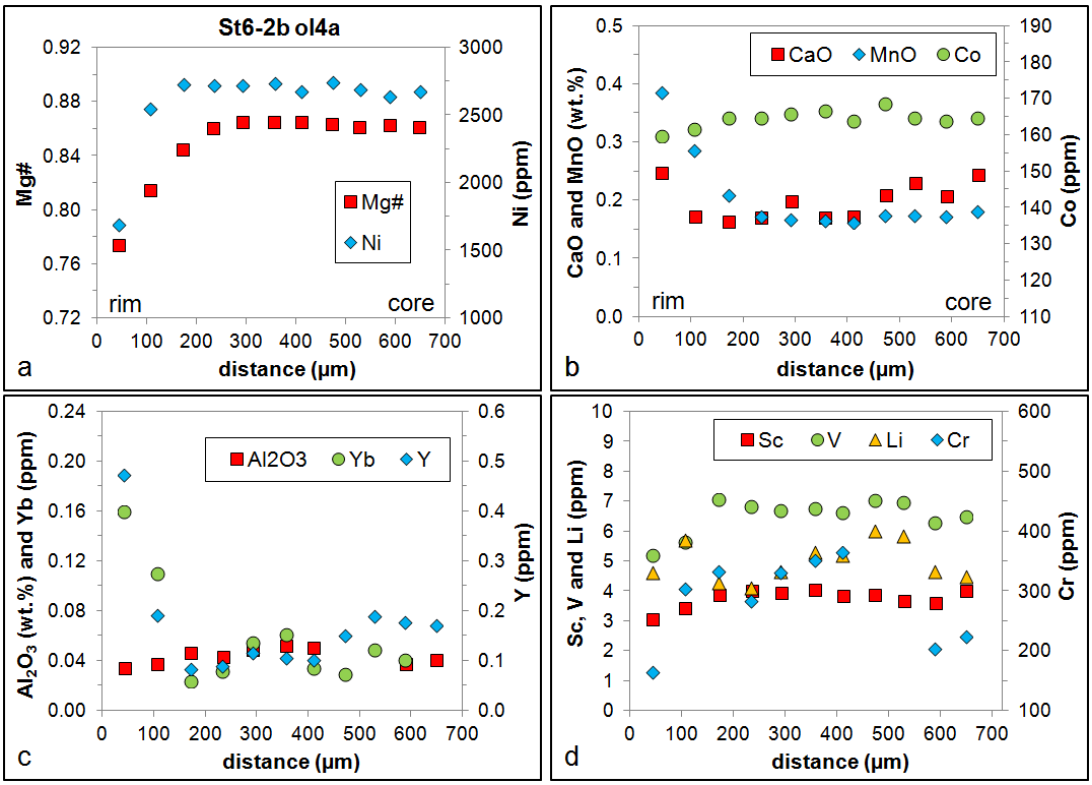

Figure A-IV.10: Mg#, minor and trace element rim-to-core profiles for a normally zoned olivine phenocryst from the Massif Central.

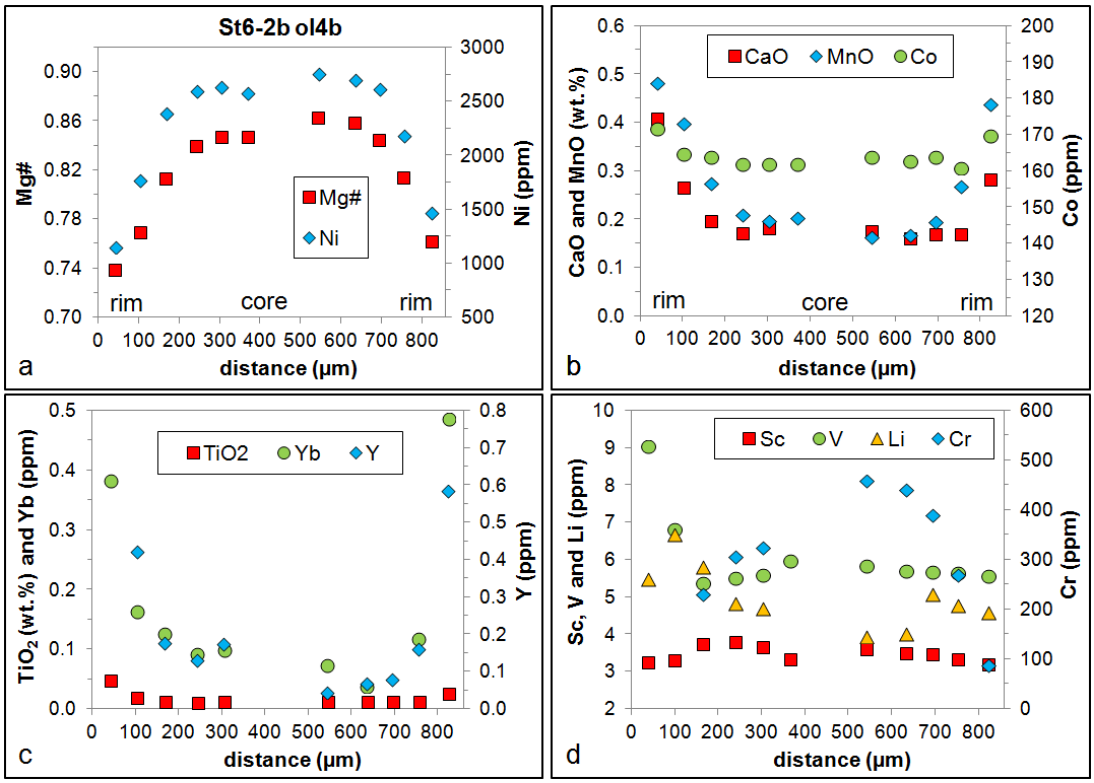

Figure A-IV.11: Mg#, minor and trace element profiles across a normally zoned olivine phenocryst from the Massif Central.

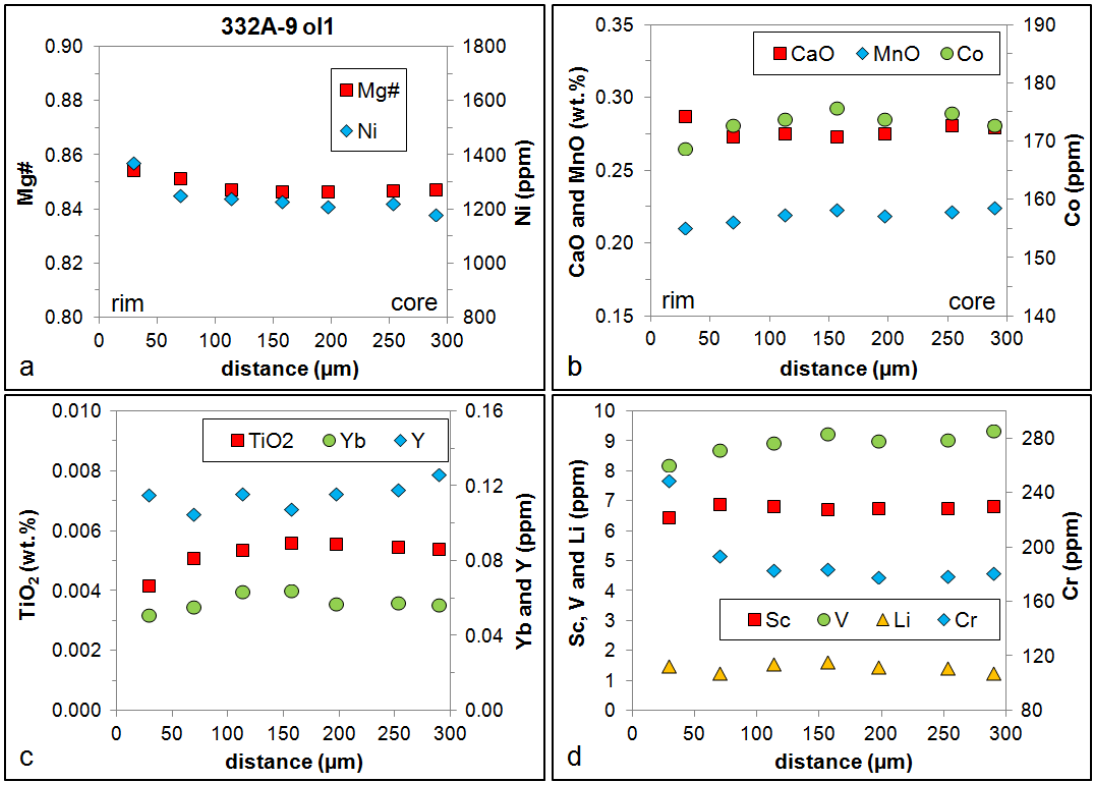

Figure A-IV.12: Mg#, minor and trace element rim-to-core profiles for a reversely/multiply zoned olivine from the MAR (sample 332A 36-R-1 72-73cm).

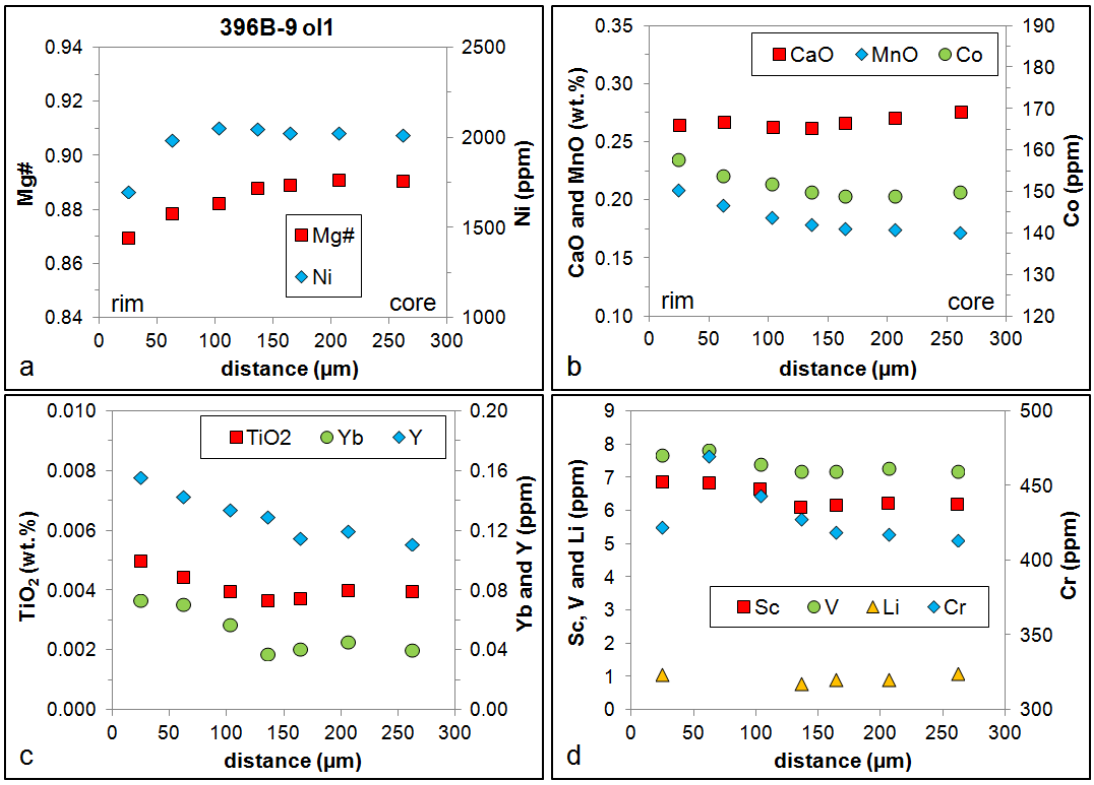

Figure A-IV.13: Mg#, minor and trace element rim-to-core profiles for a normally zoned olivine from the MAR (sample 396B 22-R-1 19-21cm).

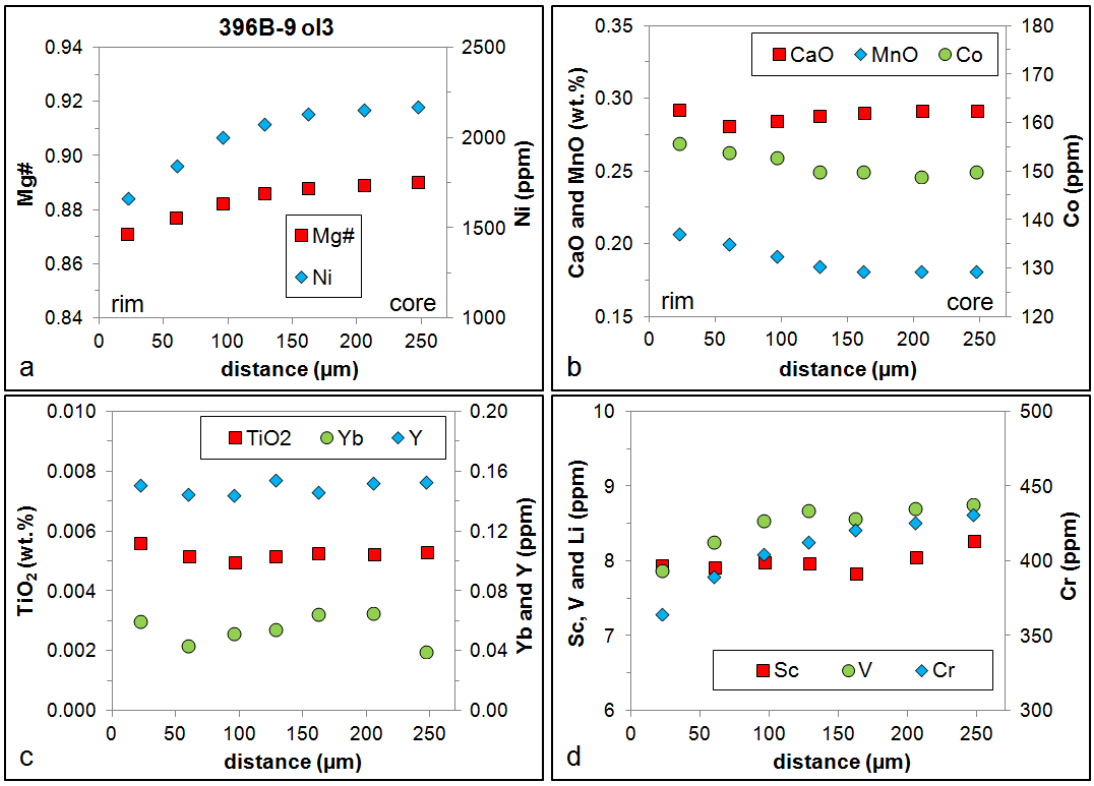

Figure A-IV.14: Mg#, minor and trace element rim-to-core profiles for a normally zoned olivine from the MAR (sample 396B 22-R-1 19-21cm).

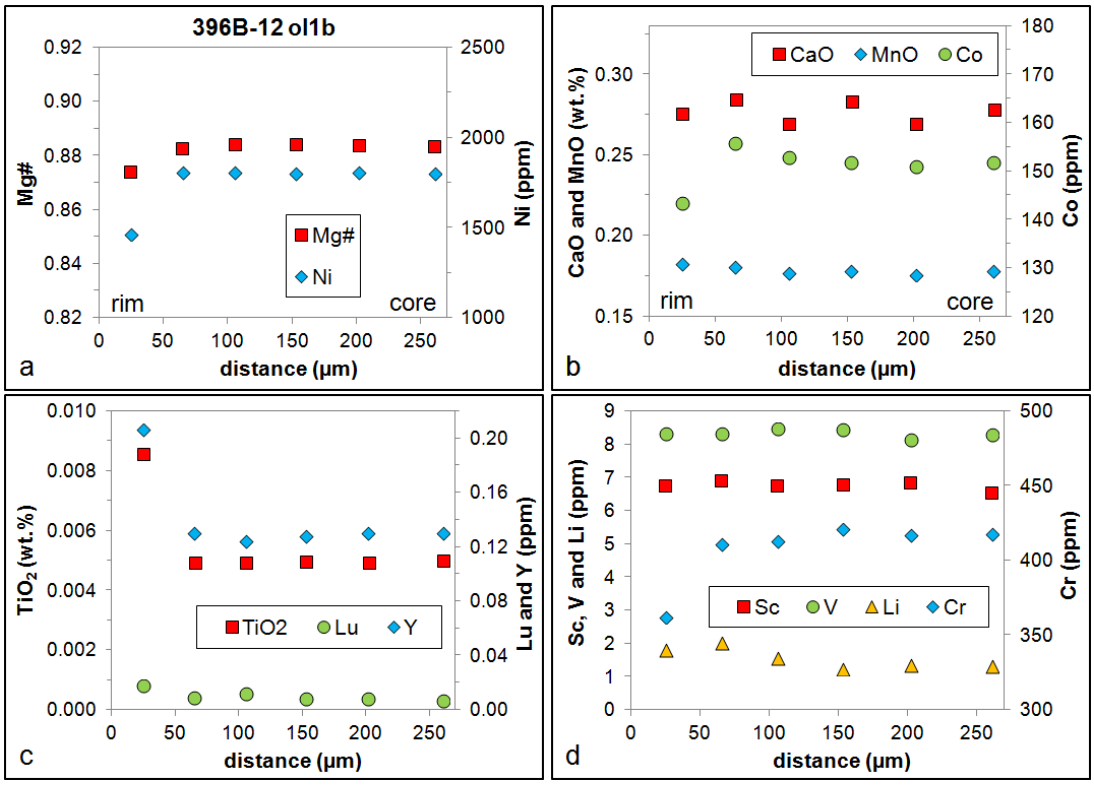

Figure A-IV.15: Mg#, minor and trace element rim-to-core profiles for a normally zoned olivine from the MAR (sample 396B 22-R-2 6-8cm).

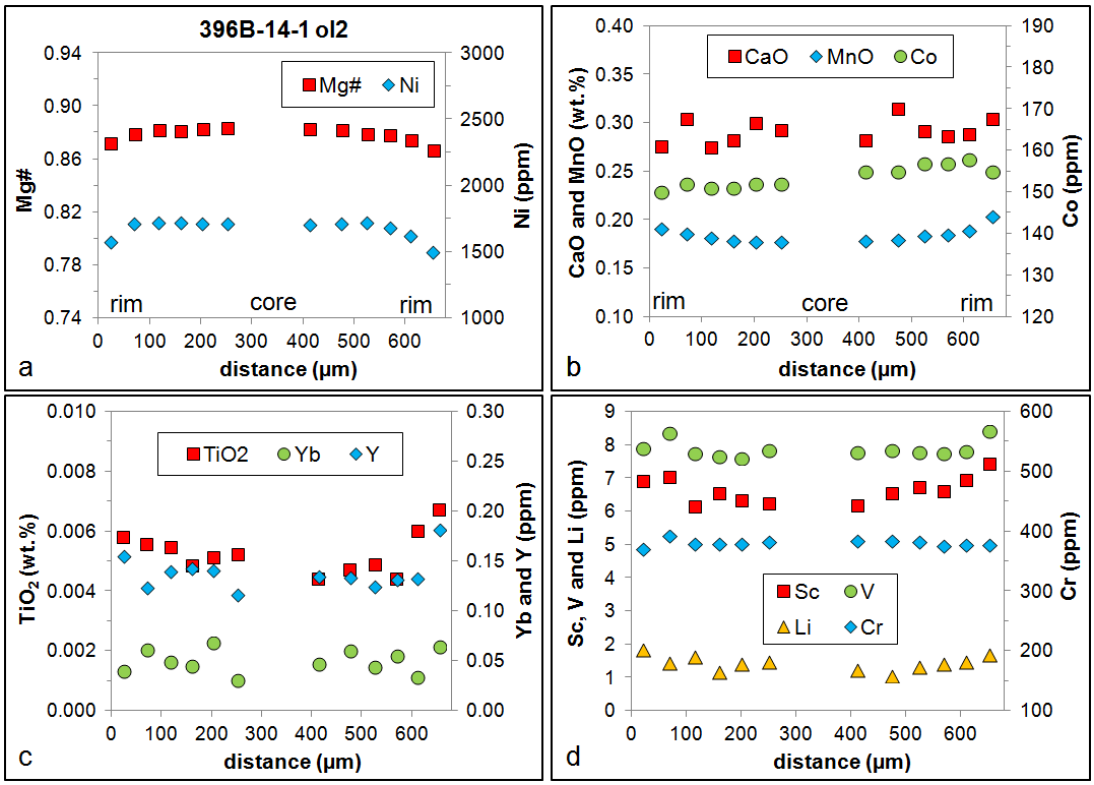

Figure A-IV.16: Mg#, minor and trace element profiles across a normally zoned olivine from the MAR (sample 396B 22-R-2 126-127cm).

Acknowledgements

First of all, I want to thank Prof. Dr. Stefan Weyer for giving me the opportunity to perform this doctoral research study, for sharing his extensive knowledge of (isotope) geochemistry, mass spectrometry and magmatic processes during always constructive discussions, and for his friendly support during the last four years.

Special thanks also go to PD Dr. Ingo Horn who excellently introduced me to isotope analyses by fs-LA-(MC-)ICP-MS and who is always ready to help if analytical problems arise. Furthermore, I want to thank Ingo for reviewing this dissertation and for keeping "the machines" up and running.

I also want to express my gratitude to Dr. Ralf Dohmen for skillfully introducing me to exciting aspects of diffusion and diffusion modeling, for inspiring scientific exchange on diffusion-driven isotope fractionation, and for the good time I had in Bochum.

I want to thank the members of the examination board, Prof. Dr. Sumit Chakraborty, Prof. Dr. Francois Holtz and Prof. Dr. Ulrich Heimhofer, for reviewing and examining my PhD thesis.

Sincere thanks are given to Dr. Stephan Schuth for managing the field trip in the Massif Central and for his help during sampling there. I want to thank Stephan also for valuable discussions on sample preparation and analytical issues and for his help at the ICP-MS.

I thank the Deutsche Forschungsgemeinschaft for funding this research study (grant # WE 2850/11).

Importantly, I dearly thank my parents for their permanent and absolute support and Katharina for the wonderful time I can spend with her and our children.

Many thanks also go to all the people at the Institut für Mineralogie – especially the geochemistry group – for the enjoyable working atmosphere.

Sincere thanks are given to Dr. Rolf Neuser for his indispensable assistance during EBSD analyses at the Ruhr-Universität Bochum.

André Stechern is thanked for his help during sampling in the Massif Central, France.

Otto Dietrich and Julian Feige are thanked for preparing sample mounts and thin sections.

Albert Galy kindly provided the Mg reference solutions DSM-3 and Cambridge-1.

I thank Frank Wombacher for his valuable advice concerning the ion exchange chromatography.

Thoughtful reviews and comments by two anonymous reviewers and by Paul Sylvester greatly improved the manuscript dealing with the Fe- and Mg isotopic compositions of the silicate reference glasses (Chapter I of this dissertation).

Klaus Roeller and Claudia Trepmann are thanked for providing the software Stereo32.

Figure 1 was generated using CrystalMaker®: a crystal and molecular structures program for Mac and Windows. CrystalMaker Software Ltd, Oxford, England. (www.crystalmaker.com)

Curriculum Vitae

Personal Details

Martin Oeser-Rabe

Lützekenstr. 18
30625 Hannover
born in Siegburg on 2 August 1984
married with Katharina Rabe
one daughter
one son

Higher Education and Work Experience

01/2011 – today	Research assistant at the Institut für Mineralogie of the Leibniz Universität Hannover (Geochemistry Group)
01/2011 – today	PhD student at the Institut für Mineralogie of the Leibniz Universität Hannover under supervision of Prof. Dr. Stefan Weyer (Geochemistry Group) • Project: Fe- und Mg isotope fractionation during magmatic differentiation
10/2008 – 12/2010	Studies of Earth Sciences at the Westfälische Wilhelms-Universität Münster • degree: Master of Science • grade: 1.1 • title of master's thesis: A Sulfur Isotopic Profile through the Oman Ophiolite
10/2005 – 09/2008	Studies of Earth Sciences at the Westfälische Wilhelms-Universität Münster • degree: Bachelor of Science • grade: 1.6

Education

05/2011	Apprenticeship as first-aider

07/2004 – 03/2005	Civilian Service at „Alten- und Pflegeheim Haus Tusculum“ in Ruppichteroth-Broscheid
06/2004	Abitur – higher education entrance qualification at the „Antoniuskolleg“ in Neunkirchen-Seelscheid • grade: 1.0 • intensive courses: English, Mathematics
09/2001 – 05/2002	School year in the USA at Lawrence Academy in Groton, Massachusetts
08/1995 – 05/2004	High School “Antoniuskolleg” in Neunkirchen-Seelscheid
08/1991 – 07/1995	Primary School in Neunkirchen-Seelscheid

Internships and Field Work

09/2011	Geological field trip to Neogene and Quarternary volcanic regions in western Europe (Eifel, Kaiserstuhl, Massif Central) • sampling for my PhD project
01/2010 und 01/2012	Geological field trips in northern Oman • guide: Prof. Dr. Jürgen Koepke, Leibniz Universität Hannover • duration: 2 weeks • geology of the Oman Ophiolite • sampling for research projects
02/2008 – 03/2008	GeoForschungsZentrum Potsdam • research internship • duration: 6 weeks • department 4 „Chemie der Erde“
07/2005 – 08/2005	Consulting Engineers “Bieske und Partner” in Lohmar • work internship • duration: 8 weeks • department „Hydrogeologie und Wassergewinnung“

Language Skills

German	native
English	very good, both oral and written
Spanish	basics

Additional Skills

Good knowledge of MC-ICP-MS, HR-ICP-MS, laser ablation, and sample preparation in clean lab facilities

Basic knowledge of ICP-OES, and electron microprobe analyses

Good knowledge of Microsoft Office and CorelDraw

Basic knowledge of MATLAB and ImageJ

List of Publications

Journals

Oeser M., Dohmen R., Horn I., Schuth S., Weyer S. (in press) Processes and time scales of magmatic evolution as revealed by Fe-Mg chemical and isotopic zoning in natural olivines. *Geochimica et Cosmochimica Acta*, DOI: 10.1016/j.gca.2015.01.025

Oeser M., Weyer S., Horn I., Schuth S. (2014). High-Precision Fe and Mg Isotope Ratios of Silicate Reference Glasses Determined *In Situ* by Femtosecond LA-MC-ICP-MS and by Solution Nebulisation MC-ICP-MS. *Geostandards and Geoanalytical Research*, v. 38, 311-328.

Oeser M., Strauss H., Wolff P.E., Koepke J., Peters M., Garbe-Schönberg D., Dietrich M. (2012). A Profile of Multiple Sulfur Isotopes through the Oman Ophiolite. *Chemical Geology*, v. 312-313, 27-46.

Strauss H., Bast R., Cording A., Fugmann A., Diekrup D., Garbe-Schönberg D., Lutter A., **Oeser M.**, Rabe K., Reinke D., Teichert B., Westernströer U. (2012). Sulfur cycling in marine sediments revealed by multiple stable sulfur isotope data. *Isotopes in Environmental and Health Studies*, v. 48, 166-179.

Abstracts

Oeser M., Weyer S., Dohmen R., Horn I., Schuth S. (2014). Time scales of magma evolution derived from diffusion modeling of Fe-Mg chemical and isotopic zoning in natural olivines. *IODP/ICDP Kolloquium*, Erlangen (Germany).

Oeser M., Weyer S., Dohmen R., Horn I., Schuth S. (2013). Using Coupled Fe-Mg Chemical and Isotopic Diffusion Profiles to Model Magma Residence Times of Crystals. *Mineralogical Magazine*, v. 77 (5), 1879.

Oeser M., Weyer S., Dohmen R., Horn I., Schuth S. (2013). Estimating magma residence times by diffusion modeling of Fe-Mg chemical and isotopic zoning in natural olivines. *Joint meeting of DMG and GV*, Tübingen (Germany).

Oeser M., Horn I., Weyer S. (2012). High precision in situ Fe- and Mg isotope analyses of olivine and reference glasses by femtosecond laser ablation MC-ICP-MS. *European Mineralogical Conference,* v. 1, EMC2012-525.

Oeser M., Strauss H., Peters M., Wolff P.E., Koepke J., Garbe-Schönberg D., Dietrich M. (2012). Hydrothermal Alteration of the Oman Ophiolite: The Message from Multiple Sulfur Isotopes. *International Conference on the Geology of the Arabian Plate and the Oman Mountains*. Sultan Qaboos University, Muscat (Sultanate of Oman).

Oeser M., Strauss H., Peters M., Wolff P.E., Koepke J., Garbe-Schönberg D., Dietrich M. (2011). A Profile of Multiple Sulfur Isotopes for the Oman Ophiolite. *Mineralogical Magazine*, v. 75 (3), 1560.

Thomazo C., **Oeser M.**, Strauss H., Philippot P. (2010). Late Archean oceanic redox fluctuations revealed by iron speciation in the 2.73Ga old Tumbiana Formation. *Geochimica et Cosmochimica Acta*, v. 74 (11) Supplement 1, A1042.